

**INFILL STRUCTURES PROTECTED AGAINST SEISMIC
EXCITATIONS BY POLYURETHANE FLEXIBLE JOINTS**

by

Ahmet Tuğrul Akyıldız

A Dissertation

Submitted to

the Faculty of Civil Engineering of Cracow University of Technology

In Partial Fulfillment of the Requirements for the degree of

Doctor of Philosophy

Supervisor

Prof. Arkadiusz Kwiecień, Ph.D., D.Sc., Eng.

Co-supervisor

Łukasz Hojdys, Ph.D., Eng.



**Politechnika Krakowska
im. Tadeusza Kościuszki**

Kraków, 2023

To my family

It would be impossible to accomplish this without your support

ACKNOWLEDGMENTS

First and foremost, I would like to thank Prof. Arkadiusz Kwiecień for accepting my application to conduct the doctoral study under his supervision, which gave me the chance to pursue my dreams. His continuous support and guidance, as well as the patience and genuine kindness he showed throughout the years helped me achieve what I have today. He has been truly a role model for me not only from the academic perspective but also in terms of being a concerned and compassionate leader that never hesitates his support.

I am also grateful for the supports of Dr. Alicja Kowalska-Koczwara and Dr. Łukasz Hojdys, who agreed to be my co-supervisors at the different stages of my studies, and for being the co-authors of my various academic papers and sharing with me their valuable knowledge and guidance.

Last but not least, the institutions and academic organizations which funded my studies and travel costs that enabled me to participate multiple events and helped me broadening my horizons by means of meeting with valuable researchers across the world are acknowledged herein. These are in the alphabetical order; COST (European Cooperation in Science and Technology), CUT (Cracow University of Technology) and SERA (Seismology and Earthquake Engineering Research Infrastructure Alliance for Europe). Moreover, it was glad to be in cooperation with the IZIIS (Institute of Earthquake Engineering and Engineering Seismology in Skopje) and ZAG (Slovenian National Building and Civil Engineering Institute) laboratories, where I had the chance to work with their hardworking professional staff who made it possible to succeed many rigorous tasks. The material supports provided by Sika Poland and KEBE Northern Greece Ceramics companies are also highly appreciated.

TABLE OF CONTENTS

LIST OF TABLES	7
LIST OF FIGURES	8
LIST OF ABBREVIATIONS	16
LIST OF SYMBOLS	18
ABSTRACT	22
CHAPTER 1. INTRODUCTION	24
1.1 Background and problem statement.....	25
1.2 Proposed solution.....	28
1.3 Objectives	30
CHAPTER 2. EARTHQUAKES AND INFILL WALLS	31
2.1 Basics of the earthquakes.....	31
2.2 Overview of the structural dynamics	37
2.3 Infill wall behaviors during earthquakes.....	43
CHAPTER 3. LITERATURE REVIEW	47
3.1 Experimental tests of the infilled systems	47
3.2 Infill wall modeling techniques	61
3.2.1 Analytical (Strut) modeling approach	62
3.2.2 Numerical (FEM) modeling approach.....	84
3.3 Earthquake protection methods and retrofitting solutions for the infill walls	89
3.3.1 Joint methods	90
3.3.2 Jacketing methods.....	96
3.4 Chapter summary	101
CHAPTER 4. EXPERIMENTAL INVESTIGATION	103
4.1 Quasi-static in-plane shear tests of the infill wall specimens	103
4.1.1 Material properties.....	104
4.1.2 Wallet tests.....	109
4.1.3 Large-scale test setup.....	112
4.1.4 Preparation of the large-scale specimens.....	115
4.1.5 Method of measurement	117
4.1.6 Loading protocol.....	119
4.1.7 Results of the tests	119

4.1.8	Comparison of the measuring methods	125
4.1.9	Section summary of the in-plane tests	127
4.2	Shake table tests of the infill walls in an RC building	128
4.2.1	Test setup	128
4.2.2	Materials	129
4.2.3	Details of the structure	130
4.2.4	Testing facility and equipment	133
4.2.5	Instrumentation	133
4.2.6	Testing methodology	134
4.2.7	Details of the seismic loading	134
4.2.8	Testing phases	137
	Phase 1	138
	Phase 2	142
	Phase 3	143
	Phase 4	145
	Additional remarks	146
4.2.9	Vibration tests	147
	Testing methodology	147
	Vibration results	149
4.2.10	Section summary of the shake table tests	153
CHAPTER 5. NUMERICAL INVESTIGATION		155
5.1	Material constitutive models	156
5.1.1	Concrete	156
5.1.2	Steel reinforcement	163
5.1.3	Masonry infill	165
5.1.4	Polyurethane flexible joints (PUFJ)	170
5.2	Analysis procedure	171
5.3	Results of the numerical analyses	173
5.3.1	Small-size analyses	177
5.3.2	Quasi-static in-plane analyses	180
5.3.3	Dynamic analyses of the three-dimensional building	187
5.3.4	Chapter summary	198
CHAPTER 6. SIMPLE ANALYTICAL PROCEDURE		199
6.1	Analytical calibration results	204

6.2	Dynamic response of the analytical models.....	207
6.3	Chapter summary.....	216
CHAPTER 7. SUMMARY AND CONCLUSIONS		217
7.1	Scheme of the dissertation	217
7.2	General conclusions	218
7.3	Suggestions for the future works	221
APPENDIX A. PUFJ MESH SENSITIVITY ANALYSES.....		222
APPENDIX B. MATERIAL MODELING DETAILS		225
	Concrete	225
	Masonry.....	227
	Reinforcement steel.....	232
	Equivalent strut parameters	233
APPENDIX C. ENERGY BALANCE OF THE NUMERICAL MODELS		235
APPENDIX D. MESHING DETAILS OF THE NUMERICAL MODELS		238
REFERENCES		240

LIST OF TABLES

Table 2.1. Worldwide major earthquake quantities in the recent years [adapted from USGS].	36
Table 4.1. Tests results of the triplet masonry assemblages.	107
Table 4.2. Tests results of the concrete and mortar specimens.....	108
Table 4.3. Tests results of the wallet specimens – all values.....	111
Table 4.4. Tests results of the wallet specimens – statistical values.....	111
Table 4.5. Frame geometrical dimensions and reinforcement details.	113
Table 4.6. Material properties of the shake-table specimen.	129
Table 4.7. Testing phases and loading details.....	138
Table 4.8. Sequence of the performed tests.	148
Table 4.9. Ambient vibration frequency and damping results.....	150
Table 4.10. Forced vibration selected results.....	151
Table 5.1. Concrete and masonry material properties.	175
Table 5.2. Reinforcement steel material properties.	175
Table 5.3. Traction-separation interface properties.	175
Table 5.4. Polyurethane PM hyperelasticity properties.	175
Table 5.5. Dynamic analysis results of the all models.....	195
Table 6.1. Characteristic points (equivalent strut values) of the proposed analytical model for the in-plane pushover tests.....	207
Table 6.2. Characteristic points of the proposed analytical models for the dynamic analyses.	211
Table 6.3. Maximum displacement results for different frame types.....	213
Table 6.4. Normalized maximum displacement results for different frame types.....	214
Table 6.5. Maximum inter-story drift results for different frame types.....	214

LIST OF FIGURES

Figure 1.1. Ancient great masonry buildings; Hagia Sophia (left) [Anadolu Agency] and Colosseum (right) [Wikipedia].	25
Figure 1.2. Examples of the masonry different usage areas; Pont du Gard aqueduct (top) [Flickr], Mostar bridge (bottom-left) [UNESCO] and arch-pillar-wall combination from the Ephesus ruins (bottom-right) [author own].....	26
Figure 1.3. Masonry related failures; (a) infill OOP damage [Dogangun et al., 2013], (b) soft-story mechanism [Sezen et al., 2000], (c) corner crushing of the wall and shear damage on column [Gur et al., 2009] and (d) total collapse of the first floor due to soft-story [Sezen et al., 2000].	28
Figure 1.4. Deformed shapes of the PUFJ specimens (left) and deformation-strength comparison between different joint types (right).....	29
Figure 2.1. Tectonic plates of the Earth [USGS].	31
Figure 2.2. Layers of the Earth [USGS].	32
Figure 2.3. Typical earthquake motion; (a) before energy accumulation, (b) strained and (c) after earthquake [adapted from Celep, 2011].	32
Figure 2.4. Earthquake hypocenter & epicenter [USGS] (left) and seismic waves (right).	33
Figure 2.5. Idealized ground motion derivatives from a point source [adapted from Clough and Penzien, 1995].....	34
Figure 2.6. Accelerogram record of the El Centro 1940 earthquake.	35
Figure 2.7. Seismic hazard map of Europe [Giardini et al., 2014].	35
Figure 2.8. Comparative graph showing earthquake magnitudes and corresponding energy equivalents together with important seismic records and exemplary events [adapted from Bolt, 2003].	36
Figure 2.9. Description of the motion on; (a) actual frame and (b) idealized SDOF system. .	38
Figure 2.10. Comparison between random undamped and damped waves.	38
Figure 2.11. Seismic response of SDOF systems with different natural vibration periods and corresponding spectral displacements.....	39
Figure 2.12. Schematical plots of the spectral response values of displacement (S_d), velocity (S_v) and acceleration (S_a) with respect to the natural vibration period (T_n).....	41
Figure 2.13. Typical normalized response spectra used for the design purposes.	41
Figure 2.14. Moment diagrams for pure gravity loads and earthquake effects separately.	42
Figure 2.15. Typical frame–infill contact mechanism under lateral loads.	43
Figure 2.16. Common structural irregularities; (a) slender columns, (b) sudden vertical stiffness change, (c) undistributed mass, (d) wall configuration in elevation, (e) frame configuration in elevation, (f) in-plane discontinuity, (g) vertical member offsets, (h) torsional sensitivity, (i)	

non-orthogonal systems and (j) soft-story mechanism [adapted from Anderson and Brzev, 2009].	44
Figure 2.17. Common earthquake failures in RC buildings.	45
Figure 2.18. Typical infill wall related damages in RC buildings.	46
Figure 3.1. Vertically uniform wall distribution (left) and soft-story effects inclusion (right) [adapted from Negro and Verzeletti (1996)].	51
Figure 3.2. Plan (left) and elevation (right) views: hatched parts represent the infill walls (units in cm) [adapted from Fardis et al. (1999)].	53
Figure 3.3. Single-story (left) and two-story (right) test specimens [adapted from Zarnic et al. (2001)].	55
Figure 3.4. Typical section detail of the frame-infill joint [from Sahota and Riddington (2001)].	56
Figure 3.5. Three-story structure before the tests [from Pujol and Fick (2010)].	58
Figure 3.6. Test specimen on the shake table [from Stavridis et al. (2011)].	59
Figure 3.7. Infill masonry modeling methods.	61
Figure 3.8. Parameters of the equivalent diagonal strut model proposal of Stafford-Smith and Carter (1969).	63
Figure 3.9. Derivation of the effective width (w) from the equivalent strut width (W) as proposed by Abdul-Kadir (1974).	65
Figure 3.10. Effective strut width proposed by Liauw and Kwan (1984).	67
Figure 3.11. Different strut models (left) and corresponding bending moment diagrams (right) [adapted from Crisafulli (1997)].	69
Figure 3.12. Multi-strut model with shear spring [adapted from Crisafulli (1997)].	69
Figure 3.13. Hysteresis loops for axial (left) and shear (right) responses [adapted from Crisafulli (1997)].	70
Figure 3.14. Multi-strut idealization (left) and load-displacement paths (right) [adapted from Chrysostomou (2002)].	71
Figure 3.15. Three-strut idealization [adapted from El-Dakhakhni et al. (2003)].	72
Figure 3.16. Force-deformation relation of the strut model [adapted from El-Dakhakhni et al. (2003)].	72
Figure 3.17. Schematic strut positions and related definitions [adapted from Fiore et al. (2012)].	74
Figure 3.18. Strut and mass configuration (left) and force-drift relation of the central element [adapted from Furtado et al. (2015)].	75
Figure 3.19. Equivalent strut hysteresis model [adapted from Klinger and Bertero (1976)].	76
Figure 3.20. Mathematical model of the failure mechanism [adapted from Zarnic and Tomazevic (1984)].	77

Figure 3.21. Equivalent strut hysteresis model [adapted from Doudoumis and Mitsopoulou (1986)].....	78
Figure 3.22. Equivalent strut hysteresis model [adapted from Fardis and Panagiotakos (1997)].	79
Figure 3.23. Equivalent strut hysteresis model [adapted from Madan et al. (1997)].	80
Figure 3.24. Shear stress-strain envelope (left) and hysteresis curves (right) [adapted from Kappos et al. (1998)].....	81
Figure 3.25. Envelope curve of the equivalent strut [adapted from Decanini et al. (2004)]. ..	82
Figure 3.26. Equivalent strut hysteresis model [adapted from Rodrigues et al. (2008)].	83
Figure 3.27. Hysteresis pivot model for a generic tension-compression activated situation (left) and modified version for the equivalent struts (right) [adapted from Cavaleri and Di Trapani (2014)].....	84
Figure 3.28. Finite-element discretization of masonry infill (left) and RC members (right) [adapted from Stavridis and Shing (2010)].....	88
Figure 3.29. Infill masonry seismic prevention methods.....	90
Figure 3.30. Sliding mechanism proposal; initial (left) and upgraded version (right) at the end of tests [adapted from Mohammadi et al. (2011)].	91
Figure 3.31. Special design blocks details (left) and construction process (right) [adapted from Vailati et al. (2016, 2018)].....	92
Figure 3.32. Compression disk element (left) and completed construction phase (right) [adapted from Aliaari and Memari (2007)].	93
Figure 3.33. Frame-infill joint detail (left) and construction process (right) [adapted from Tsantilis et al. (2018)].....	94
Figure 3.34. Details of the elastomeric buffering solution [adapted from Marinkovic and Butenweg (2019)].	95
Figure 3.35. Typical gap visualization between frame and infill wall.....	96
Figure 3.36. Horizontal GFRP strips positioning [adapted from Almusallam and Al-Salloum (2007)].....	97
Figure 3.37. CFRP anchorage details [adapted from Erdem et al. (2006)].	98
Figure 3.38. CFRP implementation alternatives [adapted from Yuksel et al. (2010)].	98
Figure 3.39. ECC implementation process [adapted from Kyriakides and Billington (2014)].	99
Figure 3.40. Mortar application with different fiber percentage (left) [adapted from Sevil et al. (2011)] and perforated steel plate bending test (right) [adapted from Aykac et al. (2016)]....	99
Figure 3.41. Steel mesh installation (left) [adapted from Cumhuri et al. (2016)] and ferrocement panel (right) [adapted from Leeanansaksiri et al. (2018)].	100
Figure 3.42. Step by step TRM application on the wall [adapted from Akhoundi et al. (2018)].	101

Figure 4.1. Schematic views of the samples; Frame A (left), Frame B (middle) and Frame C (right).	103
Figure 4.2. KEBE OrthoBlock K100 Brick [adapted from the manufacturer’s catalog].	104
Figure 4.3. Test setups for the triplet specimens; vertical compressive (left), horizontal compressive (middle) and shear (right).	105
Figure 4.4. Horizontal compressive specimens.	105
Figure 4.5. Failures on the compressive specimens; vertical (left) and horizontal (right). ...	106
Figure 4.6. Failure on the shear specimen.	107
Figure 4.7. Cube and beam shaped specimens prepared for the compressive (left) and flexural (right) tests.	108
Figure 4.8. Details of the loading instrumentation (left) and test setup of the specimen WD3 (right).	109
Figure 4.9. Typical damage pattern of the wallets; bottom (left) and top (right) corners.	110
Figure 4.10. Wallet D1 test results; (a) force-time and (b) force-shortening.	111
Figure 4.11. Wallet D2 test results; (a) force-time and (b) force-shortening.	111
Figure 4.12. Wallet D3 test results; (a) force-time and (b) force-shortening.	112
Figure 4.13. Visualization of the frame reinforcement details [dimensions in mm].	113
Figure 4.14. Brick blocks arrangement in the frame.	114
Figure 4.15. Test setup of the frames [dimensions in cm].....	114
Figure 4.16. Construction process of the Frame A.	115
Figure 4.17. PUFJ application on the Frame B.....	116
Figure 4.18. Prefabricated PUFJ laminates (left) and application on the Frame C (right). ...	117
Figure 4.19. Schematic view of the measurement techniques [dimensions in mm].....	117
Figure 4.20. Distribution of DIC reference points on Frame B [dimensions in mm].....	118
Figure 4.21. Utilization of the DIC method on Frame B.	118
Figure 4.22. Loading protocol of the horizontal excitation.	119
Figure 4.23. View of Frame A at the end of horizontal loading test – 1.6% drift ratio.	120
Figure 4.24. Load-displacement hysteresis response of the Frame A.	120
Figure 4.25. View of Frame B at the end of horizontal loading test – 3.5% drift ratio.	121
Figure 4.26. Load-displacement hysteresis response of the Frame B.....	122
Figure 4.27. View of Frame C at the end of horizontal loading test – 4.4% drift ratio.	123
Figure 4.28. Load-displacement hysteresis response of the Frame C.....	123
Figure 4.29. OOP resonance frequency tests; Frame B (left) and Frame C (right).	124

Figure 4.30. Load-displacement hysteresis response of the Bare-Frame.	124
Figure 4.31. Envelope curves of the hysteresis loops.	125
Figure 4.32. Horizontal displacement values of DT and DIC methods for Frame B.	126
Figure 4.33. Drift ratio differences of DT and DIC methods for Frame B.	126
Figure 4.34. Views of the 3D building; schematic drawing (left) and real (right).	128
Figure 4.35. Side section view of the structure [units in cm].	130
Figure 4.36. Cross section view of the RC members [units in mm].	131
Figure 4.37. Implementation of PUFJ on Type B wall (left) and Type C wall (middle), FRPU intervention (right).	132
Figure 4.38. Construction process; slab and hidden beams reinforcement (left) and wall creation on the prefabricated PUFJ laminates for Type C walls (right).	132
Figure 4.39. Construction process; (a) in-situ injection of PUFJ for Type B walls, (b) FRPU intervention application on the Type C wall.	132
Figure 4.40. Schematic view of the measuring instruments from different angles.	133
Figure 4.41. Observed damages from the Kefallonia earthquake reconnaissance reports; shear damages on the walls (left) and severe failures on both RC and masonry elements (right) [adapted from ITSAK, 2014].	135
Figure 4.42. Kefallonia earthquake acceleration-time history record.	135
Figure 4.43. Four-story numerical model; loads and design (left) and damage levels of the RC members (right).	136
Figure 4.44. Top-floor response acceleration-time curve.	136
Figure 4.45. Reduced top-floor response (77% KEF) acceleration-time curve.	137
Figure 4.46. Phase 1 results of the dynamic characteristics of the structure: (a) frame drift, (b) Y-direction stiffness change and (c) X-direction stiffness change.	139
Figure 4.47. Masonry Type B damages at the end of Phase 1; North side wall (left) and South side wall (right).	141
Figure 4.48. Crack pattern on the masonry Type C at the end of Phase 1.	141
Figure 4.49. RC column damages; top end (left) and bottom end (right).	142
Figure 4.50. FRPU intervention on Type B infills; front (left) and perspective (right) views.	142
Figure 4.51. Phase 3 results of the dynamic characteristics of the structure: (a) frame drift, (b) Y-direction stiffness change and (c) X-direction stiffness change.	144
Figure 4.52. FRPU intervention on Type C infills; front (left) and perspective (right) views.	145
Figure 4.53. Phase 4 results of the dynamic characteristics of the structure: (a) frame drift, (b) Y-direction stiffness change and (c) X-direction stiffness change.	146

Figure 4.54. Vibration generator placement; schematic perspective (left) and real (right) views.	147
Figure 4.55. Vibration generator details.	148
Figure 4.56. Mass rotational mechanism; (a) initial position and (b) at time equals to “t”...	149
Figure 4.57. Acceleration-time history results measured by ACC2 device.....	152
Figure 4.58. Acceleration-time history results measured by ACC3 device.....	152
Figure 4.59. Displacement-time history results measured by LP1 device.....	153
Figure 4.60. Displacement-time history results measured by LP2 device.....	153
Figure 5.1. Masonry discretization approaches.	156
Figure 5.2. Yield surfaces in the deviatoric plane for different K_c values.	158
Figure 5.3. Yield surface in the plane stress for CDP model.....	158
Figure 5.4. Uniaxial loading cycle for compression and tension in CDP model [adapted from ABAQUS (Dassault Systemes, 2016)].	162
Figure 5.5. Uniaxial compressive stress-strain relation for concrete.....	162
Figure 5.6. Uniaxial tensile stress-strain relation for concrete.	163
Figure 5.7. Steel reinforcement bar modified stress-strain relation.....	165
Figure 5.8. Stress-strain relationship for masonry compressive model.....	167
Figure 5.9. Stress-strain relationship for masonry tensile model.....	168
Figure 5.10. Possible failure types of the cohesive surfaces.....	169
Figure 5.11. Traction-separation contact mechanism.....	170
Figure 5.12. Plain polymer specimens testing visuals [adapted from Kisiel, 2018].....	171
Figure 5.13. Concrete and masonry inelastic stress-strain curves; (a) compressive and (b) tensile.....	176
Figure 5.14. Reinforcement steel stress-strain relationship.....	176
Figure 5.15. Polyurethane PM test results for plain specimens [adapted from Kisiel, 2018].	176
Figure 5.16. KEBE 100 type orthogonal hollow clay brick (left) and geometrical simplification for the numerical analyses (right).	177
Figure 5.17. Triplet vertical compression test; load-displacement results (left) and numerical model (right).	178
Figure 5.18. Triplet horizontal compression test; load-displacement results (left) and numerical model (right).	179
Figure 5.19. Triplet shear test; load-displacement results (left) and numerical model (right).	179

Figure 5.20. Wallet diagonal shear test; load-displacement results (left) and numerical model (right).	180
Figure 5.21. Bare-Frame cyclic loading results; (a) hysteresis loops and (b) envelope curves.	181
Figure 5.22. Frame A cyclic loading results; (a) hysteresis loops and (b) envelope curves..	181
Figure 5.23. Frame B cyclic loading results; (a) hysteresis loops and (b) envelope curves..	182
Figure 5.24. Frame C cyclic loading results; (a) hysteresis loops and (b) envelope curves..	182
Figure 5.25. Envelope curves of the numerical analysis results.	184
Figure 5.26. Damage visualization of the quasi-static numerical models at the different drift levels.	186
Figure 5.27. Reduced seismic record for the dynamic analyses.	188
Figure 5.28. Dynamic analysis results of the PUFJ – 0 model; (a) displacement, (b) drift, (c) reaction force and (d) acceleration.....	191
Figure 5.29. Dynamic analysis results of the PUFJ – 90 model; (a) displacement, (b) drift, (c) reaction force and (d) acceleration.....	192
Figure 5.30. Dynamic analysis results of the TRM model; (a) displacement, (b) drift, (c) reaction force and (d) acceleration.....	193
Figure 5.31. Dynamic analysis results of the BF model; (a) displacement, (b) drift, (c) reaction force and (d) acceleration.....	194
Figure 5.32. Comparison of the dynamic analysis results (a) drift, (b) reaction force and (c) acceleration.	195
Figure 5.33. Damage visualization of the PUFJ – 0 model at the end of dynamic analysis..	196
Figure 5.34. Damage visualization of the PUFJ – 90 model at the end of dynamic analysis.	197
Figure 5.35. Damage visualization of the TRM model at the end of dynamic analysis.....	197
Figure 5.36. Damage visualization of the BF model at the end of dynamic analysis.....	198
Figure 6.1. Geometrical features of the equivalent strut model.....	200
Figure 6.2. Force-displacement behavior of; (a) different frame configurations regarding the infill presence and (b) multi-linear idealization for the strut modeling.	202
Figure 6.3. Force-displacement features of the proposed multi-linear strut model for different joint configurations.	203
Figure 6.4. Process flow of the strut properties determination.	204
Figure 6.5. Modeling details for the calibration purposes.	205
Figure 6.6. Comparison between the proposed analytical model and in-plane cyclic test results.	206
Figure 6.7. Extraction of the representative frame from the original model; plan (left) and three-dimensional (right) views.	208

Figure 6.8. Details of the multi-story model created for the dynamic analyses.	208
Figure 6.9. Elastic response spectra for the matched, original and target curves.	209
Figure 6.10. Comparison between the matched and original records in terms of the acceleration, velocity and displacement results.	210
Figure 6.11. Displacement results of the different story levels under seismic loading.	212
Figure 6.12. Maximum displacement results under seismic loading; (a) positive and (b) negative directions.	213
Figure 6.13. Visualization of the maximum drift results for different frame types.	214
Figure 6.14. Hysteresis curves of the ML-Links; (a) full and (b) focused views.	215

LIST OF ABBREVIATIONS

AAC	: Autoclaved Aerated Concrete
AFAD	: Turkish Ministry of Interior, Disaster and Emergency Management Presidency
ALC	: Autoclaved Lightweight Concrete
ASCE	: American Society of Civil Engineers
ASTM	: American Society for Testing and Materials
AV	: Ambient Vibration
BF	: Bare Frame
CDP	: Concrete Damaged Plasticity
CFRP	: Carbon Fiber Reinforced Polymer
COST	: European Cooperation in Science and Technology
CoV	: Coefficient of Variation
CUT	: Cracow University of Technology
DEM	: Discrete Elements Method
DIC	: Digital Image Correlation
DT	: Displacement Transducer
EC	: Eurocode
ECC	: Engineered Cementitious Composite
FEM	: Finite Elements Method
FEMA	: Federal Emergency Management Agency
FFT	: Fast Fourier Transform
FRP	: Fiber Reinforced Polymer
FRPU	: Fiber-Reinforced Polyurethane
FV	: Forced Vibration
GFRP	: Glass Fiber Reinforced Polymer
INMASPOL	: Infills and MASONry structures protected by deformable POLYurethanes
IP	: In-Plane
ITSAK	: Institute of Engineering Seismology and Earthquake Engineering (Greece)
IZIIS	: Institute of Earthquake Engineering and Engineering Seismology in Skopje
LP	: Linear Potentiometer
LVDT	: Linear Variable Differential Transformer
MDOF	: Multi Degree of Freedom
ML	: Multi Linear
OOP	: Out-of-Plane
PGA	: Peak Ground Acceleration
PMC	: Polymer Matrix Composite
PUFJ	: Polyurethane Flexible Joints
RC	: Reinforced Concrete
RM	: Reinforced Masonry
SDOF	: Single Degree of Freedom
SERA	: Seismology and Earthquake Engineering Research Infrastructure Alliance for Europe
SIM	: Semi-Interlocking Masonry
SIWIS	: Seismic Infill Wall Isolator Subframe
SLS	: Serviceability Limit State
ST	: Strut Type
TRM	: Textile Reinforced Mortar / Traditional Masonry

TSC : Turkish Seismic Code
ULS : Ultimate Limit State
URM : Unreinforced Masonry
USGS : United States Geological Survey
ZAG : Slovenian National Building and Civil Engineering Institute

LIST OF SYMBOLS

A_{bm}	: Beam cross-sectional area
$A_{c,eff}$: Effective concrete area under tensile effects
A_{col}	: Column cross-sectional area
A_s	: Strut area
A_{st1}	: Single leg area of reinforcement stirrups
A_{wn}	: Wallet surface net area
b_c	: Ratio of plastic to inelastic compressive strain for concrete
b_{cs}	: Width of concrete element cross section
b_t	: Ratio of plastic to inelastic tensile strain for concrete
B_{st}	: Function for calculating steel properties
c	: Equivalent viscous damping
c_{dws}	: Wave speed of materials in explicit analyses
c_p	: Coefficient related to diagonal Poisson's ratio
C_c	: Concrete cover length
C_j	: Factor depends on mortar strength
C_{RD}	: Rayleigh damping matrix
d, d_{inf}	: Infill strut diagonal length
d_b	: Steel bar diameter
d_c	: Damage variable for compression in CDP model
$d_{c,m}$: Compressive damage variable of masonry
d_{cs}	: Effective depth of concrete element cross section
d_t	: Damage variable for tension in CDP model
$d_{t,m}$: Tensile damage variable of masonry
e_{vg}	: Eccentricity of the lumped masses in vibration generator
E	: Young's modulus
E_{br}	: Brick Young's modulus
E_{ci}	: Concrete initial Young's modulus
E_{c1}	: Concrete secant modulus at peak compressive strength
E_f	: Frame material Young's modulus
E_{jm}	: Masonry joint Young's modulus
E_m	: Masonry Young's modulus
E_{st}^*	: Modified Young's modulus for steel bars
f_{br}	: Brick compressive strength
f_{cm}	: Mean value of compressive strength for concrete
f_{ctm}	: Concrete tensile cracking strength
f_{ck}	: Concrete characteristic compressive stress
f_d	: Damped frequency
f_{jm}	: Joint mortar strength
$f_{m,c}$: Masonry compressive strength
$f'_{m,c}$: Masonry peak compressive stress
f'_{m-0}	: Wall orthotropic strength – 0 deg.
f'_{m-90}	: Wall orthotropic strength – 90 deg.
f_n	: Natural frequency
$f_{y,st}$: Steel bar yielding stress

$f_{y,st}^*$: Embedded steel bar actual yielding stress
F_{cr}	: Cracking strength value of infills
$F_{d,max}$: Maximum force value obtained from wallet diagonal tests
F_{peak}	: Peak strength value of infills
F_v	: Column vertical load
g	: Ground acceleration unit
g_w	: Extensometer length
G	: Shear (rigidity) modulus
G_{br}	: Brick shear modulus
G_{CDP}	: Non-associated plastic flow equation of CDP model
G_{cl}	: Concrete crushing energy
G_{Fc}	: Concrete fracture energy
G_{jm}	: Masonry joint shear modulus
G_w	: Wall (or wallet) shear modulus
h, h'_{inf}	: Height (story)
h_{cs}	: Total depth of concrete element cross section
h_w, h_{inf}	: Wall (or wallet), infill height
I	: Moment of inertia
\bar{I}_i	: Deviatoric stress invariants in Mooney-Rivlin hyperelasticity model
J^{el}	: Elastic volume ratio in Mooney-Rivlin hyperelasticity model
k	: Stiffness matrix
k_v	: Parameter of column vertical load effects
K_c	: Second stress invariant in CDP model
K_{cr}	: Stiffness value at initial cracking of infills
K_{dw}	: Wallet diagonal stiffness
K_{EC}	: Constant indicating different masonry groups
K_j	: Cohesive stiffness matrix
K_{peak}	: Stiffness value at peak strength of infills
K_{RD}	: Rayleigh stiffness matrix
K_{soft}	: Stiffness value at tangential softening of infills
l_{eq}	: Characteristic length of the finite-element integration point in CDP model
l_{inf}	: Infill horizontal length
l'_{inf}	: Infilled frame span
l_{st}	: Bonding transmission length of steel bars
L_{min}^e	: Minimum characteristic length of meshed elements
m	: Mass matrix
m_{vg}	: Vibration generator mass
M_{pb}	: Moment capacity of beam
M_{pc}	: Moment capacity of column
M_{pj}	: Moment capacity of joint
M_{RD}	: Rayleigh mass matrix
n_w	: Ratio of the solid area to gross on wallet perforated surfaces
$p_{vg}(t)$: Resultant centrifugal force produced by vibration generator
\bar{p}	: Hydrostatic pressure effective stress in CDP model
P, P_d	: Diagonally applied load on the wallet specimens
P_i	: Pivot points for the strength envelope
\bar{q}	: Mises equivalent effective stress in CDP model

S_a	: Spectral acceleration
S_d	: Spectral displacement
S_{rm}	: Average space between concrete flexural cracks
S_{st}	: Spacing length of the reinforcement stirrups
S_{sw}	: Shear strength of the wallet specimens
S_v	: Spectral velocity
t_j	: Traction stress vector of joints in respective direction
t_w	: Wall (or wallet) thickness
T_n	: Natural vibration period
u	: Displacement matrix
\dot{u}	: Velocity matrix (first derivative of displacement)
\ddot{u}	: Acceleration matrix (second derivative of displacement)
\ddot{u}_g	: Ground acceleration matrix
U_{SE}	: Strain energy in Mooney-Rivlin hyperelasticity model
w, w_{inf}	: Strut width of infill
w_c	: Stiffness recovery factor for compression in CDP model
w_t	: Stiffness recovery factor for tension in CDP model
w_w	: Wallet width
z_{inf}	: Infill panel shape
a	: Strut width equation
a_{CDP}	: Parameter used in CDP calculations
a_h	: Strut contact length (column)
a_l	: Strut contact length (beam)
β_{CDP}	: Parameter used in CDP calculations
β_p	: Coefficient related to diagonal Poisson's ratio
γ_c	: Parameter controlling the stress-strain curve in concrete
γ_{CDP}	: Parameter used in CDP calculations
γ_{sw}	: Shear strain of the wallet specimens
$\gamma_{sw,peak}$: Shear strain value of the wallets corresponding the peak load
δ	: Deflection
δ_j	: Separation matrix in cohesive surfaces
δ_{st}	: Maximum slip of steel bars
Δ_f	: Stress increment constant for concrete
Δt_{stable}	: Stable time increment requirement for explicit analyses
ΔH_w	: Horizontal elongation of the wallets under tension
ΔK	: Stiffness decay
ΔV	: Strength decay
ΔV_w	: Vertical shortening of the wallets under compression
ε_c	: Compressive strain
ε_{c1}	: Strain value at peak compressive strength
ε_c^{pl}	: Compressive plastic strain in CDP model
ε_c^{in}	: Tensile inelastic strain in CDP model
$\bar{\varepsilon}_c^{pl}$: Hardening variable for compression in CDP model
ε_{eng}	: Engineering strain
$\varepsilon_{m,c}$: Masonry compressive strain
$\varepsilon'_{m,c}$: Masonry strain value at peak strength
ε_{st}	: Steel bar strain
ε_t	: Tensile strain

$\bar{\varepsilon}_t^{pl}$: Hardening variable for tension in CDP model
ε_{ti}	: Initial tensile elastic strain limit in CDP model
ε_{true}	: True strain
ε_v	: Column vertical deformation parameter
ϵ	: Flow potential eccentricity in CDP model
ζ	: Damping ratio
θ	: Strut angle
λ	: Non-dimensional parameter defining strut properties
λ_{inf}^*	: Stiffness characterization parameter for struts
μ_{fr}	: Friction coefficient
ν	: Poisson's ratio
ν_d	: Diagonal Poisson's ratio
ρ_{eff}	: Effective reinforcement ratio
ρ_{st}	: Longitudinal steel reinforcement ratio
σ_{b0}/σ_{c0}	: Stress ratio in CDP model
σ_c	: Compressive stress
$\bar{\sigma}_c(\bar{\varepsilon}^{pl}_c)$: Effective cohesion stresses for compression in CDP model
σ_{eng}	: Engineering stress
$\hat{\sigma}_{max}$: Maximum principle effective stress in CDP model
σ_t	: Tensile stress
$\bar{\sigma}_t(\bar{\varepsilon}^{pl}_t)$: Effective cohesion stresses for tension in CDP model
σ_{ti}	: Uniaxial tensile stress at failure in CDP model
σ_{true}	: True stress
ψ	: Dilatation angle in CDP model
ω_{vg}	: Angular velocity of vibration generator

ABSTRACT

Earthquakes are among the most destructive natural disasters that threaten not only the human life but have influence on the economic and social aspects, too. As the civilization grows and evolves into the new stages, our needs have been changing constantly. That being said, we require larger and more complex premises in order to sustain our existence in the modern times. Such developments lead us to understand the nature more comprehensively and find solutions against its harsh conditions. Especially in the seismically active regions of the world, it is anymore largely accepted that the earthquakes do not kill but the buildings. Accordingly, structural engineers working in this field have been looking for protective solutions against the ground shakes for several decades already. In this study, one of these solutions is presented which particularly aim to mitigate the seismic effects on reinforced concrete (RC) buildings constituted with masonry infill walls. For this purpose, flexible joints made of a polymer-based material, called polyurethane flexible joints (PUFJ), is used as a buffer zone between the RC frame and infill wall members. In this way, earthquake induced detrimental effects are aimed to be mitigated by means of dissipating the seismic energy at the critical structural zones.

This dissertation consists of several chapters. In the first two chapters, a brief information about the layout of the work as well as the earthquake phenomenon and its influence on the buildings are provided. Third chapter is dedicated to an extensive literature review for addressing the problem from different point of views and introducing a variety of offered solutions in this regard. The original proposed solution of this study is experimentally investigated in the fourth chapter, and divided into two main campaigns. Firstly, in-plane direction quasi-static cyclic shear tests imposed on the large-scale single-bay and single-story RC frames are tested. The flexible joint solution is implemented in two different ways aiming to provide this technique in new (to-be-built) or old (existing) buildings. As the reference frames for enabling the comparison, additional specimens representing the traditionally constructed masonry infill walls with the stiff mortar joints and the bare-frame without the infill wall are also tested. The results are evaluated in terms of the lateral displacement (and its derivative – the drift ratios) and force resistance capacities. Two distinctive measuring methods, namely the displacement transducers (DT) and the digital image correlation (DIC), are also utilized and the outcomes are compared. In the second experimental campaign, a three-dimensional box-shaped RC building comprised of the masonry infills is built with the aforementioned two different PUFJ solutions and tested against the real earthquake records on

a seismic shake table. Multiple testing steps are followed as the loading methodology for exposing the gradually increasing seismic intensities on the building in the orthogonal loading directions of its horizontal plane. Drift capacities as well as the damage patterns are investigated corresponding the different test stages. In addition, a protective method for providing the quick seismic intervention is investigated, which uses the fiber-reinforced polyurethane (FRPU) wrapping sheets on the masonry members. These diagonally placed FRPU strips are offered particularly for enhancing the drift and strength capacities of the damaged structure in a reasonable level. Moreover, harmonic vibration tests are also performed by a special vibration generating device which led to illuminate the dynamic behavior in the resonance frequency domain. The fifth and sixth chapters are aimed at exhibiting the possibility of computer modeling of the experimental tests and introducing a simple yet noble solution of implementing the PUFJ proposal for the engineering practitioners, respectively. In this regard, appropriate material constitutive models are determined suitable for the finite elements method (FEM) and various numerical analyses are executed. In the final chapter, the findings are summarized and concluded with the future research suggestions.

Overall outcomes of the dissertation demonstrate that the proposed flexible joint solution is an effective seismic protection method, which can be utilized either on new or old buildings. Besides, it is able to be modeled with the commercially available computer programs that provides opportunity of implementing the alternative variations by the engineers working in the field.

CHAPTER 1.

INTRODUCTION

Masonry structures were arguably the most common construction practice had been used for the ages until the modern days. Advances in the building technology has enabled to utilize new techniques, of which reinforced concrete (RC) frames are among the most popular ones. Traditional masonries found new usage areas in such framed systems, particularly being configured as the infill walls which are mainly used for creating dwelling spaces in the multi-story frames. There are certain advantages of the preference of infill walls in the framed systems such as; easy accessibility of the resources for the constituting materials in all around the world, relatively cheaper costs, high thermal insulation features and being suitable for configurations in different forms. However, major concerns arise in the earthquake zones due to the intrinsic characteristics of the infilled frames. Both RC frame and infill walls exhibit brittle behaviors under loads. During a strong ground shake, it is inevitable that damages occur on these members because of the high relative displacement (drift) demands due to the fact that no sufficient ductility could be provided. Failures emerge in the vicinity of boundary connections between the frames and walls, then potentially progress to the other zones based on the intensity of earthquake. Damages might occur simultaneously on both of these structural members that potentially cause the partial or total collapse of the buildings.

In order to prevent frame-infill interaction induced failures, an alternative solution is proposed in this dissertation. Polymer based flexible material called polyurethane flexible joints (PUFJ) are to be utilized as the buffer zone between the infill walls and RC frame. Experiments on the large size specimens are conducted for determining the effectiveness of the solution. The tests are performed in a comprehensive extent under different loading conditions, hence in-plane (IP), out-of-plane (OOP), harmonic and resonance frequency responses are investigated and the results are compared with the traditional construction methods. Following that, numerical analyses are developed and calibrated with the experimental results for simulating the behavior of such systems. Finally, a simplified estimation of the potential strength of PUFJ implemented infill walls is proposed particularly for the engineering practitioners.

1.1 Background and problem statement

Humanity has been challenged by the extreme conditions of nature, since the very beginning of its existence journey. Among those obstacles, it is obvious that the need of accommodation is an uttermost priority to be handled. Our ancestors primarily aimed to find safe places in order to protect themselves from the wild environment, thus they utilized the available existing natural formations according to their needs, such as caves and tree hollows. Gradually and in parallel to the development of human consciousness, the accommodation need has also been evolved over the years and ages. Humankind started to shape the nature in different forms, left their original lands and settled down all around the world. By doing this, various materials that were available in the specific regions were preferred. For instance, timber was popular in the vicinity of forests, whereas clay or earth based other materials were the most common in some other parts of the world. Stone had been also used widely, once the people recognized that some materials could be used as binders for gathering different pieces of the stones into a whole element. In this way, the early stages of the technique of masonry construction have started. Thanks to these developments, in the ancient Egypt, pyramids were able to be built and large span of beams were anymore possible to be placed on the top of high pillars while constructing the large temples. The Romans who recognized how to eliminate the drawbacks of tensile effects, developed the systems working with only pressure forces affecting on the different units of elements which were used for building the multi-story and complex constructions by means of utilizing arches and domes. Hagia Sophia in Istanbul and the Colosseum in Rome are two of the famous examples still standing today since that era, Figure 1.1. Moreover, masonry was also used in the past for different purposes other than residential premises or temples, such as bridges and aqueducts, see Figure 1.2.



Figure 1.1. Ancient great masonry buildings; Hagia Sophia (left) [Anadolu Agency] and Colosseum (right) [Wikipedia].



Figure 1.2. Examples of the masonry different usage areas; Pont du Gard aqueduct (top) [Flickr], Mostar bridge (bottom-left) [UNESCO] and arch-pillar-wall combination from the Ephesus ruins (bottom-right) [author own].

Despite its obvious advantages e.g., strength and durability, stone was not always the most suitable material for the masonry constructions. It is a heavy material and hard to form in different shapes. Therefore, mud bricks were invented in the early stages of civilization in Mesopotamia and the near east. Thus, it was anymore possible to mold the earth in any desired formation. Later on, this phenomenon had evolved to use the modern clay in a similar manner instead of the dry mud. In the near history, another milestone had been reached and the industrial revolution led to the mass production of clay bricks particularly in the western world. Thanks to its versatile usage options and high demand on it, masonry as the primary loading carrying system, kept its popularity until the first decades of the twentieth century. Although steel and concrete took the position of masonry as the main structural source, the variations of masonry systems are emerged upon the new developments in the industry. Currently, different configurations of the masonry origin methods are being used widely. Cladding and architectural design as well as insulation purposes are some of the usage areas. Today,

additionally to the clay made bricks, we are also able to use other modern materials such as lightweight or aerated concrete.

Among the many other usage areas where masonry systems are preferred, infilled wall systems are one of the most popular ones particularly in the urban areas. Typically, the walls are placed in the multi-story frame systems – either made of concrete or steel – and attached to the building by traditional methods such as cement or lime mortar. Very often, the walls are not considered as a part of structural system but merely taken into the account with their weight contribution on the overall building. This is a convenient method of design as long as the loads are predictable and it is assured that the walls are not expected to get damaged. However, it is seen that the infill walls can drastically change the building performance once their stability is lost. This situation can be seen most commonly in the earthquake zones, where relatively unpredictable and massive magnitude of forces threaten the structures in very short time periods. In the frame type ordinary buildings, seismic loads are primarily resisted by the structural walls due to their high inertia capacities. In the absence of specially designed RC shear walls or steel braces, those horizontal forces are received by the remaining members that have relatively higher inertia capacities than columns or beams, such as masonry infill walls. However, these members are commonly not intended for contributing to the structural load carrying capacity but merely designed as auxiliary elements for providing different usage purposes e.g., partition, insulation, decoration etc.

Past studies showed that infill walls significantly change the building response during earthquakes (Asteris, 2003; Kocak et al., 2013; Hermanns et al., 2014). Primarily, the strength and stiffness increase in a building overall or on some particular local zones occurs which depends on the configuration of the masonries at the horizontal and vertical plans. Due to the brittle characteristics of its own and insufficient connection detailing to the surrounding frame, infill walls are prone to get damages quickly. In many occasions it was observed that such failures might lead to partial or total collapse of the infill walls, which progressively cause the redistribution of inertial forces across the rest of structural system that jeopardize the construction stability in terms of several aspects including but not limited to the soft-story and torsional irregularity effects. In Figure 1.3, typical masonry infill related failures occurred during past earthquakes are presented (Sezen et al., 2000; Gur et al., 2009; Dogangun et al., 2013). Moreover, bare-framed buildings are initially designed for behaving in a flexural manner during earthquakes, however, masonries restrict the ductility capacity and therefore causing unpredicted forces on the structure (Al Louzi, 2015). In case of relatively weaker infill wall usage in such systems, the masonries are most likely the vulnerable point and thus, they

are exposed to the damages earlier than the rest of system. On the other hand, designing such walls stronger than the RC members might potentially lead to additional shear forces on the frame itself. Furthermore, the repairing cost of the non-structural parts (e.g., masonries) might be proportionally very high, the most often several times higher than that of the structural member repair needs associated with the earthquake damages (Tiedemann, 1980).



Figure 1.3. Masonry related failures; (a) infill OOP damage [Dogangun et al., 2013], (b) soft-story mechanism [Sezen et al., 2000], (c) corner crushing of the wall and shear damage on column [Gur et al., 2009] and (d) total collapse of the first floor due to soft-story [Sezen et al., 2000].

All in all, despite the positive intentions of constructing infilled systems, detrimental effects are also the matter of concern for the certain situations. In the next chapters throughout the dissertation, different aspects of the problem as well as the proposed solutions are further discussed with details.

1.2 Proposed solution

In the light of above information, an innovative solution constitutes the core of this dissertation which is intended to protect such systems against the aforementioned destructive effects of the earthquakes. Polyurethane flexible joints (PUFJ) aim to dissipate the seismic energy that emerges on the interface between the RC frame and infill walls. Thanks to its highly

deformable hyper-elasticity and strong bonding features, the material is claimed to be an effective way of preventing seismic damages by means of distributing the earthquake induced stresses evenly and thus behave as a buffer joint between the brittle elements, i.e., RC frame and infill walls. Another advantage can be stated as the potential of sustaining wall stability and integration due to providing effective bonding as the joint material.

The flexible joint material that is used between the infill walls and frame members called Polyurethane PM, is chosen from the product catalog of Sika Company. The idea of using the polymer flexible joints in concrete and masonry structures has been pronounced for more than a decade already (Kwiecień, 2012; Kwiecień and Kuboń, 2012). Primarily tested for repairing the cracks in historical masonries as an alternative of the stiff counterparts (Kwiecień et al., 2008; Kwiecień, 2013), the usage purpose of the material has been extended to replace the traditional mortar between the masonry infills and concrete frames (Kwiecień et al., 2017a; Viskovic et al., 2017). Its high bonding strength as well as elongation capacities are proved through experimental and numerical campaigns, which enabled to establishing material constitutive models (Kisiel, 2015; Kwiecień, 2017b; Gams et al. 2017), see Figure 1.4.

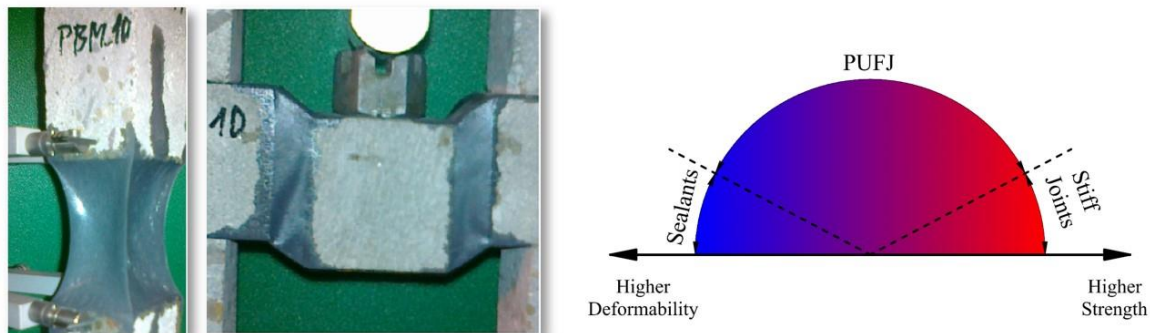


Figure 1.4. Deformed shapes of the PUFJ specimens (left) and deformation-strength comparison between different joint types (right).

Moreover, thanks to its flexible nature, higher stress concentrations at the joints can be prevented, which is a concern in case of using the stiff joints such as epoxy resins (Zdanowicz et al., 2015). The most recent studies also showed that various derivatives of this polymer-based material (with different strength and elongation properties) could be used as a quick seismic protective and repairing solution for the structural components (Zdanowicz et al., 2020) and its effectiveness against the extreme outdoor conditions were presented elsewhere (Kwiecień et al., 2020). It was also shown that the polyurethane flexible adhesive was highly capable of reducing the natural vibrations, hence it provides a source for additional damping mechanism (Lasowicz et al., 2020).

Taking the advantage of all these research programs where the PUFJ was extensively studied, this work focuses on the application of this material in the framework of aforementioned problem needs, rather than focusing on further tests on the material itself.

1.3 Objectives

Accordingly, following objectives are determined while aiming to investigate the hypothesis and propose reasonable solutions:

- Investigating potential damage types on the infilled frames in terms of earthquake engineering and conducting a literature review. In this manner, particularly focusing on the failure mechanisms of the in-plane (IP) and out-of-plane (OOP) damages for the infill walls, and shear effects and drift capacities for the RC members.
- Performing comprehensive experiments on large size specimens for observing the actual behavior and gathering data for determining the effectiveness of the proposed solution.
- Developing non-linear numerical models for predicting the real-like conditions that enables to analyze vulnerability of such systems without the need of costly experiments for the future studies. Besides, testing the proposed solution of PUFJ in the computational environment and calibrating the results with the actual experiments for further applications.
- Proposing a feasible analytical approach compatible with the current seismic codes, especially to be used for the practitioners in the field of structural and earthquake engineering.

CHAPTER 2.

EARTHQUAKES AND INFILL WALLS

Behavior of the infill walls under earthquake effects are discussed in this chapter. Firstly, nature of the seismic motions is briefly shared. Later, influence of the infills are given in terms of different aspects including opposite claims; positive contributions and potential hazards to the structures.

2.1 Basics of the earthquakes

Earthquakes are one of the most destructive natural disasters that occur on many regions around the world. Apart from being extremely fatal itself, an earthquake might be the reason for other catastrophic events including tsunamis on open seas or fires and explosions in urban areas. Although different incidents such as volcanic activities, landslides, mine blasts and nuclear tests can trigger the ground shakes, major earthquakes are caused by the tectonic events related to energy releases in the crust of Earth along the rupture zones (faults). Such earthquakes are the results of seismic waves arising from the sudden movement of plates on the active faults and occur mostly around the tectonic plate boundaries, Figure 2.1.

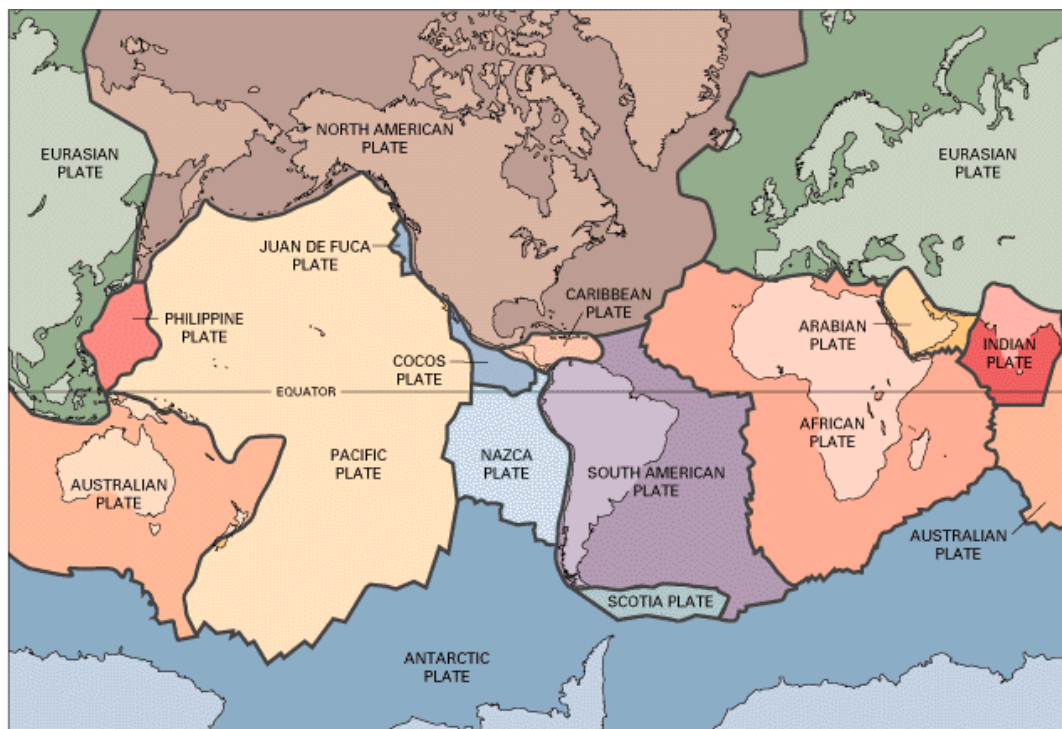


Figure 2.1. Tectonic plates of the Earth [USGS].

The Earth has multiple structural layers as shown in Figure 2.2, and the crust which is the thinnest layer with the average depth around 40 km is located on the outermost part of the Earth. It floats on the surface of the mantle where tectonic plates are also located. Convective circulations in the mantle level trigger the floating motion and therefore, the plates on the crust cannot continue to be in a steady state but rather exhibit movements on the plate edges. However, the boundaries are in rough shapes thus they get stuck at some parts while the remaining zones of the plate are in motion. It is the moment that earthquakes start, when the stress concentration is suddenly released due to the movement of those stuck parts after all. In Figure 2.3, a typical earthquake motion is described.

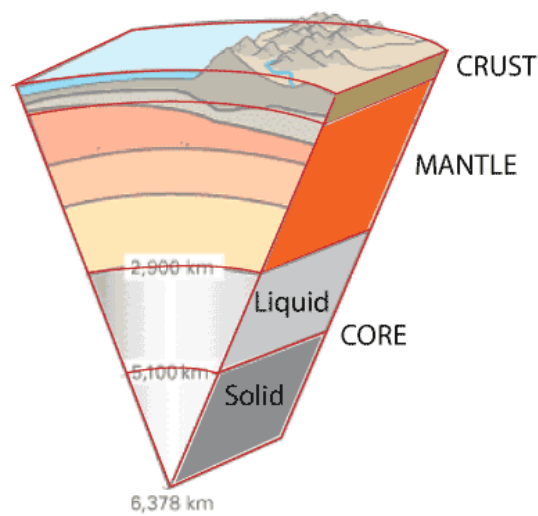


Figure 2.2. Layers of the Earth [USGS].

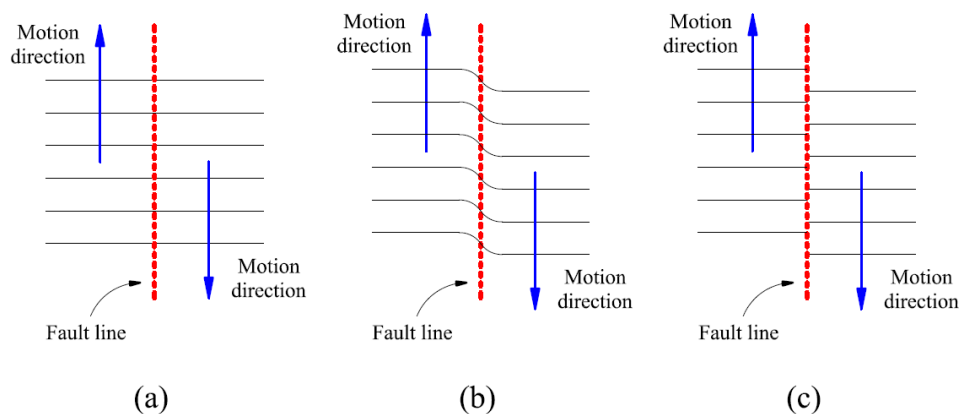


Figure 2.3. Typical earthquake motion; (a) before energy accumulation, (b) strained and (c) after earthquake [adapted from Celep, 2011].

Sizes of the earthquakes are measured by their magnitudes in the logarithmic scale, which depends on the fault size and the amount of slip on it. The actual location of an earthquake under the deep ground is defined by the term of hypocenter (or focus). On the other hand, the point at the surface level directly above the hypocenter is named as epicenter, Figure 2.4. The seismic waves coming from the deep interior of Earth are categorized under four types; of which two are called body waves and the other two as surface waves. The body waves, P (primary) and S (secondary), are the ones used for locating the earthquakes and they can travel through the beneath lithosphere. P waves are relatively much faster and thus could be felt firstly from a distant location. In this type, particles of the materials follow the motion in a way that tension and compression deformations are altered along the wave. For the case of S waves, the shear deformations are induced due to the movement of particles perpendicular to the wave propagation path with relatively larger wave sizes. On the other hand, the surface waves which are named after scientists Love and Rayleigh, cause the most destructive damages on the buildings. They can only travel through the earth surface and the majority of the earthquake related kinetic energy is carried by those. In Figure 2.4, these waves are schematically depicted in the time-amplitude form.

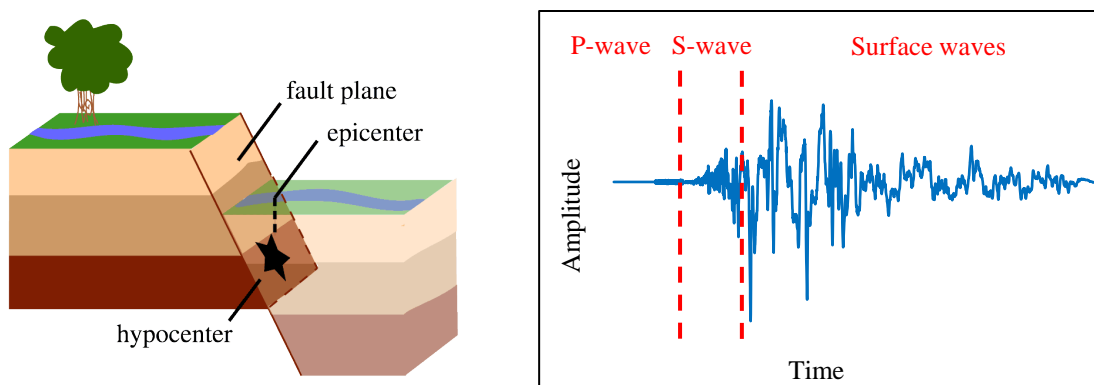


Figure 2.4. Earthquake hypocenter & epicenter [USGS] (left) and seismic waves (right).

When a rupture occurs in the hypocenter, displacement waves evolve at the focus point and spread radially from the source. Schematically, a representative single amplitude displacement wave can be drawn as in Figure 2.5a. Derivation of this displacement with respect to time gives the velocity and acceleration curves as shown in Figure 2.5b and Figure 2.5c, (Clough and Penzien, 1995). However, in a major earthquake there is not only single rupture in the hypocenter, but multiple locations along the fault can be broken in a length of hundreds of kilometers. Therefore, an accelerogram record consist of many of those acceleration values and it plots curves similar of the one given in Figure 2.6, El Centro 1940 earthquake. In the

same figure, highest value of the acceleration history is highlighted in a circle. This point is called as peak ground acceleration (PGA) and it is simply the amplitude of the largest peak acceleration recorded on an accelerogram at a site during a particular earthquake (Douglas, 2003). This value is especially important for the earthquake engineering solutions, since the seismic design codes very often refer to this term as the basis of various calculations. In addition, seismic hazard maps that treat the earthquake phenomenon in a probabilistic approach, utilize the PGA values while determining the seismic risks in a respective zone. For instance, Figure 2.7 represents the seismic hazard map of Europe, where light and cold colors indicate low hazard ($PGA \leq 0.10 \text{ g}$), yellow-orange colors stand for the moderate hazard ($0.10 < PGA \leq 0.25 \text{ g}$) and darker red parts show the higher hazard in the color spectrum due to the possibility of potentially higher PGA occurrence ($PGA \geq 0.25 \text{ g}$) (Giardini et al., 2014).

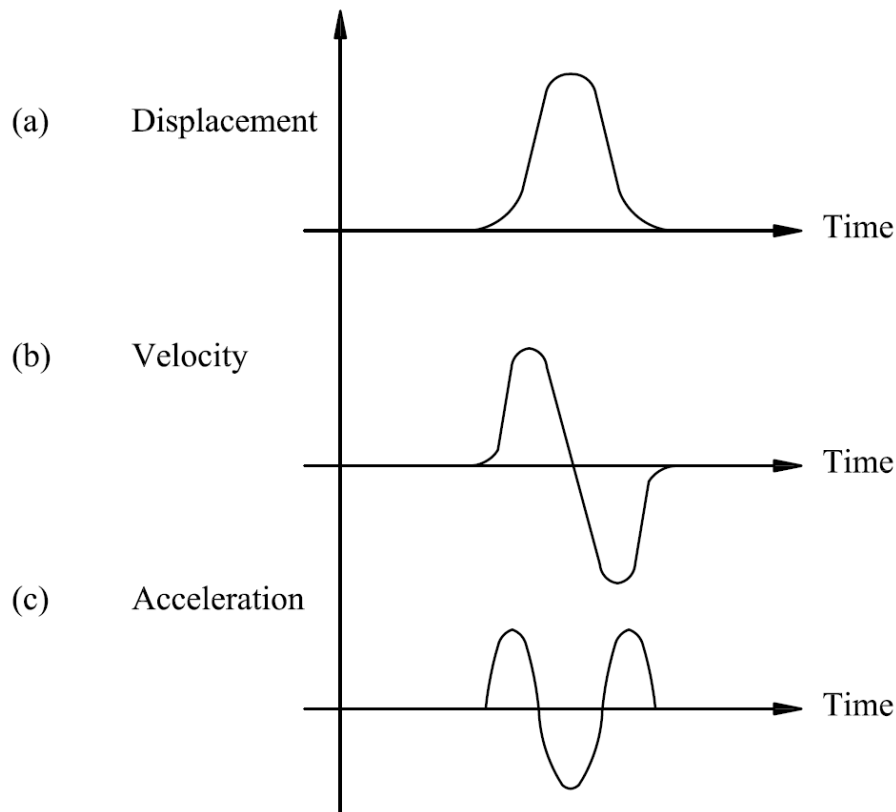


Figure 2.5. Idealized ground motion derivatives from a point source [adapted from Clough and Penzien, 1995].

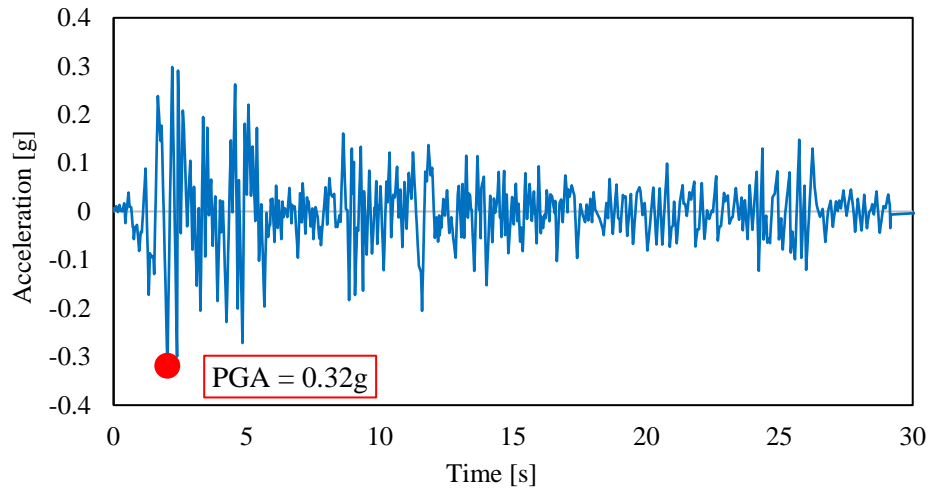


Figure 2.6. Accelerogram record of the El Centro 1940 earthquake.

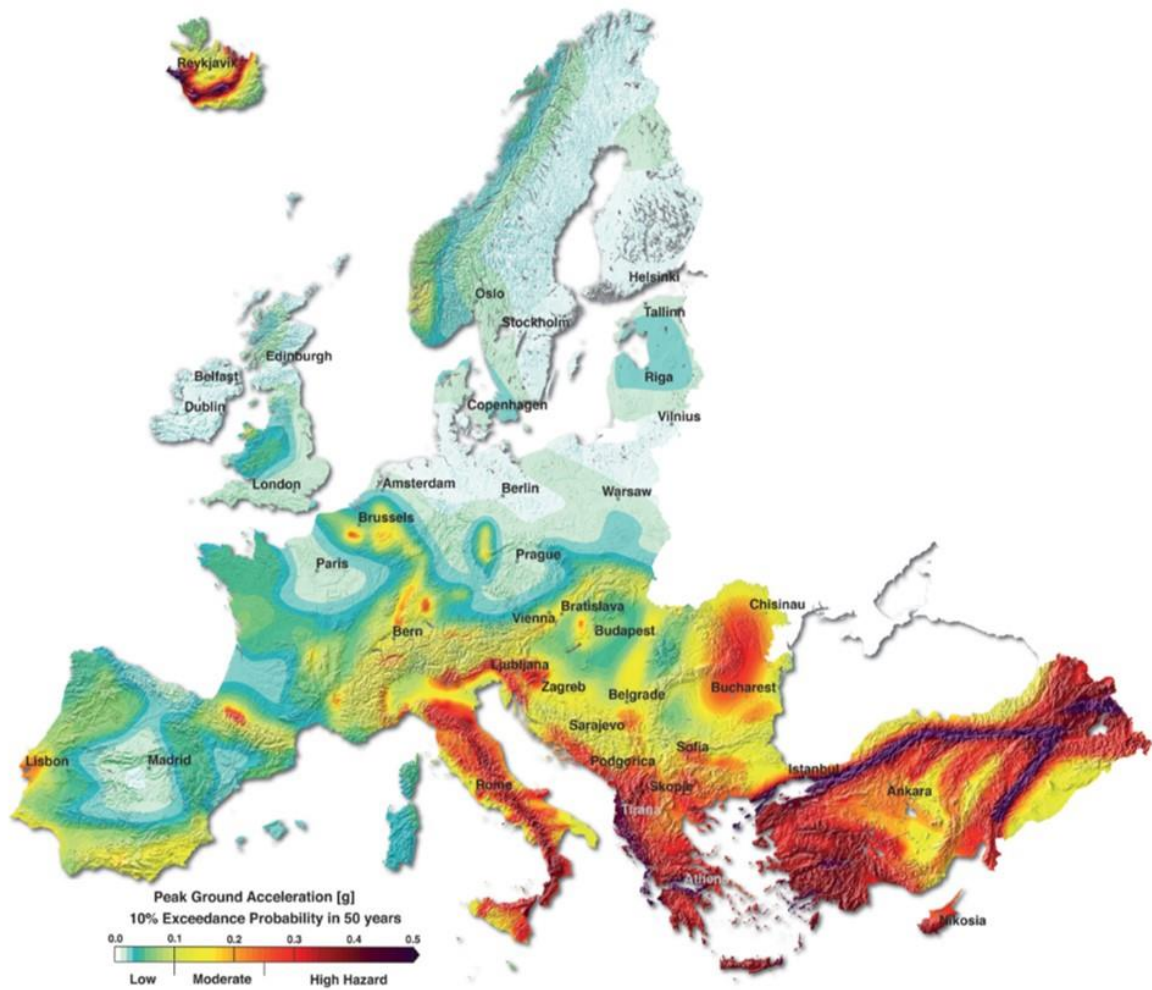


Figure 2.7. Seismic hazard map of Europe [Giardini et al., 2014].

In order to comprehend the impact of earthquakes deeper, Figure 2.8 and Table 2.1 are shared below, where the magnitudes in comparative scales and some other numbers related to the catastrophes are given.

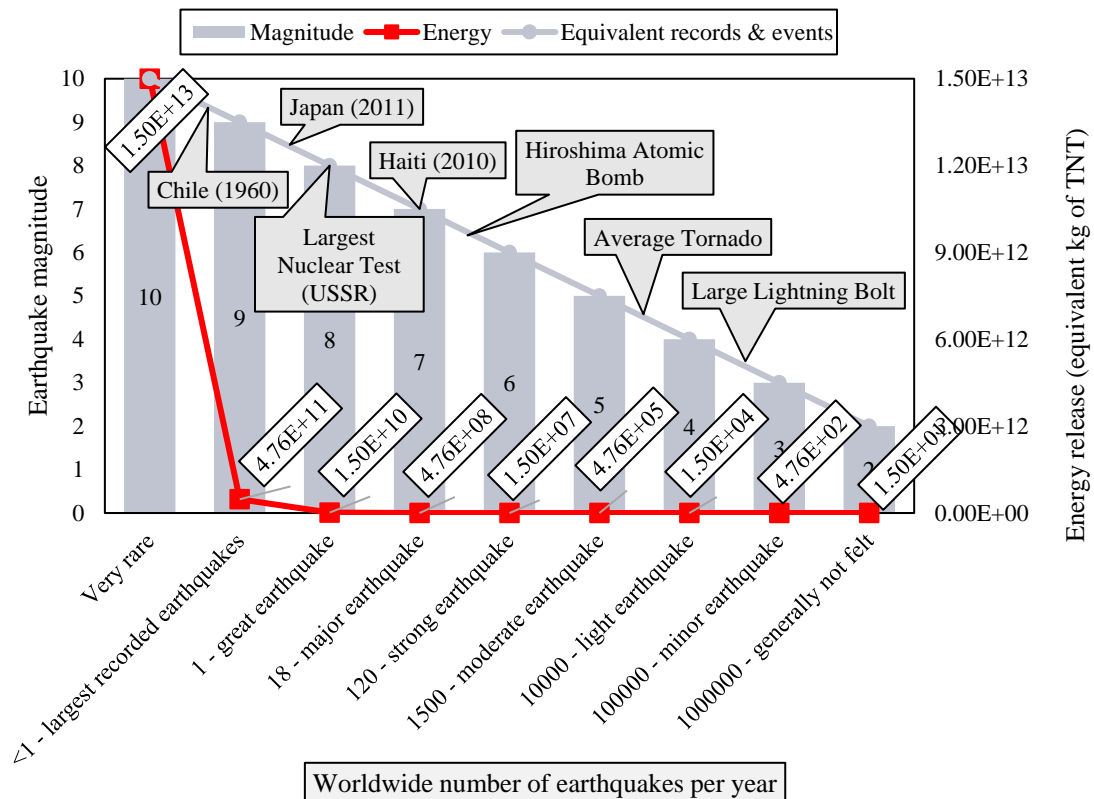


Figure 2.8. Comparative graph showing earthquake magnitudes and corresponding energy equivalents together with important seismic records and exemplary events [adapted from Bolt, 2003].

Table 2.1. Worldwide major earthquake quantities in the recent years [adapted from USGS].

Magnitude	Period [year]			
	2000 – 2005	2006 – 2010	2011 – 2015	2016 – 2020
8.0+	6	8	7	3
7 – 7.9	80	74	77	56
6 – 6.9	815	782	686	598
5 – 5.9	8,180	9,659	8,123	7,483
Estimated deaths	443,185	323,861	34,583	7,088*

* Data not available for 2020

2.2 Overview of the structural dynamics

The field of structural engineering officially started to consider the effects of seismicity and created the first written norms only after twentieth century (Chopra, 1995). In terms of the earthquake engineering, impacts of the ground shakes on the structures constitutes the main interest for engineers. In this sense, dynamic motion of equation for the structural systems can be represented in the simplest form by a structure with the single degree of freedom (SDOF), Figure 2.9. When such a system having a lumped mass “ m ” and lateral stiffness “ k ” is forced to free vibration, meaning an initial horizontal displacement of “ u ” provided without any external excitation e.g., applied force, it oscillates back and forth freely about its initial equilibrium position. In this case, Equation 2.1 can be written where an over-dot on the displacement denotes differentiation with respect to time, therefore \dot{u} and \ddot{u} represent the velocity and acceleration, respectively.

$$m\ddot{u} + ku = 0 \quad (2.1)$$

However, structures in the real life have intrinsic damping features, which steadily reduces the amplitude of vibrations. The damping mechanism is a complex phenomenon that contains multiple factors such as thermal effects of repeated elastic straining of materials and internal frictions arising from solid deformations. For example, friction on the steel joints or opening-closing of micro cracks in concrete matrix as well as interaction between structural and non-structural elements (e.g., infill walls) are some of the natural damping sources. Therefore, an idealization of damping is required for the practical calculations which considers different parameters as mentioned above. Usually, this simplification is represented by the “equivalent viscous damping” denoted by “ c ”. Equation 2.2 shows the damping effect and substituting the Equation 2.1 as below (Chopra, 1995). In Figure 2.10, damping effect of a random sin wave is shown.

$$m\ddot{u} + c\dot{u} + ku = 0 \quad (2.2)$$

Earthquakes affect structures by means of inertial forces and these loads are directly associated with the structural mass, hence the external forces induced by earthquakes can be added into the Equation 2.2. Consequently, $m\ddot{u}_g$ corresponds to the earthquake impact in Equation 2.3, where the term \ddot{u}_g is the ground acceleration.

$$m\ddot{u} + c\dot{u} + ku = -m\ddot{u}_g \quad (2.3)$$

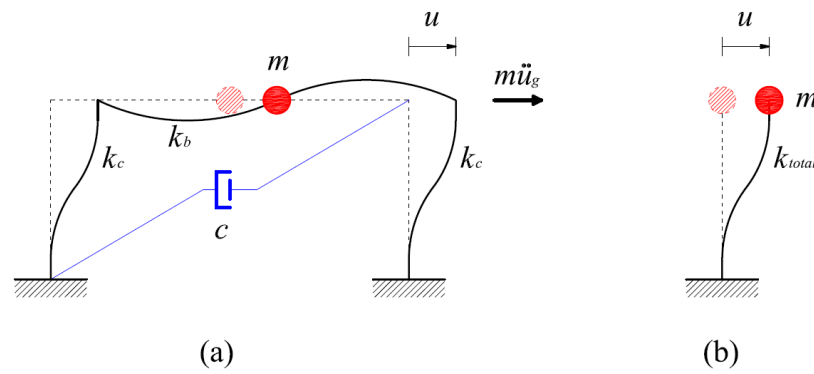


Figure 2.9. Description of the motion on; (a) actual frame and (b) idealized SDOF system.

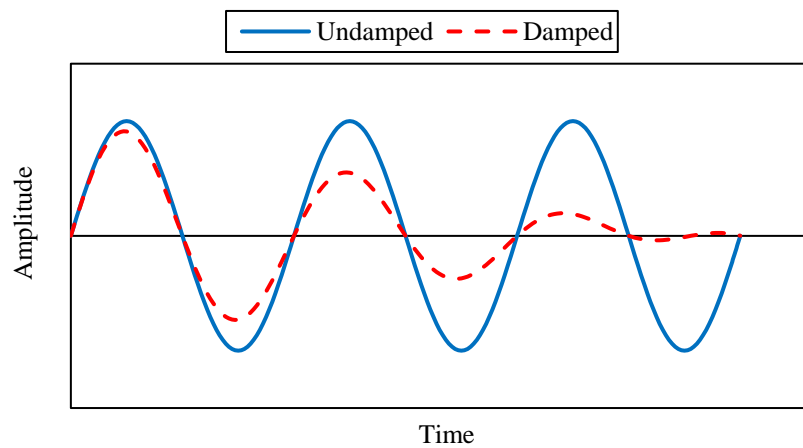


Figure 2.10. Comparison between random undamped and damped waves.

In the design practice of earthquake engineering, unless for some specific purposes, it is not common of using the time history records obtained from the real earthquakes directly. Because, such records are very random in terms of their amplitudes and durations, besides, they do not represent necessary data for the desired seismicity conditions such as soil features. Therefore, instead of the real ground shake records, elastic response spectrums are largely used almost in any modern seismic design code such as Eurocode-8 (CEN, 2004a), ASCE-7 (ASCE, 2010) and Turkish Seismic Code (AFAD, 2018). In this method, SDOF systems having constant damping ratio (ζ) but different natural vibration periods (T_n) are subjected to excitations in the form of acceleration–time plots (e.g., earthquake records), and structural responses of those are calculated. Since it is often sufficient to estimate the largest displacement amplitude with respect to time, the integrated response of different T_n values provides a spectrum for structures with various natural periods. In this way, spectral displacement (S_d) and corresponding T_n values can be plotted, as shown in Figure 2.11. The range of natural

vibration for typical buildings usually takes place between 0.03 to 3 seconds (Chen and Lui, 2006), however, it can be also longer especially for the high-rise buildings. Nevertheless, the design codes usually provide equations for estimating responses in different periods. On the other hand, the provisions rely on the spectral acceleration (S_a) values while standardizing the response spectra behaviors. Since the acceleration is the second derivative of the displacement with respect to time, below equations can be written where S_v is the spectral velocity (Chopra, 1995).

$$S_v = \left(\frac{2\pi}{T}\right) S_d \quad (2.4)$$

$$S_a = \frac{2\pi}{T} S_v = \left(\frac{2\pi}{T}\right)^2 S_d \quad (2.5)$$

Finally with the aforementioned information, response spectra of S_a , S_v and S_d can be schematically illustrated as in Figure 2.12. Moreover, many of the modern earthquake norms provides normalized S_a spectrums for enabling to solve problems smoother and easier for the designers, see Figure 2.13. In order to take into account the specific soil types in construction sites and probabilistic earthquake hazard conditions mentioned earlier, additional parameters are also used in the seismic codes for determining the design response spectra. In this way, initially assumed ground acceleration for the SDOF systems can be modified for the desired earthquake intensities.

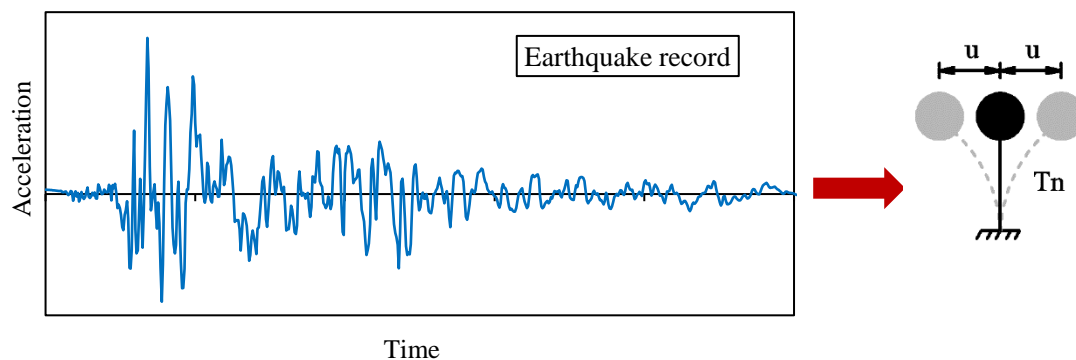


Figure 2.11. Seismic response of SDOF systems with different natural vibration periods and corresponding spectral displacements.

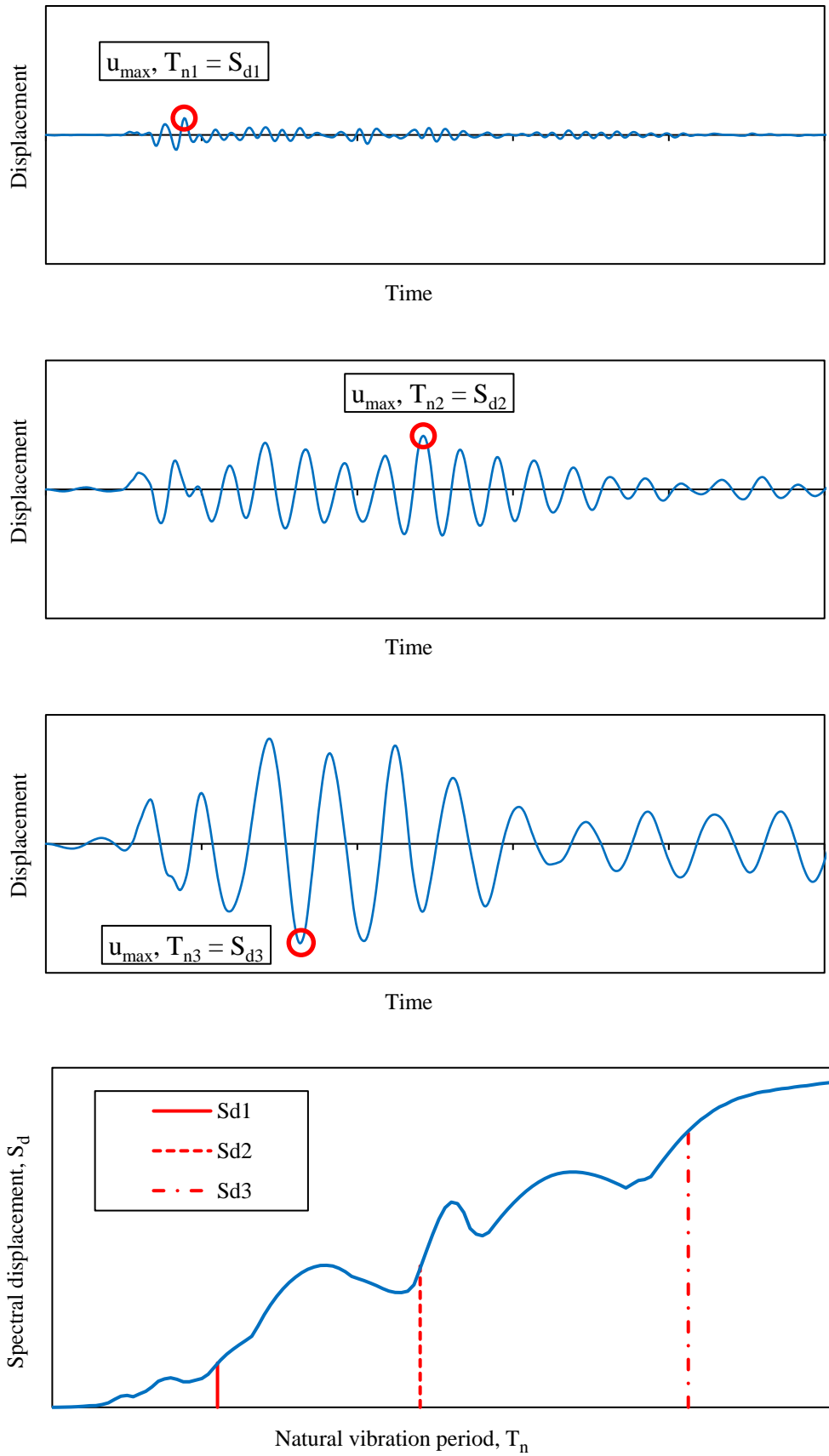


Figure 2.11. (continued).

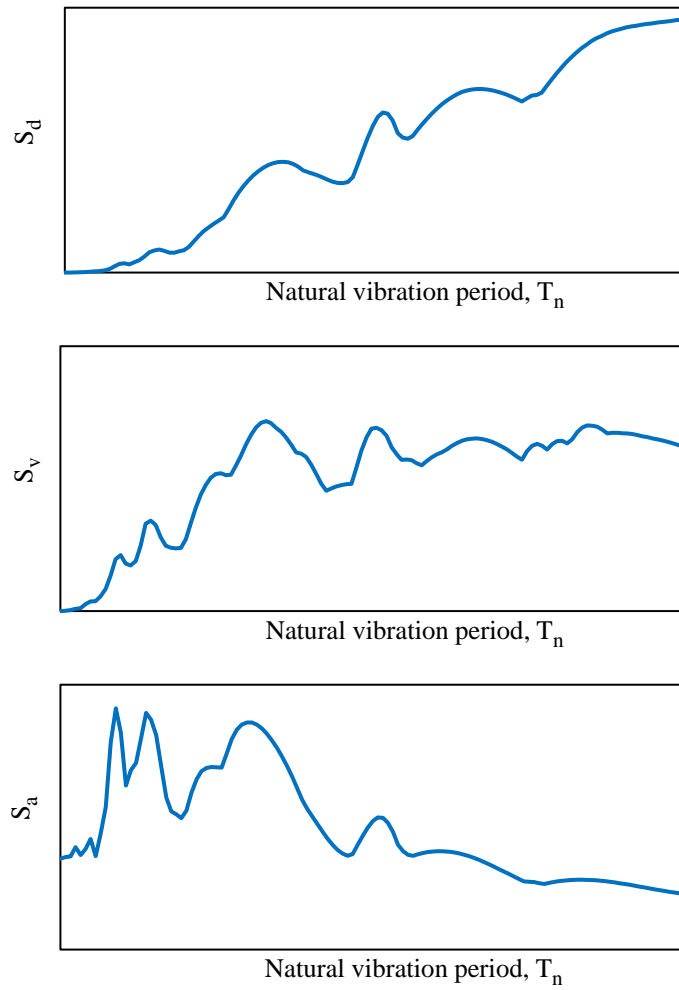


Figure 2.12. Schematical plots of the spectral response values of displacement (S_d), velocity (S_v) and acceleration (S_a) with respect to the natural vibration period (T_n).

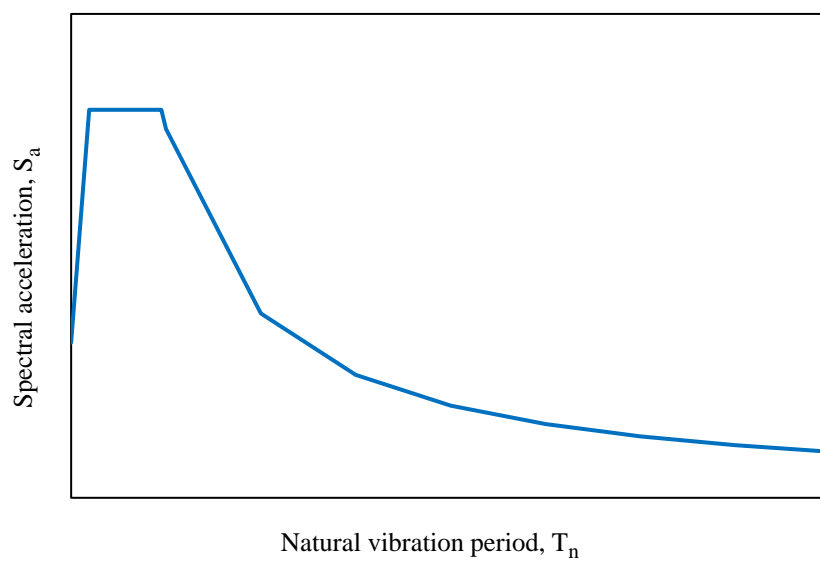


Figure 2.13. Typical normalized response spectra used for the design purposes.

In a multi-story building, obviously there are more structural elements than idealized single degree of freedom systems. On the other hand, the behavior of earthquake response is quite similar, such that inertial forces affect on the parts with larger masses – which is mostly the floor levels in a building – and vertical members e.g., columns and walls that resist to those forces as long as their stiffness and strength capacities permit. Typically, while a building starts to swing in a similar way of the oscillation of SDOF systems, joint zones of the different structural members (beam-column, beam-wall, column-wall etc.) receives the greatest forces on the floor levels. This situation is rather different than the usual moment diagrams drawn under the effects of merely vertical loads. Lateral loads induced by an earthquake cause butterfly shaped moment diagrams on the frame, where the peak values are accumulated at the joint zones. Particularly columns are highly affected by these additional loads, since in a multi-span frame the moments are generally balanced through neighbor spans, see Figure 2.14. As a result, columns tend to exhibit lateral displacements and thus initial shapes of the voids between the columns and beams are distorted. In case there any structural elements placed in those voids, commonly it is the case where the infill walls are constructed, aforementioned additional joint loads are transferred also to the infilled parts. At this stage, compressive forces emerge starting from the contacted corners and continue through the wall in-plane direction, whereas disconnection of the wall-frame joints is the concern for the other corners. This situation is visualized in Figure 2.15. In brief, this is one of the failure mechanisms of the infill walls in frame structures. Further details will be discussed in the next sections.

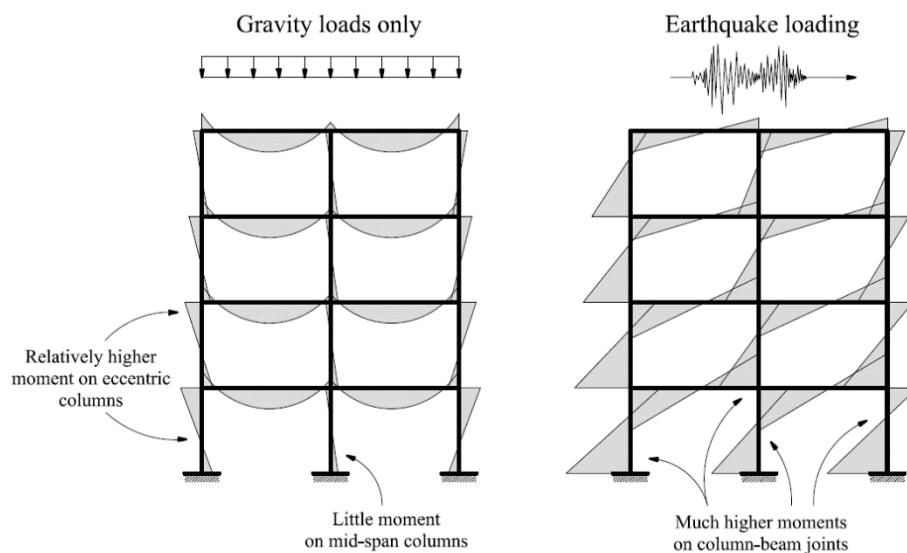


Figure 2.14. Moment diagrams for pure gravity loads and earthquake effects separately.

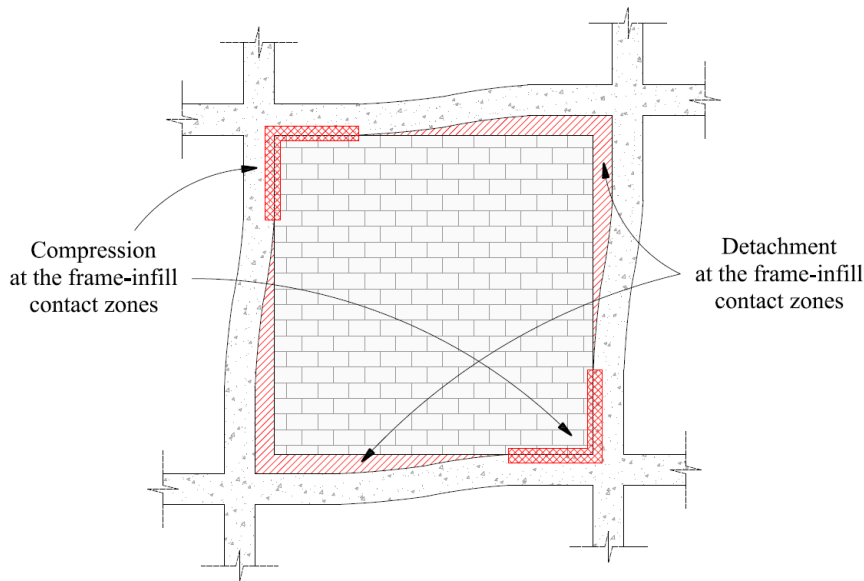


Figure 2.15. Typical frame–infill contact mechanism under lateral loads.

2.3 Infill wall behaviors during earthquakes

Before providing more details regarding the infilled systems, it is wiser to comprehend the earthquake influence on structures a little bit more. The process of seismic resistant design starts from the very first sketch drawings of the architectural phase and take its final shape in the calculations of engineers. There are simple, yet crucial aspects of the seismic resistant design. Principally, symmetrical and architecturally less complex systems are recommended. For example, joints are required for separating geometrically irregular structures and preventing pounding effects on the adjacent buildings and besides long cantilever offsets (vertically unsupported large balconies, terraces etc.) should be avoided as much as it is possible. However, it is not always feasible to simplify the architectural demands. In this case, below points are some useful tips while providing feasible solutions (Bachmann, 2003). Respective informative visualization of the most common structural irregularities is provided in Figure 2.16.

- Avoiding soft-story floors in a way that infill walls do not pose any risk to the drift capacity of the floors.
- Configuring bracing mechanisms e.g., shear walls and steel braces, symmetrically in plan and sustaining their continuity vertically.
- Avoiding strong masonry utilization in frame buildings and providing convenient joint solutions for the infilled systems.

- Matching flexural and displacement capacities of the structural (e.g. frame) and non-structural elements (e.g. infill walls)
- Eliminating possible short column risks by means of avoiding ribbon windows on infill walls (partially infilled frames) and following the strong column & weak beam principle.
- Providing ductile solutions that can absorb the seismic energy as per the capacity design principles of buildings.

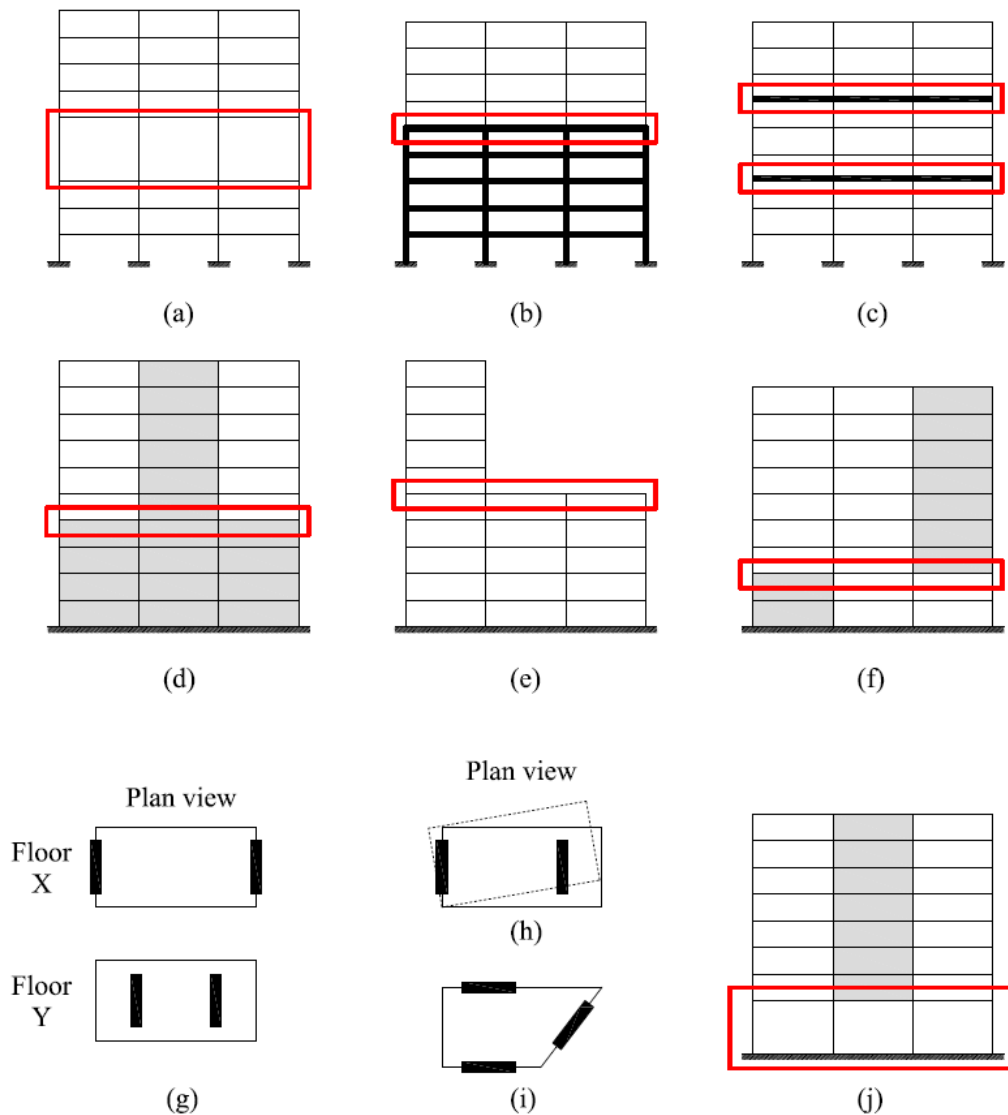


Figure 2.16. Common structural irregularities; (a) slender columns, (b) sudden vertical stiffness change, (c) undistributed mass, (d) wall configuration in elevation, (e) frame configuration in elevation, (f) in-plane discontinuity, (g) vertical member offsets, (h) torsional sensitivity, (i) non-orthogonal systems and (j) soft-story mechanism [adapted from Anderson and Brzev, 2009].

Furthermore, specifically for RC buildings, the most common failure mechanisms of the individual structural elements are listed in Figure 2.17 (Griffith, 2008).

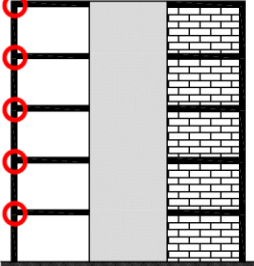
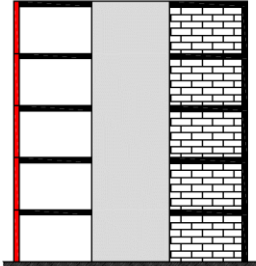
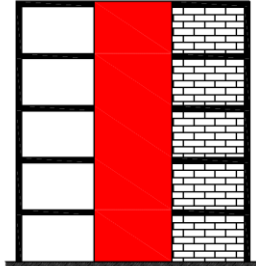
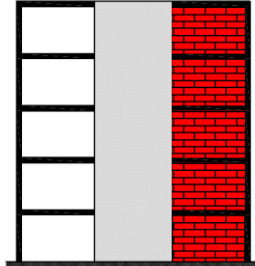
Failure Types			
Beam-column joint	Column	Shear walls	Infill walls
Deficiency of joint stirrup reinforcement and/or anchorage of beam longitudinal rebars	Inadequate flexural and/or shear strength	Deficiency of overall reinforcement and/or poor connection detailing to the surrounding frame	Lack of masonry IP shear and/or OOP flexural strength
			

Figure 2.17. Common earthquake failures in RC buildings.

Above remarks address that majority of the failure types are either primarily or indirectly related to the infill walls. Moreover, infill wall damages hold a special position among those failure types due to the fact that these members are in most instances thought as non-structural elements. Unlike the other RC members, it is known that interaction of the masonries with the rest of system is practically omitted during the design phase [Longo et al., 2016; Preti et al., 2015; Razzaghi et al., 2015]. On the other hand, as it is mentioned previously, the interaction of these different elements can cause damages on each other and jeopardize the building overall strength. Nevertheless, possible failure mechanisms specifically associated with the infill walls are also studied previously (Mehrabi et al., 1996; El-Dakhakhni et al., 2003) and the most common damages are determined as shown in Figure 2.18.

Accordingly, Figure 2.18 exhibits a fact that in-plane (IP) related forces constitute the biggest proportion of the infill wall related damages. However, it is known that out-of-plane (OOP) damages are natural outcomes of the progressively developing IP related failures on the masonries (Lourenco, 1997) and normally expected not to occur as long as an appropriate connection detailing to the surrounding frame is provided.

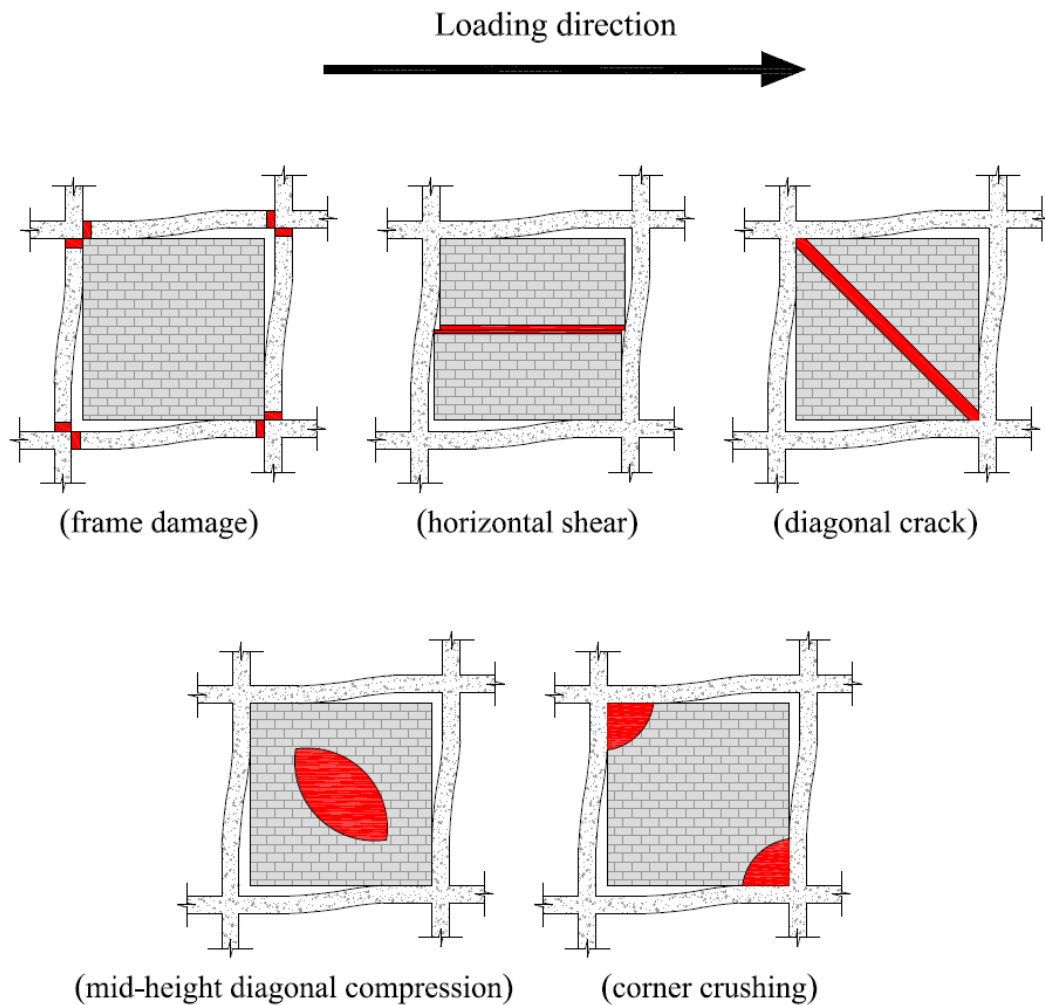


Figure 2.18. Typical infill wall related damages in RC buildings.

Today, structural engineers are well aware of that infill wall influence on the dynamic characteristics of a building cannot be neglected. However, there is not a consensus whether the infill walls contribute to the dynamic performance (Spence et al., 2003) or adverse effects might outweigh the positive ones (Saatcioglu et al., 2001). There are different concerns and claims declared by the researchers. Following chapter is dedicated for reviewing the literature in this regard.

CHAPTER 3.

LITERATURE REVIEW

First discussions on the topic of influence of the masonry panels in a structural frame is dated back to the late 1930s (Mohyeddin et al., 2013). In the following years, experts in the field started to investigate the issue in variety of ways and therefore conducted experimental campaigns. Moreover, analytical and numerical methods have been developed in order to simulate the infill wall behavior. In the first section of this chapter, particularly the test results received from some remarkable experiments are highlighted; and later, the masonry infill modeling techniques are discussed in the following sections. Furthermore, several seismic preventative methods specifically designed for the infill walls are reviewed at the end of this chapter.

3.1 Experimental tests of the infilled systems

Sachanski (1960) conducted one of the first comprehensive studies regarding the theoretical and experimental investigation on a building comprised of an RC frame infilled with brick or lightweight concrete masonries, where in total 29 half and full-size infilled frames with and without openings were tested. The effects of the infill distribution on the plan and related irregularities were pointed out which eventually influence the overall stiffness features of buildings. In the theoretical part, the behavior of masonry, infill and joints were evaluated separately in terms of the horizontal force induced stresses. Masonry was considered as an elastic material and the stress functions were presented by some polynomial expressions which were also used for defining the contact behavior and the load transfer from the frames. Load carrying capacity, deformations, stiffness and distribution of the forces between the frame and masonry were aimed to be explained accordingly. The test results indicated that the typical damages occurred on the walls without openings were due to the tensile forces at the center of masonries in a form of diagonal cracking. Experimental results also revealed that full-size elements were essential for correctly understanding the nature of such systems, since the reduced size specimens exhibited inconsistencies with the actual size results. Other than that, by the theoretical method, the load which caused the first diagonal fissures on the masonry could be obtained with a close match to the experimental results.

Mallick and Severn (1968) performed probably one of the earliest studies concerning the dynamic nature of the infilled frames. In this regard, half-cyclic experimental tests (only considering the compressive stresses) were actualized and these were attempted to be explained by some simple analytical methods. Their study was important particularly because of two reasons; the significance of the damping effects was pronounced while determining the natural frequencies and mode shapes. Besides, it was demonstrated that the infilled frames were prone to move as a cantilever beam rather than the typical unconfined masonry which would be expected to behave in a shear dominant form.

Fiorato et al. (1970) prepared a technical report to the governmental authorities related to the interaction between the RC frames and masonry infill walls, as there was a need of experimental evidence regarding the response of multi-story systems under lateral loads. To this end, one-eighth scale specimens were prepared in the following forms; eight single-story and single bay, twelve five-story and single-bay, and lastly six two-story and three-bay infilled frames with and without openings. Other than these configurations, frame reinforcement and vertical loads on the columns were also additional variables. All specimens were tested up to the failure. It was concluded that, the combined behavior of the infill panels and frames led to stiffer structural system than the cumulative acting of the frames and walls alone, therefore interaction of those cannot be ignored in order to execute an accurate representation of such systems. Furthermore, the initial response of the frames was similar to the typical cantilever beams until first cracks occurred on the walls. After that, the system rather exhibited a behavior of the knee-braced like frames. It was also remarked that the openings caused more ductile systems with reduced strength.

Klinger et al. (1976) prepared a technical report in a similar manner of the aforementioned study of Fiorato et al. (1970); however, this time the concern was related to the behavior of infilled systems under reversed cyclic loads in order to simulate an earthquake-like scenario. Therefore, the experimental phase of their study was focused on the quasi-static cyclic tests. For this purpose, one-third scale specimens as the representative of the lower three-story levels from an eleven-story building were extracted and then constructed in one and a half bay infilled frame shape. While designing the specimens, a careful attention was shown towards the structural detailing so that capabilities of the infilled systems could be revealed precisely. Accordingly, the frame members – especially columns – were constructed with high ductility design principles and closely spaced infill reinforcement details were provided for a gradual panel strength degradation. Besides, the wall thickness was kept relatively limited, thus any premature frame failures could be prevented. Firstly, the bare-frame was tested and

following that the same frame was infilled with clay bricks and tested again. Finally, two new frames, one with the clay bricks and the other with the concrete blocks, were tested. According to the results, the infilled frames exhibited visibly better performance of the energy dissipation even above the excessive drift levels of 2%, thanks to the presence of the infill panels where the friction related mechanisms absorbed the substantial amount of hysteretic loading energy. On the other hand, the bare-frame could only resist such forces through the plastic hinges which made such systems vulnerable when it comes to sudden collapse risks. Moreover, an analytical study was conducted in this regard, however the details are shared next, in the Section 3.2.1.

Dawe et al. (1989) aimed at investigating the dynamic response of the infilled structures with the shake table tests. Accordingly, total amount of ten one-third scale single-bay and single-story specimens were divided into different groups based on the various frame dimensions and rigidity conditions, namely with flexible corners or with rotationally rigid corners provided by a concrete slab on the top-beam level. Bare-frames with these variations were also included in the tests for the comparison purposes. The specimens consisted of masonries made by solid clay bricks enclosed with rigidly connected rectangular steel frame members. As the testing procedure, sinusoidal waves were utilized in a way that each specimen was subjected to gradually increasing ground motions and frequency intensities, thus possible seismic frequency ranges were aimed to be covered. The tests were continued until the panels were destructed. The results indicated that the presence of infills substantially increased the stiffness and strength of the frames and helped to prevent resonance frequency excitations. Moreover, initial relative stiffness of the frame members and joint details also altered the results, such that the highest stiffness and strength performance was achieved with rotationally rigid corners though this detail typically concerns the steel frames rather than RC buildings. In addition, crack patterns of the masonries were also distinguishable for those.

Mehrabi et al. (1994, 1996) conducted a large experimental survey on the masonry infilled RC frames and constructed twelve half-scale single-bay and single-story specimens. In addition, two double-bay and single-story specimens were also tested. The frames were divided into two main groups for representing weak (designed for the wind loads only) and strong (compliant with the seismic demands) frames. Variety of the other conditions were also taken into account, namely type of masonry units (no infill, hollow or solid concrete blocks), wall aspect ratio (height-to-length of 1/2 or 2/3), lateral loading type (monotonic or cyclic) and distribution of the vertical loads (either on columns or beams). In general, the results demonstrated a fact that the presence of the infill walls can substantially enhance the strength and stiffness performance of the frames, as long as these are properly designed and constructed.

Being more specific, the combination of strong-frame and strong-panel revealed the best performance in terms of the load carrying and energy dissipation capabilities. Other than that, it was seen that increment of the vertical loads could result some improvements on the stiffness and maximum strength values by 30% and 25%, respectively. Another remarkable outcome was that the frames which were subjected to the cyclic excitations could resist relatively lower loads and a faster strength degradation was observed for those, when compared to the frames excited with the monotonic loading. Therefore, the distinctive characteristics of these testing methods should be considered for such studies.

Abrams et al. (1996) were motivated to study a relatively new subject. They claimed that the out-of-plane topic of the masonry infill panels took the attention of the blast related scenarios by that time rather than the seismicity induced hazards. In terms of the earthquake engineering, majority of the studies focused on the in-plane behavior, except only a few researches which were primarily concerned with the out-of-plane effects. The authors stated that there was a lack of evidence regarding the out-of-plane behaviors of the infill walls which were previously damaged due to the in-plane loads. Therefore, eight real-size infill panels were tested which had various masonry and mortar unit types as well as different panel height-to-thickness ratios (h/t). The frames were firstly exposed to the in-plane cyclic loads until the initial cracks were observed, and then the out-of-plane forces were subjected to the panels by an airbag in order to produce the arching mechanism. Moreover, an analytical model was also developed for predicting the aforementioned conditions. As an important outcome of that study, it was declared that the transverse strengths of the panels were highly dependent on the h/t ratio. Besides, there was no linear correlation between the h/t ratio and the applied out-of-plane pressure, since the decrease on the h/t ratio resulted exponentially growing pressure capacity.

Negro and Verzeletti (1996) carried out pseudo-dynamic tests on a full-scale high-ductility four-story RC building with two spans in each orthogonal direction as a part of the program for providing an auxiliary inventory for the Eurocode 8. Due to the sizes of the elements and the testing methods, it could be said that their study was quite advanced than the majority of the former investigations up to that date in this field. Initially, the bare-frame formation was tested by a modified version of a real earthquake record and the damage patterns were recorded. Overall, there were no substantial damages thanks to the proper seismic detailing, hence the experiments proceeded without any repair on the frame members. Following that, two additional pseudo-dynamic tests were performed with the identical

excitation that of the bare-frame, however this time the frame was configured with different infill panel layouts. First, a uniform wall distribution was provided vertically on the external side of the frame. Later, the test was repeated but now the walls in the first story were removed in order to practice the soft-story effects, see Figure 3.1. In this sense, their study was particularly focused on the infill distribution irregularities in elevation. The infill walls were constructed with typical light-weight non-structural hollow clay bricks which were bonded with traditional cement-lime mixed mortar. The results indicated that the infill panels could change the structural dynamic response drastically, despite being considered as non-structural members and labeled as light-weight elements. Energy absorption could be achieved by the infills, though severe damages are expected to be accumulated on those parts in return for protecting the RC elements. Furthermore, it was emphasized that panel distribution irregularities could pose high risks and therefore cannot be ignored during the design process. For instance, maximum top story displacement values for those bare-frame and soft-story buildings were comparable, though the uniformly distributed infills led to limit such deflections up to 2.5 times lower values.

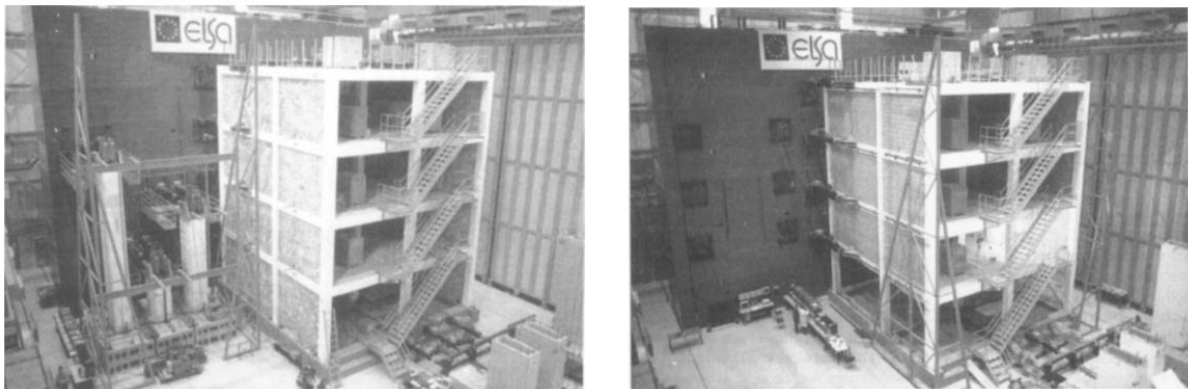


Figure 3.1. Vertically uniform wall distribution (left) and soft-story effects inclusion (right) [adapted from Negro and Verzeletti (1996)].

Mosalam et al. (1997) pointed out the importance of cyclic loading schemes as an experimental methodology and conducted a series of quasi-static tests with the concrete block infilled quarter-scale one-story steel frames. No shear connectors were provided around the panels and the frames were designed according to the gravity-load carrying philosophy only for representing a structure located in a low or moderate earthquake region. Several parameters were considered as follows; relative strengths of the masonry blocks and mortar, number of bays (either one or two) and openings on the walls (door vs window or symmetric vs asymmetric). According to the results; mode of failure of the infill walls were highly affected

by the relative strengths of concrete and mortar. However, the ultimate load capacity was found nearly independent of the mode of failure, though this value was observed to drop to the levels around 50% of the initial state. On the other hand, two-bay frames exhibited ultimate strength values almost as twice the amount of that of the single-bay ones. Regarding the openings, it was seen that more ductile behavior could be obtained when the size of openings is increased, which caused roughly 40% less initial stiffness compared to the solid infilled frames. Besides, the ultimate loads for the panels with openings were found significantly higher than the cracking loads.

Fardis et al. (1999) drew attention to the fact that irregularities of the infill distribution in plan might potentially lead to torsional unbalance in a building which eventually cause excessive stress concentrations on the columns. Consequently, the eccentricity related failure mechanisms are highly anticipated after such scenarios as also largely quoted by the earthquake engineering society. In order to investigate this subject, the authors addressed the problem by means of testing a full-size two-story RC frame having single-bay in each perpendicular direction on a shake table. The masonries were constructed on two adjacent sides only and extended from bottom to the top of building as visualized in Figure 3.2. These infill panels were assigned to relatively low slenderness features for observing their out-of-plane performances more visibly. The loading was done in a way that bidirectional simultaneous loading was exposed to the frames and later the response was measured. Accordingly, it was seen that the corner column placed between the adjacent two infills behaved as the rotational axis. Other than that, the opposite corner column which did not have any panel contact exhibited more or less similar displacement values, those of the bare structure. In this sense, it was suggested that the common corner column of the voided frame parts needed to be designed proportionally to the simultaneous action of the bidirectional peak forces, whereas the remaining frame parts could be detailed as if these belong to the bare-frame. An interesting finding was that single eccentricity was found more dangerous than the double eccentricity as it was in that study, according to the dynamic calculations made by the authors. This was attributed to the beneficial effects of the infill presence on the orthogonal direction. Lastly, the slender walls could withstand the out-of-plane excitations even up to 1.75g without any important damage.

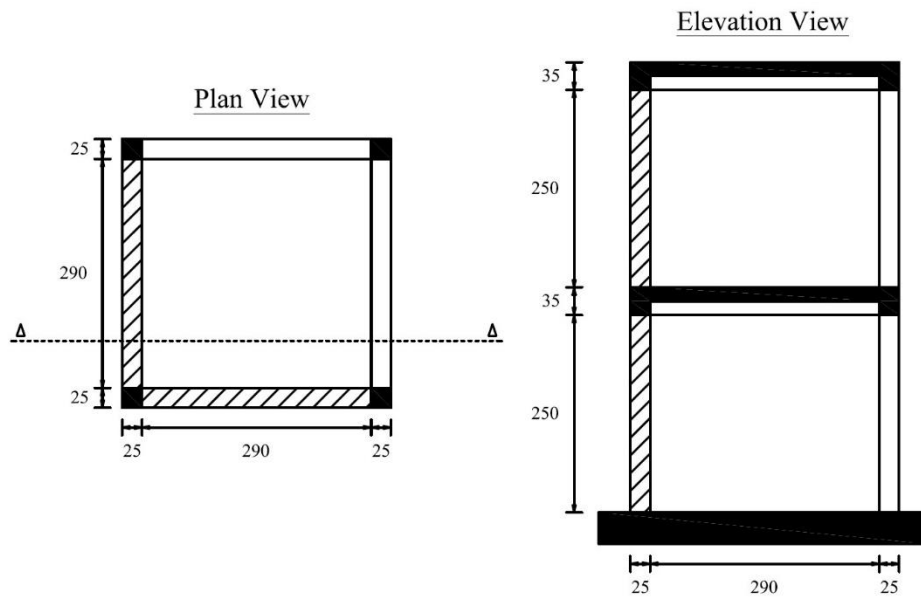


Figure 3.2. Plan (left) and elevation (right) views: hatched parts represent the infill walls (units in cm) [adapted from Fardis et al. (1999)].

In another study using the pseudo-dynamic method, Buonopane et al. (1999) assessed the seismic response of a half-size two-story and two-bay RC frame infilled with masonry panels. The first story was constituted with the solid infill scheme whereas window openings were provided at the second story level. Gradually increasing four adapted real-earthquake motions, in the order of 0.10g, 0.35g, 0.55g and 0.80g, were exposed on the specimen. The outcomes revealed that compressive strut actions of the walls were closely associated with the type of cracking. The second story, where the window openings were present, demonstrated a ductile behavior due to owning the stepped crack patterns. Contrarily, bed joint sliding shears were the dominant damage mechanism at the first story, which caused sudden strength drop beyond a certain loading level. Therefore, it was suggested for the designers to take into account the localized forces on the frame members that emerged upon such sudden infill deteriorations.

Lee and Woo (2001) studied the influence of masonry infills in RC frames constructed with non-seismic detailing. Their work was particularly aimed at investigating the typical low-rise building practice in Korea, therefore an existing 3-story and 2-bay infilled building was replicated to the one-fifth scale of its original and constructed on a shake table. Two different types of masonries were considered. First, the frames were constituted with infills in two bays and therefore it was called as full-infill model. Later, nearly half of the infill panels were removed and the tests were repeated on the reduced infilled frame. Upon the shake table excitations, pushover tests were performed, too. At the end of shake table experiments, it was

concluded that no significant damage was observed neither on the masonries nor on the frames. This could be attributed to the choice of relatively low magnitude seismic loads for such tests (0.4g as the maximum intensity), since the authors intended to simulate a real-life scenario that might occur only in a local and narrow part of the world. Nevertheless, the pushover analyses which were conducted in the pursuit of representing extreme situations showed that masonry infills were failed due to the bed joint shear sliding mechanism and the soft-story failure was pronounced for the case of the bare-frame type. In summary, it was claimed that masonry infills had beneficial effects on the buildings as the outcome of their study due to the fact that the strength contribution of the walls to the rest of system was found higher than the additional earthquake inertia forces caused by those.

Calvi and Bolognini (2001) constructed full-scale single-story and single-bay infilled RC frames and tested their in-plane and out-of-plane performances. They chose hollow clay weak masonry panel for the infills as being preferred largely in the seismic prone countries in Europe, particularly in the Mediterranean region. On the other hand, the frames were designed according to Eurocode-2 (CEN, 2004a) and Eurocode-8 (CEN, 2004b) standards, thus no early frame damages were expected during the experiment. As one of the main arguments in that study, the efficiency of infill strengthening topic was evaluated by means of dividing the samples into three categories; no reinforcement, mortar reinforcement and external wire mesh in the plaster. The test protocol consisted of in-plane cyclic loads up to 3.6% drift level and the out-of-plane disturbance at the certain points on the wall corresponding specific damage limits. Several comments and suggestions were made by the authors, which could be summarized that the infill walls significantly increased the initial stiffness, yet the frame responses in all cases at the collapse limit state were similar to the that of the bare-frame. On the other hand, any kind of the reinforcement was effective of avoiding the high strength deteriorations of the masonries, though the wire mesh method exhibited the best performance.

Zarnic et al. (2001) intended to explore the simultaneous in-plane and out-of-plane performance of the infilled frames on a shake table. Therefore, they followed explicit scaling rules from the prototype buildings and constructed two quarter-scale specimens; one in a box shape and had infills around the perimeter, the other with the infills distributed on the 2×1 bay plan in the “H” letter form and had two stories, see Figure 3.3. The masonry blocks were chosen relatively strong, whereas weak mortar was preferred, thus typical bed and head joint cracks were anticipated without the cracking or crushing of the brick blocks. The scaling related over-strength possibilities were also mentioned particularly for the frame elements. Both specimens

were excited in a single horizontal direction and were subjected to two intensity levels of sequential sine waves, where the second wave represented the stronger after-shock circumstances. The global results were evaluated in the acceleration response, damping shifts and frequency reduction domains. The crack patterns on the masonries were also checked. Accordingly, for the both frames, the frequency values were dramatically dropped upon reaching the respective resonance levels and some damping development was observed while the shaking continued thanks to the friction mechanisms on the cracked parts of the specimens. The resonant effects also caused discrepancies between the accelerations of the shake table and the response of models. In conclusion, it was shown that Eurocodes compliant buildings were able to sustain strong ground shakes because of the overstrength design rules.

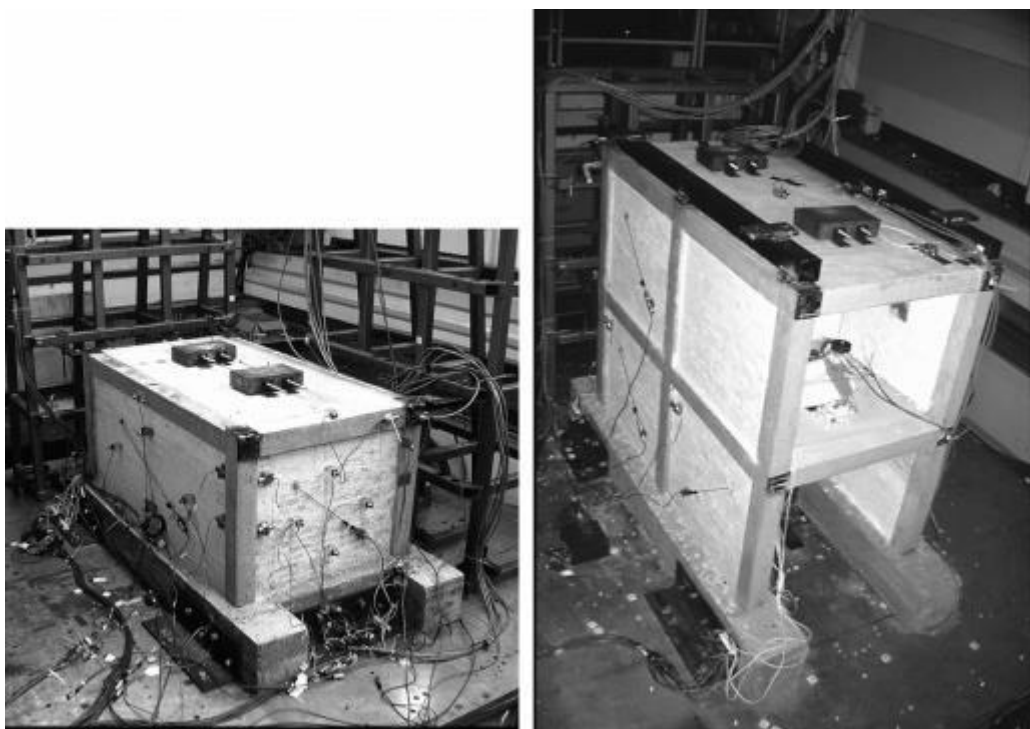


Figure 3.3. Single-story (left) and two-story (right) test specimens [adapted from Zarnic et al. (2001)].

In a rather unusual study for this field, Sahota and Riddington (2001) focused on the time-dependent creep and shrinkage effects. According to their claim, such mechanisms often occur on the RC columns which in return results excessive and unpredictable vertical load transfers onto the infill walls. Therefore, a copper-tellurium lead layer was proposed to be used between the top beam and masonry panel within this context. In order to test this, three half-scale steel frame enclosed infilled systems were built, one without lead and the other two with lead but had different load applying rates. Typical connection detail is presented in Figure 3.4.

The choice of steel frame rather than the concrete material was related to the easier feasibility of simulating the shortening behavior of columns. The experimental program was divided into two stages; firstly, short-term and long-term creep tests were done in a period of total 6 months. Following that, the specimens were subjected to the cyclic racking loads in order to test whether the presence of the leads had any adverse effects regarding the seismic performance. In short, it was concluded that the lead layers had a positive impact in terms of reducing creep and shrinkage related compressive load transfers to the columns. Besides, no unfavorable situation was observed because of the usage of the lead layers in terms of the horizontal in-plane load capacities of the frames. Contrarily, a stiffer initial behavior was noticed for those.

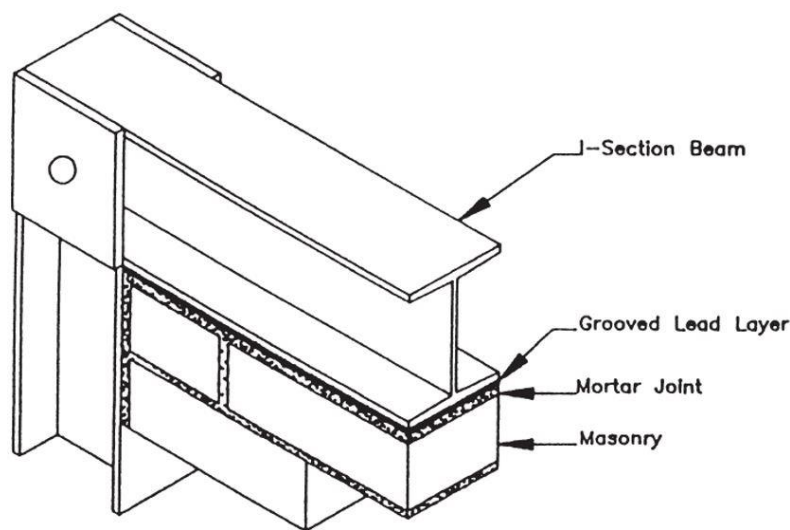


Figure 3.4. Typical section detail of the frame-infill joint [from Sahota and Riddington (2001)].

Al-Chaar et al. (2002) operated a research program in order to determine the earthquake performance of a certain type of governmental buildings in the United States which were constructed several decades ago when there were no reliable seismic provisions enforced in place. In this purpose, five half-scale infilled RC frame models were extracted from a prototype, all had one-story but different number of bays, namely one, two or three. The masonry materials were chosen from either brick or concrete blocks. A bare-frame without the infills was also tested as a reference. The specimens were tested under the gradually increasing monotonic pushover loads up to the excessive lateral drift levels, i.e., 9%. As expected, the results revealed the positive contribution of the infill panels since much higher peak loads, residual strengths and initial stiffnesses were achieved, although the improvement of these features were not linear with the number of bays. Because, the non-uniform shear stresses were the main causing effect which need to be acknowledged in the design or evaluation methods as the authors

suggested. It was also reported that the prediction of failure mechanisms could be possible if the shear and compressive strengths as well as the system geometry is properly accounted.

Colangelo (2005) presented the in-plane pseudo-dynamic test results for thirteen half-size scale single-bay and single-story RC frames constituted with the various masonry types. The frames were also different in terms the strength, reinforcement and aspect ratio details. The specimens were tested two times; initial stage when there was no damage and the post-cracking stage. Following that, the results were evaluated in the global and local levels. Accordingly, the uncracked infilled frames exhibited visibly different behaviors than the bare-frame ones, as the initial stiffness and the peak strength of those could be one or two times higher, respectively. Despite the reduced drift outcomes of the infilled specimens, the energy absorption capacities were found higher in comparison to the bare-frames. On the other hand, it was seen that the masonry damages altered the way how seismic forces act. As a result, the stress and deformation distribution were asymmetric and these were locally concentrated on some specific parts.

Hashemi and Mosalam (2006), in a study where an infilled frame model was extracted from a hypothetical multi-story prototype building, focused on the dynamic properties of such systems and performed a shake table experiment which was later used for the calibration purposes of developing a new computational modeling strategy. In this regard, a three-fourths scale one story specimen was constructed representing the middle-bay of the aforementioned considered building. The specimen was subjected to two different input ground motions which were effective sequentially with specific scaling factors. It was remarked that the infill walls substantially changed the strength and ductility features of the tested structure, thus any design and analysis process should include their effects. In terms of the global response, stiffness values were reached to 4 times higher than that of the bare-frame. Similarly, the natural period was reduced by approximately 50%, whereas the energy dissipation could be enormously increased thanks to the masonry related damage mechanisms which could rise the coefficient up to 12% with respect to the viscous damping features and inelastic deformations. It was also seen that the effects of the infill walls on the local zones cannot be neglected, especially on the adjacent elements i.e., top and bottom ends of the surrounding frame elements.

Pujol and Fick (2010) were among the a few researchers who addressed the infill wall related questions with a full-scale large experiment. They tested a three-story RC frame building in a single direction loading. The building consisted of flat slabs (beams hidden in the floor slab) and it was designed to resist only the gravity loads, see Figure 3.5. Cyclic lateral loads were applied at each floor level in the reversed triangular form in a way that the top floor

received the highest displacement demands. First, the bare-frame formation of the building was tested. Totally four reversed cycles were imposed and the maximum drift ratio of 3% was achieved. At the end of test, punching shear failures were observed in the vicinity of some column-slab joints. In the second phase of the experiment, two out of four open bays in each floor were filled by the masonry panels laying parallel to the direction of loading. The modified building was subjected to the gradually increasing twenty displacement cycles in that phase, which was much higher than the bare-frame case and was a result of intention to study the cycle sensitivity in terms of the reversal numbers. Maximum roof drift ratio was reached at 1.75% and the experiment was stopped because of the concerns emerged from the previously cracked slab caused by the punching shear, which could jeopardize the tests. The results exhibited different damage types such as corner crushing of the walls, shear cracks on the columns and diagonal cracking through the panels. However, the main emphasis was made by the authors on the infill wall contribution, which enormously increased the overall shear strength and stiffness capacities. It was also proven that despite having relatively weak frame, the structure was able to resist lateral drifts safely up to 1.5% without significant strength drop.



Figure 3.5. Three-story structure before the tests [from Pujol and Fick (2010)].

During the shake-table tests conducted by Stavridis et al. (2011), it was investigated a building typology constructed in California in the first decades of the twentieth century. Therefore, a 2/3 scale non-ductile building was constructed, which had two bays and three

stories. The masonry infills were constituted with both solid panels and window openings as shown in Figure 3.6. The bricks were planned as three wythe scheme for the prototype as it was a common practice for that era, yet these were configured with two wythes in the reduced scale model. The test protocol comprised of a series of sequential dynamic motions. In total, 44 tests were performed, of which 14 were the adjusted earthquake records and the rest of records included the ambient vibration and white-noise tests. The results pointed out that the shaking intensities up to the moderate levels could not pose a serious risk to the building, since it almost behaved elastically. On the other hand, significant damage developments occurred beyond moderate to high seismic magnitudes. At some point, the first story columns also experienced severe diagonal cracks which led to the soft-story mechanism. Moreover, the authors indicated that the building performed quite well considering its construction standards and it was also demonstrated that the infilled frames could contribute to the building safety as long as their numbers and detailing properties were sufficient.



Figure 3.6. Test specimen on the shake table [from Stavridis et al. (2011)].

Ozkaynak et al. (2013) conducted a series of quasi-static and pseudo-dynamic cyclic tests on 1/3 scale infilled RC frames in order to determine the damping characteristics of the bare-frame, masonry infilled frames and retrofitted infilled frames with various configurations of the carbon fiber reinforced polymers (CFRP) strengthening strips. Firstly, experimental cycles were evaluated while determining the equivalent damping and later an iterative procedure was established utilizing the energy balance method for obtaining the equivalent

damping ratio. It was remarked that the earthquake energy could be dissipated through several mechanisms in a structure as follows; elastic strain, kinetic, hysteretic and damping. In this sense, the effectiveness of the infill masonries was proved since the results showed that the damping ratio for the infilled frames could be estimated around 12% for the virgin shape and 14% in case of the retrofiting, whereas this value was given as only 5% for the bare-frames.

Cavaleri and Di Trapani (2014) carried out quasi-static cyclic experimental tests on single-bay and single-story 2/3 scale RC frames constructed with various masonry types. The study was primarily aimed at revealing the nature of such systems for enabling to modeling them analytically, which is explained in this dissertation in the section dedicated for the analytical modeling techniques. Therefore, the test data was enhanced with the information from Cavaleri et al. (2005). In this way, the experiments were conducted in two different series. Twelve infilled frames were built in total, all were designed to reflect the constructions types of only gravity load carrying frames without any seismic detailing. The masonry blocks were selected from three commonly preferred materials; calcarenite, clay and lightweight concrete and these had either perforated or solid shapes. The specimens were initially loaded with 200 kN vertically effective constant axial forces on each column. Later, cyclic lateral loads were subjected on the frames. The results revealed that the infilled frames could resist substantially higher loads compared to bare-frames regardless of the brick material or frame detailing type.

In a more recent study, Butenweg et al. (2019) reviewed the past earthquake reports and came to a conclusion that in-plane and out-of-plane mechanisms of the infill walls need to be considered together while verifying the safety of such systems under seismic forces. Therefore, they determined to conduct an experiment for investigating the infilled frame behaviors against those failure mechanisms in the occurrence ways of separate, sequential or simultaneous. A test program was generated accordingly and four different full-scale frame configurations were made such that the bare-frame was only tested with the in-plane cyclic loads whereas the infilled frames were tested against the out-of-plane, in-plane and out-of-plane separated-sequential and also in-plane and out-of-plane combined loads. As the main outcome of their study, the authors expressed the importance of the boundary conditions, namely frame-to-masonry joints, especially when the out-of-plane effects exist. Because, the assumption of the intact wall boundary condition could be invalid under such combined in-plane and out-of-plane loads, hence it was suggested to focus on providing a robust full-contact solution.

3.2 Infill wall modeling techniques

Several obstacles related to the performance evaluation of the infill walls through experimental tests directed engineers to seek for alternative solutions. The experiments are costly in terms of both time and financials, limited to the specific conditions and materials and they do not provide much chances to repeat the tests with different configurations or parameters. In addition, the curiosity of understanding the nature of the infilled systems have been triggering the researchers in this field for many years, in the pursuit of illuminating the mysterious complexity of the infills with simple yet reliable answers.

There are different approaches of modeling the walls and these can be categorized as below, Figure 3.7. Analytical models are the most suitable ones for the rapid analyses and especially if the rough results are adequate for the concerns of specific issue. With the growing accuracy from macro to micro modeling strategies, it is possible to simulate the infill wall behaviors; however, in a cost of higher computational efforts. In a nutshell, each method has its own advantages and therefore the correct one should be carefully chosen based on the specific problem needs.

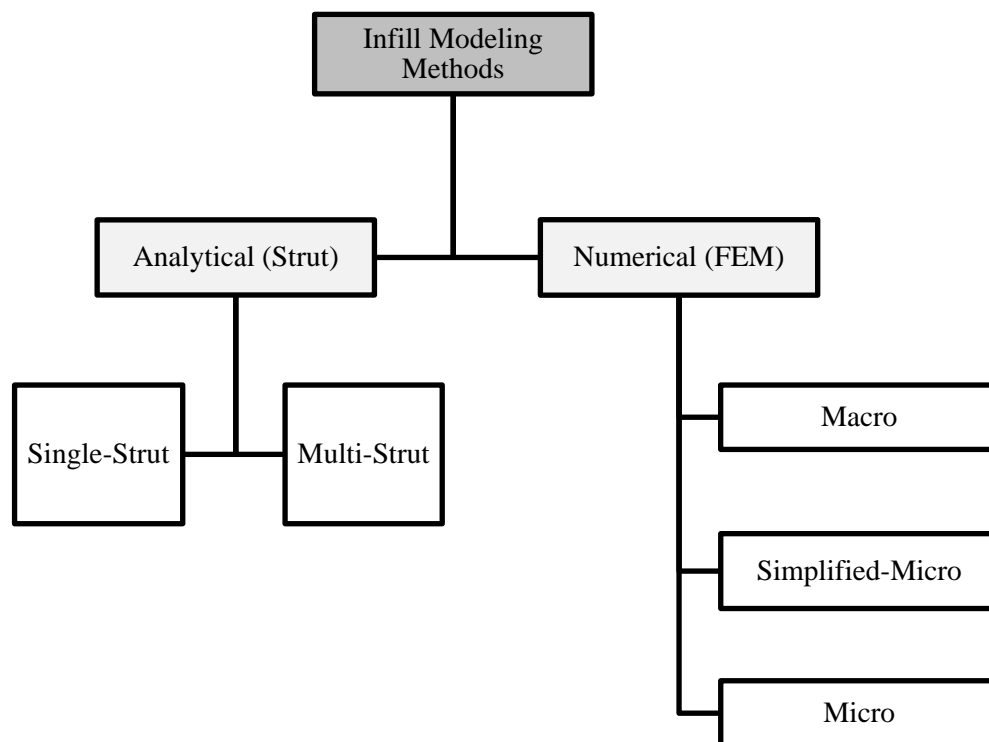


Figure 3.7. Infill masonry modeling methods.

3.2.1 Analytical (Strut) modeling approach

In the 1950s, early discussions of representing the infill walls with equivalent struts had begun. According to FEMA-306 (1999), Polyakov (1956) had performed the first studies on the interaction of infill walls and the surrounding frames of the buildings. In that research, it was suggested to replace the infill masonries with equivalent diagonal bracing elements. Later, Holmes (1961) adapted this idea by means of simulating the brickwork or concrete made infill panels in steel frames with an equivalent pin-jointed diagonal strut approach that was intended for computing the ultimate strength and elastic stiffness of the walls. The assumption was made on the basis of assigning the same material properties and thickness values of the walls to the equivalent struts, which had the width length – w , equals to one thirds of the strut diagonal length – d , as shown in Figure 3.8. and given mathematically in Equation 3.1.

$$\frac{w}{d} = \frac{1}{3} \quad (3.1)$$

In the following years in 1960s, Stafford-Smith conducted several experimental studies on small size specimens in order to investigate the lateral stiffness properties of the infill panels. In one of these pioneer researches, masonry infilled steel frames were tested and the effective width for the equivalent strut was derived theoretically. Accordingly, it was found that w/d ratio varied between 0.10 and 0.25 (Stafford-Smith, 1962). Another research on the behavior of square shaped infilled frames (Stafford-Smith, 1966) utilized the free beam theory laying on the elastic foundation (Hetenyi, 1946) and revealed that the length of contact between the infill panel and frame significantly affects the strut width as well as the stiffness and strength of the infills. Next, experiments were conducted on single and multi-story infilled steel frames with the wall length/height proportions up to 2.5, and it was found that relative stiffness of the columns and infills change the lateral stiffness and the ultimate strength of the systems, although the size or stiffness of the beams practically did not alter the results (Stafford-Smith, 1967). It was also demonstrated that the wall length/height aspect ratio influenced the equivalent strut width (Stafford-Smith, 1967). Finally, above findings were compiled to another study of Stafford-Smith and Carter (1969), and it was proposed to determine the equivalent strut width taking into consideration the infill contact length – a , with the surrounding frame. This length was assumed as a function of the relative stiffness of the infill to the frame and given by Equation 3.2, where h indicates the frame height from the centerlines of beams and lambda (λ) is a non-dimensional parameter given by Equation 3.3, in which E_w , t , h_w and θ are the Young's modulus, thickness, height, and slope of the diagonal to the

horizontal dimensions of the infill, respectively; and E and I are the Young's modulus and moment of inertia, of the column respectively, see Figure 3.8.

$$\frac{a}{h} = \frac{\pi}{2\lambda h} \quad (3.2)$$

$$\lambda = \sqrt[4]{\frac{E_w t \sin \theta}{4EI h_w}} \quad (3.3)$$

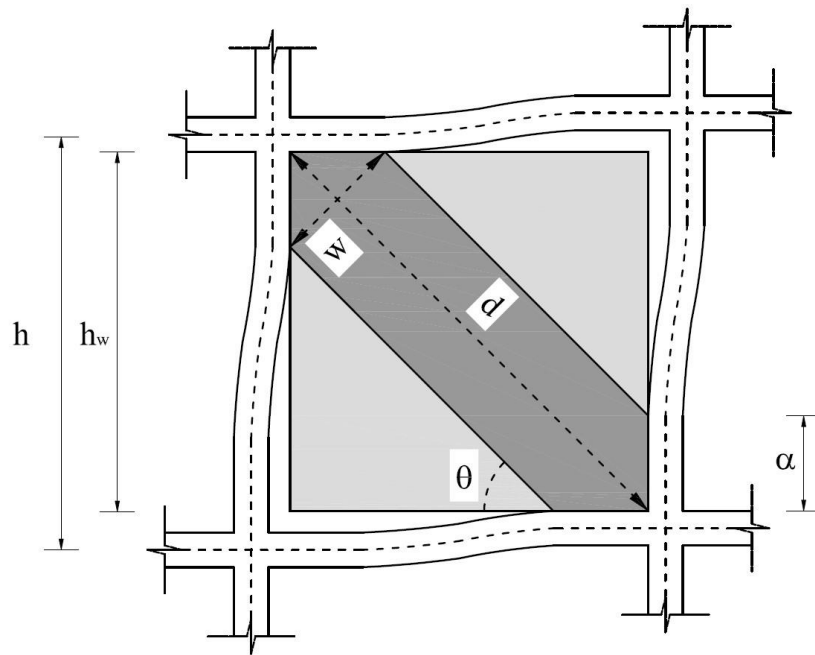


Figure 3.8. Parameters of the equivalent diagonal strut model proposal of Stafford-Smith and Carter (1969).

Mainstone and Weeks (1970) and Mainstone (1971) adapted the aforementioned equations proposed by Stafford-Smith and his associates, and established the strut width on the basis of experimental and analytical campaigns as given in Equation 3.4, which was later assimilated largely by the experts in the field (Asteris et al., 2011). Eventually, the structural engineering codes have also included this approach in their provisions (FEMA-273, FEMA-306, FEMA-356).

$$a = 0.175(\lambda h)^{-0.4} d \quad (3.4)$$

Smolira (1973) analyzed the response of infill walls against the lateral forces, where the effects of perfectly fitting infills as well as gaps at the interface spaces between the frame and wall were taken into consideration. In the proposed analytical formulation, force-displacement based matrices were utilized while adopting the principles of the equivalent strut

analogy. Although the effective bracing width was assumed constant without a clear explanation and neither axial nor shear deformations were considered, it was shown that the diagonal strut theory is effective up to low or moderate loads, whereas double arching effects were pronounced at high level loads that were also observed in the experiments.

Abdul-Kadir (1974) investigated the behaviors of one-third sized steel frame encased square and rectangular shaped brickwork infills with and without openings through experimental tests as well as by means of utilizing the equivalent strut based analytical approach and numerical solutions using the finite elements method. It was highlighted that previous studies on this subject were barely focused on the brickwork materials, thus masonry infills took the attention in that study. Methods for predicting the lateral stiffness and strength were developed. Besides, a simple method for the analysis of multi-story frames was introduced. In terms of the equivalent strut approach which was based on the similar assumptions made previously by the other researches, namely Holmes (1961) and Stafford-Smith (1962), it was stated that the in-plane stresses vary through the diagonal compression zone – minimum at the center and maximum near the loading corners. On the other hand, the unloaded diagonal would exhibit a stress variation as zero values at the corners and reaching to the maximum at the center of panel. Accordingly, a triangular stress distribution was assumed which could be simplified in a uniform compressive stress form over the half of width – W , see Figure 3.9. In this way, Equation 3.5 could be written for representing the effective width – w , where a_h and a_l are parameters indicating the column and beam contact lengths, respectively. It was claimed that this approach yields relatively closer results to the experiments compared to the assumptions of the previous studies of Holmes (1961) and Stafford-Smith (1962). Moreover, the possibility of replacing the solid panels with the diagonal bracing elements was established, whereas it was concluded that an equivalent frame acting along the loaded diagonal could be a more proper choice for the panels with openings. In addition, finite elements method was found sufficient for predicting the behaviors of any type of panels – with or without the openings – as long as appropriate boundary conditions were defined.

$$w = \frac{1}{2} \sqrt{a_h^2 + a_l^2} \quad (3.5)$$

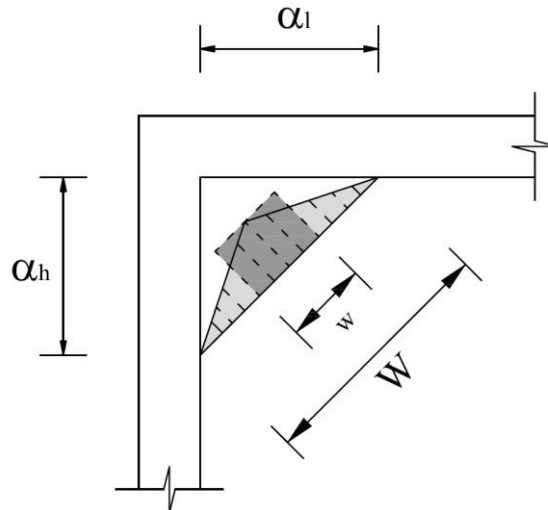


Figure 3.9. Derivation of the effective width (w) from the equivalent strut width (W) as proposed by Abdul-Kadir (1974).

Liauw and Lee (1977) performed tests on small size four-story steel frames infilled by reinforced concrete panels with and without openings, and besides, with and without connectors between the frames and the infills. According to their investigation on the strength and stiffness of such systems, analytical models were presented for both infilled frames with and without the connectors. Presence of the connectors, which were made of steel and welded to the frame, caused a distinguishable difference in terms of the structural behavior. It was declared that the equivalent strut analogy is sufficient while reproducing the infill contribution, whereas the connectors invalidate this assumption due to the fact that a composite behavior is pronounced, thus an equivalent frame approach was determined to be more convenient rather than the equivalent strut phenomenon. The main difference between the presence and absence of the connectors was stated as; the former model requires to take into consideration the composite action of the frames and infills, whereas the latter case was justified on the fact that slip and separation in the vicinity of frame-infill boundary leads to an early-stage connection loss. In the light of aforementioned assumptions, the equivalent strut model was established on the basis of a strain energy method for determining the strut cross sectional area. On the other hand, for the case of frames utilized with the connectors, actual properties of two different materials – frames and infills – were transformed in a way that a homogeneous and isotropic, elastic-perfectly plastic fictitious cross sections were obtained. Later, properties and stiffness matrix of the new model were calculated by means of considering the shear strain energy. According to the results, it was found that both models predicted lower strength and stiffness values compared to the experiments, though the difference was relatively substantial when the

equivalent strut analogy was utilized. This discrepancy was attributed to the assumptions made about the contact lengths as well as the forces emerged on these regions. The authors concluded that the presence of the infill walls substantially increase the overall strength and stiffness of the systems, particularly when a reliable joint connection could be provided between the frame and infills.

Endeavor on the topic of strut modeling strategies continued its popularity in the following decades. Thanks to the advancements in the computing technology and better understanding of the researchers regarding the behavior of such systems, versatile solutions have been developed. Bazan and Meli (1980) investigated the seismic behaviors of structures comprised of the infilled frames. A finite elements method based numerical model was developed for predicting the load-deformation curves and cracking patterns of single-bay and single-story masonry infilled RC frames. Equivalent strut analogy proposed by Stafford-Smith (1962) was adapted, hence a diagram was produced that aimed to make a correlation between the strut width and the strength degradation due to the cracking of the panels. Liauw and Kwan (1984) focused on the non-linear behaviors of non-integral infilled frames (initially no bonding between the frames and infill panels) and established an empirical equation, which was also benchmarked with the numerical calculations and previous experimental outcomes. Accordingly, it was found that the ultimate strength of such type of frames are very much dependent on the bending capabilities of the frame members alone. Besides, the effects of friction were negligible, especially if conservative results for both strength and stiffness are sufficient. Regarding the strut width – w , upon investigations on the panel stresses, it was claimed that it yields better results if the width was expressed by the $h \cos \theta$ equation that enables an approach independent of the span/story height ratio rather than a definition on the basis of a fraction of the diagonal length – d , as presented in Equation 3.6, and illustrated in Figure 3.10.

$$(a, b)_{min} \begin{cases} a = \frac{w}{h \cos \theta} = 0.45 \\ b = \frac{0.86}{\sqrt{\lambda h}} \end{cases} \quad (3.6)$$

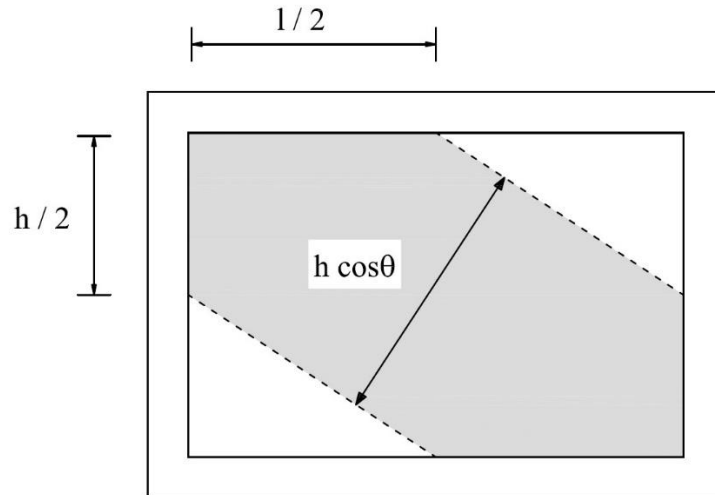


Figure 3.10. Effective strut width proposed by Liauw and Kwan (1984).

Unlike the earlier proposals from various researchers, Thiruvengadam (1985) suggested to use multiple-struts instead of the single pin-jointed bracing technique. In that study, it was primarily focused on developing reliable methods for identifying the natural frequencies of the infilled frames. Firstly, emphasize was made on the importance of considering infill effects on the multi-story frames, due to the fact that these walls substantially affect the building dynamic characteristics, namely natural frequencies, free vibrational mode shapes and damping features. Before establishing an approximate strut model, the contact length effect was tested through the finite elements analyses. It was concluded that, defining a proper solution for this phenomenon was highly indeterminate, therefore practitioners might use approximate evaluations. Later, the need of a multiple-strut model was justified by claiming that single strut methods are only valid if the infill and the surrounding frame are in contact in diagonal opposite corners. However, in fact, a finite length of the contact is the matter in most instances, especially when the infills are attached to the frames by shear connectors or strong bonding mortars. Therefore, the multi-strut model was developed by means of configuring a certain amount of vertical and diagonal struts in different formations, while taking into account the infill separations and openings. The outcomes indicated that the new idealization of utilizing multiple bracing elements led to obtain closer natural frequency results to that received from the experiments, in comparison to the familiar single-strut models. Moreover, it was shown that infill openings because of the windows or doors, could also be taken into account with the multi-strut approach.

In another early study on this topic, Mochizuki (1988) investigated the slip failure of the infill panels. The wall behavior was simulated by two diagonal braces in two phases, before and after cracking. At first, elastic braces were substituted with the wall which were assigned the same shear stiffness equivalent to the panel. In the post-cracking phase, the panel was replaced with the tensile and compressive effective braces inclined at 45 degrees.

In the following years – especially in the last three decades – anymore it was evident that single struts were unable to capture the actual infilled system behavior, since the bending moments and shear effects were mostly ignored in this method. Therefore, more advanced macro models were developed by means of evolving the typical strut analogy, although some researchers still kept enhancing the existing single strut methods; Paulay and Priestley (1992), Durrani and Luo (1994), Saneinejad (1995), Flanagan and Bennett (1999, 2001), Papia (2003). However, the next paragraphs under this section are merely devoted to the aforementioned multi-strut based new proposals.

Crisafulli (1997, 2007) performed extensive research on the behaviors of masonry infilled frames. Initially, three different strut models were examined – single, double and triple models. After that, the bending moment diagrams were compared with the FEM results, see Figure 3.11. Single strut model underestimated the results since the truss mechanism primarily carry all the lateral loads. Double strut model exhibited much greater moment values. Triple model converged better compared to the other ones, though slight differences were observed at the column ends. Overall, single strut was found adequate for representing general structural response, though refined models – such as triple-strut – are needed for realistic simulation of the bending and shear effects on the frame members. Pinching behavior observed in the experiments was characterized as the result of sliding shear forces particularly effective on the masonry panel. This phenomenon is very complex to be represented with ordinary macro-models. Therefore, a new model of 4-node panel was developed in which two diagonal struts were positioned in a way that each had one end at the corner and the other end intersecting with the column. Moreover, a shear spring was placed in order to capture the pinching mechanisms, as shown in Figure 3.12. The vertical distance between the both struts – h_z , varies in a range from $a/3$ to $a/2$, where a is the contact length proposed by Stafford-Smith (1967) and given in Equation 3.2. In this shape, the model was able to reflect the bending moments and shear forces of the frame members as similar of the aforementioned triple-strut model, besides, the shear springs were primarily active initially until the sliding starts. After that point, the mechanism shifts to acting purely on the other diagonal struts and eventually on the frame members. The model was established on the assumption that debonding of mortar joints (or

sliding shear between the masonry blocks) is the most common failure type for such systems. Therefore, it was indicated that further research is required especially if the corner crushing of the panels is expected. Nevertheless, a detailed hysteresis model was proposed, too. Axial and shear behaviors were handled distinctively and this model was claimed to be suitable for the other fragile materials as well, e.g. concrete. Different than the standard hysteresis models where full cycles were considered only in the constitutive laws, this model also included small (inner) cycles that could be observed very often during an earthquake which also took into account the compressive and shear hysteresis loops separately as briefly presented in Figure 3.13.

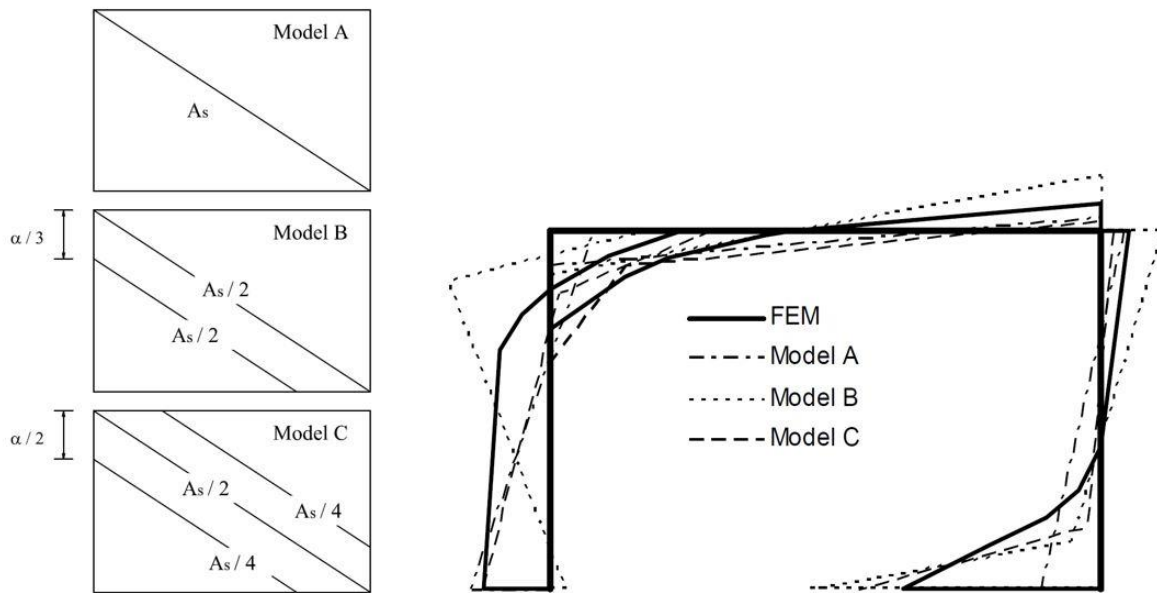


Figure 3.11. Different strut models (left) and corresponding bending moment diagrams (right) [adapted from Crisafulli (1997)].

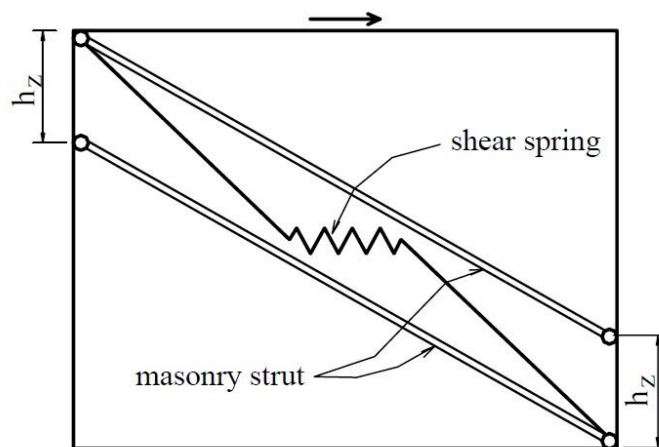


Figure 3.12. Multi-strut model with shear spring [adapted from Crisafulli (1997)].

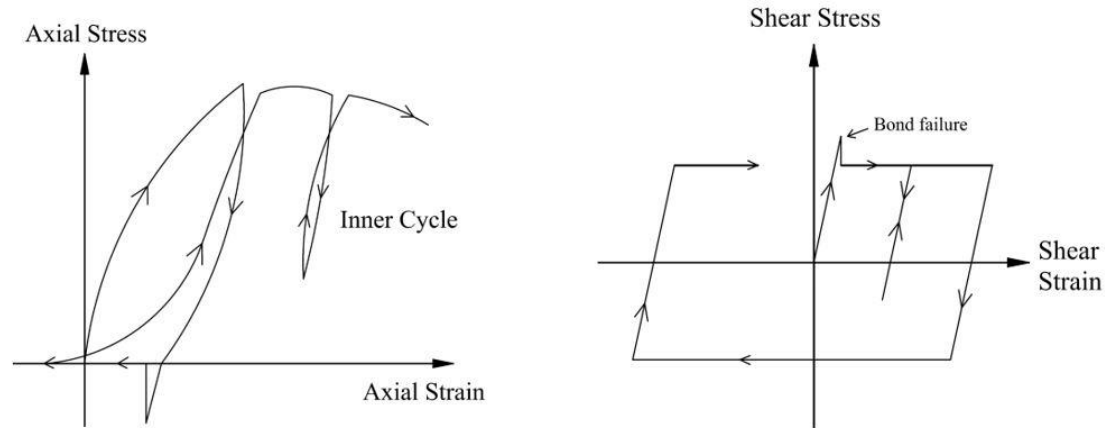


Figure 3.13. Hysteresis loops for axial (left) and shear (right) responses [adapted from Crisafulli (1997)].

Chrysostomou et al. (2002) developed a macro model for simulating the response of the infilled steel structures under the effects of dynamic cyclic loads considering the strength and stiffness degradation factors. Infill wall was modeled with total six diagonal struts, all working only in compression, and split in a way that three of those laid on the same direction whereas the other half was being activated when the system was loaded from the opposite side. One out of three struts in each direction was connected to the frame at the corners and the remaining two were positioned at the off-diagonal critical locations along the frame members, which were defined according to the plastic hinge zones and assumed equal for simplifying the model in a rough approach, see Figure 3.14. On the other hand, such a configuration enabled to take into account the interaction effects between the infill and frame as well as the deformation developments on the frame members by means of the plastic hinges. However, drawback of this assumption was that the contact length variation was not considered, which would be normally a result of the relative strength between the infill and surrounding frame. Nevertheless, the other parameters such as the interface conditions and openings were included in the model indirectly, through creating a comprehensive wall hysteresis relation properly. The envelope curve as well as the hysteresis loops were defined based on the proposals of Soroushian (1983, 1988), yet modified slightly that affecting parameters were reduced for the simplification purposes while still considering to have all variables to reflect the actual physical meanings. Therefore, one could easily adapt this model as long as the experimental results exist. In Figure 3.14, these continuous smooth hysteresis curves are given, where numbers 1-2 and 3-4 denote the strength envelopes and loading-unloading paths, respectively.

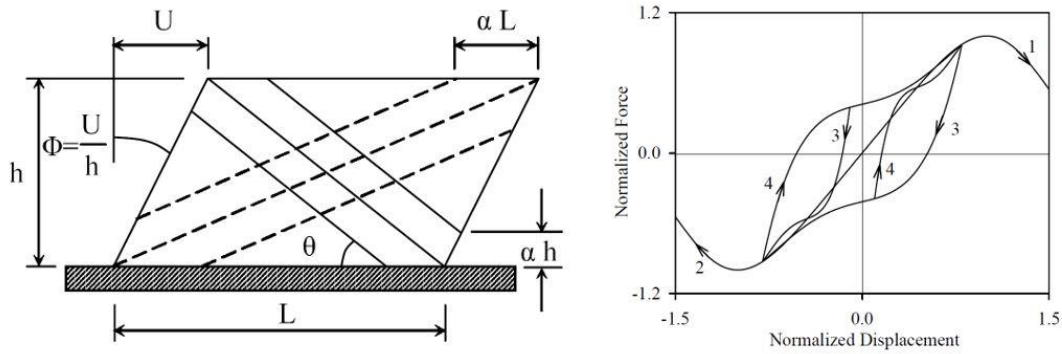


Figure 3.14. Multi-strut idealization (left) and load-displacement paths (right) [adapted from Chrysostomou (2002)].

El-Dakhakhni et al. (2003, 2004a) idealized the infill walls with three inclined struts in each loading direction that aimed to predict the stiffness and ultimate load capacities of the steel frames filled with concrete brick blocks. Firstly, possible damage type was identified for that kind of structures and it was concluded that the corner crushing most likely occur as being the most common failure type. Following that, constitutive laws for the steel frame and infill panel were established. Accordingly, frame members were assumed to behave elastically except the connection joints where the non-linear rotational springs were assigned due to the fact that infill wall peak loads were reached much before the plastic moment capacities of the sections were exceeded (Saneinejad, 1995). In terms of the infill panels, the contact lengths were defined distinctively for the column and beam connection zones, considering the plastic moment capacities of the joints (M_{pj}), beams (M_{pb}), columns (M_{pc}) and the wall orthotropic strength values (f'_{m-0} or f'_{m-90}) with the condition of limiting the length as 40% of the respective frame member's dimension, either beam or column, Equation 3.7. The strut effective area was formulated explicitly using the contact lengths and geometrical features of the wall, as given in Equation 3.8. Moreover, the central strut was attributed to reflect the half of the total strut area whereas the remaining half was split equally among the off-diagonal ones, as presented in Figure 3.15. Later, the Young's Modulus of the masonry was assumed to have anisotropically different features, therefore the constitutive relations primarily established for the orthotropic plates were adapted to the masonry elements as the properties of the perpendicular axes were utilized whilst determining the panel overall Young's Modulus on the basis of strut inclination angle as represented in Equation 3.9. Subscripts of 0 and 90 stand for defining the angular properties of the Young's Modulus E parallel and normal to the bed joints,

respectively. On the other hand, ν_{0-90} represents the Poisson's Ratio as the strain occurrence in the direction normal to the bed joints caused by the strain in the direction parallel to the bed joints. G is the shear modulus.

$$a_c h = \sqrt{\frac{2(M_{pj} + 0.2M_{pc})}{t f'_{m-0}}} \leq 0.4h ; a_b l = \sqrt{\frac{2(M_{pj} + 0.2M_{pb})}{t f'_{m-90}}} \leq 0.4l \quad (3.7)$$

$$A = \frac{(1 - a_c) a_c h t}{\cos \theta} \quad (3.8)$$

$$E_\theta = \frac{1}{\frac{1}{E_0} \cos^4 \theta + \left[-\frac{2\nu_{0-90}}{E_0} + \frac{1}{G} \right] \cos^2 \theta \sin^2 \theta + \frac{1}{E_{90}} \sin^4 \theta} \quad (3.9)$$

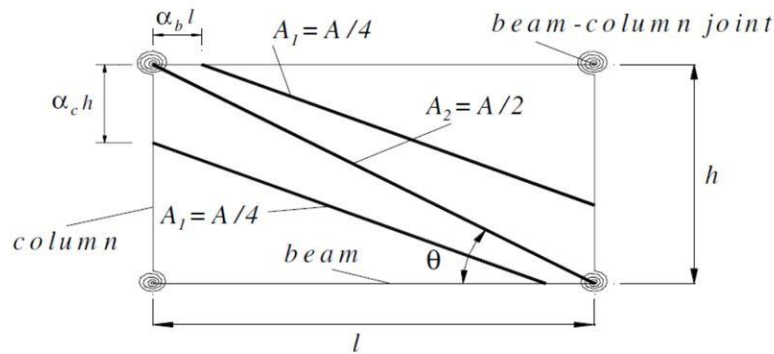


Figure 3.15. Three-strut idealization [adapted from El-Dakhakhni et al. (2003)].

Finally, a simplified tri-linear force-deformation relation for the struts was defined, as shown in Figure 3.16.

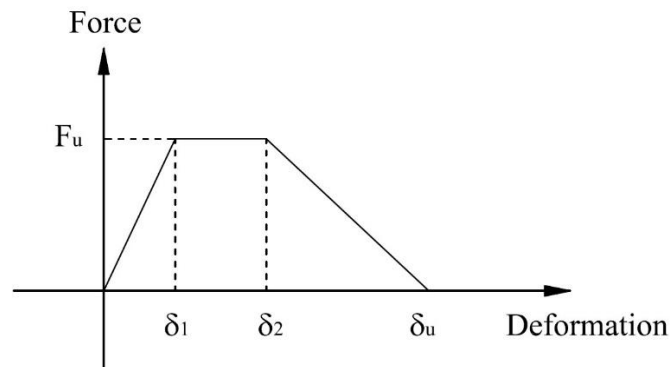


Figure 3.16. Force-deformation relation of the strut model [adapted from El-Dakhakhni et al. (2003)].

Analytical results were compared with five different experimental results from other independent studies. The proposed method provided reasonably close stiffness results to the experimental ones for single-story and single or two bay frames, especially up to the failure. It was justified that multi-strut model generated rather real-like bending moments on the frame members compared to the single strut. Besides, it was also effective of capturing the progressive damage nature of the infill walls, which typically starts from the corners and spread around.

In the study of Fiore et al. (2012), FEM analyses were primarily performed as the basis of their macro-model proposal. Later, the results were compared with the experimentally verified an equivalent strut model that was proposed by Amato et al. (2009). In that single-strut model, a refined approach of Mainstone's study (1974) was derived which aimed to manifest the importance of considering the vertical loading effects on the frames and the Poisson ratio variations of the masonry materials. Accordingly, an equation of the strut width – w was formulated which was also utilized in the analyses of Fiore et al. (2012). As a result, the benchmark analysis exhibited a good agreement performance between the FEM and strut models. Moreover, the friction influence on the interface between the frame and infill was investigated and it was stated that friction does not necessarily affect the global behavior, but altering the interaction forces particularly on the columns where stresses were dissipated away from the so-called contact zones with the panel as the friction increased. Upon making the calibration of the FEM model with the strut approach of Amato et al. (2009), another macro modeling technique was proposed. In this new model, it was particularly underlined the lack of ability of the single strut analogy regarding representing the bending and shear forces on the frame members, therefore Crissafuli's (1997) previously mentioned double-strut model was adapted. However, the struts were not configured parallel to each other unlike the former study; instead, these were inclined with different angles which were needed to be calculated by some equations. For this purpose, in total, 18 parametric analyses considering different number of stories and aspect ratios as well as soft story mechanism were conducted. The results were evaluated within the elastic range only, since the strut model was not developed for simulating the behavior in the plastic stage. Several sensitivity analyses were run and it was concluded that the geometry of the wall and the story numbers were the dominant factors while determining the positions of the struts. Accordingly, Equations 3.10-3.13 were produced, where b_1 , b_2 , d_1 , d_2 , l , h , θ_1 , θ_2 have geometrical meanings as shown in Figure 3.17. All in all, it was highlighted that this model was not completely applicable for the low magnitude seismicity concerns due to possible inactivity of the double-struts.

$$\text{first strut, first level} \quad \begin{cases} \frac{d_1}{h} = 0.10834\left(\frac{l}{h}\right)^{-1} + 0.0073141\left(\frac{l}{h}\right)^2 \\ \frac{b_1}{l} = 0.48689\left(\frac{l}{h}\right)^{-2} + 0.16302\left(\frac{l}{h}\right)^{0.5} \end{cases} \quad (3.10)$$

$$\text{first strut, upper levels} \quad \begin{cases} \frac{d_1}{h} = 0.11609\left(\frac{l}{h}\right)^{-1} + 0.0061624\left(\frac{l}{h}\right)^2 \\ \frac{b_1}{l} = 0.56509\left(\frac{l}{h}\right)^{-1} + 0.1287\left(\frac{l}{h}\right)^{0.5} \end{cases} \quad (3.11)$$

$$\text{second strut, first level} \quad \begin{cases} \frac{d_2}{h} = 0.157621\left(\frac{l}{h}\right)^{-1} + 0.084484\left(\frac{l}{h}\right)^{0.5} \\ \frac{b_2}{l} = 0.408621\left(\frac{l}{h}\right)^{-0.5} + 0.44431\left(\frac{l}{h}\right)^{0.5} \end{cases} \quad (3.12)$$

$$\text{second strut, upper levels} \quad \begin{cases} \frac{d_2}{h} = 0.1025\left(\frac{l}{h}\right)^{-0.5} + 0.046736\left(\frac{l}{h}\right)^{0.5} e^{\left(\frac{l}{h}\right)^{-0.5}} \\ \frac{b_2}{l} = 0.312751\left(\frac{l}{h}\right)^{-1.5} + 0.467931\left(\frac{l}{h}\right)^{0.5} \end{cases} \quad (3.13)$$

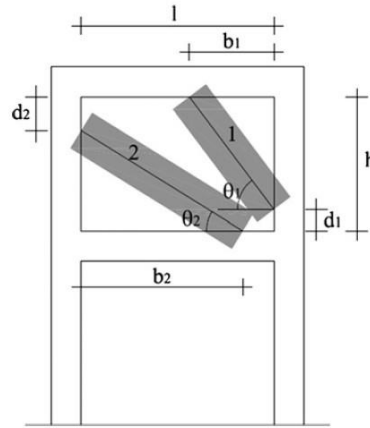


Figure 3.17. Schematic strut positions and related definitions [adapted from Fiore et al. (2012)].

Furtado et al. (2015, 2017) improved the macro model of Rodrigues et al. (2010) which was initially created for simulating the in-plane behavior of the masonry infill walls, and included the out-of-plane effects in that approach. The original model consists of a central element where non-linear features were assigned by means of the axial force-resistance mechanism and four inclined rigid struts that connects the central element to the bounding frame at the corners. In the improved model, two additional central nodes with panel masses were assigned for simulating the out-of-plane behavior that was inspired by the proposal of Kadysiewski and Mosalam (2009), see Figure 3.17. Nonlinear hysteresis rules were assigned

to the in-plane loading conditions only by means of an envelope curve characterized by the multiple linear branches defined by eight parameters as shown in Figure 3.18, where F and d stand for force and displacement and the subscripts c , y , cr , u denote the cracking, yielding, crushing and ultimate (or residual) phases, respectively. Additional parameters for controlling the stiffness and strength degradation as well as pinching effect were used for the hysteresis rules, too. Following that, some suggestions were given regarding the default values of these parameters. Later, this model was introduced in the earthquake engineering simulation program OpenSees (McKenna, 2011), and a hysteresis model existing in the element library was combined with it for the analyses. In terms of the OOP hysteresis rules, only linear elastic curves were followed; however, IP and OOP curves were later merged in a way that mutual interaction of these two distinctive behaviors could be evaluated simultaneously. Upon conducting numerical analyses, overall satisfying performance was achieved on the global level. On the other hand, it was also stated by the authors that the proposed model is limited for actualizing the contact interactions with the surrounding frame, because of the absence of multiple struts that need to be connected to the other parts than just to the corners of the frames. However, the model still triumphs over the ordinary single strut models, since the compressive and tensile effects on the panel could be captured simultaneously regardless of the loading direction.

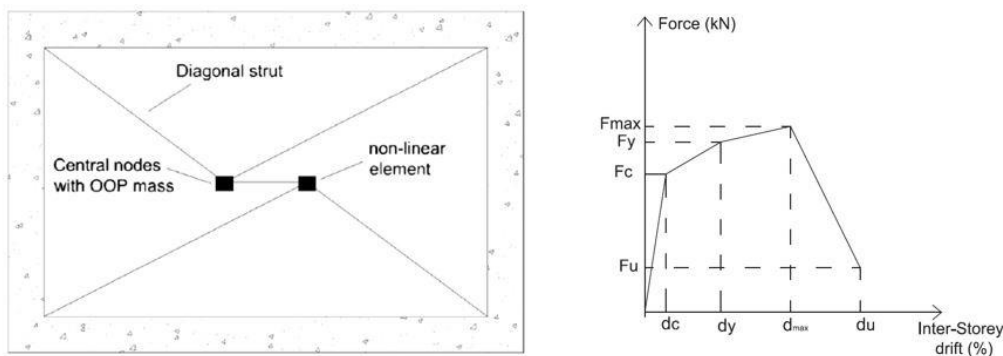


Figure 3.18. Strut and mass configuration (left) and force-drift relation of the central element [adapted from Furtado et al. (2015)].

Despite a few exceptions, only the strut mechanisms working under monotonic loads were mentioned until now. However, any type of cyclic loads – such as earthquakes – require a hysteresis model definition, where load reversals and other material deteriorations are defined. Therefore, following paragraphs in this section are dedicated for the hysteresis model propositions of the infill walls.

One of the first proposals regarding the infill panel hysteresis behavior came from the extensive study of Klinger and Bertero (1976), which was previously mentioned from the experimental perspective in Section 3.1. As a result, only the analytical model is discussed below. The infill panels were idealized with a single strut approach and the equivalent width was calculated by the method suggested by Mainstone (1971), though the validity of the method prediction of the lateral force-deformation behavior is rather a concern of suitable non-linear mathematical formulation. Therefore, the emphasis was on the accurate representation of the initial stiffness and strength as well as the degradation of these features particularly due to the pinching effects. Accordingly, three different strut models were developed that the successive trials had slight improvements while obtaining closer approximation to the experiments. Consequently, the mechanical behavior of the tested systems was transformed in a hysteresis curve form as presented in Figure 3.19. Although not very common for such systems, some tensile resistance was introduced to the model which was observed in the experiments and mainly attributed to the panel steel. The model was designed to be able to simulate the elastic and inelastic loading-unloading phases and according to the results it was correlated well with the test outcomes, despite the slight force over-estimations of the analytical model upon the initial crushing. However, it was also stated by the authors that the model was primarily developed to reflect the experimental conditions for their study e.g., solid panels without openings or full loading cycles neglecting the possibility of sudden loading reversals. Further investigation was suggested in this manner.

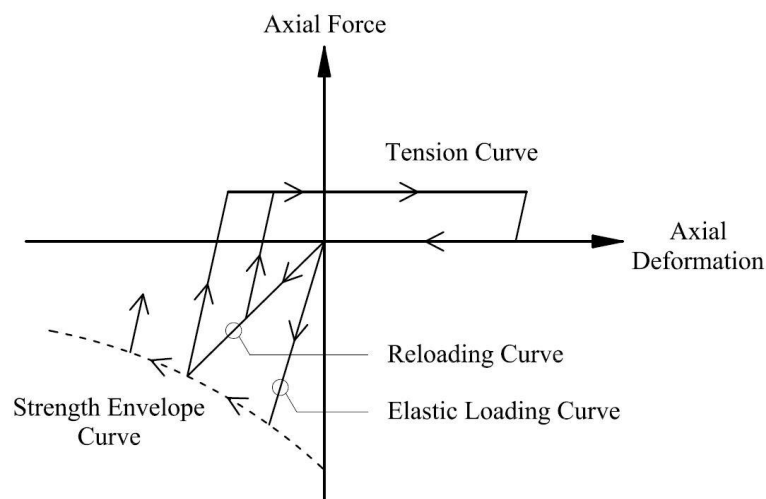


Figure 3.19. Equivalent strut hysteresis model [adapted from Klinger and Bertero (1976)].

Zarnic and Tomazevic (1984) conducted cyclic tests on single-bay and single-story RC frames with masonry infills. In that study, a single strut off-diagonal model was developed assuming that upon cracking of the wall, only lower triangular part of the panel carries the horizontal load which intersects with the windward column at the two thirds of the height – h_t , as shown in Figure 3.20. Some calculations were made taking into consideration the lateral load level at the first diagonal cracking on the wall, at the separation between the frame and infill as well as initial and ultimate stiffness of the system, and a bi-linear hysteresis curve envelope was proposed. The results were compared with the experimental ones and seen that analytical solution underestimated the overall load capacity and stiffness, though the authors did not particularly focused on this point.

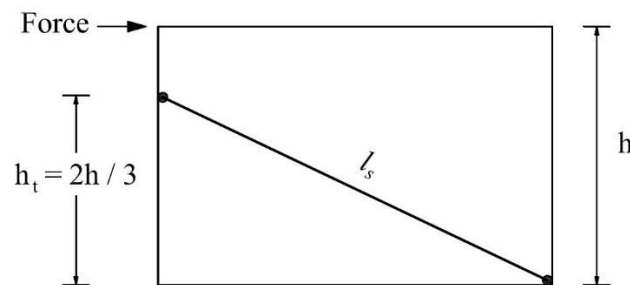


Figure 3.20. Mathematical model of the failure mechanism [adapted from Zarnic and Tomazevic (1984)].

Doudoumis and Mitsopoulou (1986) investigated the non-integral infilled frames with initial gap presence due to the shrinkage effects. Using a typical single strut model, it was attempted to establish a non-linear law for the axial force-displacement interactions of the equivalent compression struts. The model comprised of different paths while creating a load-deformation loop, namely initial gap closing path, elastic loading increment, compressive yielding, gradual cracking and subsequent unloading paths as shown in Figure 3.21. It is important to highlight that the strength degradation was considered in this model but stiffness degradation or pinching effects were omitted by any means. Nevertheless, in order to test the assumption, numerical calculations were done for a hypothetically created five-story partially infilled framed structure. However, it was rather presented the influence of the gaps and infill wall presence on the building overall behavior. Since no experiments were performed, the authors could not compare their proposal with the actual situations.

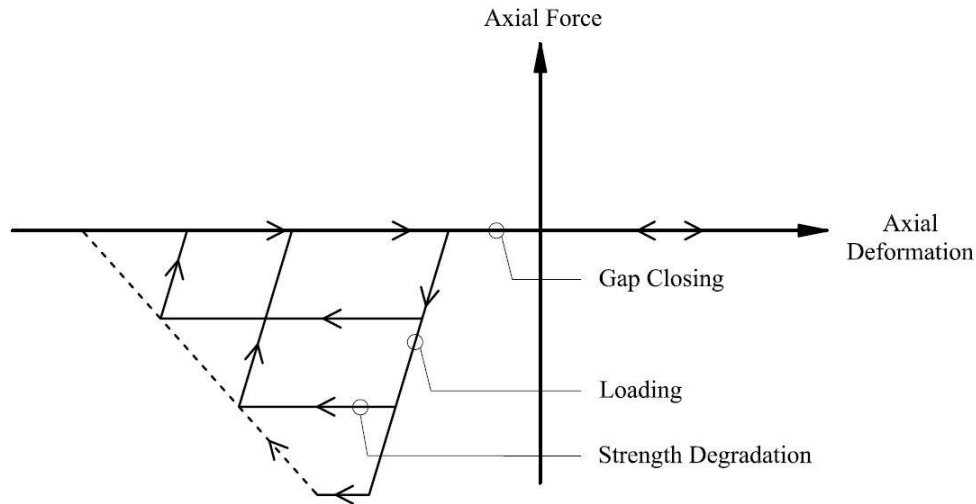


Figure 3.21. Equivalent strut hysteresis model [adapted from Doudoumis and Mitsopoulou (1986)].

Fardis and Panagiotakos (1997) conducted a series of parametric comprehensive analyses regarding the seismic design principles of the masonry infilled buildings and later presented an extended version of the hysteresis model of Tassios (1984) which takes into account the infill wall related damping effects as well. The efficiency of the method was firstly tested by means of evaluating the inelastic spectral response of the single degree of freedom (SDOF) systems. After that, it was also implemented into the multi degree of freedom (MDOF) systems and compared with the multi-story large size experiments. The envelope curve was created with four linear curves, where the ultimate load F_u was taken as 1.3 times of the cracking load F_{cr} . The slope of the initial stiffness K_1 was quantified by a derivation of the diagonal shear modulus with respect to the panel cross-sectional area and the clear height. In addition, the post cracking hardening ratio defined by $p = K_2/K_1$ was declared to take values between 1/7 and 1/10. Furthermore, in order to control the fractions of the branches in the hysteresis loops, parameters of α , β and γ were taken equal to 0.15, 0.1 and 0.8, respectively. Description of the hysteresis curve is given in Figure 3.22.

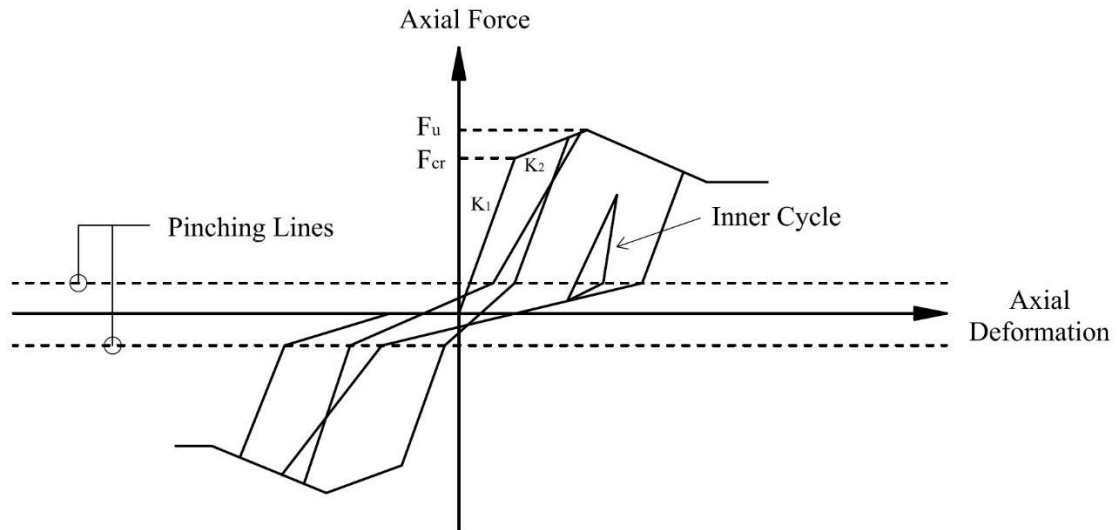


Figure 3.22. Equivalent strut hysteresis model [adapted from Fardis and Panagiotakos (1997)].

Madan et al. (1997) utilized the single strut model definition of Saneinejad et al. (1995) for the infill panels and improved it by including a hysteresis constitutive law. In this sense, the proposal was introduced for evaluating the overall inelastic structural response rather than investigating the local effects which would require more detailed analytical or numerical solutions. Accordingly, the well-known stress-strain relationship of Mander et al. (1988) that was developed for the concrete material was adapted for determining the strength envelope curve of the masonry infills. Later, a comprehensive hysteresis model was created which was mainly based on the Bouc-Wen approach (Bouc, 1967; Baber and Wen, 1981). The model comprised of information from various past researches while establishing the smooth curve presented in Figure 3.23, where ΔK and ΔV denote the stiffness and strength decays, respectively. Moreover, pinching effects due to the masonry cracks were also included. However, probably the most interesting part of this model could be stated as its focus on the endeavor of including the time-rate dependent properties into the equations, since this factor was mostly neglected previously. Authors claimed that such approach would enable their model to be a proper alternative for simulating the dynamic loading actions such as earthquakes. Finally, the hysteresis proposal was analyzed with a computer program and the results were compared with the experimental specimens. Overall, the outcomes exhibited reasonable match with the actual tests in the force-displacement field.

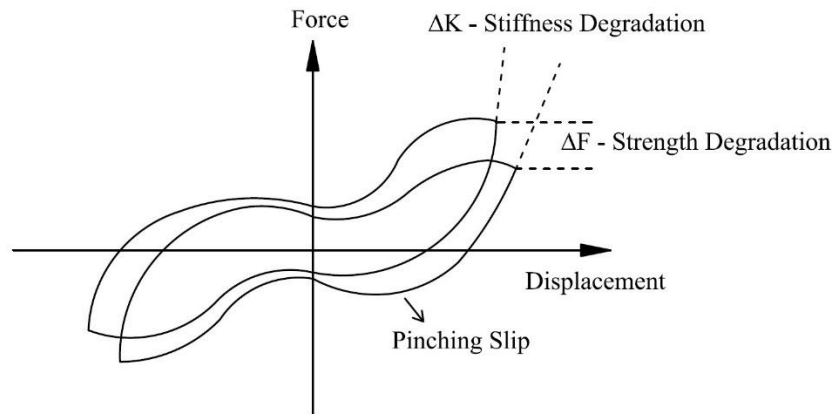


Figure 3.23. Equivalent strut hysteresis model [adapted from Madan et al. (1997)].

Kappos et al. (1998) developed analytical models for the brick masonry infilled RC frames under lateral loading. In this regard, firstly a study was conducted which considered only the elastic material properties. Bare frame, infill panel with finite elements and diagonal struts models were compared for single-story single-bay and multi-story models. The bare frame model exhibited more ductile behavior whereas the panel and strut models yielded similar axial and lateral displacement results under static and dynamic loads. Following that, in order to modeling the inelasticity, previously conducted extensive experiments (Valiasis and Stylianidis, 1989) were analyzed. The one-third scale single-story and single-bay RC frame test samples constituted with clay brick masonry were subjected to the quasi-static cyclic loads. Later, these test results were utilized for developing a hysteresis model. For this purpose, shear forces carried by the frame and infill wall were extracted and evaluated separately, thus their contributions were investigated individually. Three-branch envelope curve in the form of shear stress vs shear strain was created based on the experiments. First branch corresponds to the elastic phase, whereas second and third branches are for the post-cracking and post-yielding (descending) phases, respectively, see Figure 3.24. Following that, hysteresis rules were defined taking into consideration the strength and stiffness degradation as well as the pinching behavior caused by the shear induced slippage. In Figure 3.24, these curves are given, where the dotted lines indicate the pinching effects and the unloading trend starts using the elastic stiffness when these dotted lines are reached. It was also emphasized that ordinates of these lines would only vary based on different axial loading levels. Moreover, a new hysteresis model was also briefly proposed specifically for the random amplitude loading histories such as earthquakes, since the original hysteresis loops were obtained using the gradually increasing lateral load amplitudes. Finally, both strut and FEM panel models were compared and it was

stated that the strut model significantly increases the axial forces in columns; however, this issue was less pronounced if the elastic foundation features are added to the model (e.g., normal direction springs at the base level). Therefore, authors recommended to include such effects for the design practitioners since their study showed that infill wall presence drastically changed the structural behavior.

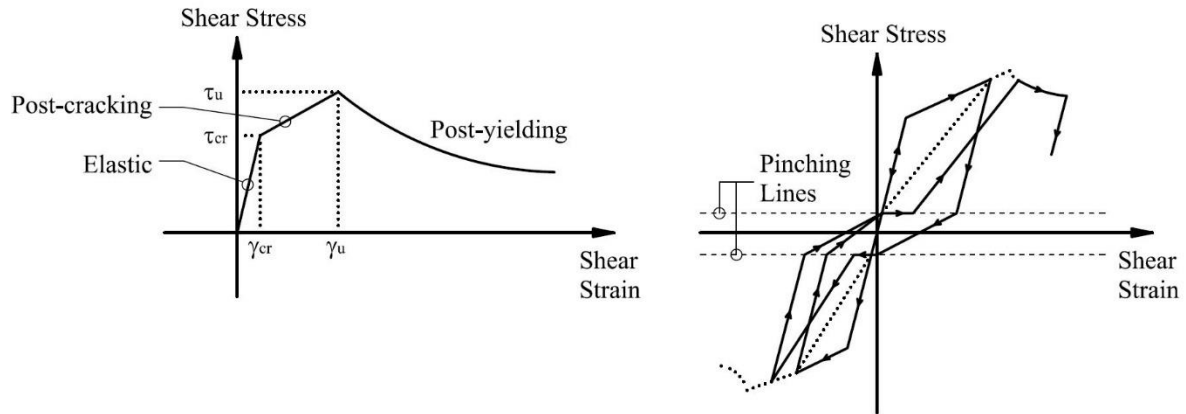


Figure 3.24. Shear stress-strain envelope (left) and hysteresis curves (right) [adapted from Kappos et al. (1998)].

Decanini et al. (2004) investigated the infill panel influence in RC frame multi-story buildings analytically and considered three types of masonry infills that each represented weak, intermediate or strong masonry assemblages. For this purpose, a new hysteresis model was developed, Figure 3.25. However, for defining the strut width – w , previously mentioned Stafford-Smith’s (1962) well-known single strut stiffness parameter – λ_h was utilized, yet introduced with additional constants which were required to be obtained from the experiments. On the other hand, the equivalent strut stiffness for the cracking stage was defined separately and labeled as K_{mfc} , which is given Equation 3.14.

$$K_{mfc} = \frac{E_m e \omega}{d} \cos^2 \theta \quad (3.14)$$

Moreover, the infill panel resistance was simulated by means of defining fictitious failure compressive stresses corresponding four distinctive failure modes; diagonal tension, sliding shear at the horizontal joints as well as corner crushing and diagonal compression failures of the panels. Based on the different compressive failure stresses obtained, the minimum value of those was assumed to be the determinant of the failure, hence the strength of the equivalent strut was given as in Equation 3.15.

$$H_{mfc} = (\sigma_{br})_{min} e \omega \cos \theta \quad (3.15)$$

This hysteresis model was compared and validated with the previous experimental tests of Parducci and Mezzi (1980) and Stylianidis (1988), and reportedly yielded reasonably close results.

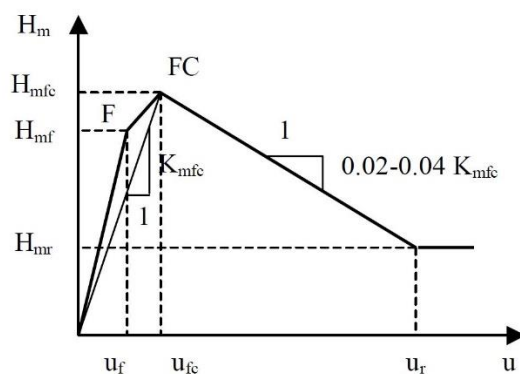


Figure 3.25. Envelope curve of the equivalent strut [adapted from Decanini et al. (2004)].

Rodrigues et al. (2008, 2010) developed the commonly used models with the bi-diagonal equivalent struts which works separately depends on the loading direction and proposed an integrated solution that claimed to consider the infill panel interactions in both directions simultaneously. This model was previously mentioned in this chapter while describing the model of Furtado et al. (2017), therefore it is only focused on the hysteresis model of the original study in here. Accordingly, the central element shown in Figure 3.18 was provided with nonlinear properties and a hysteresis rule was adapted that was mainly inspired by the previous tri-linear model of Costa and Costa (1987). The curve paths of the hysteresis loops were elaborated in order to reflect the material's actual behavior, thus the loading stages were divided into multiple steps. Loading, unloading, pinching effects, stiffness and strength degradations as well as inner cycles were attributed to the different rules, and all were primarily constituted on the basis of stiffness or displacement changes of the previous loading stages. In addition, some other parameters for representing specific conditions were used as well. The hysteresis curve for this model is shown in Figure 3.26, where each letter has merely the labeling meaning without the need of further explanation. Nevertheless, the model was calibrated in different numerical analyses and exhibited decent performance when compared to the large-scale experiments.

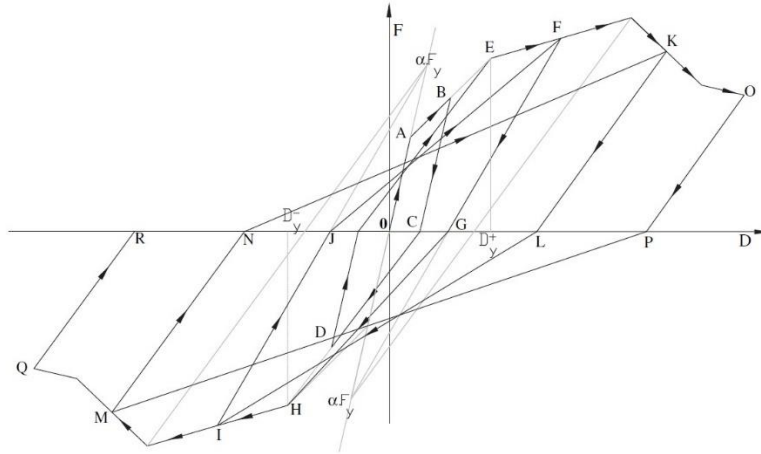


Figure 3.26. Equivalent strut hysteresis model [adapted from Rodrigues et al. (2008)].

As a companion study of the aforementioned experimental campaign of Cavaleri and Di Trapani (2014), an analytical model was developed as well. The approach comprised of multi-linear plastic link elements that governed by the pivot hysteretic law which was originally proposed by Dowell et al. (1998) for predicting the cyclic actions on the RC columns. Accordingly, strength of the bare frame was expressed by a limit equilibrium condition, which later was used for determining the parameters of the pivot model that principally works on the basis of geometrical rules rather than complex analytical equations. The hysteresis rules were defined to be controlled by the parameters of α_1 , α_2 , β_1 and β_2 . Using these parameters, pivot points P_1 , P_2 , P_3 and P_4 as well as the pinching points PP_1 and PP_2 could be determined, as shown in Figure 3.27. However, the model was exposed to a substantial simplification when applied on the masonry walls, since the tensile resistance of such panels do not play an important role, thus could be negligible. In this way, the model was derived to another shape as presented in Figure 3.27, which now was governed by only P_2 parameter. In order to determine the remaining values such as stiffness and strength variables, additional efforts were made. Firstly, Papia et al. (2003)'s definition of the diagonal strut expression was used for defining the initial stiffness of the equivalent truss mechanism, which takes into consideration the vertical loads acting on columns in an approximate way. Following that, the peak strength S_2 was formulated through calculating the relative strength of the infilled system to the bare frame and also by means of performing several iterations for obtaining some other required parameters empirically. Consequently, the other variables; S_2 , S_3 , δ_1 , δ_2 and δ_3 were identified, see Figure 3.27. Finally, the analytical model was validated with the previously mentioned experimental quasi-static cyclic tests, besides it was applied to solve a case of the

nonlinear time-history analysis of a multi-story frame. All in all, the proposed model was claimed to be suitable for the global behavior concerns e.g., displacement, ductility or energy dissipation. On the other hand, it was stated that further studies are required due to the uncertainties caused by the number of specimens, scale effects and different masonry properties which also affects the value of crucial α_2 parameter.

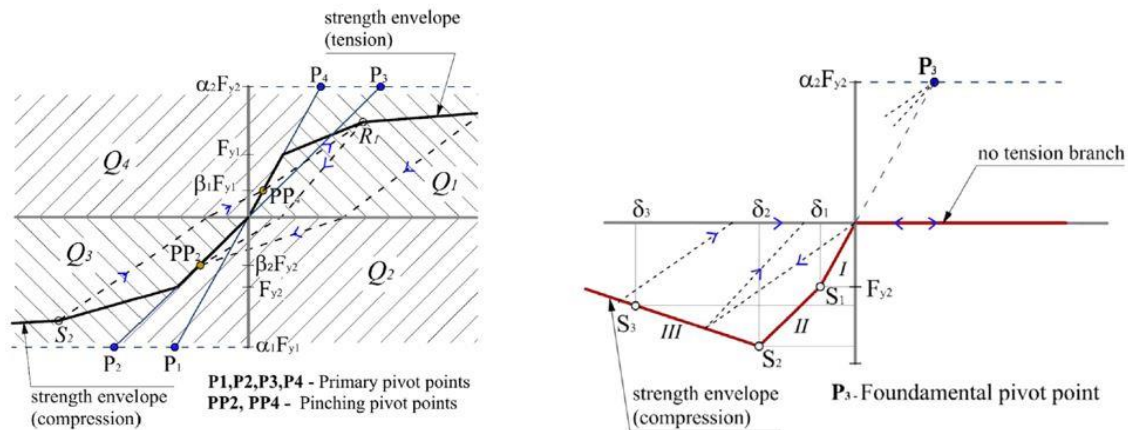


Figure 3.27. Hysteresis pivot model for a generic tension-compression activated situation (left) and modified version for the equivalent struts (right) [adapted from Cavaleri and Di Trapani (2014)].

More recently, De Risi et al. (2018) and Huang et al. (2020) analyzed the database of masonry infill wall experiments and proposed empirical solutions in this regard. The first research group originated their study from the work of Fardis and Panagiotakos (1997) and developed it by means of reducing the CoV values. On the other hand, the latter study also focused on obtaining the backbone curve but the authors conducted multivariate regression analyses and established the parameters of axial strut response accordingly.

3.2.2 Numerical (FEM) modeling approach

History of the mathematical analysis is as old as the primeval human consciousness. Initially starting from the simple real-world problems, it was eventually possible to handle more difficult questions such as the ones related to astronomy. Therefore, it was not a coincidence that prominent astronomers such as Euler, Gauss, Jacobi, Lagrange, Newton etc. were great mathematicians too, who were the inventors of numerical analyses for studying complex algorithms and their properties. In order to do that, complicated problems were converted to simpler ones by proper discretization techniques, hence it could be anymore convenient to acquire the linearized equations (Brezinski and Wuytack, 2001). Thanks to such

transformation, the modern computational problems are being solved using partial differential equations, which firstly emerged the finite differences method (FDM) and then also developed as the finite elements method (FEM) (Thomee, 2001). In the following paragraphs, it is focused on the FEM based modeling strategies for the infilled systems due to being by far the most popular one among the engineers, though some other options such as discrete elements method (DEM) or boundary elements method (BEM) also exist.

As reported by Abdul-Kadir (1974) and Asteris et al. (2013), the pioneers of implementing the FEM solutions into the infilled frame structures were Karamanski (1967) and Mallick and Severn (1967). Although the study of Karamanski (1967) could be considered disputable, since an unbroken tie assumption was made between the frame and infill panel which does not represent the reality, it was still a remarkable contribution to the endeavor of the computational modeling of the infilled systems (Abdul-Kadir, 1974). On the other hand, the study of Mallick and Severn (1967) addressed the interface condition problem of the frame-infill interface more accurately as the points of separation were able to be found. Relative slip behavior was also taken into account. It was concluded that the results were satisfactory as long as the panel aspect ratio was restricted with a certain limit due to the bending formation concerns.

King and Pandey (1978) showed that infill-frame interaction could be modeled with the friction elements. The frame members were idealized with bending beams having three degrees of freedom at each node whereas four-node rectangular plane stress elements were used for the infill panels, which were also able to be assigned a non-linear behavior. The interface conditions were provided with four-node friction elements that were attributed to normal and shear stiffness coefficients, which were also suggested by the authors on the basis of experiments.

Liau and Kwan (1984) divided the infilled structure into three separate elements; frame, panel and their interfaces. They used triangular plane stress elements which reflected the non-linear behavior of the infills with a multi-linear curve idealization. It was assumed that the material is isotropic before the cracking and the post-cracking phase resulted the anisotropic situation.

Dhanasekhar and Page (1986) performed biaxial tests on a large number of reduced scale panels in order to derive a failure surface scheme for the brick masonries, in which the stress conditions were defined based on the state of stresses as well as their orientation. Using this failure criteria, an iterative non-linear FEM model was created. The surrounding frame was assumed to behave elastic, while the mortar joints were described with one-dimensional

elements that were able to simulate the separation and shear failures. The loads were applied incrementally in the model. The material nonlinearity and progressive failures were taken into account for each iteration, which continued until reaching a specific tolerance limit. The finite element results were compared with the racking tests of infilled steel frames and the model provided satisfactory match with the actual experiments.

Lotfi and Shing (1991) employed the smeared crack model in their finite element analyses in order to check the capabilities of this approach while simulating the reinforced masonry shear walls. In this purpose, two phases of material behavior were defined, namely cracked and uncracked conditions. For the first one, the J_2 -plasticity model which is an elasto-plastic constitutive law based on the von Mises equivalent stress was used for defining the failure surface. On the other hand, nonlinear orthotropic models were developed for the cracked phase. The finite element results were compared with diagonal compression and in-plane cyclic loads. It was seen that flexural response could be captured with this method, whereas there were certain concerns about the accurate representation of the diagonal cracking related shear behavior.

In another study of the same authors, Lotfi and Shing (1994), unreinforced concrete masonry panels were modeled by the finite elements, where a constitutive law was proposed for the dilatant interfaces. Damage initiation and propagation under combined stresses i.e., normal and shear, as well as joint dilatation were able to be defined using the theory of plasticity. Therefore, a hyperbolic yield criterion, non-associated flow rule together with the softening rules were described. Accordingly, the finite element mesh was created with four-node isoparametric quadrilateral or interface elements for the masonry units and mortar joints, respectively. It was a mesh insensitive analysis, since the failure was associated with the joints which was also observed in the experiments.

Mehrabi and Shing (1997) also utilized the proposed smeared crack model of Lotfi and Shing (1991) for modeling the masonry infill panel and RC elements. They developed the previously announced dilatant interface constitutive model of Lotfi and Shing (1994) by means of including additional aspects in it. Therefore, a nonlinear compressive hardening behavior of the interfaces were taken into account. It was assumed that no dilatation occurs during the elastic phase, whereas geometric dilatation effects were also pronounced in the plastic regime. In this way, relative displacements at the joints could be expressed by the sum of elastic, plastic and geometric parts. In addition, a simple concrete-rebar bond-slip behavior was also considered in that finite element model, though it was stated that no major impact was observed for the infilled models. The results of the analyses were compared with a large set of

experiments and consequently, a reasonably close agreement was obtained in the global response level.

Singh et al. (1998) performed static and dynamic numerical analyses on RC infilled frames. An inelastic constitutive model was developed in a way that frame, infill panel and interfaces were introduced with 3-node beam, 8-node isoparametric and 6-node interface elements, respectively. Only in-plane stiffness of the masonry was considered and the behavior was assumed to be elastic up to failure. Cracking and crushing models were predicted by a tension cut off included von Mises criterion. Overall, it was concluded that the inelastic analysis is essential for an accurate representation of the infilled systems.

Ghosh and Amde (2002) also showed particular attention towards the mortar joint interfaces while developing their finite element model. In line with this objective, firstly a literature examination was done with the experimental tests, which was later used for the calibration purposes. In their interface element proposal, it was assumed that normal stresses had negligible effects on the friction coefficient, unlike the commonly used Mohr-Coulomb yield criterion predicts. Moreover, a simple smeared cracking formulation was made for the uncracked masonry, which was based on the von Mises plasticity model. In the post-cracking regime, the material was transformed into an orthotropic stage where Poisson's effect was ignored. The finite element results yielded fair match with the lateral load-displacement results of the experimental ones. Besides, the failure mode, ductility and cracking features of the test specimens could also be evaluated using such numerical method.

Further development endeavors of the smeared concrete (Lotfi and Shing, 1991) and joint interface (Lotfi and Shing, 1994) constitutive models continued with Stavridis and Shing (2010). They adapted the masonry and interface modeling schemes directly from these aforementioned studies. One improvement attracted the attention that each brick unit was subdivided into two smeared-crack elements that were connected with a single interface element, see Figure 3.28. Such an approach was also provided in the extensive study of Lourenco (1996) which was primarily established for the unconfined (without surrounding frames) masonry assemblages, hence a different discrete failure zone could be introduced other than the mortar joints. On the other hand, it was addressed that smeared crack elements were inadequate for simulating the RC elements due to the stress-locking issues. In order to overcome this problem, a discretized element formation was proposed so that shear cracks could be properly represented. Owing to lack of knowledge of the exact crack locations, initially quadrilateral elements were replaced with triangular smeared-crack parts and were connected by zero thickness interface elements. The reinforcement bars were also configured

for matching with this new scheme, as shown in Figure 3.28. The combination of discrete and smeared modeling also led to obtain a relatively less mesh-insensitive form. The material models were calibrated firstly and then validation analyses were performed using the experimental dataset of Mehrabi et al. (1994). According to results, especially initial stiffness and peak strength values were estimated with a reasonable match. And it was noticed that a parameter that controls the initial slope of the hyperbolic yield criterion was affecting the results mostly, which was directly attributed to the importance of mortar joint interface modeling strategy.

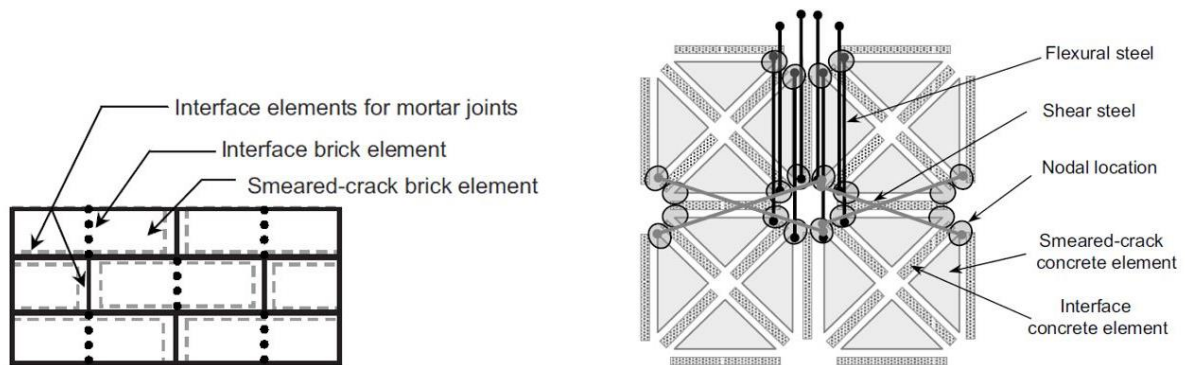


Figure 3.28. Finite-element discretization of masonry infill (left) and RC members (right) [adapted from Stavridis and Shing (2010)].

Koutromanos et al. (2011) carried the study of Stavridis and Shing (2010) one step forward, which was originally formulated to work under monotonic loading conditions only. In this sense, they complied it with the demands of cyclic and dynamic loading conditions such as earthquakes. Therefore, the discrete cohesive crack model of the original study was enhanced with a reversible shear dilation formulation. In addition, the smeared cracking model was also improved for being suitable with the cyclic loads. Following that, the updated constitutive model was analyzed numerically and the results were compared with the experimental ones; single-bay single-story specimens under cyclic loads as well as a two-bay three-story infilled frame excited on a shake table with the time history loads. The finite element outcomes were found in a good agreement with the experimental ones. It was also noticed that the lateral loading history type did not influence the results significantly, though the monotonically performed load increment would give higher peak strength values than the actual-like cyclic loads.

In this section, some of the most influential studies have been given which stand at the parallel positions with the purpose of this dissertation, though plenty of others can be found in the literature. For further details in this topic, following references might be browsed; Asteris et al. (2013), Nicola et al. (2015) and Noh et al. (2017).

3.3 Earthquake protection methods and retrofitting solutions for the infill walls

The masonries could be divided into two groups in terms of the presence of initial strengthening implementation, thus these walls could be named as either reinforced masonry (RM) or unreinforced masonry (URM). The former one typically has steel rebars placed in or around the wall during the construction process, whereas the latter one is deprived of such reinforcement. In this section, it is focused on the URM infills, since additional strengthening techniques are not common solutions for the RM infills.

The concern of strengthening the infills is a very new topic and it has started to be largely discussed only in the last two decades. In such a limited period, impressively a lot of studies were conducted. Furtado et al. (2020) made an extensive literature survey on this subject and divided the retrofitting and strengthening approaches into two main categories; i) methods of disconnecting the masonry infill walls from the rest of structural system and ii) the other techniques for the robust integration and strengthening of the infill walls. On the other hand, a similar way is followed here and two distinctive methodologies are discussed. However, the groups are categorized slightly different, as it is thought that a more precise and comprehensive definition is needed. Accordingly, the first group of the methods are gathered under the title of “Joint Methods”, since the offered solutions for those are directly related to the boundary or interface conditions between different materials (frame and infill) or same materials (masonry blocks). The second group is called “Jacketing Methods”, which basically involves the most popular ones that could be easily found in the literature such as composite wrapping or reinforced coating techniques. These solutions are outlined schematically in Figure 3.29 and discussed briefly in the following paragraphs for providing a general view about the topic. For more details, the reader is suggested to refer Furtado et al. (2020).

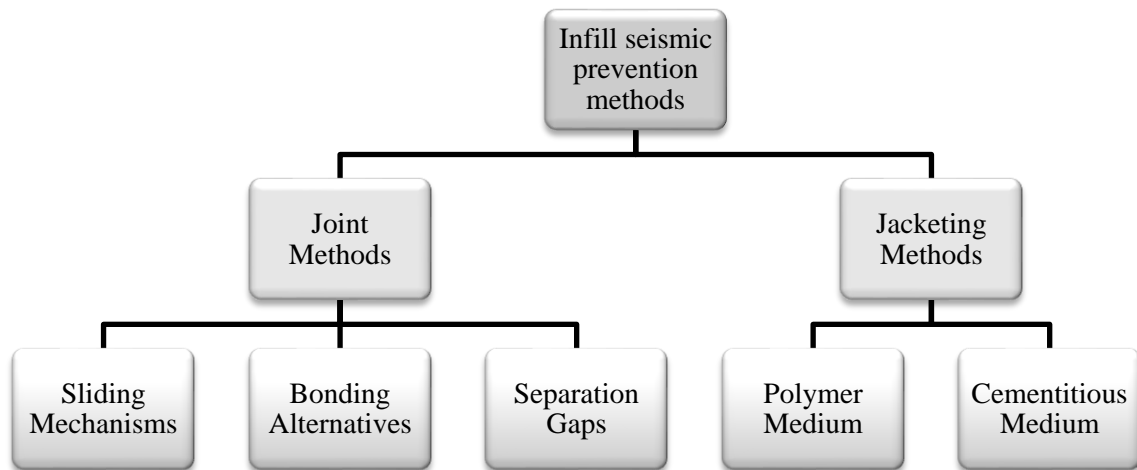


Figure 3.29. Infill masonry seismic prevention methods.

3.3.1 Joint methods

It is anymore a well-known fact that the infill panels and the surrounding frame act differently under lateral forces, hence it is obvious that both these members are prone to receive damages due to the interaction effects. Several researchers offered different solutions to mitigate this phenomenon within this context. These could be subdivided into three main techniques as; i) sliding mechanisms that particularly aimed at increasing ductility, ii) versatile bonding alternatives that could enhance ductility and/or strength features and lastly iii) separation gaps presented as the way of minimizing the frame-infill contact. Related references are made for each of these below.

i) Sliding mechanisms:

Mohammadi et al. (2011) conducted experiments in two stages. First, three different ductility improvement methods were tested on six large-size steel frames infilled with concrete-brick mixed masonries. It was found that providing horizontal sliding fuses were very effective for increasing the ductility; however, it caused shear damages on the columns and made the infill vulnerable against the out-of-plane failures, see Figure 3.30. Therefore, the second stage of the experiment was dedicated for seeking improvement ways in this regard. Accordingly, a mid-height placed frictional fuse as well as chamfered corners were utilized and the specimen was tested, Figure 3.30. On the other hand, the new model was not compared with the traditional methods in this stage, but it was declared as a better alternative by the authors.



Figure 3.30. Sliding mechanism proposal; initial (left) and upgraded version (right) at the end of tests [adapted from Mohammadi et al. (2011)].

Preti et al. (2012) also utilized the idea of horizontal sliding joints and performed in-plane tests on hollow-clay or adobe infilled large-scale steel frames. Ductility efficiency was proved when compared to the traditional methods. In the next studies, the out-of-plane stability was improved and the walls with openings were tested by Preti et al. (2015). Besides, a simplified analytical model was proposed later, Preti et al. (2017).

Misir et al. (2012) invented a patented new product called locked bricks. Horizontal hollows laid parallel to the in-plane loading direction and notch-groove formation enabled the wall integration. Besides, no mortar was used between the brick layers except the top and bottom parts of the infills where frame-to-masonry joints were provided for preventing the out-of-plane failures. In order to test their proposal, three single-bay and single-story half-scale specimens were created each for representing a different infill condition; standard bricks, locked bricks and no infill (bare-frame). The specimens were tested under quasi-static full reversal cycles up to the drift ratio 3.5%. It was seen that the locked bricks led to a ductile behavior very close to the bare-frame one, though the initial stiffness was almost same of the standard brick infilled specimen. Interestingly, the ultimate strengths were measured less for the locked brick frame than the bare-frame. Moreover, the energy dissipation capacity of the standard brick type was visibly higher than the other two frames. In this sense, it could be concluded that the innovative method was effective of protecting walls especially against the out-of-plane failures thanks to the locked-sliding mechanism. On the other hand, one should not expect an increment of the strength or energy absorption features with this method.

Vailati et al. (2016, 2018) replaced the traditional mortar bed joints with innovative recycled thermoformed joints which enabled a dry assembly option for the specially designed

blocks, as shown in Figure 3.31. It was intended to lower the strength and stiffness contribution of the walls to the rest of system, hence a sliding mechanism was made in order to reduce the interaction effects with the other structural members. The solution was claimed to keep the infills in an intact condition under low magnitude earthquakes, whereas slight damages might be expected on those when the moderate or high intensity ground-shakes are the concern.



Figure 3.31. Special design blocks details (left) and construction process (right) [adapted from Vailati et al. (2016, 2018)].

Totoev and Al Harthy (2016) developed a mortar-free solution and named it as semi-interlocking masonry (SIM). It was designed for reducing the stiffness of implemented systems by means of special interlocking bricks that allow relative sliding of the blocks through the wall in-plane direction, meanwhile preventing the out-of-plane failure. Despite the promising features, the authors agreed that the solution was not ready for the commercial usage due to the difficulties of finding proper dimensions.

Gao et al. (2018) were among the others who addressed the efficiency of horizontal sliding joints and for this reason, they tested three infilled frames; one constructed traditionally with solid and stiff details, the other two with the sliding joints and either comprised of full contact to the frame or reduced. The highest drift capacity was reached with the reduced contact-sliding joint option, though the peak and residual strength values were the lowest for that type of frame.

Morandi et al. (2018) also proposed the sliding joint approach; however, enhanced it by offering additional details; i.e., deformable joints as the frame-infill interface and specially designed edge bricks working with the steel shear keys placed on the inner surface of the frames for preventing out-of-plane failure. They conducted experimental in-plane tests on the real-size single-bay and single-story specimens for both solid walls and panels with openings. According

to results, initial stiffness and strength values were visibly higher than the bare-frame, though the traditionally constructed infilled frame had much greater maximum load carrying capacity. Dynamic characteristics of this innovative solution was also evaluated in another study conducted by Milanesi et al. (2019).

ii) Bonding alternatives:

Goodno et al. (1996) pointed out the potential of the non-structural architectural exterior cladding panels as the passive control systems in the earthquake regions. Although the idea was not directly related to the infilled systems, its authenticity introduced that the connectors of such panels could be used as the energy absorbing and damping sources. Less than a decade later, such approach was able to be tested on a shake table, where a two-story post-tensioned hybrid building comprised of dry infill walls was subjected to the seismic records. It was seen that peak accelerations at the floor levels could be dissipated through special connections, Johnston et al. (2014).

Aliaari and Memari (2005, 2007) invented a sacrificial fuse solution called seismic infill wall isolator subframe (SIWIS) made by steel rods and concrete disk, which meant to be placed between the steel frames and masonry infill walls, see Figure 3.32. It was aimed to contribute to the structural strength up to moderate earthquakes, and for the beyond, just simply expecting severe damages on these elements and being deactivated upon dissipating the seismic energy. Thus, the infills could be perceived as the parts of structural elements initially, and later to be isolated from the system. In this way, beneficial effects of the infill walls could be used up to a certain level. In-plane efficiency of the method was demonstrated through analytical and experimental studies, whereas not much information was shared regarding the out-of-plane performance except mentioning that it was maintained through connectors on the top beam level.

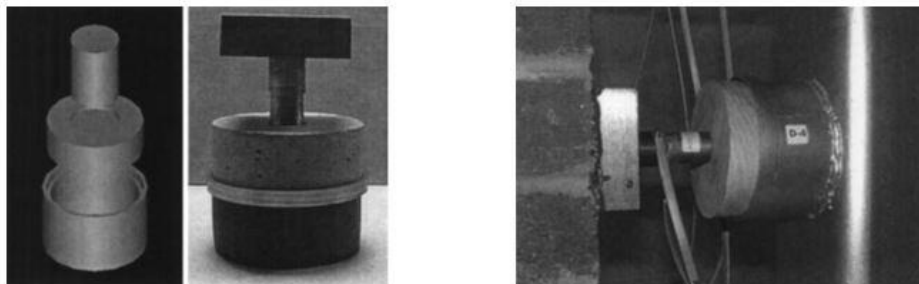


Figure 3.32. Compression disk element (left) and completed construction phase (right) [adapted from Aliaari and Memari (2007)].

The usage of flexible joints is another alternative for providing bonding between the infills and frame. Jiang et al. (2015) performed full-scale quasi-static cyclic tests on the infilled frames and investigated the performance of 20 mm thick polystyrene plates implemented in the specially designated slits, hence the one of two ends was anchored to the column whereas the other end was embedded inside the wall. The experimental results indicated that all stiffness, strength and energy dissipation capacities were dropped due to the flexible joints, though the ductility features were grown.

Tsantilidis et al. (2018) also utilized another polymer-based material for the isolation, thin polyethylene cellular strips, in two different configurations, namely either only between the columns and infill or around the entire wall perimeter covering the inner faces of the frame. They constructed 1/3 scale single-bay and single-story specimens and performed in-plane reversal cyclic tests. Besides, half-height walls were tested and the results were compared with a traditionally constructed reference infilled frame. Thickness of the foamed polyethylene was set as 1.5 mm and 3.0 mm for the full-height and half-height specimens, respectively. Representative implementation of this technique is presented in Figure 3.33. The post-experiment failure patterns showed that the isolation material was effective of reducing damages on both frame and infills. On the other hand, there was no visible drift capacity increment. Moreover, the ultimate strength values were lower than that of the reference specimen and sudden load drops were observed beyond a certain drift. Among the different implementation options, the complete perimeter covering choice exhibited a better protection performance. Above all, the authors addressed concerns regarding the out-of-plane resistance of that method. Therefore, future studies were recommended.

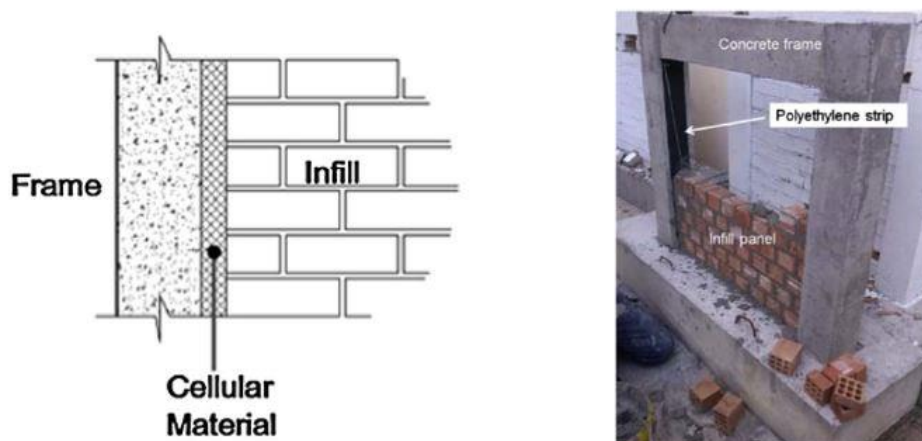


Figure 3.33. Frame-infill joint detail (left) and construction process (right) [adapted from Tsantilidis et al. (2018)].

Butenweg and Marinkovic (2018) and Marinkovic and Butenweg (2019) focused on the advantages of decoupling infill masonries from the surrounding frame in terms of the damage mitigation strategies for the infills. Their proposal was relied on an elastomeric material placed on the inner frame surfaces as a buffer zone between the frame and wall, as schematically shown in Figure 3.34. It was tested on full-size specimens by a series of in-plane and out-of-plane cyclic loads. Overall, the results demonstrated the effectiveness of the innovate solution particularly in terms of the failure prevention and lateral drift enhancement capacities (up to 3%) in return for the less load carrying capacity.

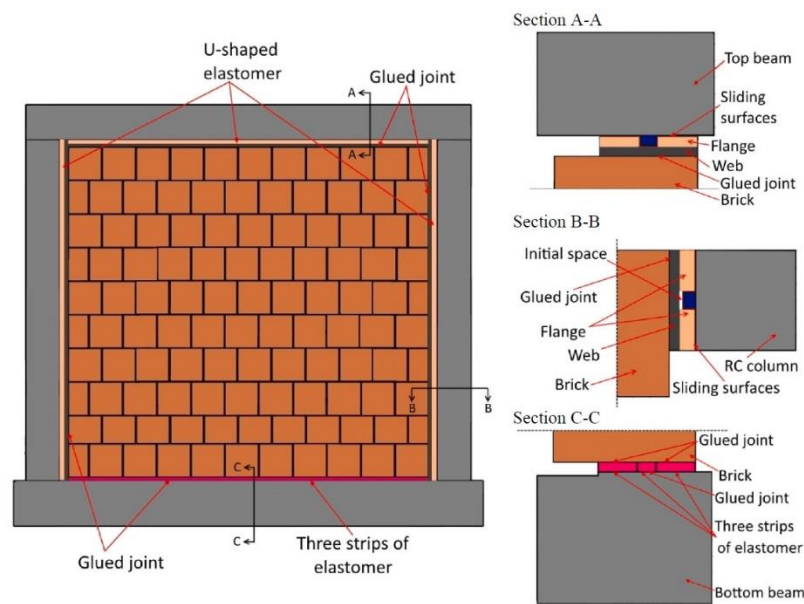


Figure 3.34. Details of the elastomeric buffering solution [adapted from Marinkovic and Butenweg (2019)].

iii) Separation gaps:

The last option regarding the joint methods could be stated as the separation gaps. Unlike the sliding or bonding mechanisms which contribute to the lateral stiffness up to a certain level, this technique has a pretty straightforward logic and it only aims to keep the infill panels intact. For this reason, gaps are provided between the frame and infill panels, mostly except the bottom parts for sustaining the out-of-plane stability which is the main concern with this method. Therefore, it is popular to implement it in steel frames rather than the concrete enclosures due to the wall stability detailing issues. A basic schematic view of this application is presented in Figure 3.35. Okazaki et al. (2007) conducted a cyclic loading experiment on a full-scale three-story steel frame building. The panels were made of autoclaved lightweight concrete (ALC) or also known as autoclaved aerated concrete (AAC) blocks and utilized as external cladding

members. It was seen that there was a very little stiffness and strength contribution of those to the frame even up to drift ratios around 4%. In another experimental study of the infilled stiff frames, Ju et al. (2012) investigated the possibilities for preventing the soft-story failures which is attributed to the relative stiffness differences between the first and the upper levels in multi-story buildings. Therefore, single-bay and single-story specimens were tested and it was proven the efficiency of initial slit separations, which enabled ductile behavior compared to that of the traditionally infilled frames.

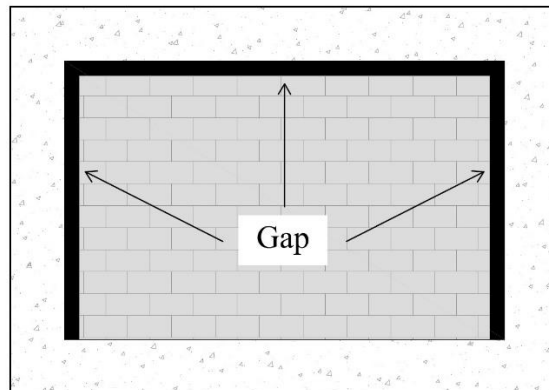


Figure 3.35. Typical gap visualization between frame and infill wall.

3.3.2 Jacketing methods

Unlike the general concept of the typical joint methods mentioned above, the jacketing methods can be defined as retrofitting interventions rather than primarily concerning with the ductility features. It is implemented on the surfaces of infills in various configurations. However, these ones can be grouped under two commonly used methods based on the medium where the reinforcement material is embedded; either polymeric or cementitious host. Some examples are given in the following paragraphs.

i) Polymer medium:

The idea of using polymer sheets was firstly pronounced for wrapping around the concrete members, which became popular especially for the columns of bridges and multi-story buildings. As reported by Furtado et al. (2020), Haroun and Ghoneam (1997) were the pioneers of implementing the fiber reinforced polymer (FRP) solution into the infill strengthening methods. Aref and Jung (2003) utilized the polymer matrix composite (PMC) technology and constructed PMC-infill wall in a full-scale steel frame and performed cyclic tests. Enhancements of the stiffness, strength and energy dissipation capacities were remarkable. El-Dakhkhni et al. (2004b) conducted an experimental investigation of the efficiency of glass

fiber reinforced polymer (GFRP) laminates which were placed to cover the exact panel dimensions for solid and open walls either on one surface or both front and rear. Almusallam and Al-Salloum (2007) positioned the GFRP sheets horizontally on the wall (Figure 3.36) and tested those under in-plane cyclic loads. Particularly, the deformation capacity was increased with such formation. Lunn and Rizkalla (2011) also used the GFRP system, however for increasing the out-of-plane resistance against the strong wind loads or tornados.

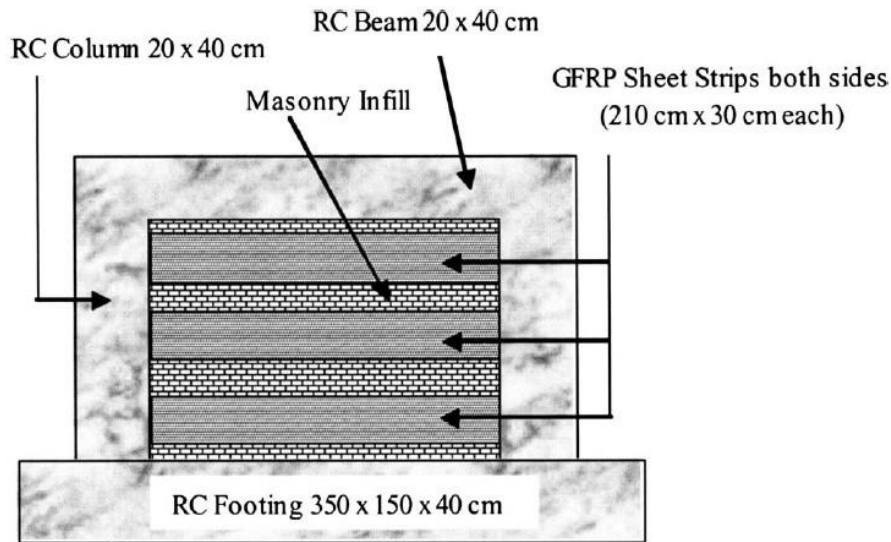


Figure 3.36. Horizontal GFRP strips positioning [adapted from Almusallam and Al-Salloum (2007)].

Erdem et al. (2006) made comparison between two strengthening techniques, namely RC infilling and carbon fiber reinforced polymer (CFRP) sheets. The latter one was implemented on the walls as diagonally placed tensile activated strips tied with special anchorage dowels, see Figure 3.37. Similar campaigns on the behavior of diagonally placed CFRP sheets were also conducted by other researchers; Ilki et al. (2007) for establishing an analytical expression, Altin et al. (2008) for checking the optimal strip widths, Kakaletsis (2011) for comparing the new method with the conventional techniques, Ozden et al. (2011) for seeing the performance of strips on multi-story frames with various anchorage conditions, Erol and Karadogan (2016) for evaluating different CFRP types and bringing analytical solutions, Kassem et al. (2016) for observing the influence of bonding conditions to the masonries.

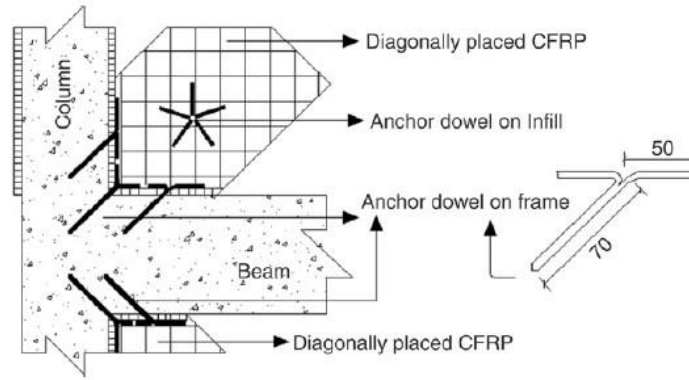


Figure 3.37. CFRP anchorage details [adapted from Erdem et al. (2006)].

In the study of Yuksel et al. (2010), configurations other than basic diagonal strips were also investigated, as shown in Figure 3.38. Moreover, Valluzzi et al. (2014) assessed the topic in terms of benchmarking the out-of-plane resistance of CFRP with some other innovative methods.

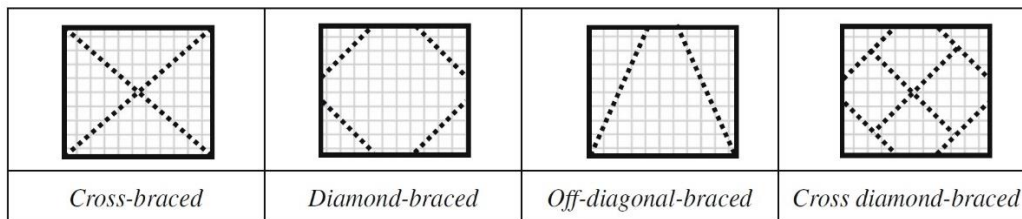


Figure 3.38. CFRP implementation alternatives [adapted from Yuksel et al. (2010)].

ii) Cementitious medium:

Infill wall retrofitting can be also actualized by encasing the entire outer shell of the masonries with so-called traditional jacketing processes utilizing cementitious mixtures as the host medium, such as; shotcreting, attaching steel plates, placing steel fibers or even using some innovative meshing options. The most popular ones are explained below.

Kesner and Billington (2005) proposed prefabricated panels made with an engineered cementitious composite (ECC) material to be used in the steel frame structures. Although it was not a typical infill strengthening offering, the solution was noble since it was advertised as an emergency intervention solution for the critical facilities such as hospitals. The effectiveness of material was proven upon cyclic tests. Later, Billington et al. (2009) and Kyriakides and Billington (2014) implemented the ECC technique for retrofitting the masonry infills in non-ductile RC frames. The ECC mix was in a sprayable form and comprised of polyvinyl alcohol (PVA) fibers (2% by volume) beside the typical cement, fly ash and so on. Due to the aesthetics

reasons, it was only applied on a single side of the wall and the thickness was provided less than 50mm. In addition, continuous steel reinforcement embedded in the ECC layer, bonding agents as well as shear dowels were implemented. Typical application process is presented in Figure 3.39. The solution was tested under in-plane horizontal loads on multiple small or mid-size specimens and its capability from both stiffness and strength perspectives were demonstrated as both were improved. In a companion paper written by Koutromanos et al. (2013), shake table tests also verified its feasibility.

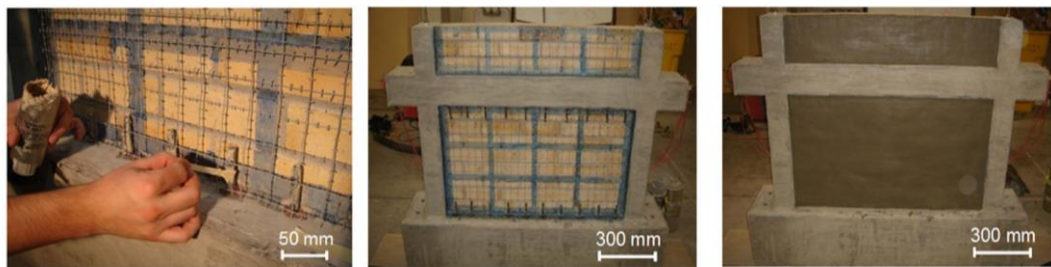


Figure 3.39. ECC implementation process [adapted from Kyriakides and Billington (2014)].

Dehghani et al. (2015) monitored the ECC performance by diagonal compressive tests on masonry wallets and utilized digital image correlation (DIC) technology for assessing the crack formation. More recently, Sharbatdar and Tajari (2021) also tested the efficiency of ECC for protecting the infills in weak RC frames and concluded that the energy dissipation capacity could be increased with this method. Besides, a simple analytical approach was proposed. Steel as a fiber material (Sevil et al., 2011) or in a perforated plate form (Aykac et al., 2016, 2017 and Cumhuri, 2016) could also be used as the coating instrument, see Figure 3.40. Moreover, ferrocement solution which utilizes small diameter steel-made wire meshes, was also suggested to be used in the plaster layer for covering the infill surfaces (Leeanansaksiri et al., 2018) as shown in Figure 3.41.

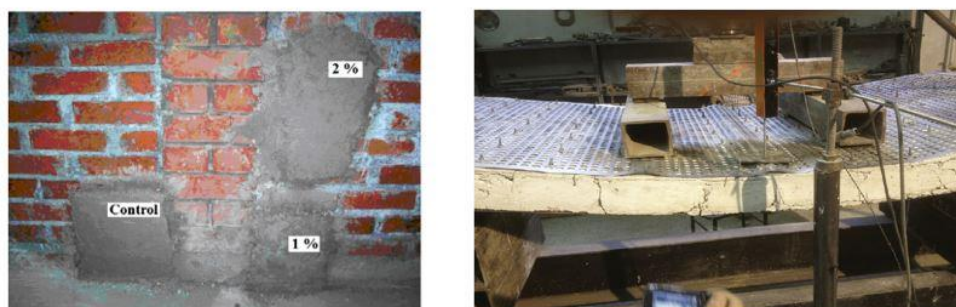


Figure 3.40. Mortar application with different fiber percentage (left) [adapted from Sevil et al. (2011)] and perforated steel plate bending test (right) [adapted from Aykac et al. (2016)].



Figure 3.41. Steel mesh installation (left) [adapted from Cumhur et al. (2016)] and ferrocement panel (right) [adapted from Leeanansaksiri et al. (2018)].

Another solution was declared by Papanicolaou et al. (2007) to use textile reinforced mortar (TRM), who made a comparative study regarding their proposal versus the typical FRP application. The TRM material consists of high-strength fabric meshes made of knitted, woven or unwoven (stitched roving) orthogonal textiles. Glass, carbon or natural materials are used as the fibers. As reported by the authors, the main advantages of this alternative when compared to its FRP counterparts could be listed as follows; higher temperature durability of the inorganic binders against the epoxy resins, better compatibility with typical construction materials such as concrete and masonry, relatively lower construction costs and improved vapor permeability. According to their in-place test results on the mid-size URM wallets, it was presented that despite being less effective in terms of the strength capacity, TRM implemented specimens exhibited better performance of enabling much higher ductility compared to the others which made of FRP. In the following years, the topic has started to be more popular among the other researchers. Da Porto et al. (2015) conducted real-scale combined in-plane and out-of-plane tests on TRM implemented clay masonry infilled frames. It was concluded that TRM strengthening did not alter the in-plane capacity significantly; however, it reduced the damages on the walls and also changed the crack patterns. Therefore, much higher out-of-plane resistance was obtained, especially if additional anchorages are used for the frame connection. Koutas et al. (2015a) tested the TRM solution on two identical 2/3 scale 3-story infilled RC frames. The only difference between those were the presence of TRM application, which was done on both columns and infills. As per the outcomes of the experiment, the effectiveness of TRM was visible, since remarkable increments on both stiffness and strength features were noted. It was also stressed by the authors that TRM application should cover the whole panel

surface and an adequate infill-frame connection is vital. An analytical approach was also proposed later, Koutas et al. (2015b). Moreover, Akhoundi et al. (2018) and Facconi et al. (2018) also conducted similar tests on single bay single-story frames, and although having configuration differences, the results were more or less aligned with the findings of previous studies. An application of the TRM on the infill walls is shown in Figure 3.42.



Figure 3.42. Step by step TRM application on the wall [adapted from Akhoundi et al. (2018)].

3.4 Chapter summary

This chapter addressed the literature survey of the infilled frame structures in three aspects; experimental studies, computational strategies either analytically or numerically and finally some of the prominent protective methods are given.

Experimental tests were mostly conducted on single-bay and single-story reduced-size specimens through their in-plane direction. In the earlier studies, monotonic loading scheme was popular which in the long run were extended to the quasi-static cyclic, pseudo-dynamic or even shake table tests. Ultimately, multi-bay and multi-story frames were able to be assessed with various configurations. Although the solid infill panels without openings comprised of the larger part of the sampling size in this study, the wall openings (doors, windows etc.) were also mentioned where relevant.

In order to establish standardized methods which could be applicable to the variety of solutions, many researchers also proposed analytical or numerical methods. Former one primarily utilizes equivalent compression struts whereas the latter option takes the advantages of FEM. Constitutive laws for each option is briefly given.

The earthquake protective methods could be classified in two manners; ductility enhancement through joints or integral panel strengthening methods by means of jacketing. Either option has advantages and rarely the combined usage of those can be found.

In a nutshell, the following implications can be expressed;

- Infill wall presence have significant effects on the structures, thus engineers should not ignore this fact while designing the buildings. The walls increase the damping, stiffness and strength features. On the other hand, there are instances that negative effects outweigh the positive ones, which are particularly attributed to the plan or elevation irregularities.
- In general, modeling the masonries is perceived as a complex task and therefore it is mostly omitted by the designers. Some approaches have been introduced for tackling this issue, but these are not still very commonly assimilated. Further studies are needed in order to establish reliable and practical methods.
- Infill wall protective methods are relatively a new topic, though many efficient ones are already proposed. Main drawbacks could be said that; either ductility or stiffness/strength features are sacrificed. Besides, cost and implementation concerns are often pronounced. Despite these challenges, it is still one the trending topics in the field.

CHAPTER 4.

EXPERIMENTAL INVESTIGATION

The experimental campaign was split into two major programs, namely in-plane quasi-static tests and dynamic shake table tests. Both test programs were run on large-size specimens considering the actual sizes of elements as much as the testing facilities permitted. Identical types of brick, mortar, flexible joint and reinforcement materials were used in the both programs, although the concrete quality might be slightly different due to being produced in distinctive local conditions. The following sections in this chapter are dedicated for explaining these experiments in detail.

4.1 Quasi-static in-plane shear tests of the infill wall specimens

In order to evaluate the performance of PUFJ on large size structures, in-plane test setups were created. The experiments were carried out at the Slovenian National Building and Civil Engineering Institute (ZAG) in Ljubljana. Three different RC frames were built and hollow clay bricks were placed at the voids between the beams and columns. The frames were identical except the bonding method chosen between the RC members and the infill wall. Among the specimens, Frame A was chosen as the reference frame which was created by the traditional construction methods, namely conventional mortars were used as the bonding material. The rest of frames on the other hand, were labeled as Frame B and Frame C that represent the implementation of PUFJ on already existing (old) and to-be-built (new) buildings, respectively. Schematic views of the test specimens are provided in Figure 4.1. Details of the in-plane shear tests are given in this chapter.

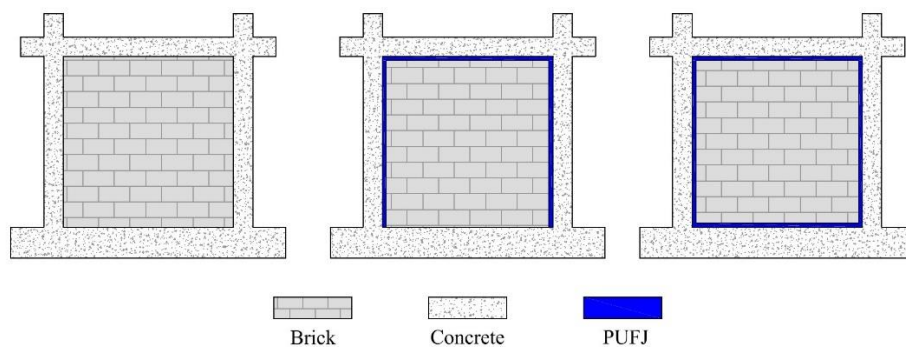


Figure 4.1. Schematic views of the samples; Frame A (left), Frame B (middle) and Frame C (right).

4.1.1 Material properties

All frames were constructed in the laboratory conditions by the accredited teams. Building materials, frame sizes as well as construction methods were carefully chosen while aiming to represent a real-like condition.

Hollow clay bricks are very common types of infill wall materials that being used all around the world, including the earthquake regions such as Mediterranean countries like Greece, Italy and Turkey. Therefore, commercially available KEBE OrthoBlock brand of brick blocks were imported from Greece for emerging the infill walls for the test specimens. The blocks had the dimensions of 250 mm and 240 mm, perpendicular (width) and parallel (height) to the hollows, respectively. Besides, the producer designed the thickness for this specific type of blocks as 100 mm. According to the information from the manufacturer's catalog, the blocks should have the compressive strength (in the stronger bearing direction, parallel to the holes) greater than or equal to 10 MPa. Net dry density of the blocks and the wall weight per square meter were measured as approximately 2000 kg/m^3 and 100 kg/m^2 , respectively. A view of the single block is given in Figure 4.2.

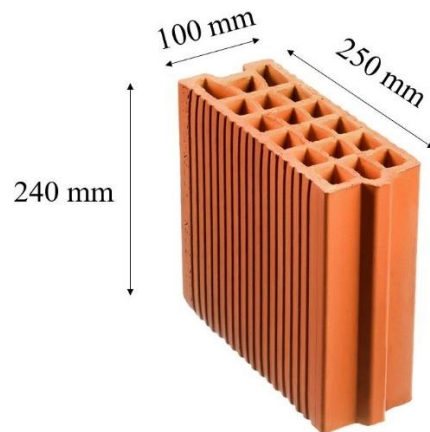


Figure 4.2. KEBE OrthoBlock K100 Brick [adapted from the manufacturer's catalog].

In addition to the information received from the brick producer, extra mechanical tests were performed on the bricks. In order to comprehend the capacity of bricks in a wall system, the bricks were formed in different shapes by means of configuring them in triplet forms, and later on these were exposed to the forces acting from different directions. For this purpose, several compressive and shear tests were conducted. Compressive tests were divided into two categories while aiming to understand the response of triplets to the loading acting parallel and also perpendicular to the hollows. Parallel to hollow compressive tests were named as “vertical”, whereas the latter ones were called “horizontal” specimens. In total, nine

compressive tests were performed in which, five out of nine were dedicated to the vertical tests and the remaining four specimens were parts of the horizontal ones. No specific standards were followed for the compressive tests. On the other hand, six shear tests were performed as a part of following the test standard of SIST EN 1052-3 (SIST, 2004). It should be noted that the test setup only included the pure shear effects, though the standard recommends to actualize a certain degree of precompression in the orthogonal direction. Therefore, the shear strengths are determined independently from the compressive effects. Test setup pictures of the specimens are given in Figure 4.3. In the triplet assemblages, bricks were bonded by thin layer mortar and specifically for providing a smooth laying surface only for the horizontal compressive specimens, cement mortar was used, see Figure 4.4.



Figure 4.3. Test setups for the triplet specimens; vertical compressive (left), horizontal compressive (middle) and shear (right).



Figure 4.4. Horizontal compressive specimens.

According to the results, rather larger variation was observed among the specimens for the compressive tests, in comparison to the shear ones. For the vertical compressive tests; minimum and maximum load carrying capacities were measured as 75.2 kN and 111.0 kN, respectively, which indicates 32% of difference at the most. On the average level; 96.3 kN of force capacity was calculated for the vertical specimens, with the coefficient of variation (CoV) 14.2%. Horizontal tests exhibited larger maximum load capacities and determined as 103.7 kN on the average. Tests on the different specimens indicate that, highest load value was 128.1 kN and the lowest one was 77.4 kN. Variation between those was equal to 40%, and CoV was calculated as 21.7% among all horizontal specimens. Failure mechanisms were spotted across the inner webs of units for the vertical tests, and outer shells were disengaged from the inner webs for the horizontal specimens. Representative failures are given in Figure 4.5



Figure 4.5. Failures on the compressive specimens; vertical (left) and horizontal (right).

Moreover, shear tests were performed for understanding the bonding capacity between the bricks. As a natural phenomenon, mortar failure was observed for these specimens. For the different tests, minimum and maximum shear forces were measured as 18.2 kN and 25.6 kN, respectively. Average value was obtained as 22.5 kN for all of the six shear tests. Besides, the difference between the most divergent results were calculated as 29%, whereas the CoV was

13.7% concerning the entire vertical samples. Typical failure of a shear test specimen is shown in Figure 4.6. Details of the triplet tests are also given in Table 4.1. Since it is difficult to determine the actual stress per area on the perforated surfaces, the strength values are calculated considering the gross area of surfaces, namely (250 mm × 100 mm) for vertical compressive, (2 × 250 mm × 100 mm) for shear and (3 × 240 mm × 100 mm) for horizontal compressive specimens. However, the net area values of the surfaces are also utilized in the next chapters where necessary, mainly for calibrating the numerical modeling properties.



Figure 4.6. Failure on the shear specimen.

Table 4.1. Tests results of the triplet masonry assemblages.

Test Type	Specimen	Fmax [kN - (MPa)]	Average [kN - (MPa)]	CoV [%]
Vertical Compressive	V_1	85.4 - (3.42)	96.3 - (3.85)	14.2
	V_2	75.2 - (3.01)		
	V_3	102.5 - (4.10)		
	V_4	107.1 - (4.28)		
	V_5	111 - (4.44)		
Horizontal Compressive	H_1	85.5 - (3.42)	103.7 - (1.44)	21.7
	H_2	77.4 - (3.10)		
	H_3	128.1 - (5.12)		
	H_4	123.7 - (4.95)		
Shear	S_1	18.2 - (0.73)	22.5 - (0.45)	13.7
	S_2	25.1 - (1.00)		
	S_3	18.7 - (0.75)		
	S_4	25.6 - (1.02)		
	S_5	22.5 - (0.90)		
	S_6	25.3 - (1.01)		

Multiple compressive and flexural tests were performed on the cube and beam shaped concrete and mortar materials in order to determine the strength of those. M10 class type of thin layer mortar was preferred for providing bonding between the brick units. Average compressive and flexural strengths were established as 10.2 MPa and 4.5 MPa, respectively. The specimens having the dimensions of 160×40×40 (units in mm) were tested according to EN 1015-11 standard (CEN, 2019a) For the cement mortar that was implemented as the bed layer between the RC frame and the bottom part of masonry, these values were determined as 30.4 kN for the compressive and 7.2 kN for the flexural strengths. Furthermore, cubic shaped concrete samples with the dimensions of 150×150×150 (units in mm) tested according to EN 12390-3 (CEN, 2019b), had the average compressive strength of 46.9 MPa. This result could be perceived as a similar value of the common concrete type, C35/45 (CEN, 2004a). Details are given in Table 4.2. Test samples are also shown in Figure 4.7. Although not tested separately as a part of this study, commercially available B500B type of steel bars with the characteristic yield strength of 500 MPa were used as the reinforcement steel. Polymer joints were produced as a combination of two types; polyurethane PM (Sika) for the flexible bodies and polyurethane PS (Sika) as the adhesive. The first one has the elastic modulus, strength and ultimate elongation ratio as 4 MPa, 1.4 MPa and 110%, respectively, whereas the latter material has these properties as 16 MPa, 2.5 MPa and 40%, in the same order (Rousakis et al., 2021).

Table 4.2. Tests results of the concrete and mortar specimens.

Material	Compressive strength [MPa]	Flexural strength [MPa]
Cement mortar	30.4	7.2
Thin layer mortar	10.2	4.5
Concrete	46.9	-

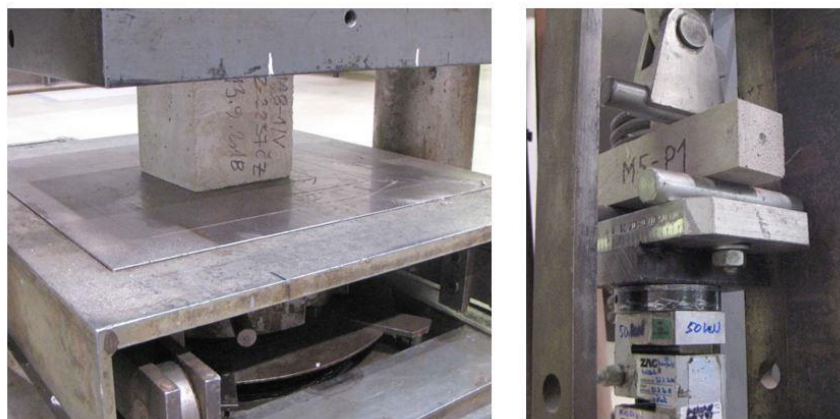


Figure 4.7. Cube and beam shaped specimens prepared for the compressive (left) and flexural (right) tests.

4.1.2 Wallet tests

Three identical wallet specimens were constructed and tested through their diagonal in-plane directions. These tests were conducted in order to foresee the possible damage mechanisms before the actual large-scale tests, and also for providing some required information for the numerical calculations that are explained in the next chapters. That being said, the brick units were configured to provide approximately square-shaped wallet dimensions and these were put in the loading shoes at their two opposite corners, as shown in Figure 4.8. Total four extensometers were utilized in order to measure the displacements. These gauges were placed on both sides, namely L1 and L2 on the same surface for measuring the tensile and compressive changes respectively, whereas L3 and L4 were on the other side for recording these values in the same order of the former orthogonal extensometers.

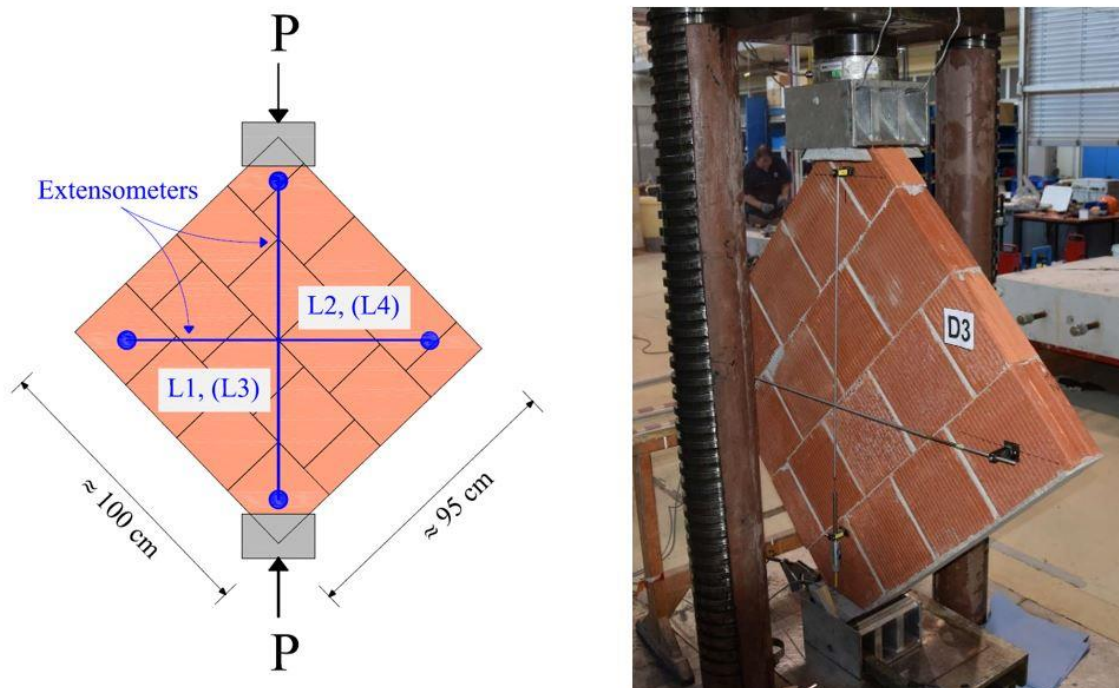


Figure 4.8. Details of the loading instrumentation (left) and test setup of the specimen WD3 (right).

The tests were performed according to ASTM E519-07 provisions (ASTM, 2010) which standardizes the diagonal shear tests on the masonry assemblages. Steadily increasing vertical load was applied diagonally on each wallet and the corresponding resistances were measured. Typical damage pattern for all of the specimens were similar. Firstly, compressive force increment until the initial failure of the brick at the bottom shoe was observed, in a crushing form. After that, the force continued raising until reaching the peak values, which was

followed by the load descending trend as a result of the compression failure of both top and bottom corners placed in the shoes. There was neither vertical cracking on the masonry nor the shear splitting at the joints, which typically characterizes the failure mechanism of these specimens as corner crushing, Figure 4.9.

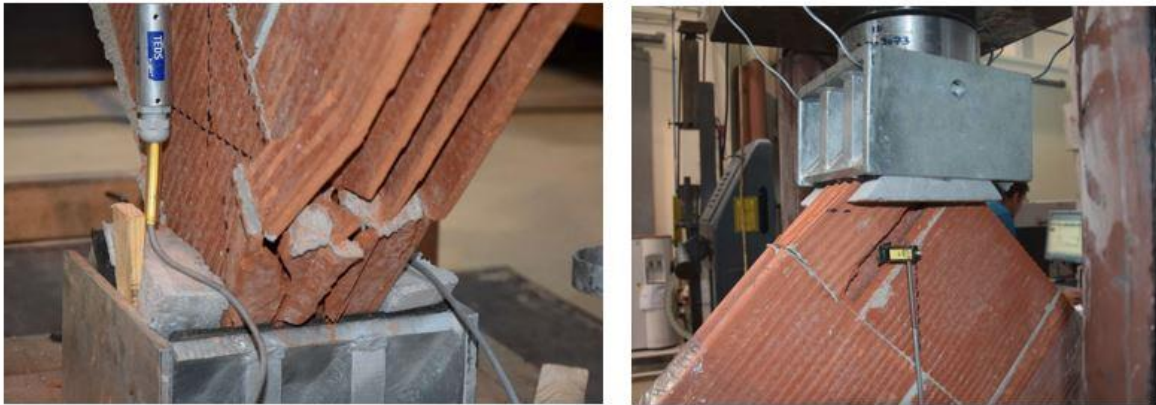


Figure 4.9. Typical damage pattern of the wallets; bottom (left) and top (right) corners.

The maximum load values, $F_{d,max}$, were found between 43.8 kN and 58.1 kN, with the average value of 50.3 kN for all three specimens. Accordingly, the CoV was 11.7%. Unlike the damage pattern and force resistance peak values, the results varied considerably among the specimens, in terms of the displacement outcomes, which also altered the diagonal wallet stiffnesses at the peak loads, K_{dw} . Average values of the diagonal displacement (d_d) and stiffness (K_{dw}) were 0.49 mm and 125.8 kN/mm, with CoV of 40.1% and 51.2%, respectively. Such considerable difference could be attributed to the sudden and non-uniform damages that occurred at the extensometer connection legs, which caused deviations even in the results of gauges placed on the different sides of the same wallets. In addition, the shear strength (S_{sw}) and strain values ($\gamma_{sw,peak}$) are calculated (see Appendix B for the details). For this, shortening (from L1 and L3 gauges) and elongation (from L2 and L4 gauges) values corresponding the peak load, $F_{d,max}$, are measured. Accordingly, the mean values of those, for the wallet specimens WD1, WD2 and WD3, are 0.452 mm, 0.428 mm, 0.578 mm (shortening) and 0.044 mm, 0.044 mm, 0.062 mm (elongation), respectively. The results are given in Tables 4.3-4.4. Compressive force-shortening results of the specimens are also presented in Figures 4.10-4.12, where the red circles indicate the initial crushing as mentioned above.

Table 4.3. Tests results of the wallet specimens – all values.

Specimen	WD1		WD2		WD3	
	L1	L3	L1	L3	L1	L3
$F_{d,max}$ [kN]	49.1	49.1	43.8	43.8	58.1	58.1
d_d [mm]	0.19	0.72	0.47	0.39	0.4	0.75
K_{dw} [kN/mm]	258.4	68.2	93.2	112.3	145.3	77.5
S_{sw} - mean [MPa]	0.712		0.635		0.843	
$\gamma_{swrpeak}$ - mean [-]	4.96×10^{-4}		4.72×10^{-4}		6.40×10^{-4}	

Table 4.4. Tests results of the wallet specimens – statistical values.

	Max.	Min.	Average	CoV [%]
$F_{d,max}$ [kN]	58.1	43.8	50.3	11.7
d_d [mm]	0.75	0.19	0.49	40.1
K_{dw} [kN/mm]	258.4	68.2	125.8	51.2
S_{sw} - mean [MPa]	0.843	0.635	0.730	11.7
$\gamma_{swrpeak}$ - mean [-]	6.40×10^{-4}	4.72×10^{-4}	5.36×10^{-4}	13.8

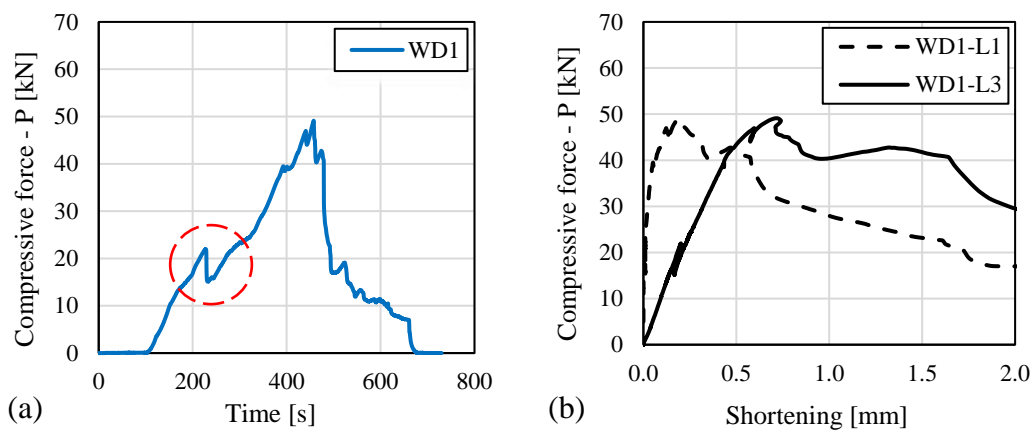


Figure 4.10. Wallet D1 test results; (a) force-time and (b) force-shortening.

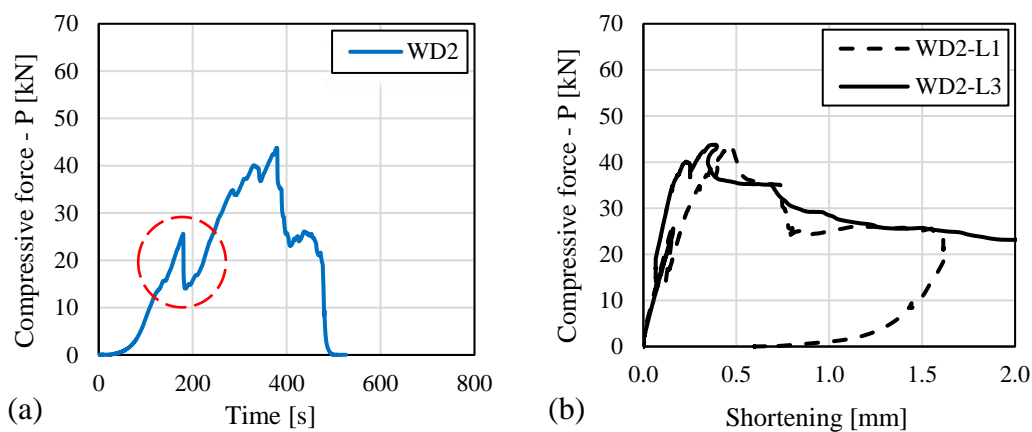


Figure 4.11. Wallet D2 test results; (a) force-time and (b) force-shortening.

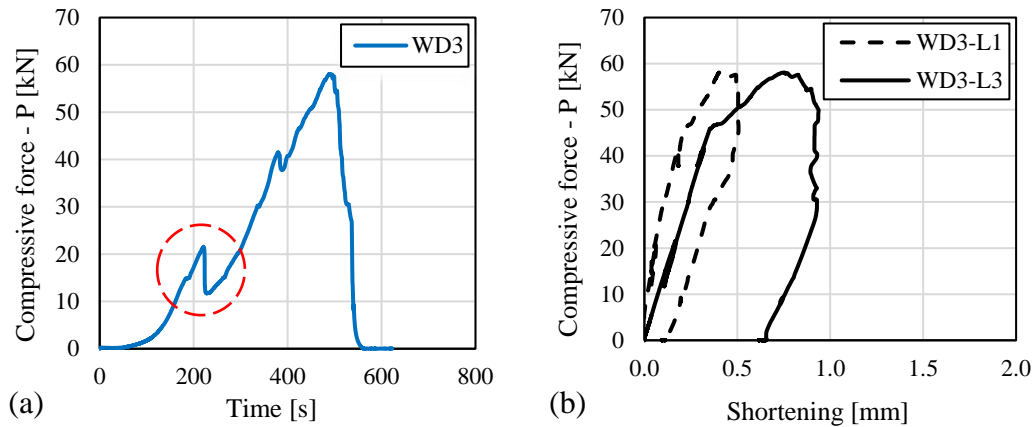


Figure 4.12. Wallet D3 test results; (a) force-time and (b) force-shortening.

4.1.3 Large-scale test setup

The frames were created in a way to reflect the seismic effects on real size structures. These single-bay and single-story frames were identical in terms of the RC details. Each one consists of a beam, two columns and a foundation beam, which was designed to be stronger than the rest of frame in terms of the reinforcement as well as concrete section details. Both beam and column elements had the square shaped sections with the dimension of 250 mm for each edge, albeit the detailing of reinforcement was different for those. As the longitudinal reinforcement, total 8 steel bars were placed in the concrete matrix of each beam and column, without lap splicing. Diameters of the bars were 14 mm and 16 mm for the beams and columns, respectively. Stirrup sizes and spacing details were chosen identically for both these RC frame members, as $\phi 10/100$ mm peripheral closed loops. Additionally, rhomboid shaped stirrups were also used for the concrete columns in the same zones of the peripheral ones. On the other hand, the foundation beam was designed to provide a robust base, hence 400 mm of height and 300 mm of width cross-sectional dimensions were determined to be sufficient in this purpose. Various types of longitudinal bars were embedded across the concrete cross section; namely $4\phi 25$ in the corners, $2\phi 16$ in the middle height and $4\phi 20$ on both top and bottom edges placed close to the corners. Stirrups were detailed with the peripheral shaped $\phi 10/100$ mm bars. Reinforcement details are given in Table 4.5 and visualized for a typical frame in Figure 4.13.

Table 4.5. Frame geometrical dimensions and reinforcement details.

Element	Width [mm]	Height [mm]	Length [mm]	Steel bar dimensions [mm]	
				Longitudinal	Stirrup
Beam	250	250	2200 *	8 ϕ 14	ϕ 10/100
Column	250	250	2200 *	8 ϕ 16	ϕ 10/100
Foundation	300	400	3550	4 ϕ 25 + 4 ϕ 20 + 2 ϕ 16	ϕ 10/100

* Clear length.

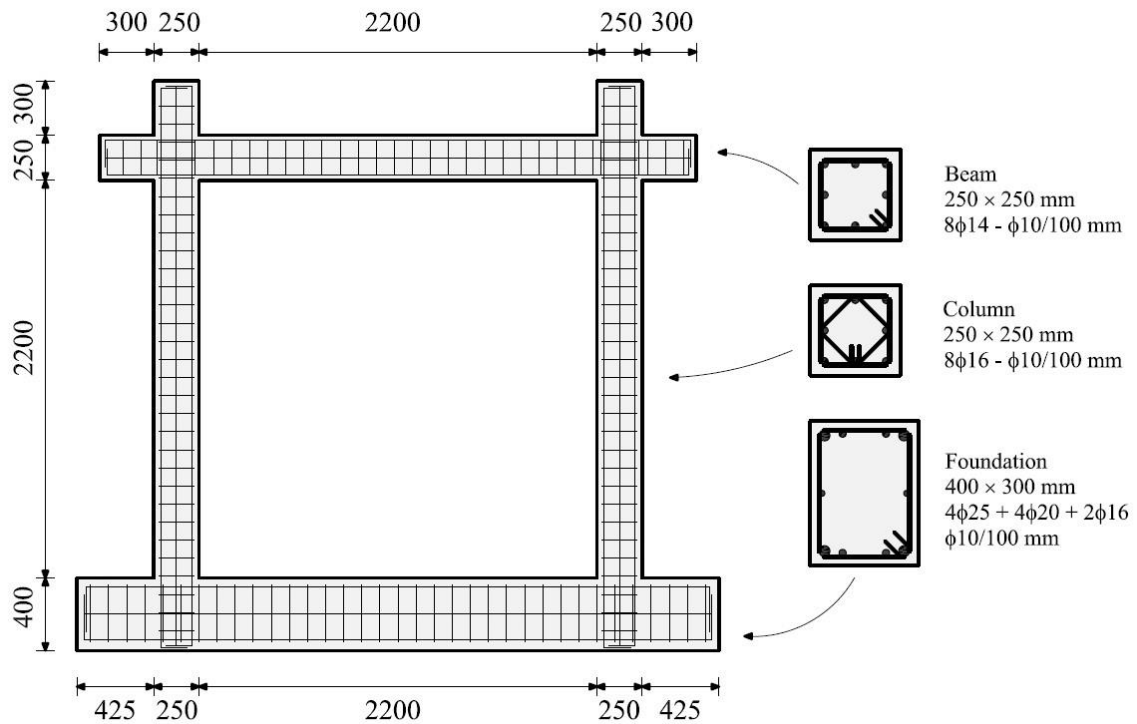


Figure 4.13. Visualization of the frame reinforcement details [dimensions in mm].

Infill walls were built by the hollow clay bricks and configured in the frame void in a way to provide height and width length of 2200 mm, and the masonry thickness of 100 mm. A view from the preparation process is given in Figure 4.14.



Figure 4.14. Brick blocks arrangement in the frame.

Following the creation of frames, these specimens were moved to the testing zone where hydraulic actuators were placed at the ends of beam (maximum horizontal loading capacity 63 tons \approx 620 kN) and column members (maximum vertical loading capacity 60 tons \approx 590 kN), see Figure 4.15.

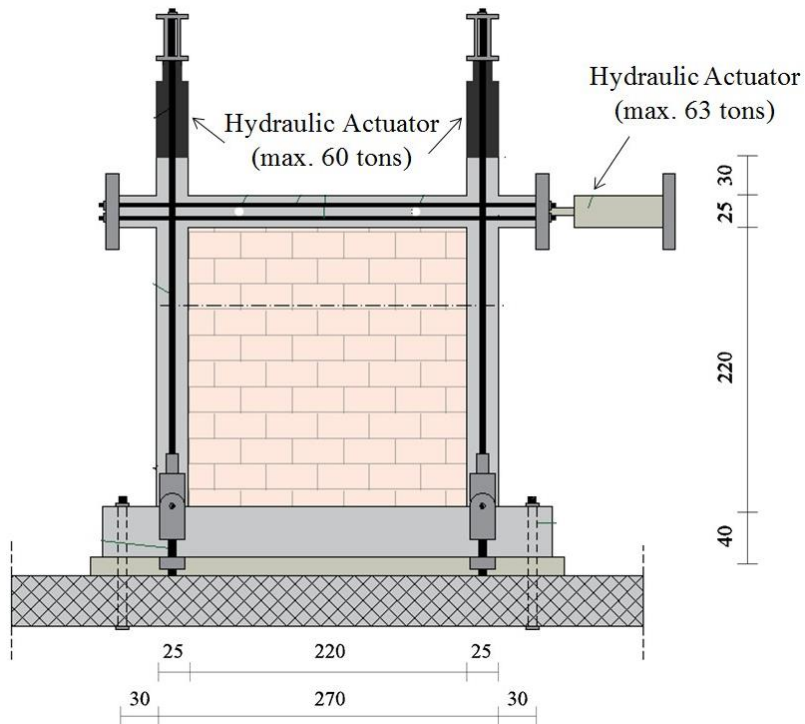


Figure 4.15. Test setup of the frames [dimensions in cm].

4.1.4 Preparation of the large-scale specimens

Upon creation of the frames, masonry walls were built. Thin layer mortar (M10) was used as a bonding material between the individual brick blocks as well as brick-to-frame interfaces except the bottom part only, where cement mortar was utilized. Frame A, the reference frame which represents the conventional building method, had the aforementioned stiff connection on all around the wall perimeter, Figure 4.16.

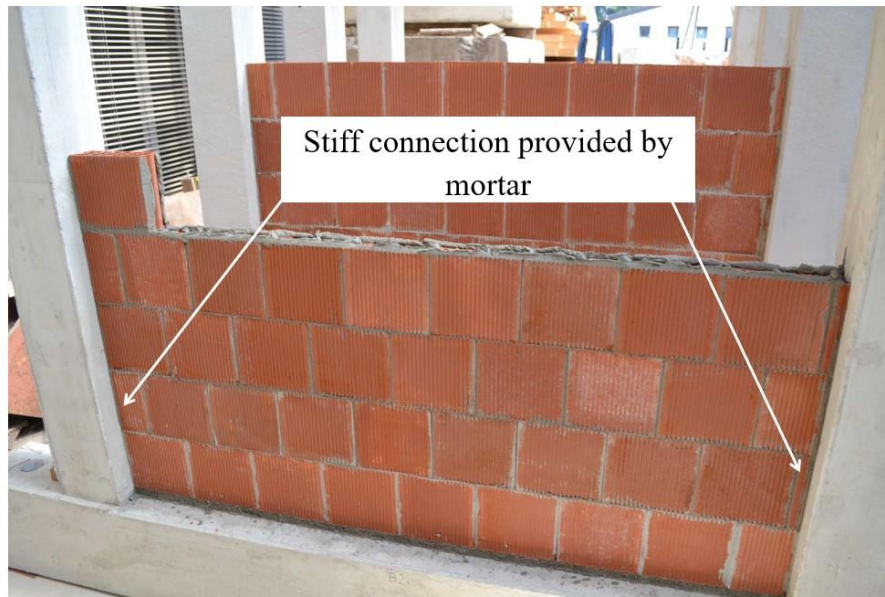


Figure 4.16. Construction process of the Frame A.

For the other two types of frames, Frame B and Frame C, innovative PUFJ method was utilized. Construction process of the Frame B was the same of Frame A, until the last step of PUFJ implementation. Since the idea of Frame B comes from the usage of PUFJ in already existing buildings, firstly, available zones were needed to be created for replacing the stiff connection with the flexible joints. For this purpose, three sides of the wall were cut by a saw providing 20 mm gap, except the bottom one. In this way, the wall stability could still be sustained temporarily thanks to having connection at the bottom of wall. Besides, a working space could be found without the need of removal of the entire wall. This is a practically useful information, as in the real-life scenario buildings cannot be evacuated easily due to several reasons. Later on, the gaps were filled by PUFJ. At first, a simple formwork was built around the gaps in order to provide a leakproof temporary system. After that, the liquid form Polyurethane PM was injected to the gaps and following this the formworks were removed once the polymer was sufficiently set and solid. A view from the end of process is given in Figure 4.17.



Figure 4.17. PUFJ application on the Frame B.

In a different way from the others, the infill wall of Frame C did not have a direct contact with the surrounding frame at any point. The frame represents the PUFJ utilization on new buildings, thus, it enables to prepare flexible joints before the construction of masonries. Accordingly, Polyurethane PM laminates of 20 mm thickness were created by means of spilling the liquid formed polymer into the formworks and waiting for those to get solid for being sufficiently ready to be placed easily around the frame inner zone. Moreover, for having a secure and strong interface connection between the PUFJ and frame, thin-layer liquid polymer was also applied on the relevant frame parts, before placing the prefabricated laminate elements. Therefore, bonding could be provided fully by the polymer itself, without any additional anchorage mechanism. In Figure 4.18, these steps are shown.



Figure 4.18. Prefabricated PUFJ laminates (left) and application on the Frame C (right).

4.1.5 Method of measurement

In-plane test results were acquired primarily by the horizontal measuring devices (displacement transducers – DT), which were placed on the back side of specimens as shown in Figure 4.19. Relative distance between down (u_0) and up (u_H) transducers was 2260 mm.

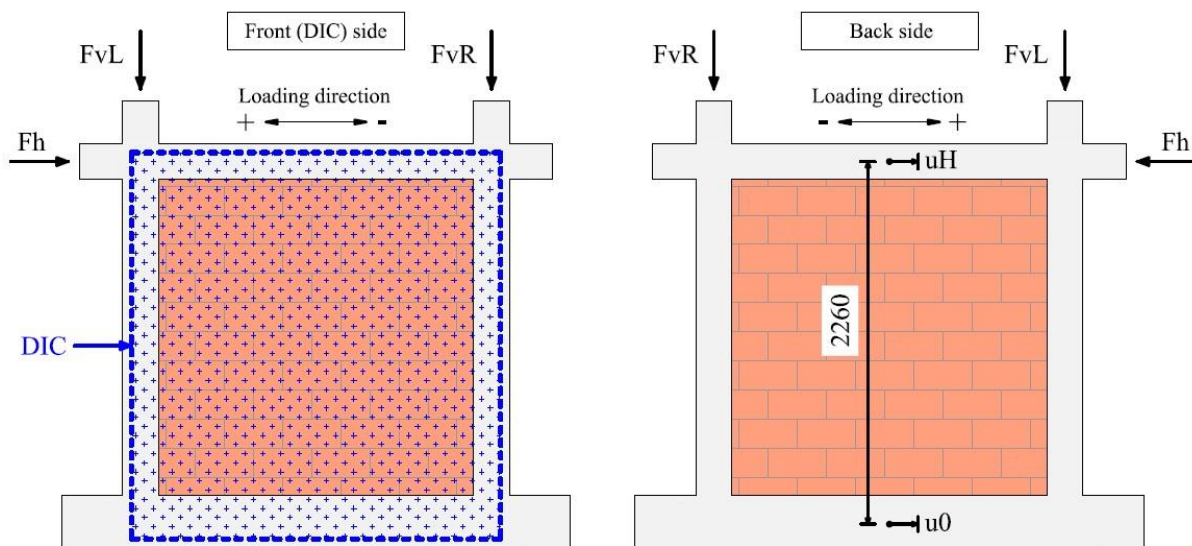


Figure 4.19. Schematic view of the measurement techniques [dimensions in mm].

Additionally to the DT method, digital image correlation (DIC) was also utilized. This method enables to visualize the behavior of experiments and it is especially useful while identifying fracture zones as well as displacements and strains. In order to track the relative drifts on the specimens, multiple reference points were identified both on the frames and infill walls. Positions of the points were carefully chosen for capturing the motions of both frame and masonry. Thus, the whole structural system could be covered in terms of the displacement measurement. Typical distribution of the reference points on the coordinate space is shown for Frame B in Figure 4.20. A view just before the initiation of test is also given in Figure 4.21. It is worth to mention that DIC method was not used as the main source of information, as already stated above. Therefore, merely the displacement results of this technique are compared with the DT results further in this study.

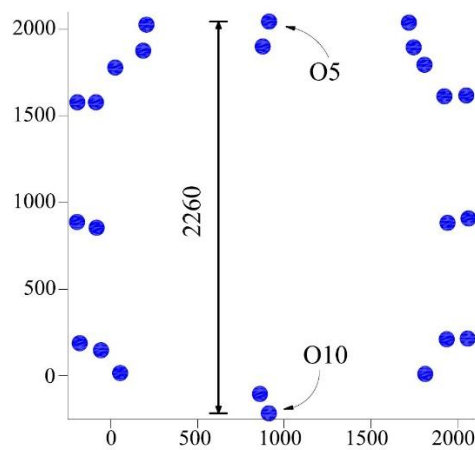


Figure 4.20. Distribution of DIC reference points on Frame B [dimensions in mm].



Figure 4.21. Utilization of the DIC method on Frame B.

4.1.6 Loading protocol

All of the frames were subjected to the same loads. On the top of each column, 375 kN vertical load (≈ 6 MPa compressive stress) was constantly effective since the beginning of experiments. Hence, a representation of a lower-floor frame in a multi-story building was actualized. For understanding the in-plane response of the frames, a hydraulic actuator was placed on the upper beam for each test specimen. Horizontal forces were then exposed to the frames in the form of quasi-static reversal cyclic loads having the average loading rate that ranges between 1.41 kN/s and 2.04 kN/s, which depends on the frame type. The cycle pattern was based on the gradually increasing predetermined specific drift ratios. In order to reach to the target of each drift ratio, three cycles were followed as the standard of steps. However, the experiments were terminated at different steps for each frame type, since the load carrying capacities of those were distinctive due to the difference of joint methods. Details of the horizontal loading scheme is given in Figure 4.22. Drift ratio (%) was calculated using the data from DT points of u_0 and u_H , see Figure 4.19.

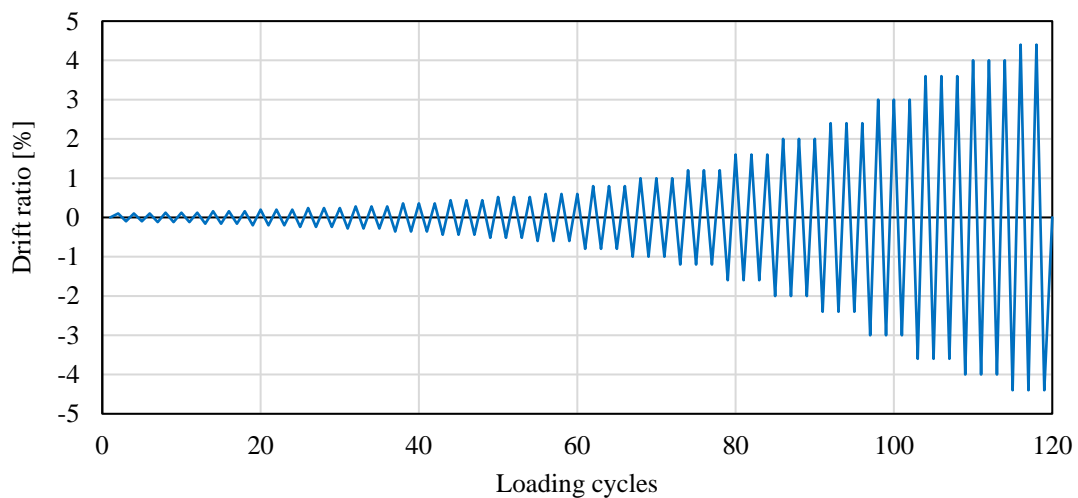


Figure 4.22. Loading protocol of the horizontal excitation.

4.1.7 Results of the tests

While performing the loading cycles mentioned in the previous section, each frame yielded different results in terms of load responses corresponding to the specific drift ratios. Frame A, reference frame having conventional stiff mortar between the RC members and masonry, could carry its stability up to 1.6% horizontal drift ratio. At this stage, corner crushes as well as severe wall detachment from the surrounding RC frame was observed, Figure 4.23. The loading was terminated at this step, due to the fact that loss of frame-infill interface

connection would lead to collapse of entire wall. This is a common type of failure for such systems, where unreinforced masonry walls (URM) are utilized as the construction practice. Ultimate horizontal load carrying capacity was measured as 165 kN at the final step. Figure 4.24 shows the load-displacement curves for Frame A.



Figure 4.23. View of Frame A at the end of horizontal loading test – 1.6% drift ratio.

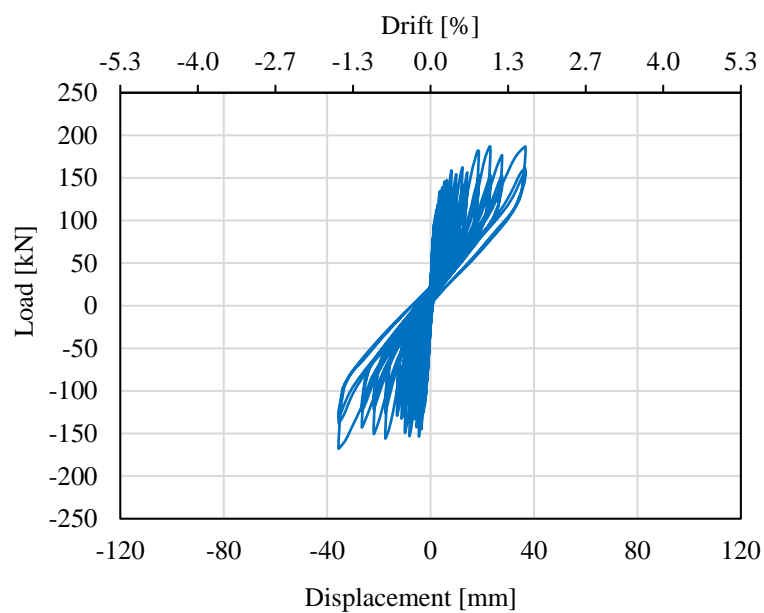


Figure 4.24. Load-displacement hysteresis response of the Frame A.

Frame B, which was one of the two specimens with flexible joints, was excited with the same loading cycles as of Frame A. PUFJ was implemented on the three sides of wall except the bottom part. Influence of the innovative joint system was visible, such that the frame could withstand higher lateral displacements, up to 3.5% drift ratio, Figure 4.26. Since the loading scheme was based on cyclic loads, response of the frame was measured by the horizontal hydraulic actuator for both pull (positive displacement) and push directions (negative displacement). Maximum base shear force was 192.8 kN for pull, and 166.6 kN for push direction. On the other hand, shear forces corresponding to the maximum drift ratio of 3.5% were 179 kN and 134.5 kN for pull and push directions, respectively. This outcome indicates that ultimate load capacity was dropped by 20% at the most, resulted from the push direction, whereas for the pull direction decrement was relatively less and equals to 8%. Although damages were observed in the vicinity of masonry corners due to the crushes, overall wall stability was still in good condition thanks to the presence of PUFJ, Figure 4.25. Hyper-elastic features of the flexible joints led to sustain bonding between the infill and frame, thereby the out-of-plane failure was prevented.



Figure 4.25. View of Frame B at the end of horizontal loading test – 3.5% drift ratio.

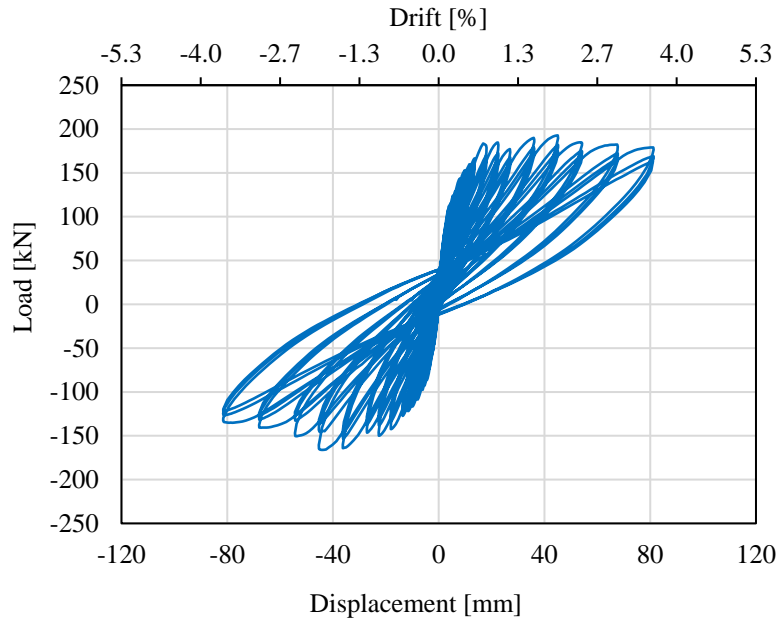


Figure 4.26. Load-displacement hysteresis response of the Frame B.

Frame C, which was the other specimen with the flexible joints, where laminated PUFJ was implemented through entire wall perimeter, exhibited a noteworthy greater performance. The frame was able to reach 4.4% drift ratio, Figure 4.28. At that point, the base shear force was 164.6 kN for the push direction that equals to the 92% of the maximum measured force of 177.6 kN. For the pull direction, a similar load decreasing trend was observed from the maximum of 222.5 kN to 207.5 kN, indicating around 7% drop. Ultimate drift ratio was equal to 4.2%. In either direction, the load carrying capacity was higher than the other frames, though relatively closer to the Frame B. Since the maximum load values were decreased within the marginal levels, it can be said that no structural failure occurred, even though visible damages were observed in the similar pattern of Frame B, namely corner crushes, see Figure 4.27.

As a side note to the above, exclusively for the PUFJ implemented frames – Frame B and Frame C – a series of resonance frequency tests following the in-plane ones were performed in order to investigate the out-of-plane performances of those. Overall, no significant strength or stability loss was observed for the any frame upon the visual inspections, despite the occurrence of slightly larger dilatations on some fissures and cracks. The test-setup is shown in Figure 4.29.



Figure 4.27. View of Frame C at the end of horizontal loading test – 4.4% drift ratio.

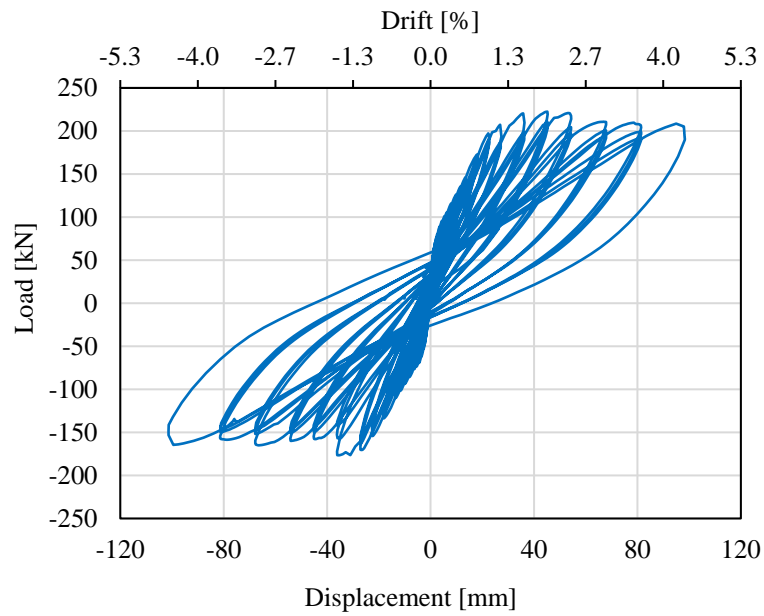


Figure 4.28. Load-displacement hysteresis response of the Frame C.

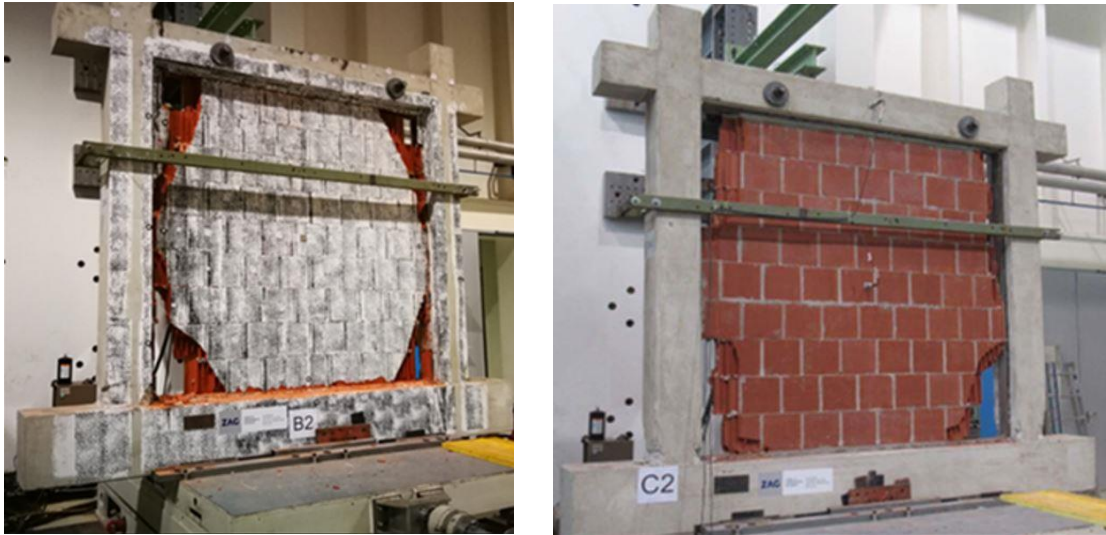


Figure 4.29. OOP resonance frequency tests; Frame B (left) and Frame C (right).

Moreover, bare-frame without the infill wall was also tested for highlighting the masonry contribution. Its load-displacement results are given in Figure 4.30. Finally, in Figure 4.31, envelope (backbone) curves belong to the hysteresis loops of the frames are shown in order to illustrate a comparison between those. Enhanced load carrying capacities as well as greater drift ratios prove that PUFJ solution in Frame B and Frame C provides more favorable behavior in comparison to the traditional mortar implemented counterpart, Frame A. Besides, the strength contribution of the infill walls is also seen clearly regardless of the frame type, since the bare-frame exhibited much lower lateral load capacity which was found ranging between 15% – 25% less (depends on loading direction) than Frame A.

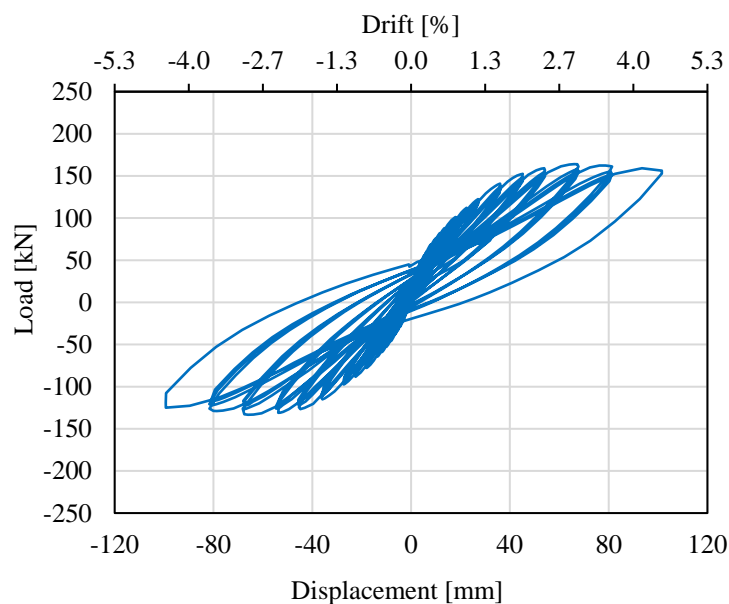


Figure 4.30. Load-displacement hysteresis response of the Bare-Frame.

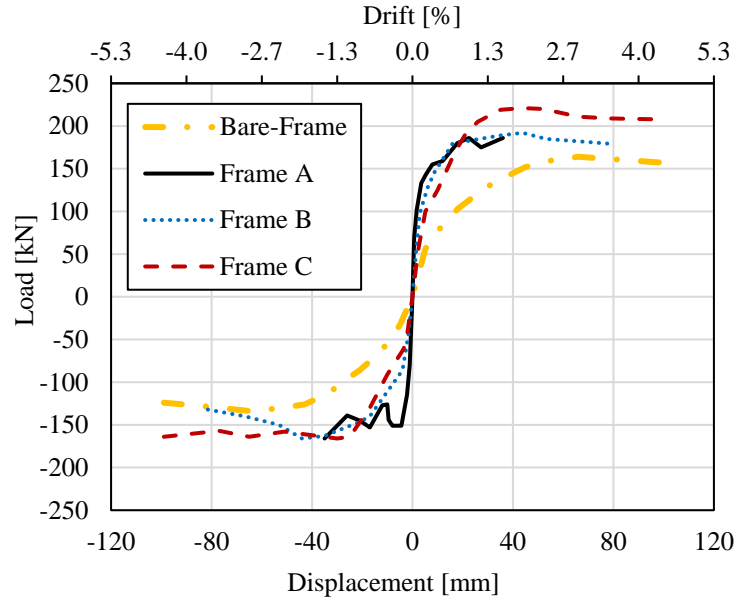


Figure 4.31. Envelope curves of the hysteresis loops.

Furthermore, one may claim that an unusual behavior exists while looking at Figure 4.31, since pull (positive) and push (negative) directions have visible load carrying capacity differences regardless of the frame type. Any experiment includes many imperfections obviously, however, this specific situation is also attributed to the relatively high vertical loading on the columns, which could not be actualized smoothly all time, due to the test setup related limitations. As a result, F_vL was measured higher than F_vR during the large portion of experiments that caused relatively higher compaction on the frame in the pull direction (Figure 4.19), which led to stiffer behavior.

4.1.8 Comparison of the measuring methods

Measuring of the horizontal displacements was done by two different methods, DT and DIC, as already mentioned in the previous sections. The displacement transducers (Novotechnik TEX 200 and TRS 100) have a combined accuracy of approximately ± 0.25 mm, while the DIC system (two cameras with 5 Mpx resolution) with a resolution of approximately 0.02 px, considering the field of view of 3×3 m², has accuracy of 0.02 mm (Akyildiz et al., 2020). In order to compare between these two techniques, horizontal displacement data was examined. Accordingly, relative displacement values of $u_{DT} = u_H - u_0$ for DT (Figure 4.19), and $u_{DIC} = u_{010} - u_{05}$ for DIC system (Figure 4.20) were considered. As it can be seen in Figure 4.32, the results were very close for the case of Frame B, with total difference

less than 1 mm in the first part of test sequence, namely up to 3 hours. On the other hand, more visible difference was observed for these two methods during the remaining part of test sequence, where 3 mm difference was spotted. Possible reason of such deviation might be due to the limited accuracy of the a-posteriori synchronization of both measurement systems (Akyildiz et al., 2020).

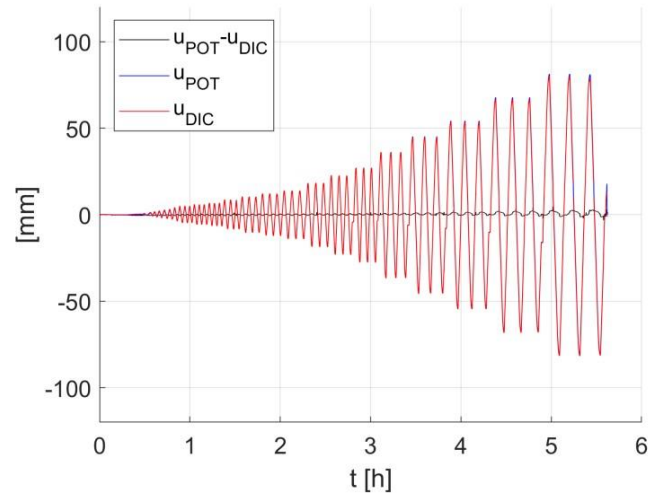


Figure 4.32. Horizontal displacement values of DT and DIC methods for Frame B.

In a similar manner of comparing the results, yet in a different way as taking into consideration the drift ratio accuracy, following outcomes were found using the Figure 4.33. Maximum drift error ranges between 0.044% (1 mm/2260 mm) and 0.133% (3 mm/2260 mm). Visual presentation of the drift ratio calculations indicates that maximum relative difference was marginal and less than 0.18% (peak to peak) for DT and DIC methods, see Figure 4.33.

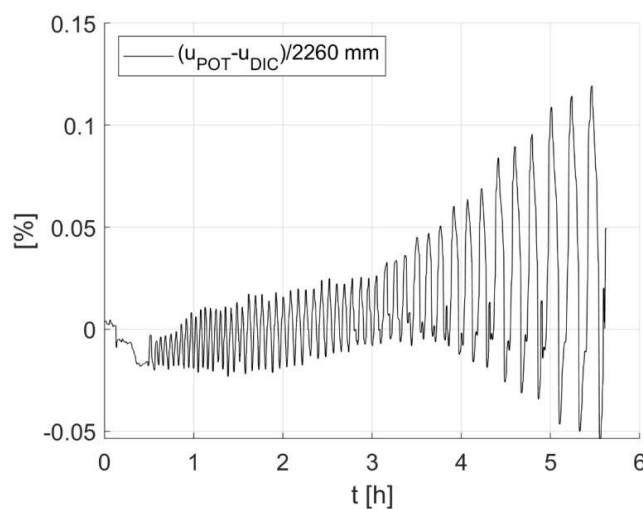


Figure 4.33. Drift ratio differences of DT and DIC methods for Frame B.

4.1.9 Section summary of the in-plane tests

Quasi-static in-plane tests were conducted on large size specimens, aiming to identify the efficiency of an innovative joint technology called as PUFJ. For this purpose, three RC frames infilled with hollow clay bricks were constructed. Frame A was considered as the reference frame representing the conventional building methods and thereby had stiff joints across the wall peripheral. The remaining frames on the other hand, Frame B and Frame C, were designed to reflect the implementation of PUFJ on existing and to-be-built buildings, respectively. According to the outcomes of horizontal displacement excitations, Frame A lost its infill wall stability at the drift ratio of 1.6% when the base shear force was around 165 kN, resulting from the severe wall detachment at the joints between the RC frame and masonry. Frame B and Frame C exhibited greater performances in terms of both drift and shear load capacities, thanks to the presence of PUFJ. Maximum drift ratio was measured for Frame B as 3.5% with the peak shear force value of 192.8 kN, whereas for Frame C the drift capacity was even larger and reached up to 4.4%. Besides, the strength reserve was sustained with a marginal drop of shear load capacity which was around 8% at the most. This is a crucial point in terms of earthquake engineering, since the ductility is a key element in the purpose of absorbing the seismic energy. Moreover, comparison between the different measuring methods state that DIC technology can also be used for such experiments, where deformation of the PUFJ implemented systems is the concern.

As an additional information; OOP resistances of the PUFJ implemented frames were remarkable, since no significant strength or stability loss was observed for those, despite being excited with the resonance loads. Other than that, FRPU implementation for enhancing the in-plane capacity of the Frame A was actualized (on the damaged frame), though it is not mentioned in this study due to being rather out of the scope of this section. Nevertheless, it is proved that such application can lead to higher drift level capacity – up to 3.6% – and it results in better energy dissipation features, namely 3.5 times higher than the original frame that was without any intervention (Triller et al., 2022).

4.2 Shake table tests of the infill walls in an RC building

As feasible as numerical solutions and simplified experiments are, comprehensive tests are still required while aiming to reveal the most possible real-like conditions. Therefore, PUFJ solution implemented three-dimensional RC building was decided to be tested against the historical seismic records. In this way, both in-plane and out-of-plane performances of the masonries could be investigated.

The project was run by the funds of the Seismology and Earthquake Engineering Research Infrastructure Alliance for Europe (SERA) and named as INfills and MASONry structures protected by deformable POLyurethanes in seismic areas (INMASPOL). The international project gathered many researchers from different institutions across Europe, in order to examine the possible usage areas of polymers for the seismic protection. Accordingly, such innovative methods were tested either simultaneously or progressively. Hence, in this section, another implementation method of the polymers needs to be mentioned, namely fiber reinforced polyurethanes (FRPU), although the main focus stays on the PUFJ as a part of this dissertation.

4.2.1 Test setup

The real-scale tested structure was a fully symmetrical single story RC building. It consists of four columns, four beams, four infill walls, a slab on the top of structure and a foundation at the bottom, all designed according to Eurocode-2 (CEN, 2004a) and Eurocode-8 (CEN, 2004b) regulations. The plan dimensions of the building were 3.8 m × 3.8 m and the height was 3.3 m (foundation and column extensions included). Schematic and real views of the building is given in Figure 4.34.

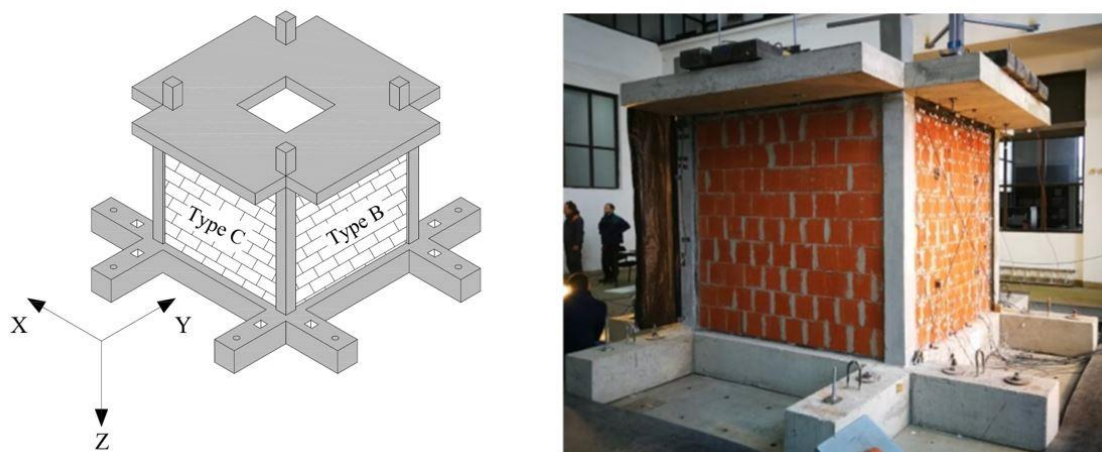


Figure 4.34. Views of the 3D building; schematic drawing (left) and real (right).

4.2.2 Materials

The materials were identical of the ones from quasi-static tests mentioned in Section 4.1, though slight quality class difference could exist for the concrete. Therefore, only concrete and polymer materials will be mentioned in here. That being said, the laboratory testing results for concrete cubes of 20 cm × 20 cm × 20 cm presented 28 days compression strength of 34.1 MPa for the foundation, 27.1 MPa for the columns and 34.2 MPa for the top slab, in which beams are also hidden. Regarding polymers, two different types were used; polyurethane PM (Sika) for constituting the PUFJ and polyurethane PS (Sika) as the adhesive for both PUFJ prefabricated laminates and FRPU layers. PM type of polyurethane had the elastic modulus, strength and ultimate elongation ratio as 4.0 MPa, 1.4 MPa and 110%, respectively. On the other hand, the elastic modulus, strength and ultimate elongation ratio of the relatively stiff Polyurethane PS were 16 MPa, 2.5 MPa and 40%, respectively. Glass fiber reinforced polymer (GFRP) meshes type of SikaWrap 350G Grid were also used as the embedding material in FRPU jackets. The real weight of the mesh was 360 g/m² and the effective area corresponding 1 m length in the orthogonal directions was calculated as 29.6 mm² having the ultimate tensile capacity of 77 kN/m (Rousakis et al., 2022). The elastic modulus, strength and ultimate elongation ratio for those were 80 GPa, 2.60 GPa and 4%, respectively. In Table 4.6, the material details are shared. The material information is either provided by the manufacturer or taken from Rousakis et al. (2021).

Table 4.6. Material properties of the shake-table specimen.

Material	Structural part	Property	Value
Concrete	Column		27.1 MPa
	Foundation	Compressive strength	34.1 MPa
	Slab		34.2 MPa
Glass fiber	FRPU mesh	Young's modulus	80 MPa
		Tensile strength	2600 MPa
		Ultimate elongation	4%
Polyurethane	PUFJ	Young's modulus	4.0 MPa
		Tensile strength	1.4 MPa
		Ultimate elongation	110%
	FRPU jacket	Young's modulus	16 MPa
		Tensile strength	2.5 MPa
		Ultimate elongation	40%

4.2.3 Details of the structure

Design of the building was done according to the capacity of shake table. Symmetrical top floor had the dimension of 2.7 m for each edge, although there were extensions in the edges for creating an available space while placing additional 18 steel ingots to provide 7200 kg mass. In the middle of slab, a square shaped hole (100 cm × 100 cm) was left in order to provide an access to the inside of building. The slab was reinforced with Q503 steel welded meshes at the top and bottom. Furthermore, there was additional reinforcement at the perimeter edges of the slab, and at the edge of the hole.

The slab was built on four columns placed at the corners. Height of the columns were 2.5 m (to the top of slab) with the cross-section dimensions of 20 cm × 20 cm. Longitudinal reinforcement was provided by 8 ϕ 10 bars and those were tied by 2 ϕ 8/50 mm stirrups (diamond and square shaped).

The beams were hidden in the slab, thus had the height of 20 cm. 8 ϕ 10 longitudinal bars were also used for the beams. Besides, ϕ 8/50 square stirrups were placed around the outer edges of bars. Concrete cover was provided by the clear distance of 42 mm.

The foundation was specially designed with holes for enabling the attachment of structure to the shake table and besides hooks were designated for lifting and manipulating the building. Side and cross section views of the structure and RC members are given in Figure 4.35 and Figure 4.36, respectively.

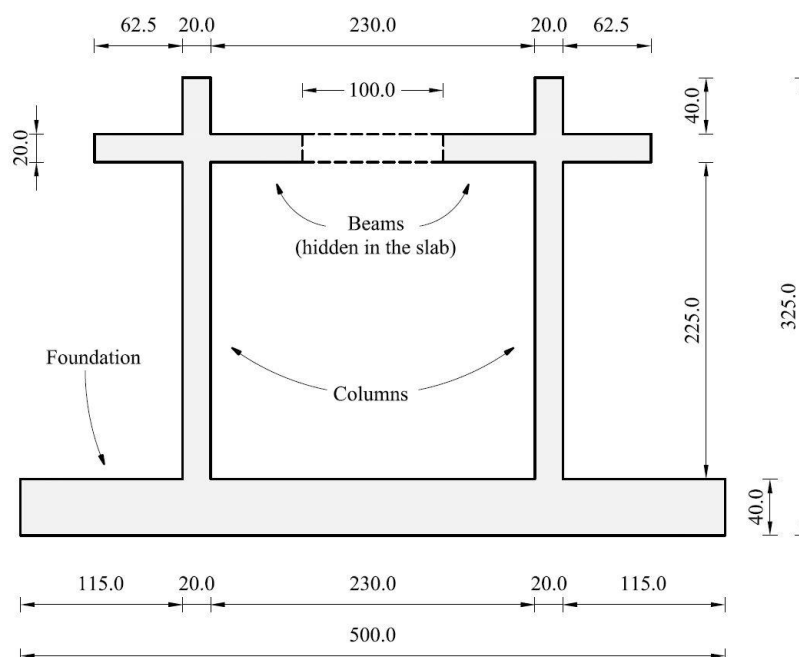


Figure 4.35. Side section view of the structure [units in cm].

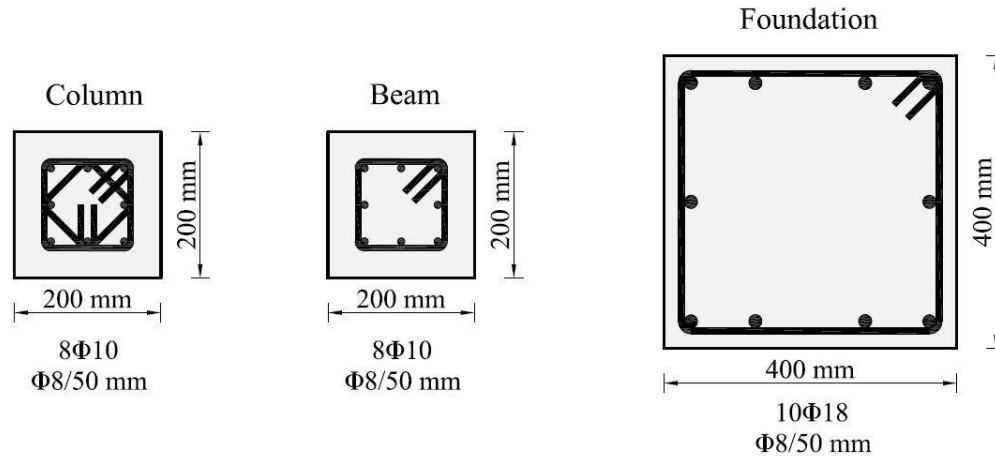


Figure 4.36. Cross section view of the RC members [units in mm].

Infill masonries were utilized with 100 mm thick KEBE OrthoBlock clay bricks and configured in a way that hollows were spanned vertically. Thin layer mortar of 3 mm thickness with nominal strength class M10 was provided both on the head and bed joints of the bricks. The walls were split into two categories; Type B and Type C, reflecting the similar labelling of in-plane shear tests mentioned in Section 4.1. Type B masonry indicates the in-situ injected PUFJ implementation around the three boundaries of walls (all edges except the bottom part), whereas Type C infill walls were constructed on the prefabricated PUFJ laminates which surrounded the entire perimeter of the masonries. Construction process of the walls were as same as the frames built in Section 4.1, namely 20 mm joint thickness was provided in the relevant parts.

The original idea of the experiment was testing the effectiveness of two PUFJ implementation methods simultaneously while preventing any external effects that might affect the results e.g., torsional forces arising from the unsymmetric configuration. In this purpose, the same types of walls were placed parallel to each other, thus they were enabled to receive loads in the same direction. Accordingly, two Type B infill walls were placed within the frame perpendicular to the other type of two walls, Type C. This approach aimed to test firstly Type B walls in their in-plane direction (Y direction), meanwhile testing out-of-plane performances of the Type C walls in the X direction, see Figure 4.34. In the next phases of the experiments, the structure was rotated by 90 degrees around its centerline, hence the loading directions were switched that enabled to testing of Type B walls for out-of-plane, while testing the Type C walls for in-plane directions. Emergency repair intervention of FRPU was also tested throughout the experiments, which will be discussed in the next sections. In Figure 4.37, those

different ways of polymer implementation techniques are presented. Some photos belong to the construction process are also given in Figures 4.38-4.39.

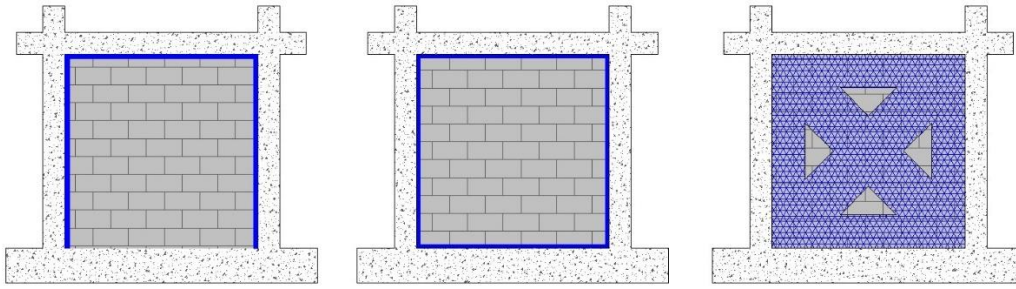


Figure 4.37. Implementation of PUFJ on Type B wall (left) and Type C wall (middle), FRPU intervention (right).



Figure 4.38. Construction process; slab and hidden beams reinforcement (left) and wall creation on the prefabricated PUFJ laminates for Type C walls (right).



Figure 4.39. Construction process; (a) in-situ injection of PUFJ for Type B walls, (b) FRPU intervention application on the Type C wall.

4.2.4 Testing facility and equipment

The shake table experiments were conducted in the laboratory of Institute of Earthquake Engineering and Engineering Seismology in Skopje, North Macedonia (IZIIS). The laboratory is in operation since 1980 and has a square shaped shake table (5.0m × 5.0m) made by prestressed concrete waffle slab weighing 33.0 tons. It is able to be loaded up to 40 tons. In total, five degrees of freedom are provided by 2 lateral and 4 vertical MTS hydraulic pistons, controlled by MTS Digital Controller 469D. In terms of the data acquisition, indigenous instruments of PXI modular system were used, which had three types of transducers, namely 23 accelerometers, 10 linear variable differential transformers (LVDT) and 2 linear potentiometers (LP) (Rousakis et al., 2020).

4.2.5 Instrumentation

In total 23 accelerometers were placed on the points remarked with the green circles in Figure 4.40. Those were utilized in order to measure the acceleration values of the infills for both in-plane and out-of-plane directions. Accelerations of the top slab and the foundation were also measured by these accelerometers. Furthermore, 8 out of 10 LVDT devices served for measuring the relative displacements between the masonries and the RC frame. The devices were placed on the perpendicular walls which enabled to capturing the motion simultaneously. On the other hand, the remaining 2 LVDTs were used to measure the diagonal deformations on the walls. All LVDTs are presented by the red markers in Figure 4.40. Moreover, 2 linear transducers were placed on the top slab for the purpose of measuring the horizontal drifts on the floor level, shown with blue markers in Figure 4.40, while the additional two were attached to the foundation support, thus relative displacements were able to be measured.

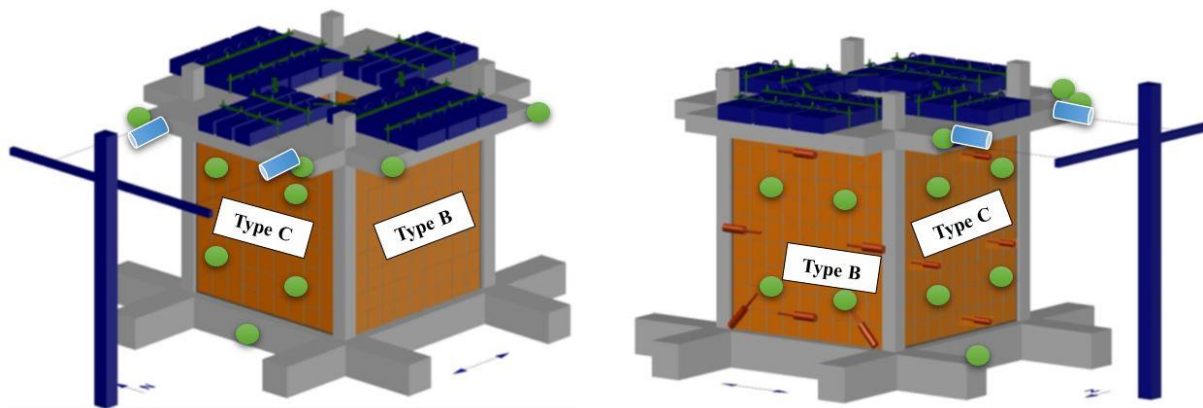


Figure 4.40. Schematic view of the measuring instruments from different angles.

4.2.6 Testing methodology

In order to investigate the dynamic behavior of the applied method, the experiments were divided into two groups; seismic loading induced shake table tests and excitations for determining the dynamic characteristics of the building. For the purpose of seismic loading, a historical record from the Kefallonia 2014 earthquake (E-W component) was adapted. The applied scaled seismic loading sequence was based on the input intensity level which gradually increased from 3% to 77% of the earthquake record, calculated for a top floor of a 4-story infilled RC numerical model (Rousakis et al., 2020). Ultimate loading level determined on the basis of structural deformation status as well as the shake table limits. Accordingly, in total, 23 seismic tests were conducted. Following the damaged states on specific intervals; resonant frequency, sine-sweeps, low intensity (0.02g) white noise as well as modal hammer tests were performed, in order to assess the dynamic characteristics of the overall building and its components. In addition to the seismic horizontal loading, 18 steel ingots were placed on the top slab with the total mass of 7.2 tons for providing extra weight, which are schematically visualized in Figure 4.40.

4.2.7 Details of the seismic loading

While determining the suitable seismic excitation to be used in the experiments, firstly inelastic numerical analyses were done (Rousakis et al., 2020). Since the aim of study was exposing the tested structures against severe conditions and only single motion data was available to be used due to the project restrictions, a strong ground shaking data was investigated. Accordingly, the seismic data was extracted from the Chavriata site of Kefallonia earthquake (E-W component) that occurred in 2014. The Peak Ground Acceleration (PGA) reached up to 0.77g, which was the greatest value recorded to that date in Greece (ITSAK, 2014). The Chavriata station was 7 km far from the epicenter of earthquake, hence could be considered as a near-field seismic record. The earthquake caused serious damages on the buildings, Figure 4.41. Seismic record details are shared in Figure 4.42, in terms of the acceleration-time data.



Figure 4.41. Observed damages from the Kefallonia earthquake reconnaissance reports; shear damages on the walls (left) and severe failures on both RC and masonry elements (right) [adapted from ITSAK, 2014].

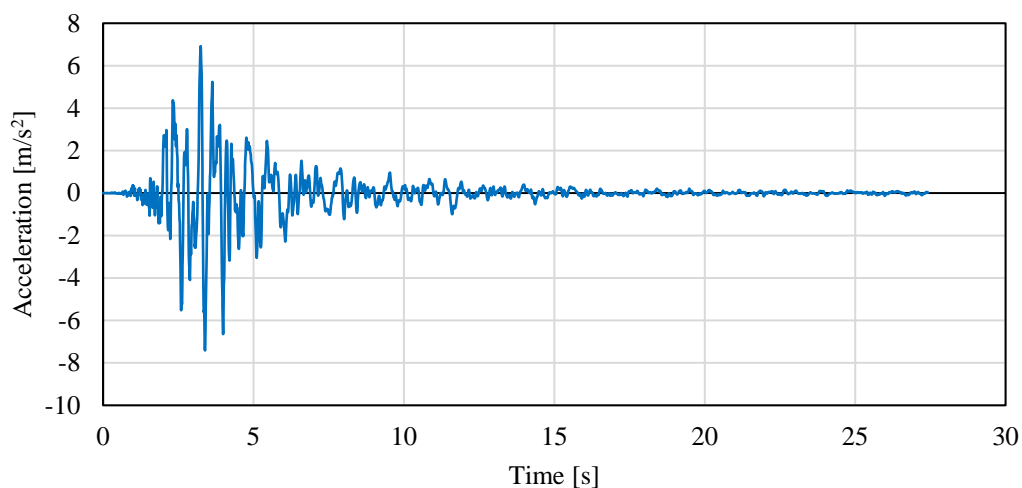


Figure 4.42. Kefallonia earthquake acceleration-time history record.

Following the determination of seismic data, a numerical model of a 4-story RC building was created (Rousakis et al., 2020). Inelastic material features were taken into consideration during the analyses and for the purpose of simplification only RC frame was modelled omitting other structural elements such as infill walls, Figure 4.43. The symmetrical model was excited by the Kefallonia record in a single direction and various outcomes were gathered from the results of analysis. Accordingly, green color denotes the crushing of concrete cover (unconfined part), whereas brown color indicates the steel yielding at end of analysis, as given in Figure 4.43. Maximum top-level displacement was measured 14 cm which

corresponds to the relative drift ratio of 1%. Acceleration response on the top level was $a_{\max} = 2.12g$, which was determined to be detrimental particularly in terms of the masonry out-of-plane strength for similar buildings where infill walls are utilized, Figure 4.44. Therefore, this response was decided to be used for the experiments. However, in order to calibrate the excitation data with the shake table capacity, the response record was slightly modified in a way that maximum acceleration value was reduced to $a_{\max} = 1.63g$, thus reflects the 77% of the original top floor response (77% KEF), see Figure 4.45. Moreover, the dominant frequency of the record was found between 2.5-4.0 Hz upon performing Fast Fourier Transform (FFT) analysis, which was later used for evaluating the building performance against harmonic loads, i.e., resonant frequency.

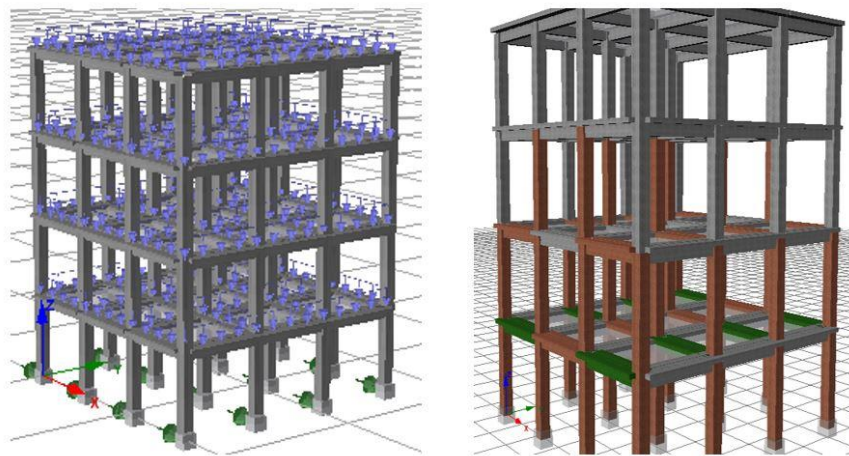


Figure 4.43. Four-story numerical model; loads and design (left) and damage levels of the RC members (right).

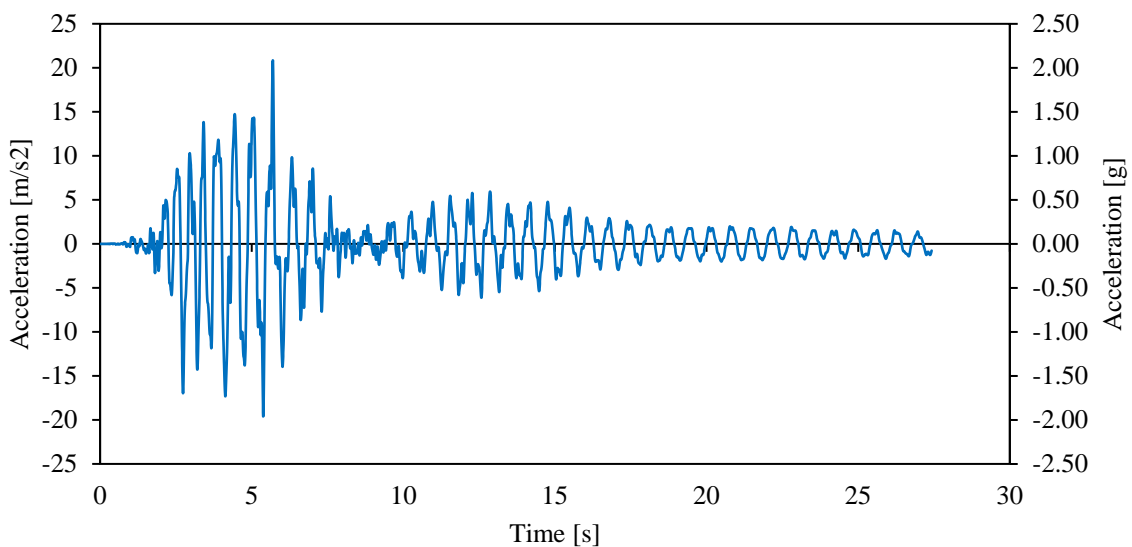


Figure 4.44. Top-floor response acceleration-time curve.

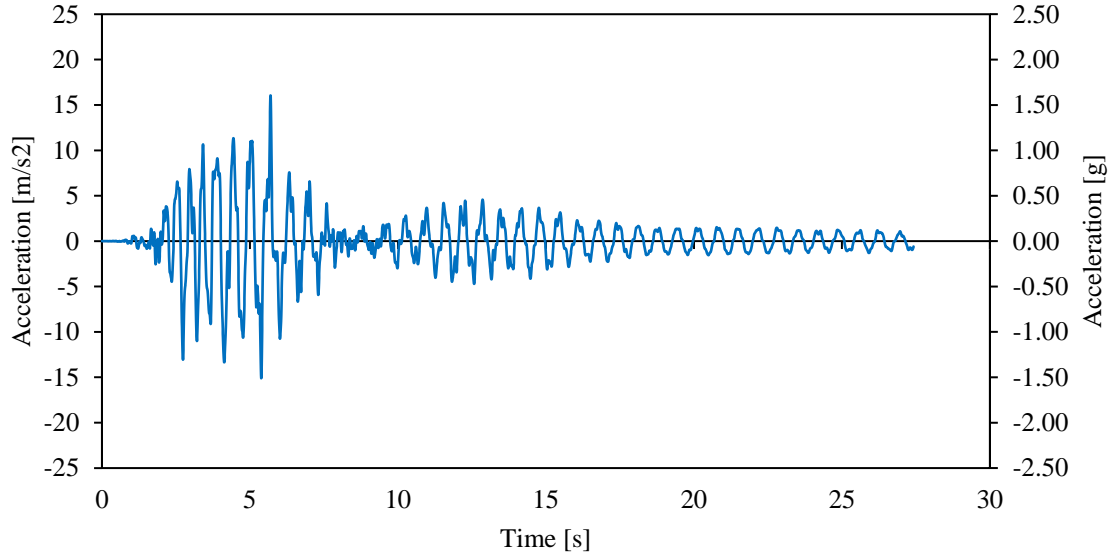


Figure 4.45. Reduced top-floor response (77% KEF) acceleration-time curve.

4.2.8 Testing phases

The building was excited only in a single horizontal direction as the dynamic loading method and the tests were divided into four phases while investigating the variables in terms of the positioning configuration as well as the strengthening methods of the infill walls. Following each earthquake loading that represents different intensity levels, the structure was exposed to the white-noise (random) excitations in order to measure the eigen frequencies. Moreover, the stiffness shifts were calculated using those frequency values by means of using the principles of structural dynamics. The frequency of an undamped oscillation for any system can be written with the well-known equation given in Equation 4.1, where f_n = natural frequency; k = stiffness and m = mass.

$$f_n = \frac{1}{2\pi} \sqrt{\frac{k}{m}} \quad (4.1)$$

Since the majority of civil engineering systems have relatively low damping features (Bernal et al., 2015), which is around 5%; for such systems, f_d : damped frequency yields similar values of the natural frequency, f_n , as shown in Equation 4.2, where ζ corresponds to the damping coefficient.

$$f_d = f_n \sqrt{1 - \zeta^2} \quad (4.2)$$

Combination of the Equation 1 and Equation 2 enables to correlating between the flexural stiffness and eigen frequencies, as shown in Equation 4.3, where E indicates the Young's modulus and I stands for the moment of inertia.

$$\frac{EI_{current}}{EI_{initial}} = \frac{(f_{current})^2}{(f_{initial})^2} \quad (4.3)$$

In Table 4.7, the testing phases are given with the seismic intensity details.

Table 4.7. Testing phases and loading details.

Phase	1	2	3	4
Remarks	No rotation No repair	No rotation Repair of infills B	90 degrees rotation No additional repair	90 degrees rotation Repair of infills C
Infill position	B - in-plane C - out-of-plane	B_FRPU - in-plane C - out-of-plane	C - in-plane B_FRPU - out-of-plane	C_FRPU - in-plane B_FRPU - out-of-plane
Intensity	3% KEF-1 (0.06g)	6% KEF-2 (0.12g)	6% KEF-3 (0.12g)	6% KEF-4 (0.12g)
	6% KEF-1 (0.12g)	11% KEF-2 (0.24g)	10% KEF-3 (0.22g)	11% KEF-4 (0.23g)
	11% KEF-1 (0.23g)	18% KEF-2 (0.39g)	16% KEF-3 (0.35g)	18% KEF-4 (0.39g)
	25% KEF-1 (0.53g)			25% KEF-4 (0.51g)
	38% KEF-1 (0.80g)			28% KEF-4 (0.60g)
	55% KEF-1 (1.16g)			34% KEF-4 (0.73g)
	72% KEF-1 (1.54g)			45% KEF-4 (0.90g)
	74% KEF-1 (1.57g)			
	69% KEF-1 (1.47g)			
	77% KEF-1 (1.64g)			

Phase 1

In the initial position of the tests, Type B walls were positioned for receiving the in-plane excitation, whereas Type C walls were simultaneously resisting to the out-of-plane forcing. The structure was firstly excited gradually up to 0.7% lateral drift level (Figure 4.46a), where damage initiation of the concrete cracking was observed without steel yielding. No

damages were visible on the masonries in any direction. The reduction of the global stiffness in Y and X directions (Figure 4.34 – 3D model) were less than 20% (Figure 4.46b) and 3% (Figure 4.46c), respectively.

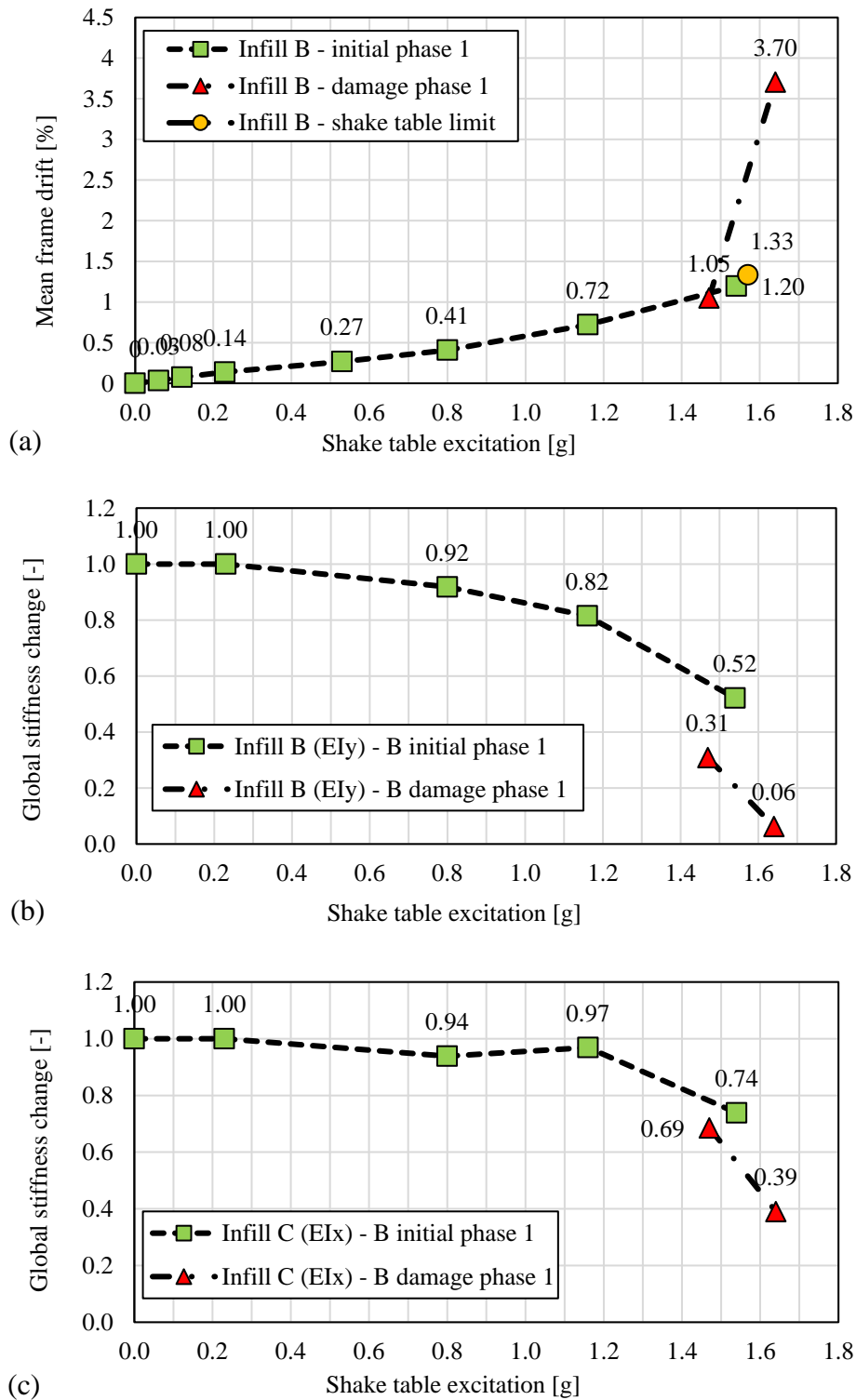


Figure 4.46. Phase 1 results of the dynamic characteristics of the structure: (a) frame drift, (b) Y-direction stiffness change and (c) X-direction stiffness change.

Then, the same excitation was gradually increased up to serviceability limit state (SLS) levels, where initial yielding of the steel bars and concrete cracks could be expected. The results revealed that RC frame experienced concrete cracking when 1.33% drift level was reached at the excitation intensity of 1.57g (Figure 4.46a). Regarding the masonries, bed and head mortar joint cracks were observed on the Type B walls, however no visible damages occurred on the Type C walls that resist against the out-of-plane loads. The reduction of the global stiffness in Y and X directions (Figure 4.34 – 3D model) were less than 50% (Figure 4.46b) and 25% (Figure 4.46c), respectively.

In order to understand the damage initiation behavior of the in-plane loaded masonries, Type B walls, ultimate limit state (ULS) drift levels were aimed (around 2% drift ratio). Therefore, load intensity level was increased in a controlled manner and until the 72% KEF-1 (1.54g) intensity level no damage was observed on the masonries. However, when the building was again loaded up to 74% KEF-1 (1.57g) intensity, the shake table capacity was disturbed which caused a sudden stop of the experiment. The test was started once again when the checking and positioning of the specimen was completed. Although there was not any visible degradation of the structure just before the sudden stop, the restarted excitation resulted significant damages in the phases with 69% KEF-1 (1.47g) and 77% KEF-1 (1.64g) intensity levels. Type B infill walls experienced cracks particularly on the center part of the walls, which was rather different than the typical cross shape (><) failures. The damages formed in an extended cross shape (>—<) pattern, which was a sign that PUFJs were effective of protecting the corner zones, Figure 4.47. Meanwhile, the out-of-plane loaded walls, Type C, were able to resist loads without any major damages during the entire Phase 1, yet cracks were observed on some joints as shown in Figure 4.48. RC members on the other hand, developed hinge mechanisms at the columns ends due to the concrete crushing which resulted weakened columns, see Figure 4.49.

Despite the minor damages occurred during the initial loading steps until the sudden stop of the shake table, the global stiffness of the building was significantly dropped at the end of damage initiation phase. The stiffness reduction was almost 95% in Y-direction (Figure 4.45b) and about 60% in X-direction (Figure 4.46c). These stiffness changes correspond to eigen-frequency shift from the initial value of 7.2 Hz to 1.8 Hz, which was determined by the modal hammer test. It should be noted that the response of structure during the damage phase is a result of overlapping the main excitation frequency band of 2.5 Hz – 4.0 Hz with the resonance frequency band. Massive inertial forces changing due to the sudden stop could be considered as another underlying factor.

Overall, the severely weakened specimen was still able to carry loads up to the drift level of 3.7% (Figure 4.46a), thanks to the presence of PUFJ which sustained the integrity of structural system without any particular element loss, though marginal amount of brick blocks was disengaged completely for the case of Type B masonries. Eventually, the structural stability of those walls was sufficient to be strengthened by the FRPU strips for the further analyses.



Figure 4.47. Masonry Type B damages at the end of Phase 1; North side wall (left) and South side wall (right).

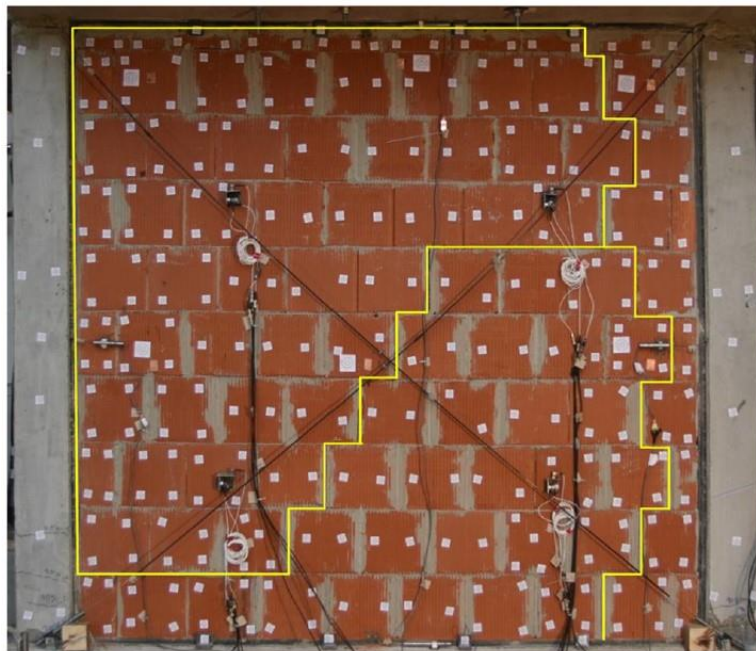


Figure 4.48. Crack pattern on the masonry Type C at the end of Phase 1.



Figure 4.49. RC column damages; top end (left) and bottom end (right).

Phase 2

In this phase, Type B walls received emergency repair by the FRPU method. Firstly, GFRP meshes were bonded to the both sides of the walls and following that flexible adhesive type of Sika PS was implemented on those 50 cm width GFRP strips. It should be mentioned that no direct connection or anchorage was provided between the FRPU intervention and RC frame, thus the infill walls had connection to the RC frame only through PUFJs. Because, it was merely aimed to protect the damaged infills for further analyses. Retrofitted Type B walls are shown in Figure 4.50.



Figure 4.50. FRPU intervention on Type B infills; front (left) and perspective (right) views.

The specimen was again loaded only 10 hours after the repair. Before that, the global stiffness values were checked and found out that there was an increase in Y-direction from 6% to 25%. Since no intervention was applied on the Type C masonries, there was not practically any stiffness changes in the X-direction.

The building was firstly loaded by the harmonic resonance frequencies in the band of 16 Hz – 32 Hz and up to 40% KEF intensity. The carried-out loading revealed that out-of-plane performance of the Type C walls remained stable though slight extensions on the existing fissures were noticed. Later on, the gradually increasing seismic loading was applied. The tests were stopped at the intensity level of 18% KEF-2 (0.39g) in order to sustain the building stability for the next phases of the experiment. Because, the plastic hinges at the column ends posed considerable risks. The corresponding lateral drift value to this loading level was measured as 1.62%.

At the end of Phase 2, no additional damages occurred on either the Type B walls or Type C walls, however the global stiffness value was decreased to 13% in Y-direction. This phase exhibited the possibility of FRPU as a quick seismic intervention method to be combined with the PUFJ implemented systems.

Phase 3

In order to execute the in-plane tests for the prefabricated PUFJ implemented Type C masonries and meanwhile examining the out-of-plane performances of the PUFJ injected Type B ones, the building was rotated by 90 degrees about Z-axis (Figure 4.34) on the seismic table using the laboratory cranes. During the rotation process, slight stiffness changes occurred possibly as a result of the compaction of debris in Type B infill walls and further disturbance on the already damaged columns. Accordingly, the stiffness in Y-direction (now Type C walls loaded in-plane) increased up to 26%, whereas in the X-direction where Type B walls were loaded out-of-plane, a small drop of the stiffness was observed from the level of 39% to 30%, see Figure 4.51. No retrofitting process was actualized in this phase.

The building was excited by gradually increasing loads following the same procedure of the previous steps. Ultimate drift level was reached to 0.67% at the load intensity of 16% KEF-3 (0.35g), Table 4.7. The tests were stopped at this level, since the damages on the Type C walls were notably visible, namely extensions of the fissures on the bed and head joints. Although it can be mentioned about a stiffness drop in both directions, those values were marginal, as the changes were from 30% to 21% in Y-direction and from 26% to 21% in X-direction, see Table 4.7. Nevertheless, for the sake of not jeopardizing further planned tests and implementing FRPU on the Type C infill walls, it was decided to conclude this phase, thus the specimen was left with an adequate strength.

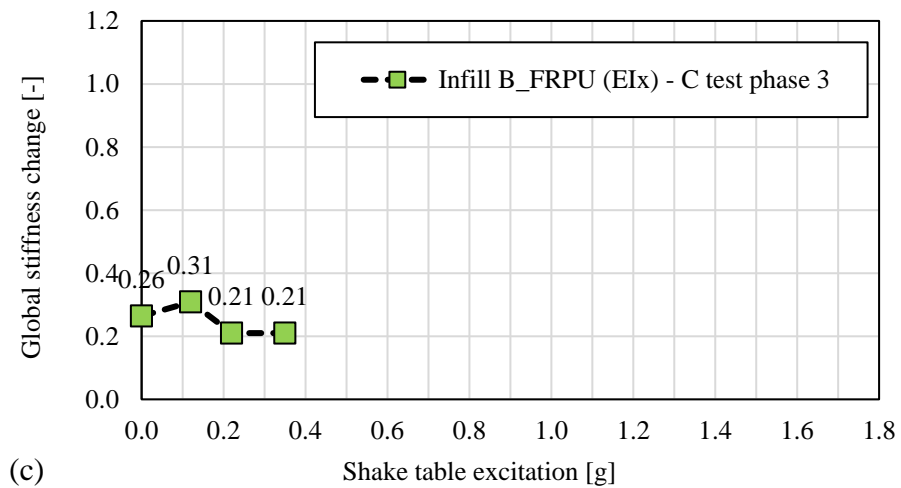
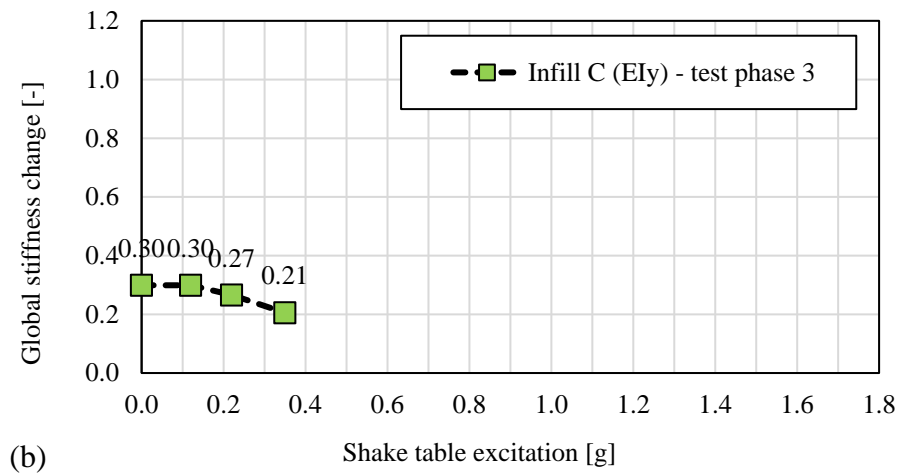
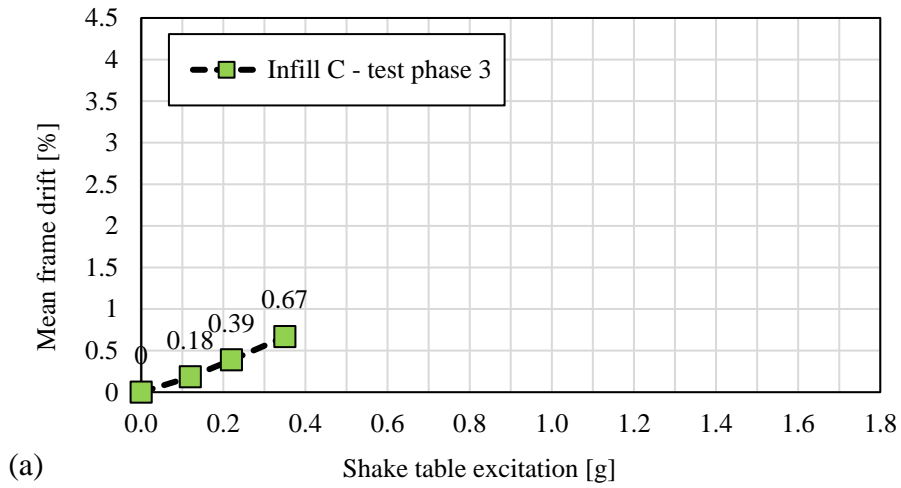


Figure 4.51. Phase 3 results of the dynamic characteristics of the structure: (a) frame drift, (b) Y-direction stiffness change and (c) X-direction stiffness change.

Phase 4

As the last phase of the tests sequence, FRPU strengthening was utilized on the Type C masonries on the both wall sides, see Figure 4.52. The FRPU strip widths were determined different than the Type B ones, since the aim was merely checking the global stiffness and dynamic response improvements of the structure rather than keeping the damaged particles together for further testing. Therefore, 35 cm and 15 cm strip widths were determined suitable for the diagonal and boundary ones respectively, and these were extended to the RC members by 5 cm. The remaining parts of the structure were left without any additional repairing interventions. However, the global stiffness increase was significant in both directions as, from 21% to 77% of the initial stiffness in Y-direction (Type C infill walls – Figure 4.53b) and from 21% to 84% of the initial stiffness in X-direction (Type B infill walls – Figure 4.53c).

Following that, the specimen with the already plastic hinged columns and repaired walls was once again loaded by gradually increasing seismic intensity on the shake table. Finally, the building was able to withstand the drift level up to 0.88% when the intensity of loading was reached to 45% KEF-4 (0.95g). The decrease of the global stiffness in Y-direction was from 77% to 52% of the initial values and from 84% to 52% in the X-direction. Although no additional damages or major failures observed on the masonries, the tests were terminated at this point due to the fact that the shake table limits were the concern in terms of a potential uncontrolled collapse.



Figure 4.52. FRPU intervention on Type C infills; front (left) and perspective (right) views.

Additional remarks

In a recent study of Hojdys et al. (2023), some other important aspects are highlighted as a part of the same experimental campaign. For example, the possibility of measuring the strain values on the entire wall surfaces is presented for the in-plane loaded infills. Horizontal force – slab displacement hysteresis loops are also extracted for checking the overall dynamic behavior from a different perspective. Other than that, various acceleration and displacement values are shown at the different positions through the wall height which enables to see the relative differences. The damage levels are also given in a slightly different way though the same eigen frequencies provided here still constitute the basis of the proposed damage indicator factors. The reader might check this reference for further information in this regard.

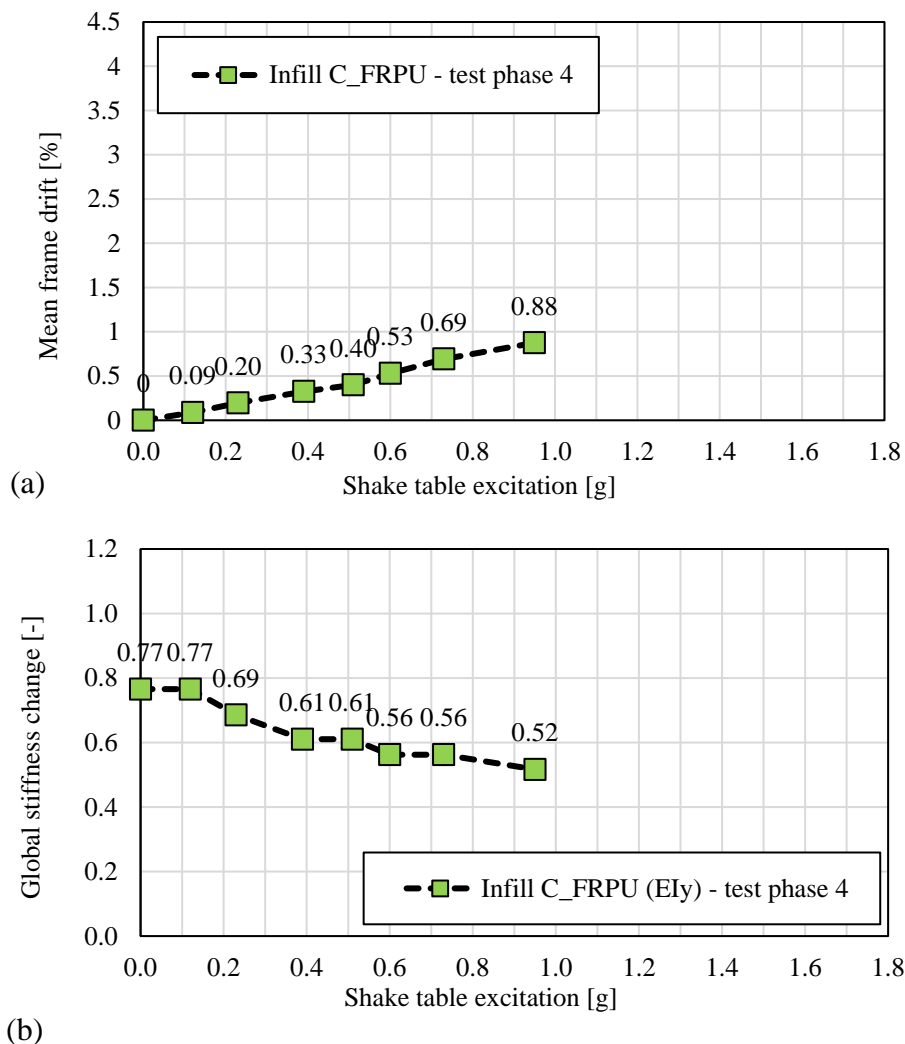


Figure 4.53. Phase 4 results of the dynamic characteristics of the structure: (a) frame drift, (b) Y-direction stiffness change and (c) X-direction stiffness change.

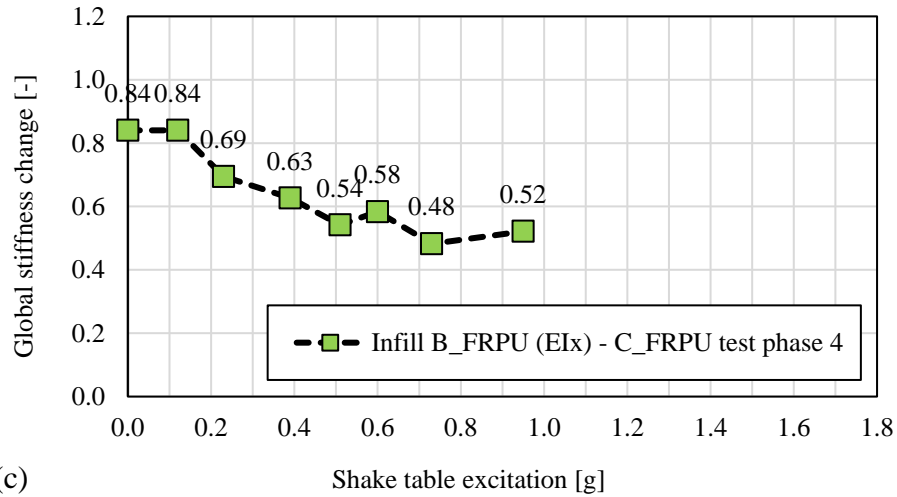


Figure 4.53. (continued).

4.2.9 Vibration tests

In another step of the experiments, forced vibration tests were conducted. At this stage, the already damaged building was exposed to long-duration (up to 10 minutes) strong harmonic vibrations. In this way, the dynamic behavior under desired shaking intensities as well as resonance effects could be observed. Below, the testing methodology and the results are given.

Testing methodology

In order to produce harmonic inertial forces, a vibration generator was placed at the top of the building. It was able to excite the structure in one horizontal direction, thus the perpendicular walls received in-plane and out-of-plane forces simultaneously. In Figure 4.54, the vibration generator is presented.

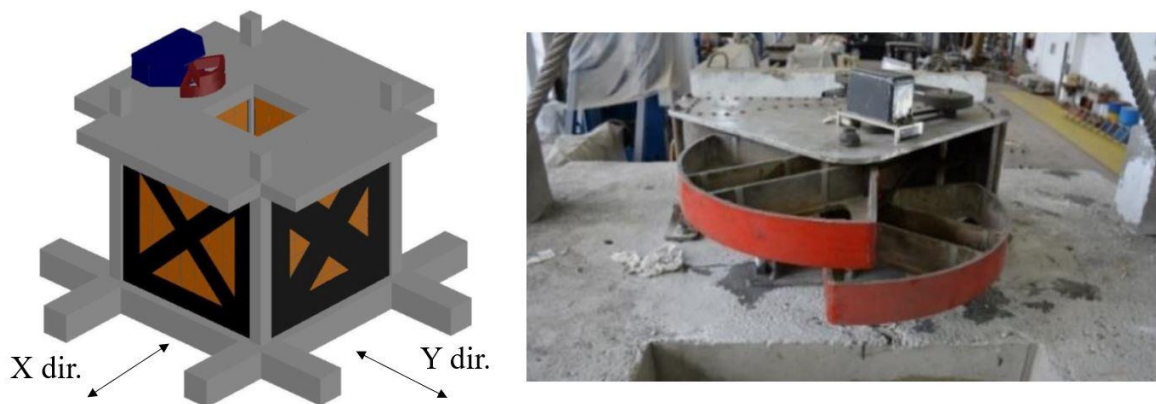


Figure 4.54. Vibration generator placement; schematic perspective (left) and real (right) views.

The forced vibration (FV) test aimed at revealing the dynamic behavior corresponding different drift levels. Therefore, ambient vibration (AV) technique was executed at specific time intervals between the forced vibration excitations. Accordingly, modal shapes and frequencies could be determined. Sequence of the tests is given in Table 4.8.

The vibration generator consisted of two separate mechanisms rotating around the same vertical axis that each basket was able to carry various number of masses. Different slots were designed in those, which enabled to adjust the different mass configurations on the basis of plate weights. In each basket, three slots were designated that either large (L) or small (S) plates could be positioned, for placing 20 kg and 10 kg plates, respectively. Accordingly, different tests were labeled based on the loads each basket carries. For example; S-1 + L-1 loading label corresponds to 100 kg total weight (2×S + 4×L plates) and similarly, S-0 + L-0 means zero mass. The schematic visualization of the plate masses is presented in Figure 4.55.

Table 4.8. Sequence of the performed tests.

Test No.	Name	Type of excitation	Load case
1	FV Test 01	Harmonic forced vibrations	S-1 + L-0
2	FV Test 02	Harmonic forced vibrations	S-1 + L-0
3	AV after FV 02	Ambient vibrations	Ambient
4	FV Test 03	Harmonic forced vibrations	S-3 + L-0
5	AV after FV 03	Ambient vibrations	Ambient
6	FV Test 04	Harmonic forced vibrations	S-4 + L-0
7	AV after FV 04	Ambient vibrations	Ambient
8	FV Test 05	Harmonic forced vibrations	S-2 + L-0
9	FV Test 06	Harmonic forced vibrations	S-3 + L-0
10	AV after FV 06	Ambient vibrations	Ambient
11	FV Test 07	Harmonic forced vibrations	L-3
12	FV Test 08	Harmonic forced vibrations	S-4 + L-1
13	FV Test 09	Harmonic forced vibrations	S-1 + L-0
14	AV after FV 09	Ambient vibrations	Ambient

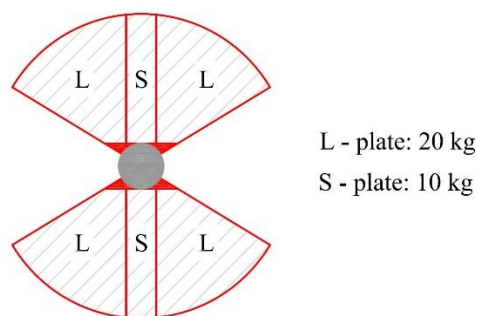


Figure 4.55. Vibration generator details.

In the principle of this methodology, while the separate mechanisms rotated in the opposite directions, the inertial forces were emerged as a result of the centrifugal forces. Initially, the masses were positioned in the counter sides of the rotation circle. If the total mass of the vibration generator, m_{vg} , is split equally between the baskets, the mechanism can be simplified as illustrated in Figure 4.56a, where ω_{vg} is the angular velocity and e_{vg} is the eccentricity of the lumped masses. At the random time of t , the masses are positioned at the opposite angles θ_t , and produce resultant centrifugal force $p_{vg}(t)$ in y direction as given in Equation 4.4. Meanwhile, the resultant force in the orthogonal direction, x , is canceled out at any time during the rotation. In this way, the maximum force is obtained when the masses overlap on each other, whereas zero resultant force occurs when the masses are positioned at the radial distance of π , that corresponds to the initial position. This mechanism is shown in Figure 4.56b.

$$p_{vg}(t) = (m_{vg}e_{vg}\omega_{vg}^2)\sin\theta_t \quad (4.4)$$

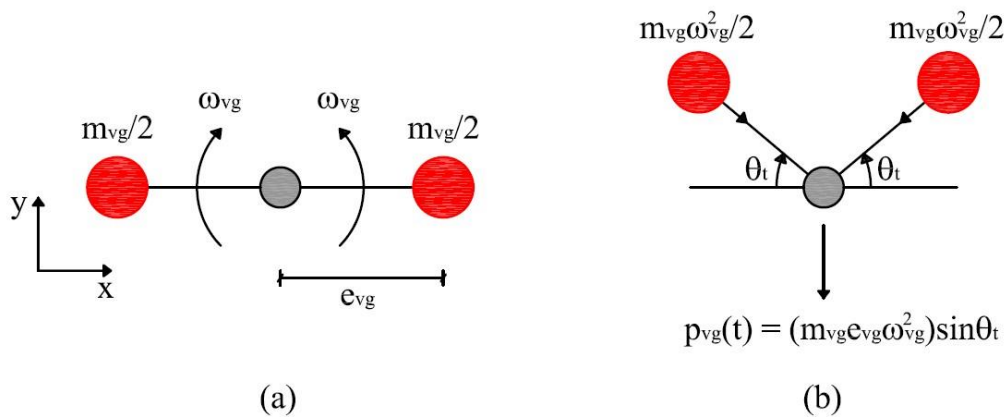


Figure 4.56. Mass rotational mechanism; (a) initial position and (b) at time equals to “t”.

Vibration results

The results are evaluated in terms of AV and FV outcomes. The first one was utilized in order to calculate the frequency and modal shapes as well as damping. The latter one on the other hand, was used for providing detailed information about the acceleration and displacement values of the system.

According to AV results, which were measured just after the specific FV tests as mentioned earlier and given in Table 4.8, the predominant frequencies were obtained using ARTEMIS Modal post-processing software. Upon performing the operational modal analysis, the natural frequencies and corresponding modal shapes could be determined by means of

combining the Peak Picking and Enhanced Frequency Domain Decomposition methods. The results are given in Table 4.9. It was seen that modal shape in X direction (perpendicular to the excitation) was pure translational during all ambient measurements, except the last test, number 14, (after FV Test 09). At that phase, rotational contribution on the modal shape was significant. The natural frequency in this direction was dropped from 4.30 Hz (Test 3) to 2.90 Hz (Test 10). On the other hand, it was difficult to clearly express the mode shapes in Y direction, where the excitation was imposed. The modal behavior was rather a combination of translation and rotation, which was mainly attributed to the difference of the stiffness of infills walls + RC columns (different configuration and initial conditions), (Kwiecień et al., 2021). The frequencies in this direction were decreased from 5.28 Hz and 7.40 Hz to 3.93 Hz and 5.82 Hz, respectively.

Table 4.9. Ambient vibration frequency and damping results.

Test No.	Name	Frequency [Hz]	Damping [%]	Comment
3	AV	4.30	3.87	Translation X
	after	5.28	1.69	Combined – Translation Y + visible rotation
	FV 02	7.40	2.46	Combined – Translation Y + visible rotation
5	AV	4.16	3.83	Translation X
	after	5.14	2.02	Combined – Translation Y + visible rotation
	FV 03	6.77	2.58	Combined – Translation Y + visible rotation
7	AV	4.12	3.26	Translation X
	after	4.75	2.15	Combined – Translation Y + visible rotation
	FV 04	6.71	2.62	Combined – Translation Y + visible rotation
10	AV	2.90	5.07	Translation X
	after	4.17	2.75	Combined – Translation Y + visible rotation
	FV 06	6.69	2.37	Combined – Translation Y + visible rotation
14	AV	3.93	2.25	Combined – Translation Y + visible rotation
	after	4.88	1.50	Combined – Translation X + visible rotation
	FV 09	5.82	1.82	Combined – Translation Y + visible rotation

Regarding the harmonic forced vibration tests, as a result of having multiple measuring devices, only selected representative results of the acceleration, displacement and frequencies are given in Table 4.10. The devices were placed at the top slab level, in the excitation direction (Y). Moreover, due to the length of some tests and changes in the input frequency, segment categorization was made. It should be also noted that acceleration and displacement results in Table 4.10 reflect the maximum values experienced in each segment, whereas the frequencies were obtained from the acceleration devices labeled as ACC2 and ACC3.

According to FV results, specifically Test 1 and Test 2, it was noticed that peak values for both acceleration and displacement were measured when the building was excited in its natural frequency that ranged between 4.5 Hz – 5.0 Hz. Furthermore, Segments 1 and 2 of the Test 1 revealed that deformed shape did not exhibit an absolute translational motion, but rather a mix of translation and rotation. To be more specific, as a consequence of having different stiffnesses of the walls, the maximum acceleration and displacement values for Segment 1 and Segment 2 were measured at the opposite positioned devices, namely ACC2-LP1 and ACC1-LP2, respectively. Since the weights in the mass baskets were adjusted for enabling to observe the behavior at different loading levels (Table 4.8), each test revealed different outcomes. According to Table 4.10, peak values of the acceleration and displacement values were measured as 1.51g and 30.15 mm, from the test numbers 2 and 9, respectively. Representative acceleration and displacement time history graphs from Test 1 are presented in Figures 4.57-4.60.

Table 4.10. Forced vibration selected results.

Test No.	Name	Segment	Acceleration [g]		Displacement [mm]		Frequency [Hz]
			Acc 2	Acc3	LP1	LP2	
1	FV Test 01	S1	1.16	0.70	6.40	12.10	4.0-5.0
		S2	0.58	1.32	10.98	4.56	5.3
		S3	0.65	0.41	4.73	8.15	4.2
		S4	0.23	0.14	1.99	3.58	3.8
2	FV Test 02	S1	1.51	0.63	6.52	13.15	4.5
		S2	0.46	1.20	11.14	4.80	5.0
		S3	0.60	0.37	4.77	8.46	4.1
		S4	0.70	0.46	5.87	10.15	4.0
		S5	1.18	0.74	8.29	14.67	4.2
4	FV Test 03	-	1.25	0.68	8.48	21.21	3.0-4.0
6	FV Test 04	S1	0.05	0.03	1.01	2.35	2.0
		S2	0.20	0.11	2.61	6.75	2.7
		S3	0.58	0.26	4.96	14.25	3.0
		S4	1.21	0.50	7.40	25.89	3.0-3.5
		S5	1.05	0.38	6.46	26.33	3.0
8	FV Test 05	S1	0.05	0.03	1.47	3.70	1.8
		S2	0.03	0.02	1.03	2.52	1.8
		S3	0.19	0.11	3.25	9.17	2.1
		S4	0.50	0.21	4.80	18.22	2.5
		S5	0.74	0.29	5.72	22.78	2.7
		S6	0.91	0.35	6.31	25.33	2.9
		S7	1.03	0.39	6.70	27.63	2.9

Table 4.10. (continued).

Test No.	Name	Segment	Acceleration [g]		Displacement [mm]		Frequency [Hz]
			Acc 2	Acc3	LP1	LP2	
9	FV Test 06	S1	0.07	0.04	1.37	4.07	2.0
		S2	1.12	0.36	5.96	27.92	2.9
		S3	0.27	1.10	13.12	5.13	4.3
		S4	1.10	0.34	6.24	28.99	2.9
		S5	0.30	1.35	16.80	6.40	4.0-4.5
		S6	0.27	0.21	5.02	8.34	3.0
		S7	0.99	0.41	9.46	28.87	2.6
11	FV Test 07	-	0.87	0.48	12.50	29.90	2.3
12	FV Test 08	S1	0.28	0.17	4.50	12.97	2.0-3.0
		S2	0.16	0.32	5.90	3.43	3.0-5.0
		S3	0.31	0.35	2.63	1.47	4.8-7.0
		S4	0.14	0.34	6.07	4.45	3.3
13	FV Test 09	-	0.77	0.51	13.78	30.15	2.2

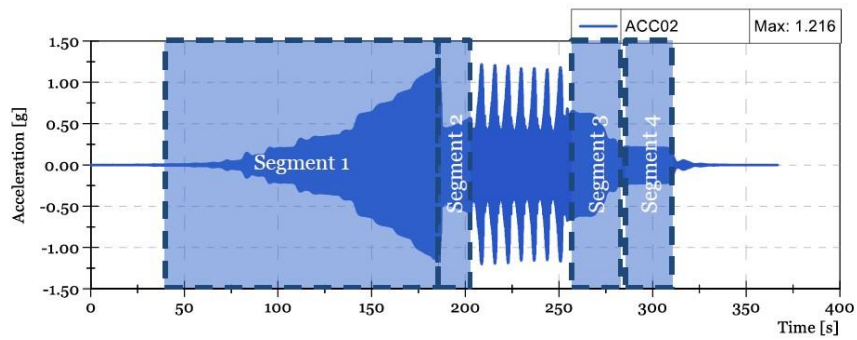


Figure 4.57. Acceleration-time history results measured by ACC2 device.

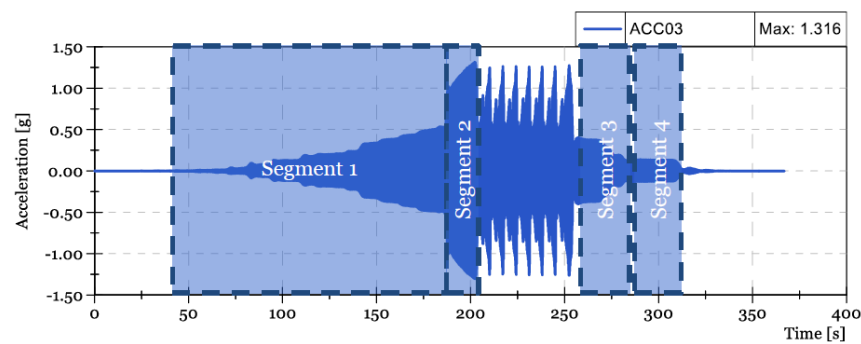


Figure 4.58. Acceleration-time history results measured by ACC3 device.

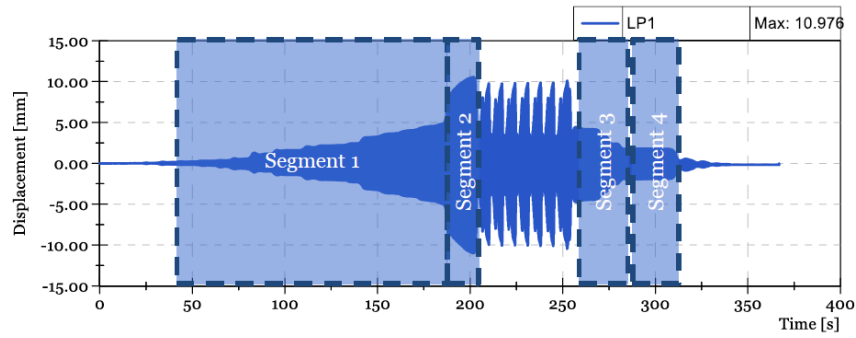


Figure 4.59. Displacement-time history results measured by LP1 device.

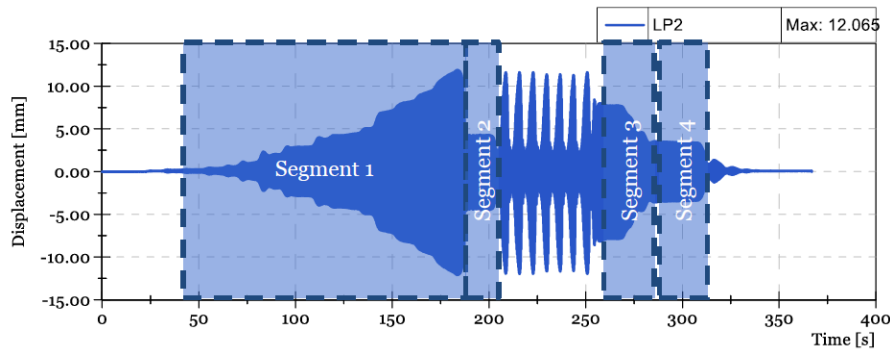


Figure 4.60. Displacement-time history results measured by LP2 device.

4.2.10 Section summary of the shake table tests

An experimental campaign was conducted in the pursuit of illuminating the performance of an innovative polymer-based solution, PUFJ, against the earthquakes. For this purpose, a large-scale RC building was constructed in the laboratory conditions and later tested on a seismic shake table. Multiple tests were performed while investigating the behaviors of differently implemented PUFJ solutions, namely prefabricated and injected. The tests were executed in a way that the masonries could be tested in both in-plane and out-of-plane directions.

The results indicate that PUFJ method enables to sustain structural integrity of different members, i.e., RC frame and masonry, and it delays the severe damages on the infill walls up to very high drift levels. The first disintegration which might cause injuries occurred only after 2.5% of lateral drift and the building was able to withstand the drift level up to 3.7%, which is already much beyond of the expectations of any modern seismic code.

Moreover, FRPU intervention technique was tested on the PUFJ implemented walls and it was noticed that this is an effective quick repairing method which does not require the need of direct connection to the RC members but can be utilized merely on the surface of the

PUFJ implemented masonries, without any anchorage detailing needs. Because, an excellent bonding performance was observed in this manner, as there was not any detachment of the FRPU from the system. Other than that, the repairing method also helped to restore the overall stiffness of building.

In addition, forced vibration tests were also conducted and it was seen that long duration strong harmonic vibrations in resonance with different intensities did not collapse the already damaged specimen. Although there was a stiffness drop at the end of all vibration tests (less than 55%), the structure was still in a safe and stable condition, thanks to the polymer protected walls that could keep their integrity and strength up to a limited level.

As a final remark, it was also seen that any implementation method of PUFJ, either on the three-sides of the wall or on the entire peripheral, could protect the infilled systems efficiently against the high intensity in-plane and out-of-plane excitations.

CHAPTER 5.

NUMERICAL INVESTIGATION

Modeling masonry infilled RC frames requires to take into account different materials i.e., concrete, steel rebar, brick, mortar and the combination of their interactions. Although there are different strategies for the simulation, any of those need to be capable of representing the actual behavior up to a desired level.

Solid mechanics in essence, deals with two types of material behavior; either linear or non-linear. The latter one is crucial to be considered while establishing an accurate material model, which usually follows the linear branch after a certain level. Therefore, experimental results are very useful for understanding the nature of any type of material. In this sense, it is reasonable to receive the empirical information for modeling concrete, which is considered as a quasi-brittle material. Another option could also be using the continuum mechanics principles such as plasticity and damage mechanics theories, though these are still dependent on the experimental data.

On the other hand, the reinforcement bars exhibit less complicated behavior thanks to the isotropic features of steel, which is assumed to behave elastic until reaching a specific stress level where yielding occurs and then a simple strain hardening branch is the concern in a plastic manner up to the ultimate stress level.

However, the masonry behavior is much complex phenomenon than concrete or steel, since it consists of discontinuities due to the presence of bricks and mortar and their interfaces (bed or head joints). Therefore, three separate modeling strategies stand out in the literature, each represents a different level of complexity. The simplest and least complicated one is assuming masonry to act as a homogenous single material ignoring any discontinuity in its body, which is called here as Macro Model. In this way, no distinction is made between the bricks and joints, since these are considered as parts of the single unity. It is suitable for the large structures, but rough results should be expected due to the fact that sliding mechanisms at the joints cannot be captured by any means.

The second option is simulating the masonry with two mechanisms; the units that correspond to a merged phase of bricks and partial mortar zones, and their so-called interfaces. Discontinuity can be modeled with this method by proper constitutive assumptions, hence it is suitable for variety of structural problems. This option is called Simplified Micro Modeling.

The last modeling strategy called Micro Modeling is the most detailed one, which requires a separate representation of each element that constitute the masonry, namely brick units, mortar and their interfaces. Although more accurate results can be obtained, computational time increases considerably and thus it is only applicable to the small-size structures. These masonry modeling strategies are presented in Figure 5.1.

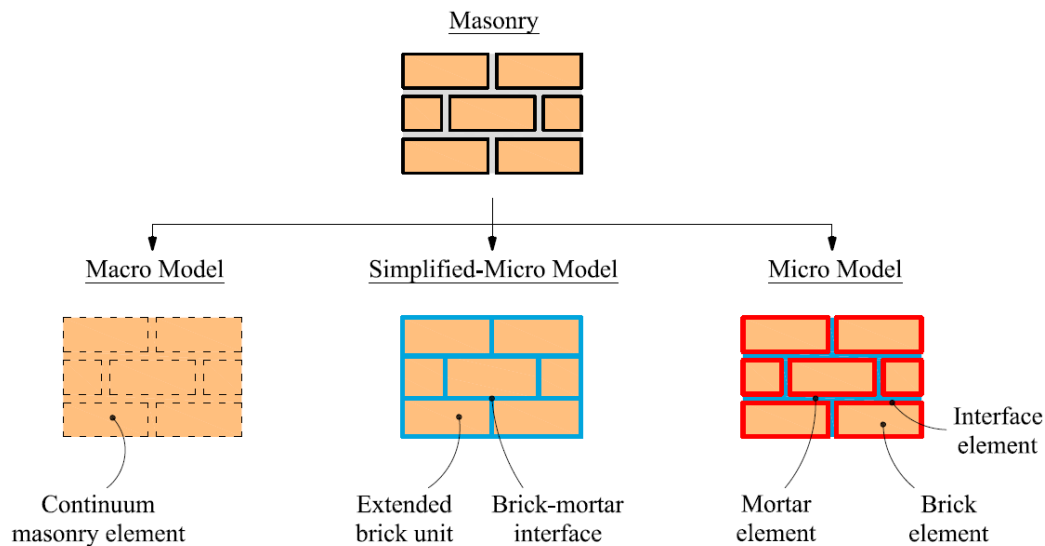


Figure 5.1. Masonry discretization approaches.

5.1 Material constitutive models

The material constitutive models for concrete, masonry units as well their interfaces and steel rebars are explained in this section. The models are simulated in the FEM program ABAQUS (Dassault Systemes, 2016), thus below paragraphs are dedicated to highlight the modeling strategies exist in the finite-elements program and how these are implemented to the problem specifics concerned in this study.

5.1.1 Concrete

ABAQUS (Dassault Systemes, 2016) offers different concrete modeling options. Among these, so-called concrete damaged plasticity (CDP) is used in the analyses. The model was derived from the studies of Lubliner et al. (1989) which was later modified by Lee and Fenves (1998). It is capable of modeling concrete and the other concrete-like quasi-brittle materials in different element types such as beams, shells and solids. The inelastic behavior is actualized by the concept of isotropic damaged elasticity in combination with the isotropic compressive and tensile plasticity. The model was developed for simulating the reinforced

concrete problems, thus it is possible to model rebars in this method. Moreover, the most advantageous part of this method in comparison to its counterparts is that, various loading conditions; namely monotonic, cyclic and dynamic can be successfully modeled.

The CDP model relies on the non-associated potential plastic flow rule – G_{CDP} , which uses the Drucker-Prager hyperbolic function as given in Equation 5.1, where ψ is the dilatation angle, \bar{p} and \bar{q} are the hydrostatic pressure and the Mises equivalent effective stresses respectively, σ_{ti} is the uniaxial tensile stress at failure and ϵ is a parameter that represents the flow potential eccentricity.

$$G_{CDP} = \sqrt{(\epsilon\sigma_{ti}\tan\psi)^2 + \bar{q}^2} - \bar{p}\tan\psi \quad (5.1)$$

The yield function, which takes into account the strength evolution differences under compression and tension is represented by a yield surface that is controlled by the hardening variables $\bar{\epsilon}_c^{pl}$ and $\bar{\epsilon}_t^{pl}$ for compression and tension, respectively. The function is given in Equation 5.2 in terms of the effective stresses.

$$F_{CDP} = \frac{1}{1-a_{CDP}} (\bar{q} - 3a_{CDP}\bar{p} + \beta_{CDP}(\bar{\epsilon}^{pl})\langle\hat{\sigma}_{max}\rangle - \gamma_{CDP}\langle-\hat{\sigma}_{max}\rangle) - \bar{\sigma}_c(\bar{\epsilon}^{pl}_c) = 0 \quad (5.2)$$

And a_{CDP} , β_{CDP} and γ_{CDP} are defined in Equations 5.3-5.5;

$$a_{CDP} = \frac{\left(\frac{\sigma_{b0}}{\sigma_{c0}}\right) - 1}{2\left(\frac{\sigma_{b0}}{\sigma_{c0}}\right) - 1}; 0 \leq a_{CDP} \leq 0.5 \quad (5.3)$$

$$\beta_{CDP} = \frac{\bar{\sigma}_c(\bar{\epsilon}^{pl}_c)}{\bar{\sigma}_t(\bar{\epsilon}^{pl}_t)} (1 - a_{CDP}) - (1 + a_{CDP}) \quad (5.4)$$

$$\gamma_{CDP} = \frac{3(1 - K_c)}{2K_c - 1} \quad (5.5)$$

Where; $\hat{\sigma}_{max}$ is the maximum principal effective stress, σ_{b0}/σ_{c0} is the initial compressive yield stress ratio of equibiaxial to uniaxial, K_c is the second stress invariant on the tensile meridian to the compressive meridian as shown with variations in Figure 5.2, and $\bar{\sigma}_c(\bar{\epsilon}^{pl}_c)$ and $\bar{\sigma}_t(\bar{\epsilon}^{pl}_t)$ are the effective cohesion stresses for compression and tension, respectively.

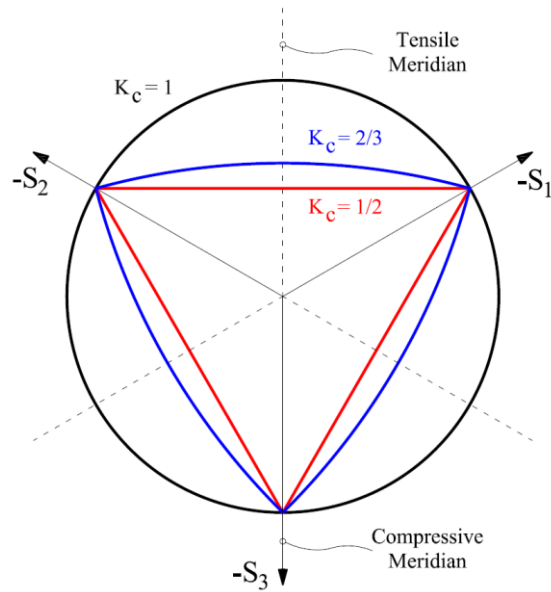


Figure 5.2. Yield surfaces in the deviatoric plane for different K_c values.

It can be seen that, other than compressive and tensile strength values which are normally taken from the experimental results, the aforementioned additional parameters – K_c , ϵ , ψ , σ_{b0}/σ_{c0} - are also need to be properly calibrated for this concrete model. Moreover, in order to regularize the viscoplastic behavior especially for eliminating the convergence issues in the analyses, the viscosity factor μ_{CDP} can be introduced to the model which permits stresses to extend beyond the yield surface. In Figure 5.3, the yield surface is schematically shown.

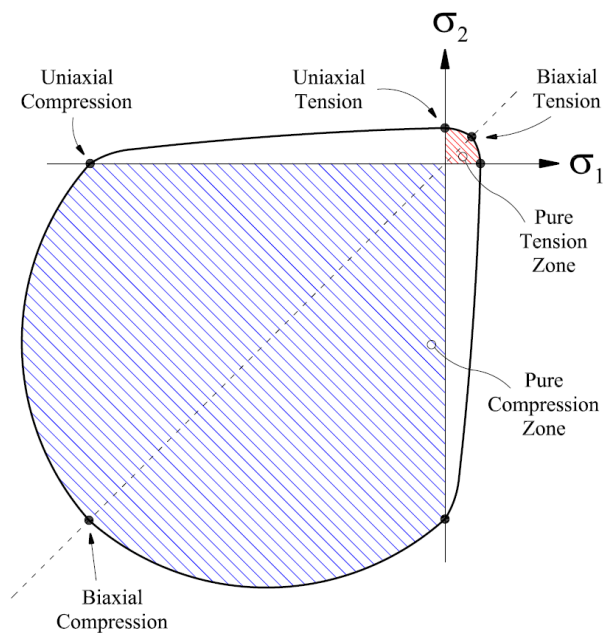


Figure 5.3. Yield surface in the plane stress for CDP model.

In this continuum and plasticity-based damage model, the failure mechanisms are split into two behaviors, either tensile cracking or compressive crushing. It is well-known that both uniaxial tension and compression responses for concrete are characterized by linear elastic branches up to the yielding points for each. Beyond this level, either instant softening due to micro-cracks (for tension) or a limited stress hardening and then followed by the softening (for compression) is observed. In CDP model, damages can be modeled at these stress softening branches through damage variables, d_c and d_t , representing stiffness degradation factors for compression and tension, respectively. These variables can take values starting from zero for representing the undamaged state, and go up to one that corresponds to the total strength loss condition, as given in Equation 5.6.

$$\begin{aligned} 0 &\leq d_c \leq 1 \\ 0 &\leq d_t \leq 1 \end{aligned} \quad (5.6)$$

The damages are actualized during unloading cycles by utilizing the aforementioned variables – d_c and d_t – for modifying the initial elasticity modulus of concrete (E_{ci}) in corresponding stress states, Equation 5.7. On the other hand, stiffness recovery factors – w_c and w_t – are also introduced for controlling the compressive and tensile stiffness recoveries in each loading reversal, respectively. These variables can also take values between zero and one as given in Equation 5.8, and the lower limit is set as default for the tensile effects assuming no strength recovery once cracks occur, whereas the upper limit was recommended for the compressive ones since closed cracks can still contribute to the material strength. A schematic uniaxial loading cycle is presented in Figure 5.4.

$$E_c = (1 - d_{c,t})E_{ci} \quad (5.7)$$

$$\begin{aligned} 0 &\leq w_c \leq 1 \\ 0 &\leq w_t \leq 1 \end{aligned} \quad (5.8)$$

Parameters of the uniaxial compression behavior are derived from the recommendations of Model Code for Concrete Structures (fib, 2010) up to the yielding level. This model can be divided into two phases; initial elastic part and following plastic hardening part until reaching the mean value of compressive strength f_{cm} , which is estimated by Equation 5.9, where f_{ck} is the concrete characteristic strength and Δ_f is a stress increment constant provided for normal type of concrete as 8 MPa. The strain value corresponds to this maximum strength is called ε_{c1} and beyond this point the code provides a limited strain increment formulation, though numerical analyses require an extended curve in order to enable successful

convergence. Therefore, third phase of the stress-strain curve was derived as proposed by Kratzig and Polling (2004). The ascending and descending phases of the compressive curve is defined in Equations 5.10-5.17, and shown in Figure 5.5.

$$f_{cm} = f_{ck} + \Delta_f \quad (5.9)$$

Initial elastic phase;

$$\sigma_{c(phase\ 1)} = E_{ci} \varepsilon_c ; (\approx 0.4 f_{cm}) \quad (5.10)$$

Stress hardening phase;

$$\sigma_{c(phase\ 2)} = -f_{cm} \left(\frac{k\eta - \eta^2}{1 + (k - 2)\eta} \right) \quad (5.11)$$

Where;

$$\eta = \varepsilon_c / \varepsilon_{c1} \quad (5.12)$$

$$k = E_{ci} / E_{c1} \quad (5.13)$$

Stress softening phase;

$$\sigma_{c(phase\ 3)} = \left(\frac{2 + \gamma_c f_{cm} \varepsilon_{c1}}{2 f_{cm}} - \gamma_c \varepsilon_c + \frac{\gamma_c \varepsilon_c^2}{2 \varepsilon_{c1}} \right)^{-1} \quad (5.14)$$

$$\gamma_c = \frac{\pi^2 f_{cm} \varepsilon_{c1}}{2 \left[\frac{G_{cl}}{l_{eq}} - 0.5 f_{cm} (\varepsilon_{c1} (1 - b_c) + b_c \frac{f_{cm}}{E_{ci}}) \right]^2} \quad (5.15)$$

Where; G_{cl} is the concrete crushing energy typically ranges between 200-500 times that of the G_{Fc} cracking (fracture) energy and l_{eq} is the characteristic length of the finite-element integration point. On the other hand, the parameter b_c represents the ratio of ε_c^{pl} compressive plastic strain to ε_c^{in} compressive inelastic strain as below and takes values between 0 and 1, Equation 5.16.

$$b_c = \frac{\varepsilon_c^{pl}}{\varepsilon_c^{in}} \quad (5.16)$$

$$0 < b_c \leq 1$$

That being said, the evolution of the damage variable d_c can be linked to the aforementioned parameters as in Equation 5.17. The uniaxial compressive stress-strain relation is shown in Figure 5.5.

$$d_c = 1 - \frac{\sigma_c E_{ci}^{-1}}{\varepsilon_c^{pl} (1/b_c - 1) + \sigma_c E_{ci}^{-1}} \quad (5.17)$$

The tensile behavior also consists of an initial elastic part that is followed by the softening regime upon first cracks. Nasiri and Liu (2017) proposed an equation derived from Maekawa et al. (2003), which takes into account the tension stiffening effects due to the presence of reinforcement. This is an important phenomenon for accurately representing the tensile behavior, since the cracked concrete can still carry tensile forces thanks to the plastic elongation of the reinforcement in the cracking plane. In order to include this effect, Equation 5.18 is proposed, where σ_t and ε_t are the tensile stress and strain defining the curve; σ_{ti} and ε_{ti} are the initial linear elastic stress and strain limits, respectively. Besides, it was reported that, this model is nearly independent of the finite-element size, crack configuration and reinforcement orientation. Damage evolution on the tensile regime is also introduced in a similar way mentioned above for the compressive behavior and given in Equations 5.19-5.20. Tensile behavior of the concrete is presented in Figure 5.6.

$$\sigma_t = \begin{cases} \varepsilon_t E_{ci}, & \varepsilon_t \leq \varepsilon_{ti} \\ \sigma_{ti} \left(\frac{\varepsilon_{ti}}{\varepsilon_t} \right)^{0.4}, & \varepsilon_t > \varepsilon_{ti} \end{cases} \quad (5.18)$$

$$d_t = 1 - \frac{\sigma_t E_{ci}^{-1}}{\varepsilon_t^{pl} (1/b_t - 1) + \sigma_t E_{ci}^{-1}} \quad (5.19)$$

$$b_t = \frac{\varepsilon_t^{pl}}{\varepsilon_t^{in}} \quad (5.20)$$

$$0 < b_t \leq 1$$

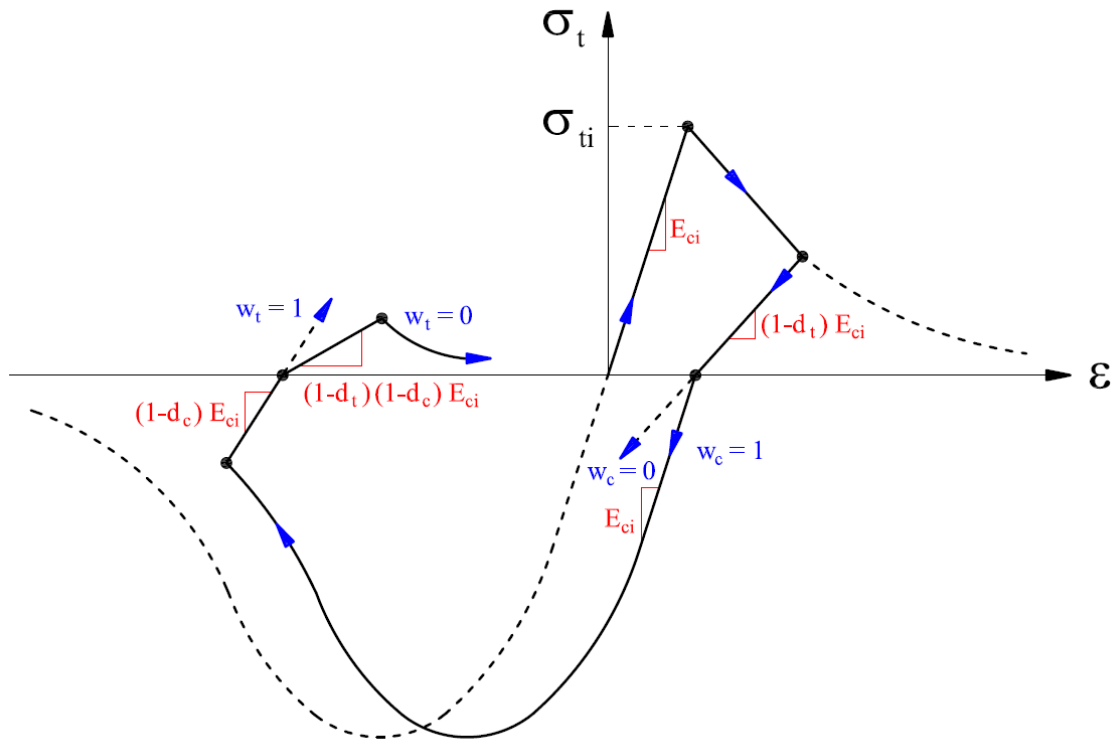


Figure 5.4. Uniaxial loading cycle for compression and tension in CDP model [adapted from ABAQUS (Dassault Systemes, 2016)].

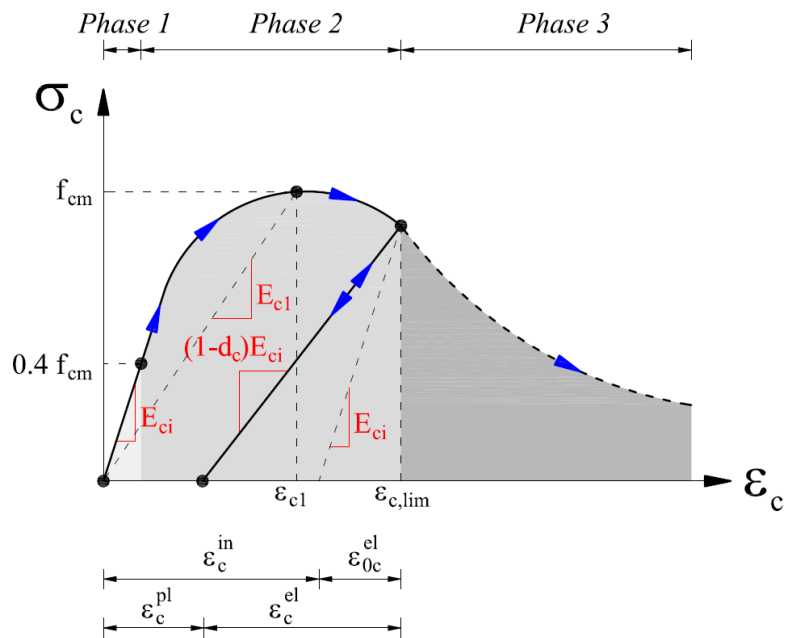


Figure 5.5. Uniaxial compressive stress-strain relation for concrete.

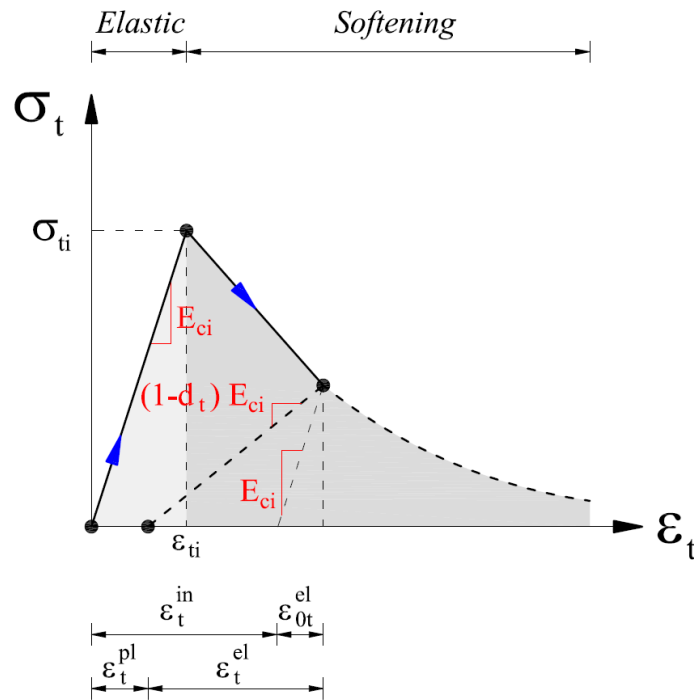


Figure 5.6. Uniaxial tensile stress-strain relation for concrete.

5.1.2 Steel reinforcement

In this study, steel bars are embedded in the concrete finite-element matrix. This approach is widely used while actualizing the reinforced concrete models, though it is also known that such assumption leads to restrict the potential relative displacements between the concrete and reinforcement elements, which in return alter the actual stress-strain behavior of bare steel bars. For example, the yield plateau does not appear in such models unlike the common expectation. Besides, the yield stress values are reached at the lower strength levels than the bare conditions (Nasiri and Liu, 2017). In order to take into account this bond-slip phenomenon, Dehestani and Mousavi (2015) developed a methodology that increases the equivalent bond strain and meanwhile it reduces the effective stiffness of the steel bars. Steel reinforcement constitutive model is created according to this assumption and utilized throughout the analyses.

The relation between the stress and strain values is very often represented by bilinear curves, where the stiffness changing point corresponds to the yielding strength of the steel bars – $f_{y,st}$. Aforementioned proposal claims that the actual yield strength of the embedded bars, $f_{y,st}^*$, can be calculated using a function called B_{st} , that is defined by the previously explained parameters $f_{y,st}$ and σ_{ti} as well as ρ_{st} the longitudinal reinforcement ratio, Equations 5.21-5.22.

$$\frac{f_{y,st}^*}{f_{y,st}} = (0.93 - 2B_{st}) \quad (5.21)$$

$$B_{st} = \frac{1}{\rho_{st}} \left(\frac{\sigma_{ti}}{f_{y,st}} \right)^{1.5} \quad (5.22)$$

Moreover, due to the stress concentrations on the bars in the vicinity of cracks, elasticity modulus is also modified as given in Equation 5.23, where δ_{st} and l_{st} stand for the maximum slip of the bars and the bonding transmission length respectively and formulated through Equations 5.24-5.32.

$$E_{st}^* = \frac{f_{y,st}^*}{\varepsilon_{st} + (\delta_{st}/l_{st})} \quad (5.23)$$

$$\delta_{st} = \frac{0.7315 + K_{st}}{5.176 + 0.3333K_{st}} \quad (5.24)$$

$$K_{st} = K_{co} + 33K_{st}^- \quad (5.25)$$

$$K_{co} = \frac{C_c}{d_b} \quad (5.26)$$

Where, C_c and d_b are the concrete cover and steel bar diameter, respectively. And the stirrup effect K_{st}^- is defined as a fraction of A_{st1} and S_{st} , which represent the one leg area of the stirrups and their spacing lengths respectively as written below;

$$K_{st}^- = \frac{A_{st1}}{C_c S_{st}} \quad (5.27)$$

In terms of the maximum slip of the bars – l_{st} , firstly the average space between the flexural cracks S_{rm} is defined, where ρ_{eff} shows the effective reinforcement ratio that is linked to the longitudinal bar area – $A_{st,l}$ and effective concrete area under working under tensile effects – $A_{c,eff}$. Considering the size effects on the cross-sectional dimensions of rectangular elements, different variations are formulated taking into account the total depth (h_{cs}), effective depth (d_{cs}) and width (b_{cs}) of the cross section.

$$S_{rm} = \left(\frac{2}{3} \right) \frac{d_b}{3.6\rho_{eff}} \quad (5.28)$$

$$\rho_{eff} = \frac{A_s}{A_{c,eff}} \quad (5.29)$$

$$A_{c,eff} = m_{cs}(h_{cs} - d_{cs})b_{cs} \quad (5.30)$$

$$m_{cs} = \begin{cases} h_{cs}/(h_{cs} - d_{cs}), & 0 \leq h_{cs}/(h_{cs} - d_{cs}) \leq 5 \\ 3.33 + 0.33h_{cs}/(h_{cs} - d_{cs}), & 5 < h_{cs}/(h_{cs} - d_{cs}) \leq 35 \\ 15, & 35 < h_{cs}/(h_{cs} - d_{cs}) \end{cases} \quad (5.31)$$

And finally, the transmission length can be defined as below;

$$l_{st} = \frac{0.67}{2} S_{rm} \quad (5.32)$$

Until now, the modified yield strength ($f_{y,st}^*$) and elasticity modulus (E_{st}^*) are elaborated, which are used for determining the elastic branch of the bilinear curve. After the yielding point, a plastic ascending regime is followed which has much lower tangential slope angle and assumed to be 3% of the initial elasticity modulus as per FEMA-356 (2000). The evaluation of this hardening modulus is given in Equation 5.33. The steel constitutive model is illustrated in Figure 5.7 with overall outlines.

$$E_{sp}^* = 0.03E_{st}^* \quad (5.33)$$

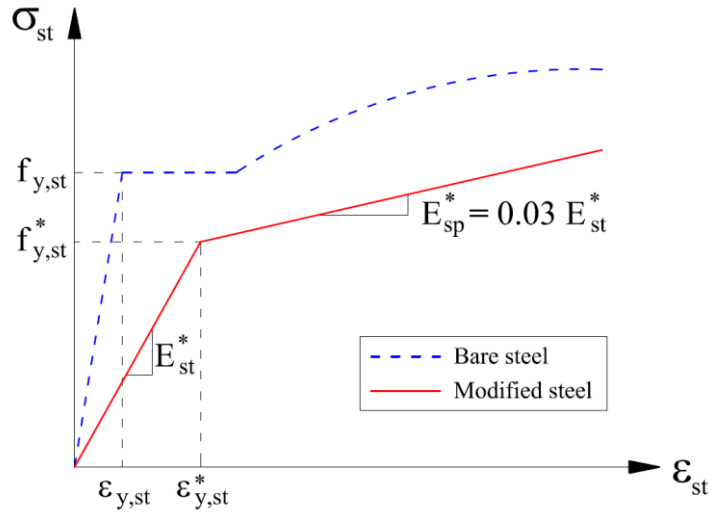


Figure 5.7. Steel reinforcement bar modified stress-strain relation.

5.1.3 Masonry infill

Infill walls are modeled using the combination of aforementioned smeared cracking approach of the CDP method for the continuum elements and the discrete scheme for the adjacent surfaces of different materials. In this way, the simplified micro modeling technique is utilized, see Figure 5.1. The methodology requires two different constitutive laws; firstly, compressive and tensile stress-strain relations are defined for the brick units. Half of mortar

thickness is also considered as a part of the extended brick unit length, since mortar is not directly modeled. However, discontinuity at the mortar joints is actualized by means of assigning interface properties on the brick-to-brick and brick-to-frame adjacent surfaces, where the second part of the constitutive law is performed. It should be noted that, the original bricks are perforated and normally would exhibit different mechanical behavior in the orthogonal directions. On the other hand, isotropic approach is followed in the numerical models while defining the material properties, which indirectly takes into account the masonry anisotropy by means of utilizing the information gathered from the diagonal wallet tests (see Section 4.1). The details are shared in Appendix B.

Because mortar is implicitly modeled in this technique, a stress-strain relation needs to take into account the effects of brick units and joints simultaneously. In this sense, it is wise to take advantage of some experimental results while defining a proper model. Kaushik et al. (2007) conducted several tests on the masonry prisms, where different type and strength of brick units and mortars were considered as the influencing parameters. Based on the experimental campaign, they established a compressive stress-strain relation for the masonry walls. In that proposal, only a few main parameters are sufficient for idealizing the curve, which is a great advantage as many of the other methods in the literature require relatively complex relations and more variables. Nevertheless, these are as follows; $f'_{m,c}$ for the masonry peak compressive strength, $\epsilon'_{m,c}$ is the strain value corresponding to the peak strength, E_m for the masonry elasticity modulus and C_j , that is factor depends on the mortar strength used at the joints f_{jm} . Some of these values can be directly obtained from the test results or from the building codes such as Eurocode-6 (CEN, 2005), whereas the authors suggested the below empirical equations which were validated through multiple regression analyses.

$$f'_{m,c} = 0.63 f_{br}^{0.49} f_{jm}^{0.32} \quad (5.34)$$

Where, f_{br} is the brick unit compressive strength obtained by the experiments.

$$\epsilon'_{m,c} = C_j \frac{f'_{m,c}}{E_m^{0.7}} \quad (5.35)$$

$$C_j = \frac{0.27}{f_{jm}^{0.25}} \quad (5.36)$$

And consequently, the relationship between the stress and strain values for defining the compressive curve can be written as below for the parabolic initial part – Equation 5.37, which

is followed by the linear softening regime until reaching the intersection point of $0.2f'_{m,c}$ and $2.75\varepsilon'_{m,c}$. This stress-strain relation is illustrated in Figure 5.8.

$$\frac{f_{m,c}}{f'_{m,c}} = 2 \frac{\varepsilon_{m,c}}{\varepsilon'_{m,c}} - \left(\frac{\varepsilon_{m,c}}{\varepsilon'_{m,c}} \right)^2 \quad (5.37)$$

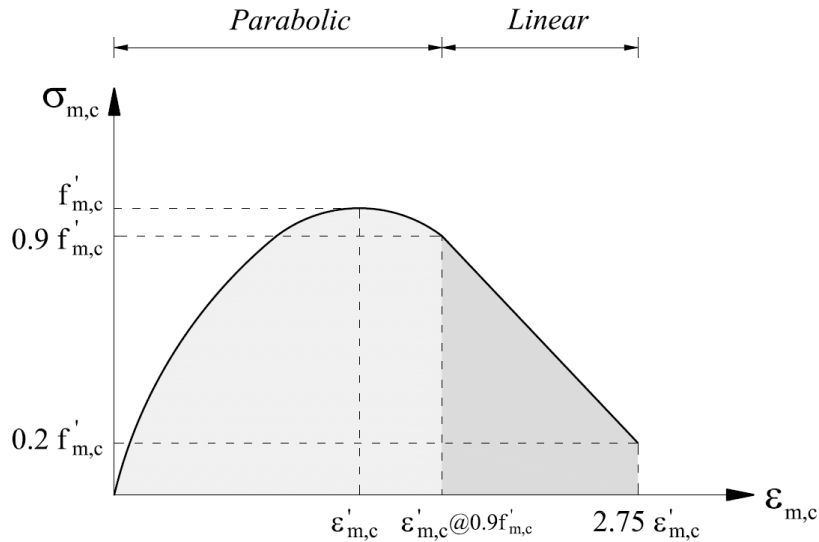


Figure 5.8. Stress-strain relationship for masonry compressive model.

Tensile stress-strain relation for the masonry is defined in a similar way of the concrete, namely an elastic branch until the fracture and beyond that point, an exponential softening is assumed representing the strength decay. Although it is difficult to determine the tensile strength of the masonry units, Schubert (1994) made a relation between the compressive and tensile capacities and found out that the ratio between the tensile and compressive strengths range between 0.03 and 0.12. Kubalski et al. (2017) also assumed this value to be approximately 10% of the compressive strength for the hollow clay units. The latter assumption is adopted for the numerical analyses and the ultimate tensile strength of the masonry – $f'_{m,t}$, is determined as a fraction of the compressive strength $f'_{m,c}$. Since the tensile capacity of the masonry structures are often represented by their total fracture energy capacities (G_{Fm}) that correspond to the area swept under the tensile stress-strain curve, iterative analyses are performed in order to find the most suitable value matching with the actual problem handled in this study. In this regard, the recommendations of Lourenco (1996) are referenced, where it was stated that the fracture energy for the clay or calcium-silicate made units typically range between 0.06 N/mm and 0.13 N/mm. Tensile stress-strain curve scheme is demonstrated in Figure 5.9. Moreover, the damage variables required for the CDP model are defined based on

the proposal of Munjal and Singh (2020) and given in Equations 5.38-5.39, where $d_{c,m}$ and $d_{t,m}$ denote the variables for the compressive and tensile regimes, respectively.

$$d_{c,m} = 1 - \frac{f_{m,c}}{f'_{m,c}} \quad (5.38)$$

$$d_{t,m} = 1 - \frac{f_{m,t}}{f'_{m,t}} \quad (5.39)$$

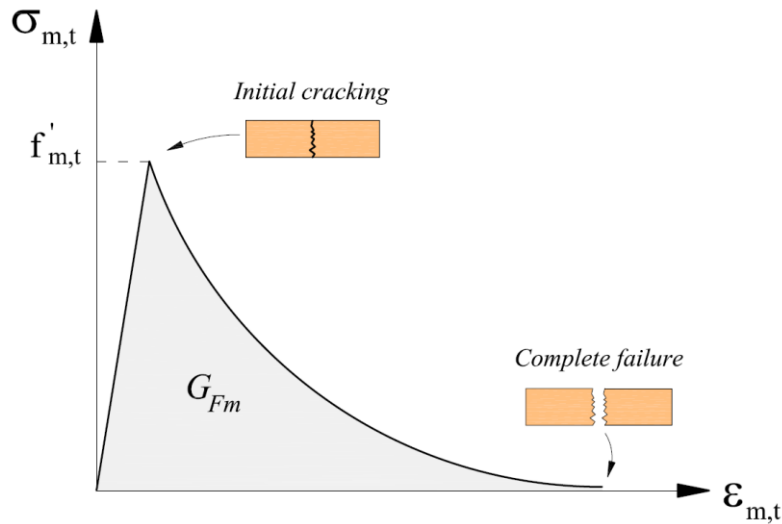


Figure 5.9. Stress-strain relationship for masonry tensile model.

As previously mentioned, the mortar joint is modeled implicitly. For this purpose, traction-separation feature of the ABAQUS (Dassault Systemes, 2016) is employed, which was primarily developed for the cohesive substrates. Since thin layer mortars are the concern of this study, surface-based interactions are utilized rather than the thick cohesive elements that are typically used for the glue-like materials. In this approach, initially linear elastic behavior is assumed until reaching the damage initiation criteria and it is followed by the damage evolution phase that can be modeled either linearly or exponentially. The failure can occur in three different directions, one to the interface normal and the other two parallel to it, as shown in Figure 5.10. Therefore, the traction stress vector of the joint (t_j) and corresponding separations (δ_j) have three components in these directions as well, Equation 5.40, where K_j represents the related terms in the cohesive stiffness matrix and subscripts d , s and t denote the normal and two orthogonal shear directions, respectively.

$$t_j = \begin{Bmatrix} t_{j_n} \\ t_{j_s} \\ t_{j_t} \end{Bmatrix} = \begin{bmatrix} K_{j_{nn}} & K_{j_{ns}} & K_{j_{nt}} \\ K_{j_{ns}} & K_{j_{ss}} & K_{j_{st}} \\ K_{j_{nt}} & K_{j_{st}} & K_{j_{tt}} \end{bmatrix} \begin{Bmatrix} \delta_{j_n} \\ \delta_{j_s} \\ \delta_{j_t} \end{Bmatrix} = K_j \delta_j \quad (5.40)$$

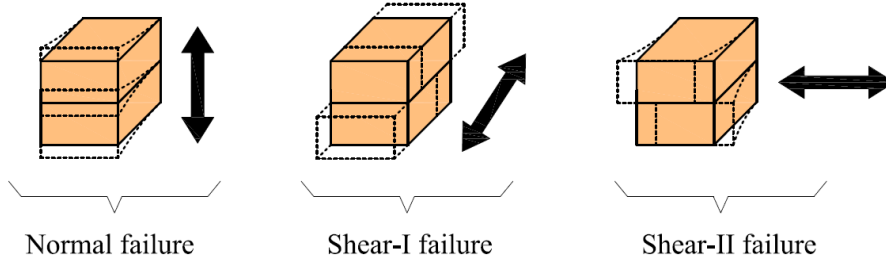


Figure 5.10. Possible failure types of the cohesive surfaces.

As per the uncoupled traction-separation law, where pure deformations in the normal and shear directions do not trigger forces on the others, the off-diagonal terms yield to zero. Hence, only the terms $K_{j_{nn}}$, $K_{j_{ss}}$ and $K_{j_{tt}}$ are sufficient to be defined. This approach is followed during the analyses due to its straightforward nature. Furthermore, shear resistance of the orthogonal directions in the same plane can be assumed as identical for the mortar joints in masonry structures, which results the strength and stiffness values for these directions to be same as well. That being said, Lourenco's (1996) proposal in Equations 5.41-5.42 is used for obtaining the stiffness matrix components, where E , G and h are the elasticity modulus, shear modulus and thickness, respectively. On the other hand, subscript br denotes brick units and jm stands for the masonry joints.

$$K_{j_{nn}} = \frac{E_{br}E_{jm}}{h_{jm}(E_{br} - E_{jm})} \quad (5.41)$$

$$K_{j_{ss}} = K_{j_{tt}} = \frac{G_{br}G_{jm}}{h_{jm}(G_{br} - G_{jm})} \quad (5.42)$$

In terms of the damage initiation, quadratic stress criterion is followed as given in Equation 5.43, which tells that combination of the traction stress states for the normal and two shear directions with respect to their pure peak values, $t_{j_n}^0$, $t_{j_s}^0$ and $t_{j_t}^0$, cause separation for the values greater than or equal to 1. It is also worth to mention that any type of pure compressive effects, either displacement or stress, do not initiate damages.

$$\left\{ \frac{t_{j_n}}{t_{j_n}^0} \right\}^2 + \left\{ \frac{t_{j_s}}{t_{j_s}^0} \right\}^2 + \left\{ \frac{t_{j_t}}{t_{j_t}^0} \right\}^2 = 1 \quad (5.43)$$

Once the damage initiation criteria are met, then the strength softening branch is followed either in a linear or exponential path, as already mentioned previously. Accordingly, it is possible to set the evolution limits either by displacement values or corresponding fracture energy that enclose the traction-separation curve area. In the post-failure state, friction effects (μ_{fr}) are activated which contribute the shear stress overall capacity proportionally to the confining stress. Other than that, various contact types are also possible to be modeled, of which the so-called hard contact is preferred in the analyses that enables the surface separation if the contact is loss, whereas no penetration is permitted among different surfaces. Traction-separation representative curve as well as illustration of the contact mechanisms are presented in Figure 5.11.

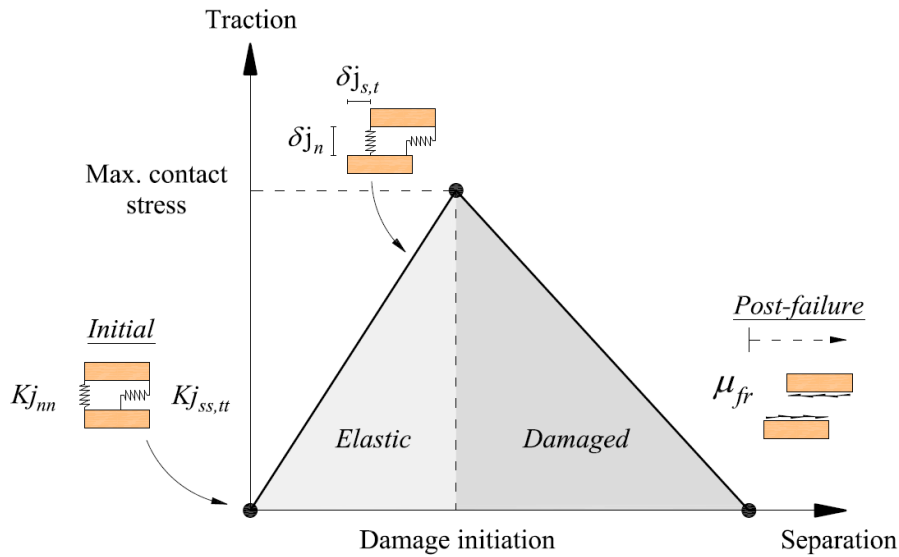


Figure 5.11. Traction-separation contact mechanism.

5.1.4 Polyurethane flexible joints (PUFJ)

In the comprehensive study of Kisiel (2018), four different well-known hyperelasticity models were investigated in order to find the most suitable one for the numerical calculations. These are; Mooney-Rivlin, second-degree polynomial, third-degree Ogden and Marlow forms. Upon performing bending, shear, compression and tension experimental tests on several specimens considering the size effects, empirical force-displacement relations were made. Using the information from these data, the Mooney-Rivlin form for compressible material in Equation 5.44 yielded the best results matching with the experimental ones.

$$U_{SE} = C_{10}(\bar{I}_1 - 3) + C_{01}(\bar{I}_2 - 3) + \frac{1}{D_1}(J^{el} - 1)^2 \quad (5.44)$$

Where, U_{SE} is the strain energy of per unit in the reference volume, the parameters C_{10} , C_{01} and D_1 are related to temperature dependent material properties, J^{el} is the elastic volume ratio, \bar{I}_1 and \bar{I}_2 are the first and second deviatoric stress invariants respectively and defined as;

$$\begin{aligned} \bar{I}_1 &= \bar{\lambda}_1^2 + \bar{\lambda}_2^2 + \bar{\lambda}_3^2 \\ \bar{I}_2 &= \bar{\lambda}_1^{(-2)} + \bar{\lambda}_2^{(-2)} + \bar{\lambda}_3^{(-2)} \end{aligned} \quad (5.45)$$

Where, the principle stretches of a compressible material, $\bar{\lambda}_i$, depends on the principal stretches of an incompressible material, λ_i , in different directions and linked to the total volume ratio, J ($J = 1$ for an incompressible material), as given in Equation 5.46.

$$\bar{\lambda}_i = J^{-1/3} \lambda_i \quad (5.46)$$

Finally, uniaxial compression and tension as well as planar tension tests were conducted on standard test dimensions suggested by ABAQUS (Dassault Systemes, 2016), see Figure 5.12. The information obtained from these results are directly utilized in this study.

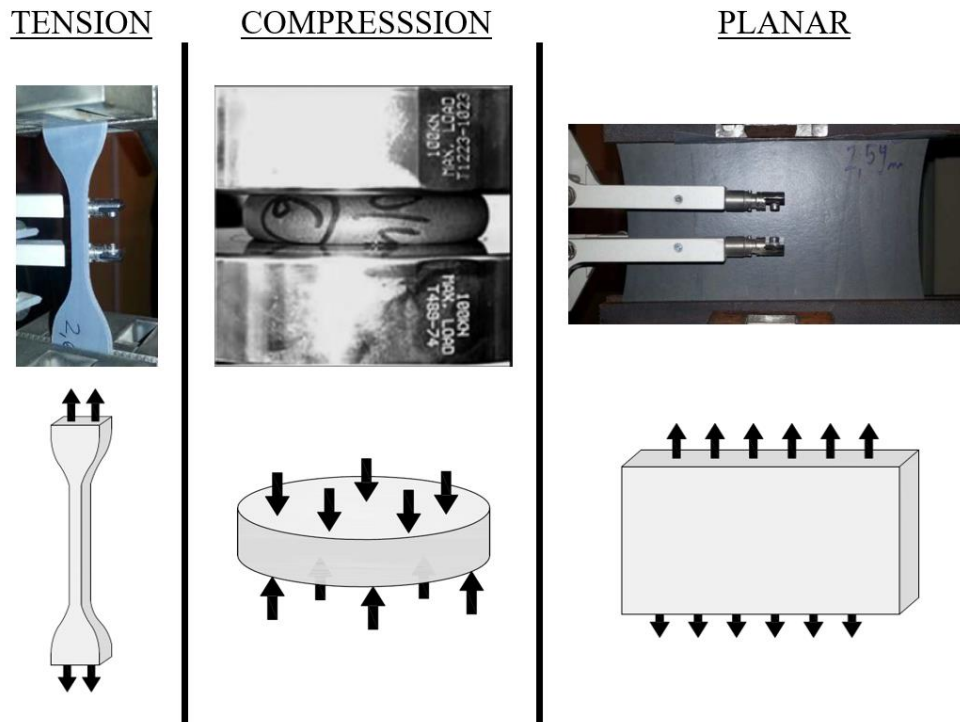


Figure 5.12. Plain polymer specimens testing visuals [adapted from Kisiel, 2018].

5.2 Analysis procedure

ABAQUS (Dassault Systemes, 2016) offers two different analysis engines for solving the time integration procedures, namely implicit and explicit. Either of these solutions can be used in variety of problems, but the main difference emerges from the algorithm of time

incrementation. Although both solvers use multiple points in a period of time and calculate the new state on the basis of conditions from the old one, the explicit algorithm can reach to a solution directly from the available data from the previous states using the central difference method. On the other hand, the implicit algorithm requires to handle nonlinear problems typically with the Newton-Raphson method. While the explicit analysis advances to next states by means of kinematic equilibrium calculations with very small time increments, the implicit one needs a large number of iterations. It is generally accepted that static or quasi-static analyses are more suitable for the implicit solver, since the integration rule is unconditionally stable which leads to obtain fast and reliable results for the smooth problems. In this sense, one may think that for civil engineering problems this algorithm is more suitable. However, convergence issues are very often encountered when dealing with nonlinear or contact problems, which is the case also in this study due to the fact that large displacements are the concern. Therefore, the explicit scheme is preferred which offers robust capabilities in order to overcome such obstacles. Since the solver is primarily designed for analyzing the short-term dynamic loads (e.g., blast or crash), its application to the current problem of this study needs to be calibrated properly. Basically, time has a physical meaning so that the solution becomes unstable if the time increment is too large. One possible way of estimating the required stable time increment Δt_{stable} for each step can be given as;

$$\Delta t_{stable} = \frac{L_{min}^e}{c_{dws}} \quad (5.47)$$

Where, L_{min}^e is the minimum characteristic element length, though using the shortest element distance does not necessarily provide conservative and reliable results. Therefore, iterative approximations may be needed. c_{dws} represents the wave speed of the material and determined using the Young's (elasticity) modulus E and mass density ρ , Equation 5.48.

$$c_{dws} = \sqrt{\frac{E}{\rho}} \quad (5.48)$$

In other words; shorter element lengths, higher Young's modulus and lower mass density complicate the analyses. In this regard, additional measures are considered throughout the analyses, such as enabling the double-precision option which causes higher computational time, but eliminating the rounding issues and thus gives more accurate results. Moreover, as an additional energy absorption mechanism, damping properties of the relevant materials can also be introduced to the program using the Rayleigh damping matrix C_{RD} , which is up to M_{RD} and

K_{RD} matrices that define the mass and stiffness features proportionally to the damping coefficients μ_{RD} and λ_{RD} respectively, as shown in Equation 5.49.

$$C_{RD} = \mu_{RD}M_{RD} + \lambda_{RD}K_{RD} \quad (5.49)$$

For different response frequencies – ω_i , damping ratio ζ_d can be written as the below function, Equation 5.50.

$$\zeta_d = \frac{\mu_{RD}}{2\omega_i} + \frac{\mu_{RD}\omega_i}{2} \quad (5.50)$$

5.3 Results of the numerical analyses

Numerical results are presented here under three subsections; namely small-size, quasi-static cyclic and dynamic analyses. All have the same modeling approach and material details, though slight changes are enforced to the models where necessary, such as modifications on the damping coefficients according to Equation 5.50 in order to relief the convergence issues and time scaling changes for preventing the noisy oscillations as much as possible. However, these interventions are rather related to the analysis procedure and the impact on the material constitutive models is kept at the minimum. In this sense, the details shared below are valid for the all models unless otherwise stated.

All structural elements are considered in three-dimensional space. Among these; concrete, brick and PUFJ are modeled with hexahedral solid (continuum) elements with the type of C3D8R, which is a first-order interpolation element and has a single integration point that accelerates the computations significantly compared to its full integration counterparts. However, enhanced hourglass control and second order accuracy options are enabled in order to reduce the mesh distortion and shear locking issues. Steel reinforcement was modeled differently, since the bars have a single dimension only through their lengths and the other dimensions are negligible. Therefore, two-node truss element with the type of T3D2 is preferred that can transfer only the axial loads and deformations. Furthermore, various mesh sizes are used depending on the element type. Accordingly, maximum meshing size for the concrete is set as 50 mm, which is in line with the smeared crack band width approach of Bazant and Oh (1983) where it was stated that heterogenous aggregate materials such as concrete exhibit the optimum crack band width approximately three-times that of the maximum aggregate size. Considering the aggregate sizes usually range between 16 mm and 32 mm for typical concrete, this assumption seems valid which was also proved elsewhere by Kytinou et

al. (2020). In order to make the steel bars to have the common nodes with the host region as well as for snapping the intersection points of the longitudinal and stirrup reinforcement, 50 mm mesh size is also determined for these elements. Since there is an available experimental data for the brick units provided in Chapter 4, preliminary mesh sensitivity analyses are conducted and it is concluded that 50 mm is suitable for those, too. Lastly, considering the reasonable stable time increment condition as defined in Equation 5.47, optimum density finer meshes are assigned to the PUFJ elements with the size of 10 mm, as the element thickness is much lower than the other ones. It is worth to mention that in the original study of Kisiel (2018), hybrid elements (C3D8H) were used which are primarily developed for the incompressible or nearly-incompressible materials. On the other hand, the explicit algorithm does not support this type in the element library, but for such cases specifically, ABAQUS manual (Dassault Systemes, 2016) recommends to use the enhanced hourglass controlling option for the hyperelastic materials, which is already enabled as mentioned above. Nevertheless, the mesh sensitivity analyses are also performed and given in Appendix A.

Material constitutive models explained in the earlier sections of this chapter are introduced to the computer program with the parameters as given in Tables 5.1-5.2. CDP parameters are taken as recommended by the program default settings, except the viscosity, which is adapted from the recommendations of Szczecina and Winnicki (2015). Regarding the steel reinforcement, E_{st}^* values calculated as proposed by Dehestani and Mousavi (2015) were found underestimating the results upon the preliminary analyses. Therefore, an arbitrary modification was done only for this parameter. Moreover, it is important to mention that true stress (σ_{true}) and true strain (ε_{true}) values are derived from the engineering stress (σ_{eng}) and engineering strain (ε_{eng}) values for all materials according to Equations 5.51-5.52, since these are the required input forms. Although this fact does not change the results of materials with relatively low deformation capacities, especially the steel members usually experience significant cross-sectional area changes. Moreover, the parameters for the brick-to-brick and brick-to-frame interfaces are defined either according to the triplet test results (shear damage criterion) or from the available information that can be found in the literature; namely normal damage criterion (Nasiri and Liu, 2019), plastic displacement evolution (Lourenco, 1996), friction coefficient – μ_{fr} (King and Pandey, 1978 and Nasiri and Liu, 2019). Determination of the stiffness values are already mentioned previously in Equations 5.41-5.42, where the mortar elastic modulus was calculated according to Kaushik et al. (2007). These values are given in Table 5.3. Other than that, the stress-strain relations of the materials are also presented in

Figures 5.13-5.15. Furthermore, the material properties of the polyurethane PM are presented in Table 5.4 with the input constants required in the numerical analyses. Using these values, one may extract the curves presented in Figure 5.15 easily by ABAQUS (Dassault Systemes, 2016).

In addition, Appendix B is provided for explaining further the calculation of the material properties. In this way, it is possible to reproduce the calculation steps and reach the same values, if one desires to follow the parameter obtaining process.

$$\sigma_{true} = \sigma_{eng}(1 + \varepsilon_{eng}) \quad (5.51)$$

$$\varepsilon_{true} = \ln(1 + \varepsilon_{eng}) \quad (5.52)$$

Table 5.1. Concrete and masonry material properties.

Material	Elastic Properties		CDP Properties				
	E [MPa]	Poisson ratio (ν)	Ψ	ϵ	σ_{b0}/σ_{c0}	Kc	Viscosity parameter (μ_{vis})
Concrete	35000	0.20	30	0.1	1.16	0.67	0.0001
Masonry	5100	0.25	30	0.1	1.16	0.67	0.0001

Table 5.2. Reinforcement steel material properties.

Material	Poisson ratio ν	Yield strength of bare steel $f_{y,st}$ [MPa]	Effective yield strength $f_{y,st}^*$ [MPa]	Elastic modulus of bare steel	Modified elastic modulus	Hardening modulus
				E_{st} [MPa]	E_{st}^* [MPa]	E_{sp}^* [MPa]
				Reinforcement Steel	200000	106205

Table 5.3. Traction-separation interface properties.

Tangential Behavior μ_{fr}	Normal Behavior Hard Contact	Stiffness [N/mm ³]			Damage			
		Kj_{nn}	Kj_{ss}	Kj_{tt}	Initiation [MPa]			Evolution
					tj_n	tj_s	tj_t	Plastic Disp. [mm]
0.70	Contact	658	267	267	0.40	0.88	0.88	0.50

Table 5.4. Polyurethane PM hyperelasticity properties.

Model	Material type	Poisson ratio (ν)	Material constants [Pa]		
			C01	C10	D1
Mooney-Rivlin	Isotropic	0.40	-51886	470475	5.11×10^{-7}

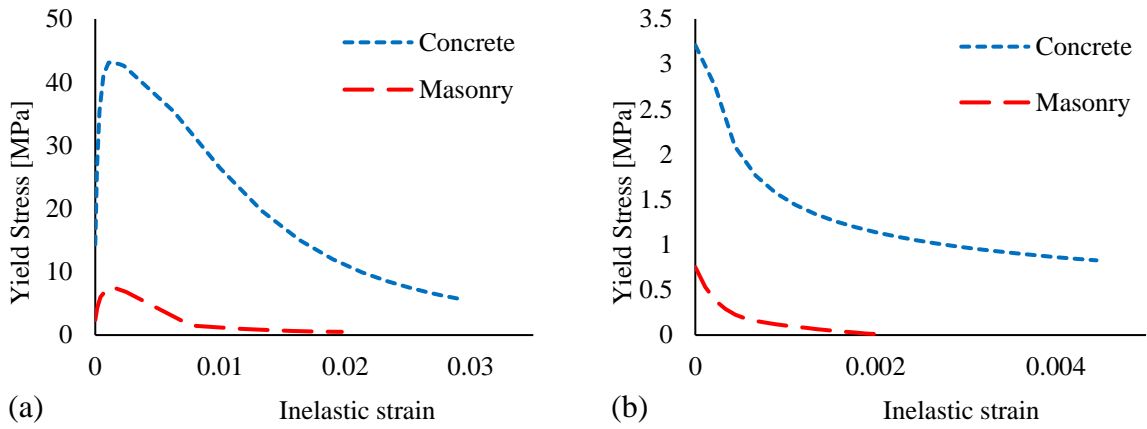


Figure 5.13. Concrete and masonry inelastic stress-strain curves; (a) compressive and (b) tensile.

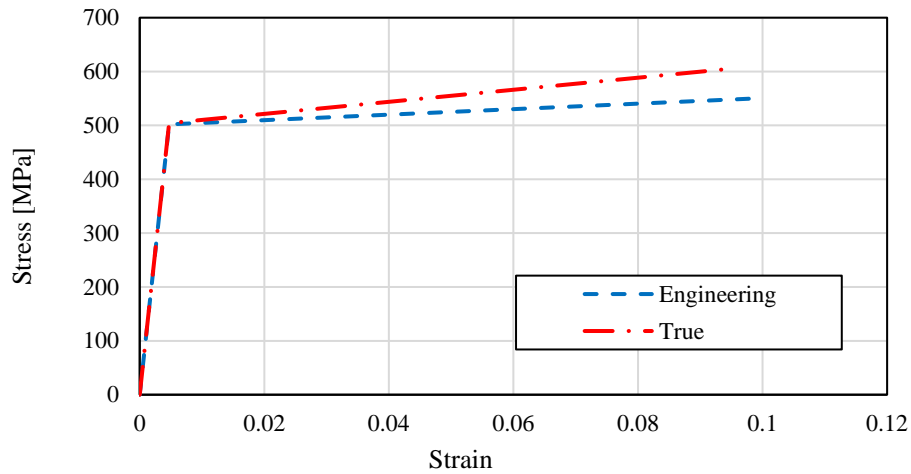


Figure 5.14. Reinforcement steel stress-strain relationship.

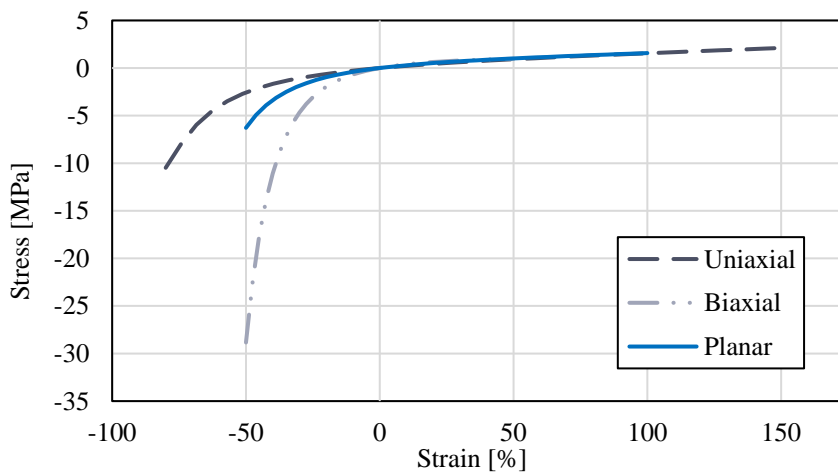


Figure 5.15. Polyurethane PM test results for plain specimens [adapted from Kisiel, 2018].

5.3.1 Small-size analyses

Before starting to model the large-scale specimens, triplet and wallet tests mentioned earlier in Sections 4.1.1 – 4.1.2 are numerically analyzed for calibrating the input parameters. For this purpose, compressive (horizontal and vertical), shear and diagonal wallet models are created. It should be noted that, the geometry of the brick units is simplified while modeling. This change is done in order to decrease the stable increment time during the analyses. Besides, relatively coarser meshing could be possible in this way. Because, the original geometry is not uniform and it contains too difficult details from the modeling perspective, Figure 5.16. That being said, the vertical hollows of the bricks are not modeled, but instead, the solid parts in the horizontal cross-sectional area are considered as a solid, single unity by means of reducing the brick thickness proportionally to the void ratio. Such approach was also implemented previously by Bolhassani et al. (2015) and close match with the experiments was observed. Nevertheless, the outer shell is measured as approximately 10 mm, whereas the inner webs are around 8 mm thick. The ratio of vertical voids to the gross area is close to 50%, thus the unit thickness is decreased by half and found as 50 mm. The simplification is illustrated in Figure 5.16.

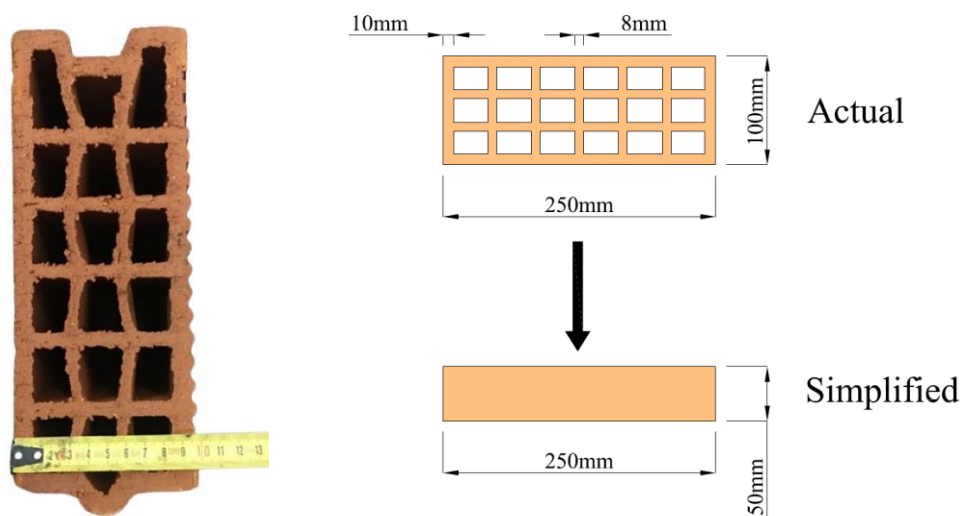


Figure 5.16. KEBE 100 type orthogonal hollow clay brick (left) and geometrical simplification for the numerical analyses (right).

The load-displacement results of the triplet specimens are presented in Figures 5.17-5.19. Average, maximum and minimum values of the tests are shown with black dotted horizontal lines, since no strain measurement was done for those during the experiments but force resistances were recorded. Numerical results are indicated with red curves and the peak

load levels are also marked with horizontal lines in the respective graphs. Deformation maps obtained from the numerical analyses are also given in terms of the logarithmic (true) strain values. Accordingly, vertical compression and shear analyses estimated peak values in a range of the test outcomes scatter, whereas the horizontal compression results over-estimated the peak values. One possible reason of this can be observed from the strain maps when comparing those with the actual failure mechanisms presented earlier in Chapter 4. Both vertical compression and shear analyses yielded close results with the actual tests, namely initial damage on the middle bricks and bond failure, respectively. On the other hand, disintegration of the outer shells which are seen in the experiments could not be modeled probably as a result of the geometry simplification, since no webs exist in the models that could be prematurely cracked. Nevertheless, overall masonry modeling is tested by means of comparing the diagonal compression tests with the numerical analysis, as shown in Figure 5.20. Although the actual failure type observed in the experiments (corner crushing of the units) diverged from the numerical results, where typical diagonal cracking is estimated, the load-displacement curves indicated reasonably close match with the actual ones. This situation is once again attributed to the aforementioned simplification, since the early corner crushing of the units were related to the weakness of webs, rather than the brick overall strength. In this regard, the analyses are proceeded to the large-size ones explained in the next sections.

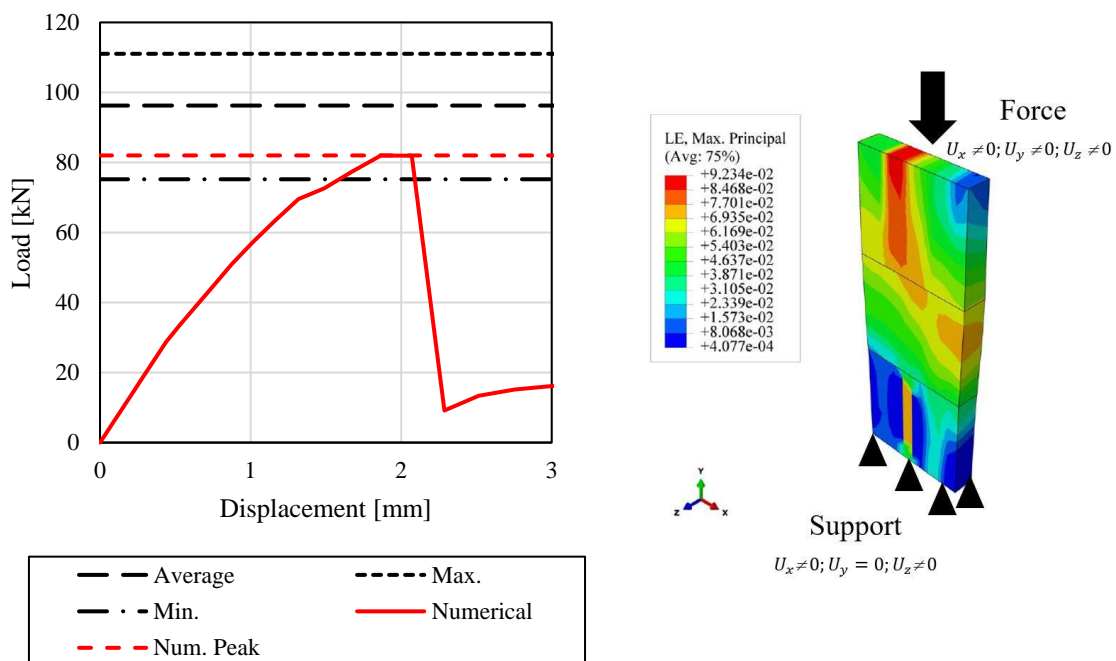


Figure 5.17. Triplet vertical compression test; load-displacement results (left) and numerical model (right).

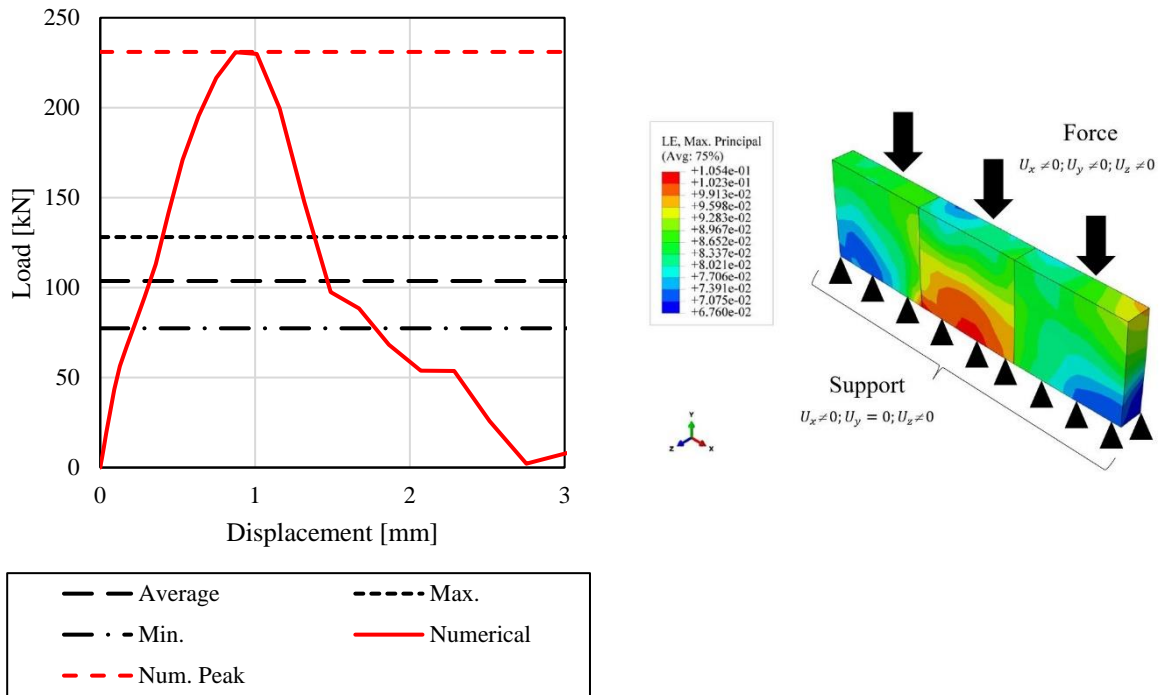


Figure 5.18. Triplet horizontal compression test; load-displacement results (left) and numerical model (right).

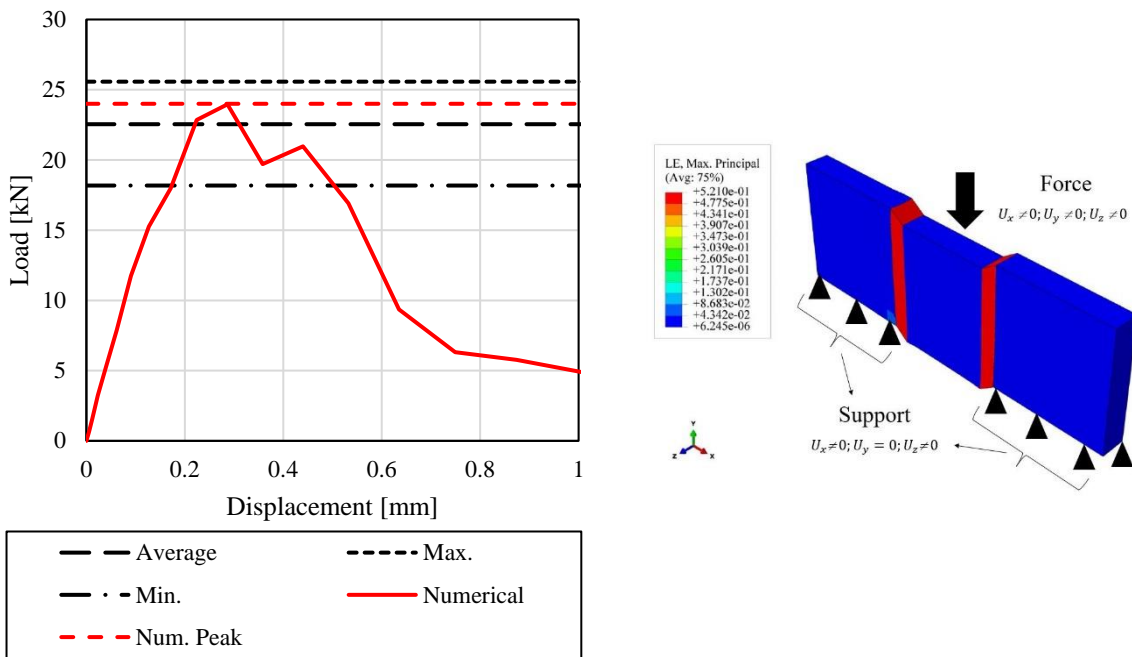


Figure 5.19. Triplet shear test; load-displacement results (left) and numerical model (right).

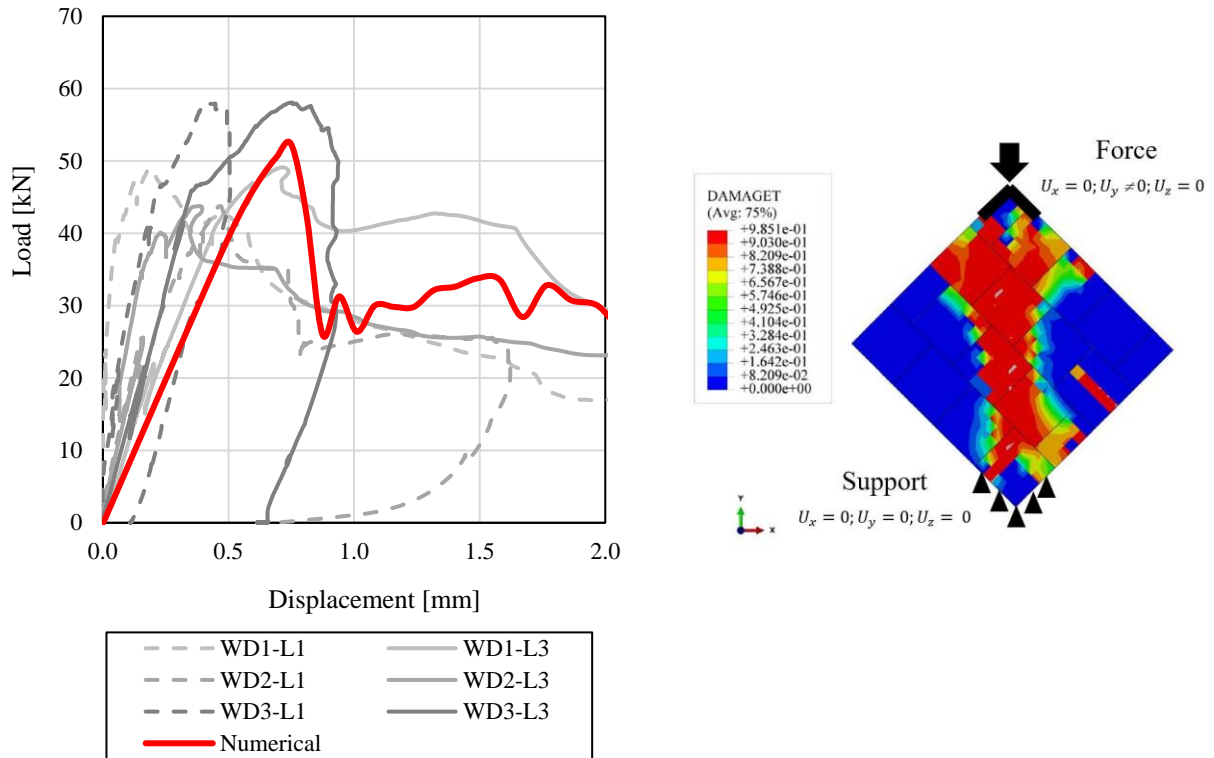


Figure 5.20. Wallet diagonal shear test; load-displacement results (left) and numerical model (right).

5.3.2 Quasi-static in-plane analyses

In this section, the large-size cyclic experiments performed on single-bay and story frames mentioned in Section 4.1 are numerically analyzed. All three frames, namely Frame A with the stiff connection and Frame B and Frame C with PUFJ, are exposed to the same loading conditions of the actual tests. In addition, Bare-Frame specimen is also modeled for the comparison purposes. The models are restrained at the bottom level with fixed boundary conditions. The vertical loads are defined on the top of columns and smoothly increased until the peak level in the first step of analyses. Later, the gradually increasing cyclic loads are enforced on the top beam level. In addition to the material nonlinearity that is assigned to the all critical parts where damages are anticipated (except the column and beam free ends as well as foundation), the geometrical nonlinearity (second order $P - \Delta$ effects) is also enabled in order to take into account the vertical loading induced effects. The cyclic load-displacement results are presented in Figures 5.21-5.24.

According to the load-displacement results; overall close match could be obtained particularly in the lower drift ratios, whereas over-estimations of the strength values were observed in the numerical analyses for the higher drift levels. In this sense, the main reason of

such difference could be attributed to the nature of the real test conditions, where the positive and negative loading results were diverged substantially. In contrast, the numerical analyses provided similar outcomes in either direction, since the imperfections regarding the real testing conditions do not exist in the computational environment. The details are shared below.

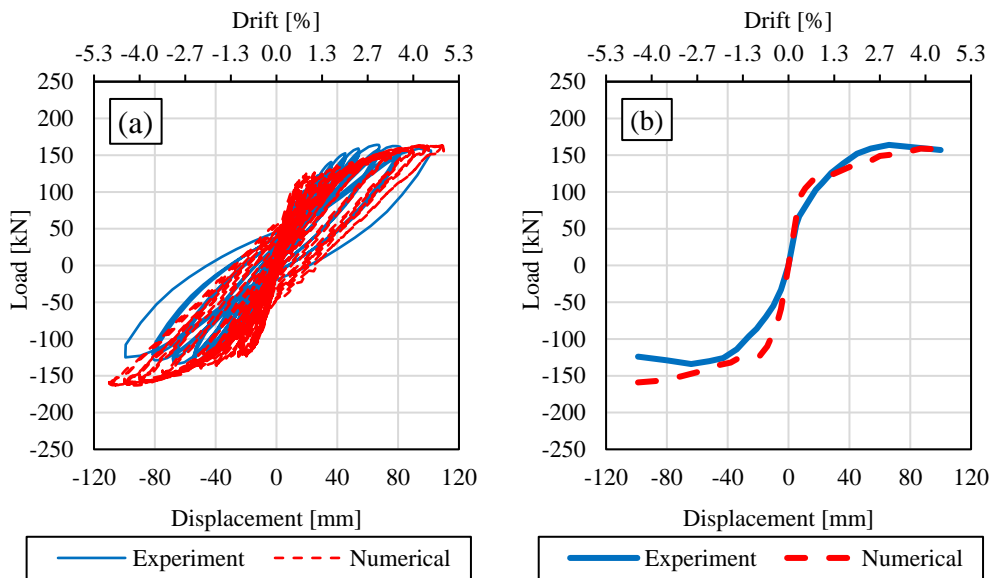


Figure 5.21. Bare-Frame cyclic loading results; (a) hysteresis loops and (b) envelope curves.

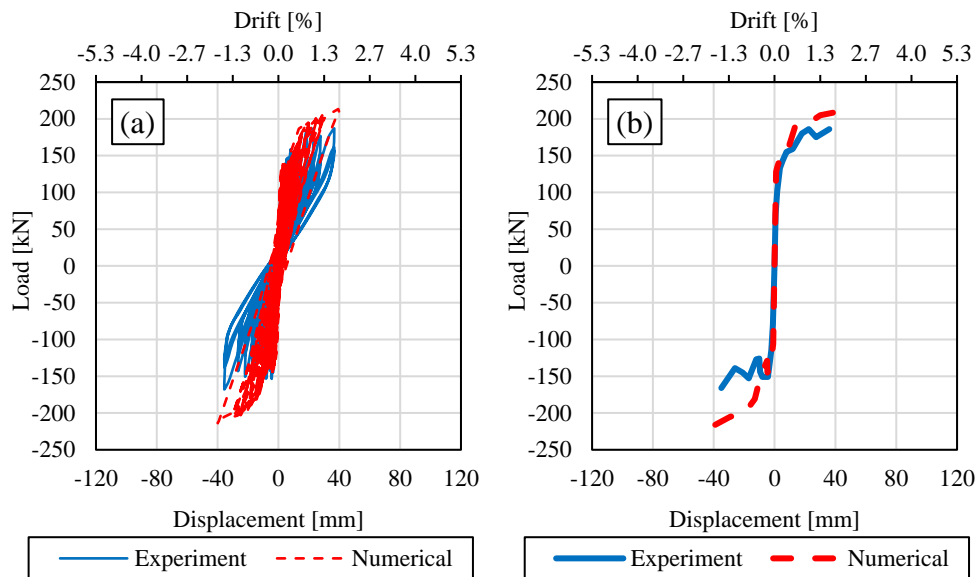


Figure 5.22. Frame A cyclic loading results; (a) hysteresis loops and (b) envelope curves.

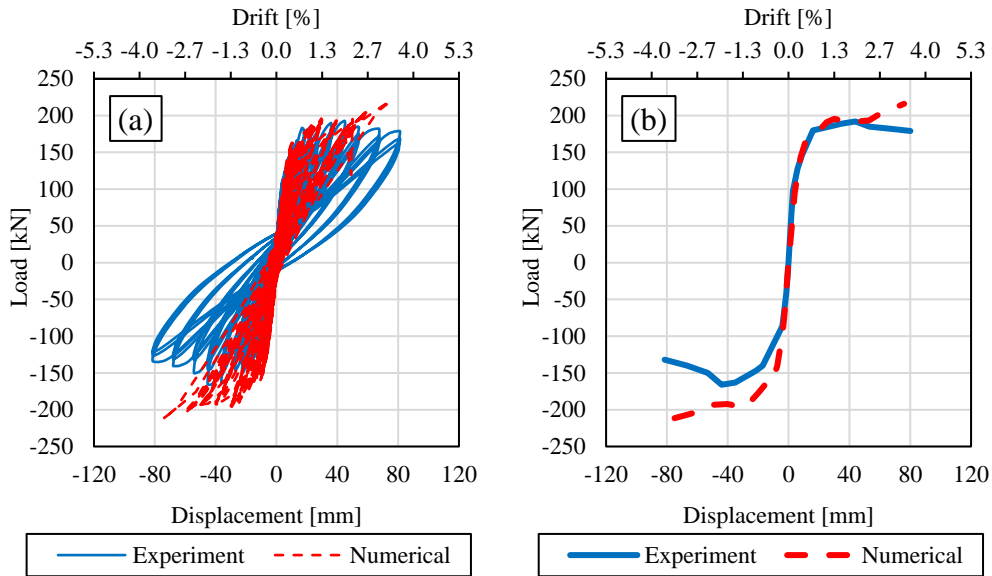


Figure 5.23. Frame B cyclic loading results; (a) hysteresis loops and (b) envelope curves.

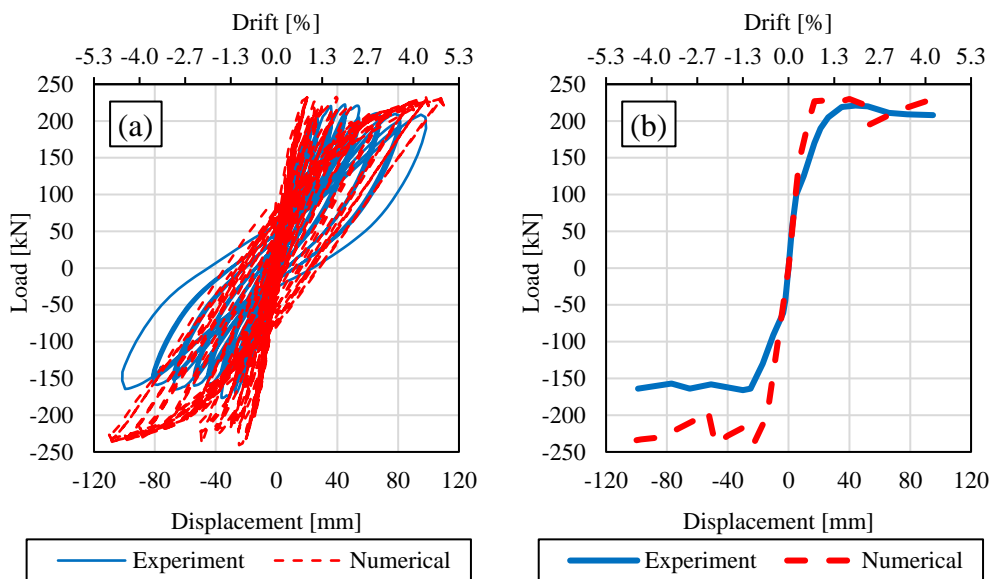


Figure 5.24. Frame C cyclic loading results; (a) hysteresis loops and (b) envelope curves.

First of all, Bare-Frame was modeled for calibrating the concrete and steel reinforcement properties with the actual experiments. Both in the positive and negative loading directions, numerical analyses exhibited stiffer behavior initially, though peak strength values converged well in the last stages for the positive direction with a marginal difference less than 1% at the ultimate displacement level. On the other hand, the numerical analysis, which yielded similar outcomes in the negative direction, reached to 159 kN loading response at the ultimate displacement point that was around 20% higher than that of the experimental one, 124 kN. In

terms of the general load-displacement trend, the experimental curve showed a slight strength decay at the higher drift ratios, whereas rather flat loading plateau was the outcome of the numerical results.

The numerical analysis of the Frame A is presented here until the drift ratio of 1.6% (approximately 40 mm lateral displacement), where the experiments were stopped at that point. The initial slope of the numerical envelope curve matched closely with the experimental one. After that point, once the yielding started, the numerical results over-estimated the strength capacity. At the ultimate drift levels, those differences were measured as 50 kN (23%) in the negative direction and 23 kN (12%) in the positive direction. Another visible difference was related to the swept area in each loading cycle, which is also about the stiffer outcome of the numerical model, since the experimental results plotted relatively larger loops.

Similar trend as of the Frame A was also observed for the Frame B, where the initial slopes of the numerical results in each loading direction followed similar paths with the experimental envelope curves until the yielding points. Beyond that, particularly the negative direction exhibited higher difference in terms of the load values at the late stages, which was measured as 79 kN (38%) at most in the negative direction, and 37 kN (17%) in the positive direction. Swept areas in the loading loops were also less in the numerical results due to the stiffer response in comparison to the experimental ones. Moreover, the softening trend of the experimental structure beyond 40mm lateral displacement (1.6% drift) could not be captured in the numerical model.

Frame C, which exhibited the highest strength capacity in the experiments, provided relatively closer numerical results when compared to the other infilled frames. Although the initial slopes were sharper in either loading direction, especially the positive envelope curve followed a similar path as of the experimental one. At the ultimate drift levels, the variations were 13 kN (6%) and 70 kN (30%) in the positive and negative directions, respectively. Furthermore, the regime of the loading carrying plateau beyond the yielding points could be achieved in the numerical results, which also presented no major strength drops. Different than the other infilled frames mentioned above, the swept areas were also alike, particularly in the positive loading direction.

Finally, the envelope curves of those are compared in Figure 5.25, where it is seen that the best performance could be achieved by Frame C, in terms of both strength and drift capacities. Frame A and Frame B provided relatively closer loading outcomes, though the lateral displacement was much enhanced with Frame B, thanks to the PUFJ presence. On the other hand, the lack of infills led to ductile and low strength response for the Bare-Frame.

Overall, the numerical envelope curves in Figure 5.25, indicate similar trend as of the experimental ones given previously in Figure 4.30.

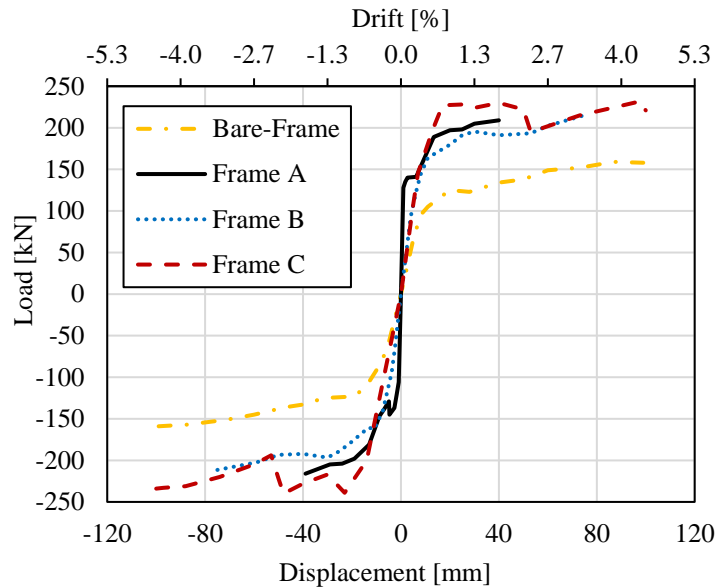


Figure 5.25. Envelope curves of the numerical analysis results.

Furthermore, damage visualization of the numerical results is represented in terms of the tensile damage variable – DAMAGET, which is a nondecreasing variable indicating the cracking status of the materials. In the color maps associated with this damage type, cold colors or damage variable 0 correspond to the uncracked condition whereas hot colors show the various cracking intensities up to the ultimate level, 1. In Figure 5.26, the damage statuses of the frames are given corresponding to the different lateral drift levels, which are chosen for the purpose of highlighting the distinguishable failure differences between those frames. Although the damage characterizations in the numerical models somewhat differ from those obtained in the experimental tests, the comparison between the joint types still provides an idea regarding the efficiency of the PUFJ implementation. Details are shared below.

Accordingly, at the 0.36% drift level all frame types received initial cracks in the vicinity of the ends of columns. Frame A also exhibited diagonally developing cracks on the masonry starting from the beam-column joints. Meanwhile, the infill wall of the Frame B experienced the first cracks in a limited portion of the wall, particularly at the bottom ends. A narrow stripe shaped vertical failure was also observed close to a column edge. On the other hand, no damage was present for the Frame C masonry. While the lateral drifts increased and reached to the 0.80%, initial cracks on the infill of Frame A became more visible and a diagonal shaped cracking appeared on the Frame B wall in addition to its intensified damages at the

initial failure zones. Frame C was nearly not affected with the increased drift level except minor cracks at the top corners of the wall.

Frame A masonry was disintegrated at the central zone when the drift level was doubled from the previous check point and reached to 1.60%. It is worth to mention that the experiment of the Frame A was terminated at this level, due to the wall instability issues mainly related to the frame-wall boundary contact failures. In this sense, it can be said that the failure point could be anticipated accurately in the numerical analyses, despite the difference of the damage type assumption. The PUFJ implemented frames also received visible damages on their masonries, particularly at the central zones, but also at the bottom specifically for the Frame B. However, wall stability of those could be sustained. Moreover, for all frame types, tensile cracks at the ends of columns started to spread along the column height.

Although the experiments were terminated at the different drift levels, 1.6% and 3.5%, for Frame A and Frame B, respectively, the numerical analyses continued for the all frames until the ultimate drift obtained during the experiments, 4.40% for Frame C. In this regard, Frame A numerical simulation indicated severe damages as the drift levels increased further, and total failure of the masonry at the ultimate point. Detachment from the surrounding frame was another visible concern beyond the drift level of approximately 2.0%. Frame B did not exhibit any bonding failures to the concrete members until the target ultimate level, whereas the connection loss was visible at this point through the bottom of wall due to the absence of PUFJ. On the other hand, implementation of PUFJ around the all edges of the Frame C masonry prevented bonding failures despite the extreme lateral drift demands. The masonry failures for both PUFJ implemented frames were concentrated at their central zones, whereas the damages of the Frame B were visible on a relatively larger portion of the wall surface.

Overall, for any type of frames, the numerical results could not capture the damage shape and its propagation with high sensitivity, since the corner crushes were the initial and dominant failure types for Frame B and Frame C observed during the experiments as mentioned in Section 4.1, though the numerical results indicated diagonally developing failures and severe damages at the central parts of the walls. This difference is mainly attributed to the nature of brick simplification process which was also mentioned previously in this chapter while discussing the small size numerical results.

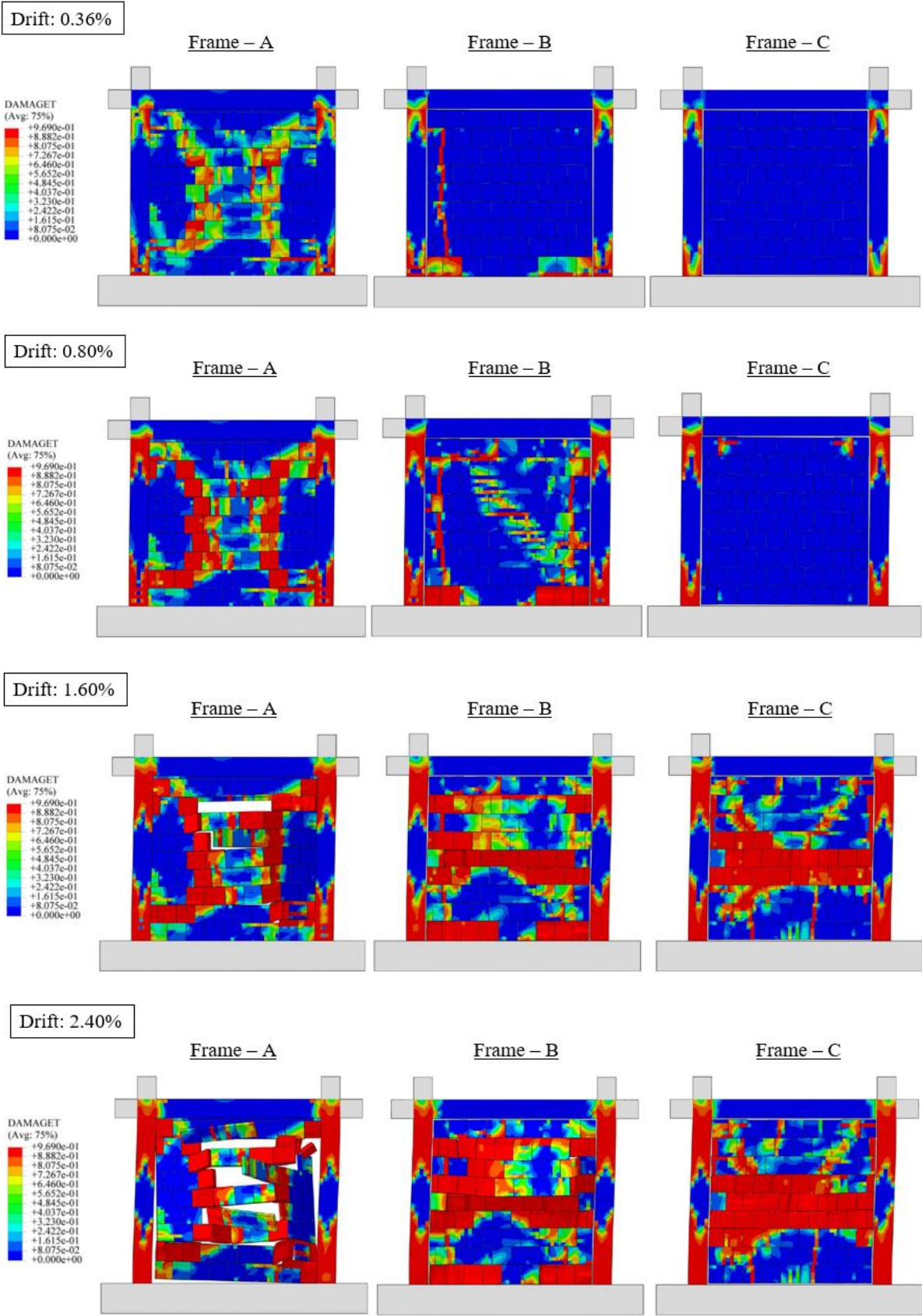


Figure 5.26. Damage visualization of the quasi-static numerical models at the different drift levels.

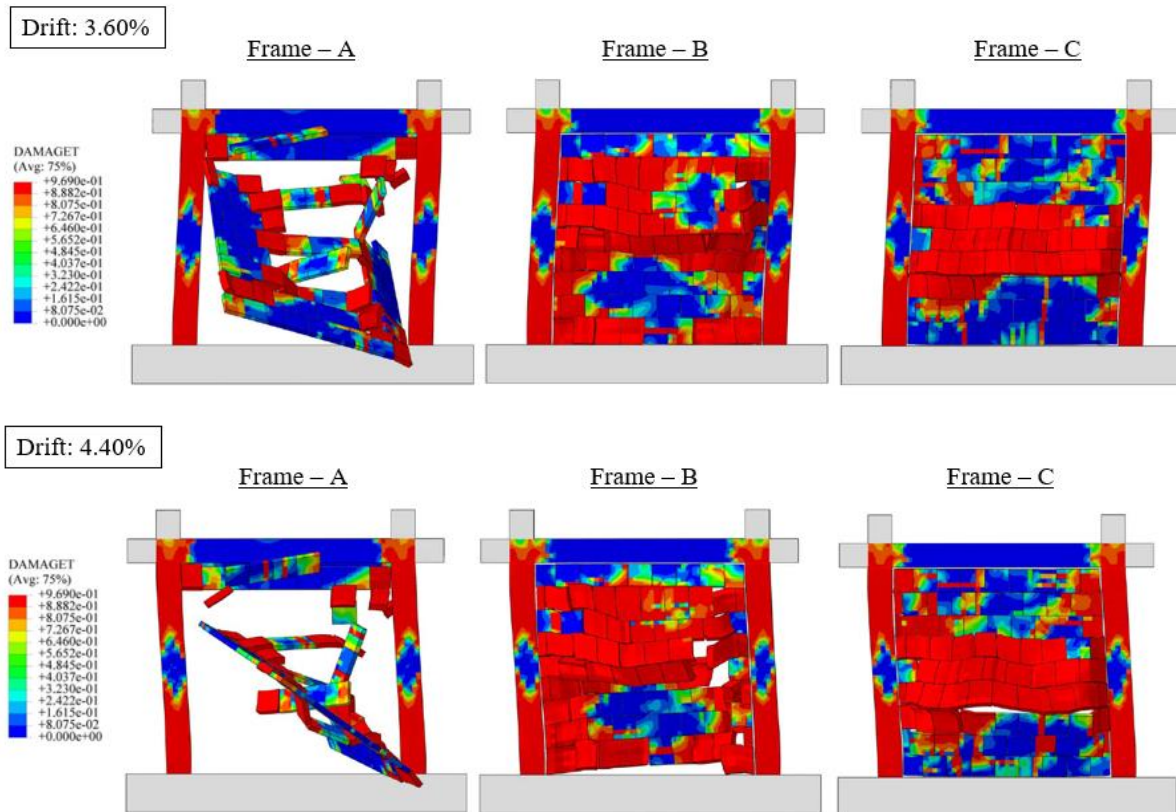


Figure 5.26. (continued).

5.3.3 Dynamic analyses of the three-dimensional building

This section is dedicated to simulate the dynamic response of the single-story building tested experimentally in Section 4.2. The original experiment consisted of a series of shake-table and vibration tests, which are practically very difficult to modeling from the numerical analysis perspective. The main obstacles are related to the length of the original excitations and the nature of the explicit solver algorithm implemented as the modeling strategy. That being said, several assumptions are made which differ the analyses from the original experiment. These are shared below;

- Only the initial strong motion part from the original accelerogram is extracted, namely the first 8 seconds. In this way, the original record time could be reduced by around 70% without neglecting the highest acceleration peaks, Figure 5.27.
- While the experiment was done on a single building following sequential stages due to the financial and time limitations, the numerical analyses comprised of various buildings including bare-frame, traditionally infilled and PUFJ implemented models. Therefore, multiple scenarios could be observed independently which enabled to compare between different construction techniques.

- Accordingly, the different models were evaluated and benchmarked in terms of their acceleration, force reaction and relative displacement (drift) responses.
- FRPU seismic intervention solution was not included in the numerical analyses, since it does not particularly fall in the scope of this study and detailed modeling of this method requires further experimental tests in order to execute reliable calibrations.
- All numerical models were created using the material and geometrical nonlinear features except the bottom support beams and top slabs, where practically no damage is expected. In other words, only the columns and relevant steel rebars of the RC frames were assigned the nonlinearity due to the fact that plastic hinges are mostly likely the concerns for these parts and the experimental results also confirm this phenomenon, see Section 4.2.
- The same concrete properties of the in-plane analyses are used, although the concrete class in the original dynamic experiments is slightly less than the in-plane ones (for columns) as mentioned earlier. However, this detail is omitted in order to provide a constant material type across all analyses for reducing the complexity of parameters.

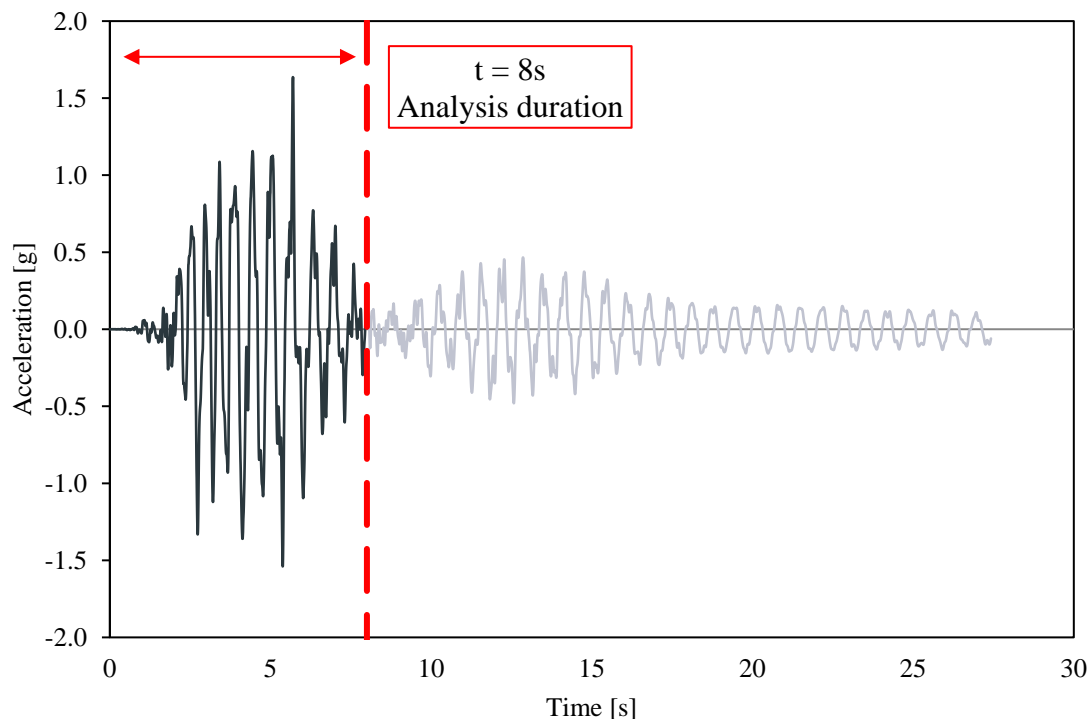


Figure 5.27. Reduced seismic record for the dynamic analyses.

In total four 3D models were created for the numerical analyses; two of those were the PUFJ implemented frames for simulating the similar conditions of the experimental tests mentioned earlier in Section 4.2. Following the experimental sequence, firstly Type B infill walls were excited through their in-plane directions while the Type C ones received the out-of-plane forces. The identical model in the intact condition was rotated 90 degrees about the vertical axis in a way that Type C walls were resisting the in-plane excitation this time whereas Type B walls were positioned against the out-of-plane loading. Since the models were identical in terms of the geometrical and mechanical features but the loading directions were the only difference, the PUFJ implemented models were labeled as PUFJ – 0 and PUFJ – 90, respectively, for denoting the specific perpendicular loading directions that they were exposed. It should be emphasized that the experiments were done merely on a single building and the specimen was already damaged before the rotating process. In this sense, only the PUFJ – 0 numerical model is a representative of the actual experiment, though some differences still exist. For instance, Phase I of the experiment was interrupted with a sudden shake-table malfunction as mentioned in Section 4.2, whereas the numerical models are exempted of such concerns. Other than that, the seismic record duration was reduced for the numerical models. The other two models were designed to reflect the reference conditions, such that traditional stiff mortar was utilized in one of those as a bonding material between the frame and masonry members instead of PUFJ and called TRM model. And the last one was a bare-frame without the walls in order to investigate the infill influence on such buildings and labeled as BF model. Figures 5.28-5.31 present the numerical analyses results of the all models in terms of the displacement outcomes of the bottom and top parts of the models and their respective relative lateral drifts were calculated accordingly. Reaction forces and acceleration results obtained from the bottom and top parts of the models are also given, respectively. Moreover, in Figure 5.32, the comparative plots are provided for the different models and the peak values of those are given in Table 5.5. The findings are shared below.

The so-called representative of the initial phase of the experiments, PUFJ – 0, reached to the peak drift ratio of 3.31% at 5.45 seconds. The highest drift ratio from the experiments was measured as 3.7%. In this sense, the numerical results slightly underestimated this value. On the other hand, it should be noted that the reduced seismic record might lead to such outcomes, since the specimen in the actual tests was exposed to the longer duration of loading which may alter the hysteresis behaviors of the materials. Besides, the experiment was suddenly stopped and initiated again that could cause further complications that are difficult to be observed in the numerical environment. Nevertheless, the numerical results still seem to be

reasonably close to the experiment despite several simplifications and assumptions. The maximum drift values of the PUFJ – 90 and TRM models were calculated as 1.89% and 3.67%, respectively. In any case, the PUFJ implemented models exhibited less values, since the walls were protected relatively better when compared to the TRM model. This can be observed from Figure 5.32a, where it shows that TRM model initially behaved stiffer than the others, yet lost its strength after a while as a result of severe infill and contact failures. Furthermore, substantial difference among the PUFJ models could be attributed to the flexible joint configurations, where 3-edge flexible jointed Type B walls were resisting against the in-plane forces in PUFJ – 0 model while the walls were surrounded by the entire perimeter in Type C walls of the PUFJ – 90 model against the in-plane forces. Apparently, the latter technique triumphs over the first one which is in line with the overall findings of this dissertation, since Type C walls were visibly better performing than the any others as presented in Section 4.1. On the other hand, the BF model failed to stay in the limits of reasonable drift levels for such systems (considered here as above 4%) beyond the first half of the excitation time (after ≈ 4.25 seconds). Practically, the system would be totally collapsed in a real-life scenario.

The reaction forces yielded rather expected results, since the PUFJ – 0 and PUFJ – 90 models exhibited similar peak values as 726 kN and 755 kN, respectively. The stiff nature of the TRM model led to higher peak value than the others with 883 kN, though Figure 5.32b shows that both PUFJ models and the TRM model came up to the similar levels during the second half of the excitation. This is another sign of the sudden failure potentials of the stiff mortar implemented systems. The BF model could resist much lower forces, at most 263 kN, due to the lack of additional loading carrying system, namely the infill walls.

The acceleration results also indicate similar outcomes for the PUFJ implemented models, as 1.96g and 2.07g for the PUFJ – 0 and PUFJ – 90 models, respectively. The stiff behavior of the TRM model could also be observed from these results that the peak acceleration value was the lowest among the infilled models, 1.50g. On the other hand, the BF model exhibited relatively lower acceleration values than the all others, on the top slab level with 1.47g. Because, the system was not able to withstand until the end of seismic loading (only until 4.25 seconds, before the PGA point is reached), see Figure 5.32c.

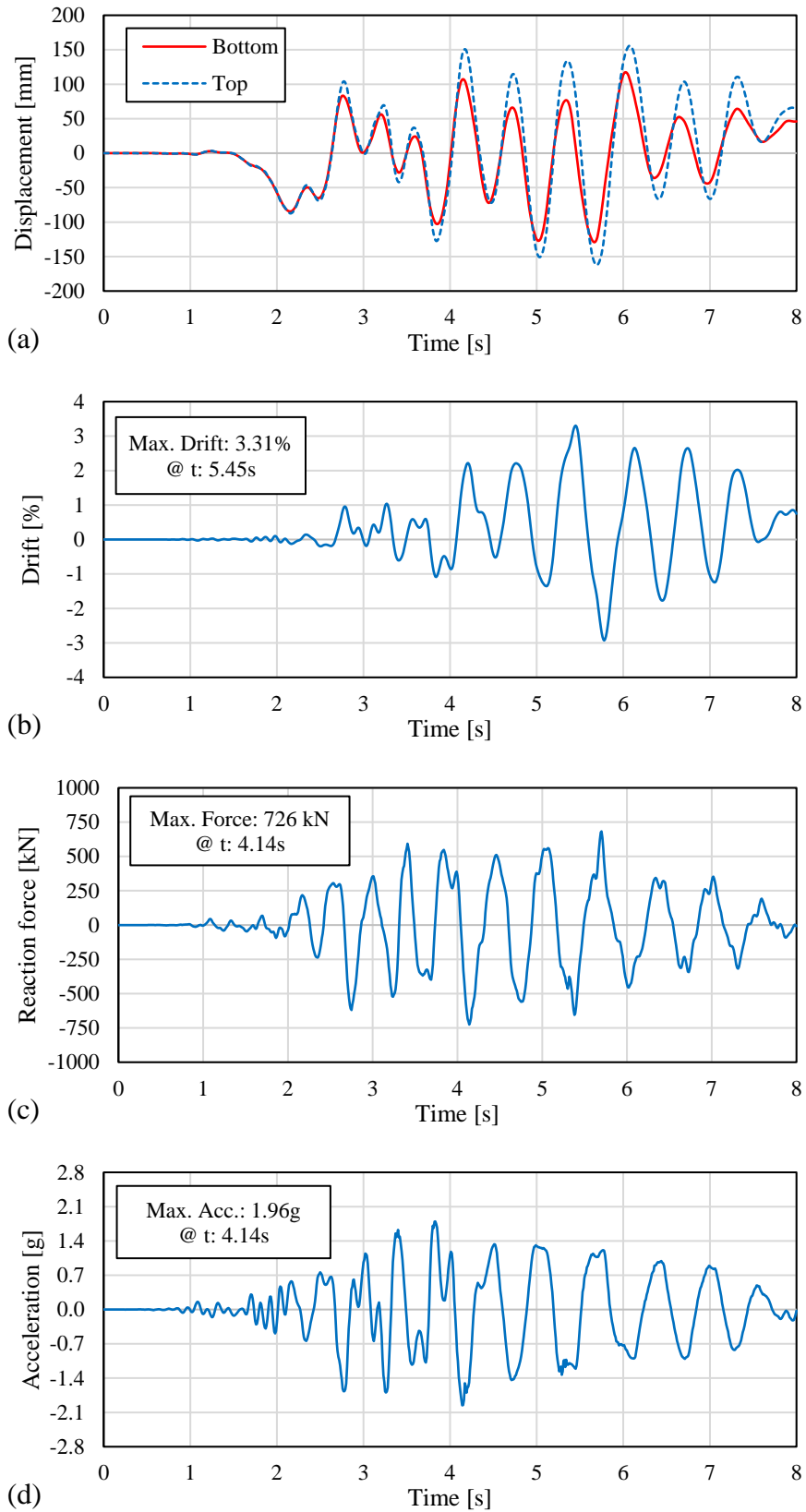


Figure 5.28. Dynamic analysis results of the PUFJ – 0 model; (a) displacement, (b) drift, (c) reaction force and (d) acceleration.

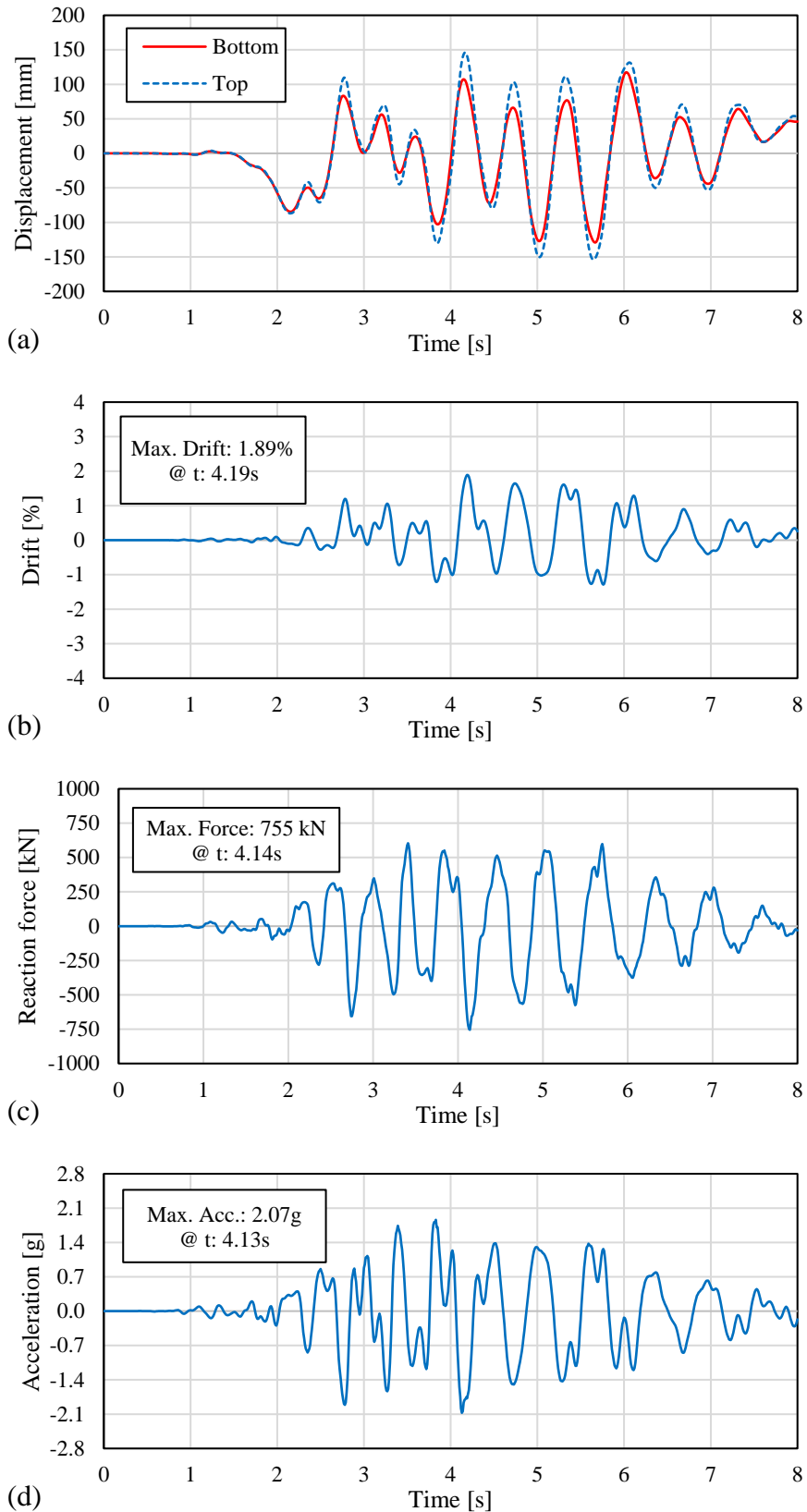


Figure 5.29. Dynamic analysis results of the PUFJ – 90 model; (a) displacement, (b) drift, (c) reaction force and (d) acceleration.

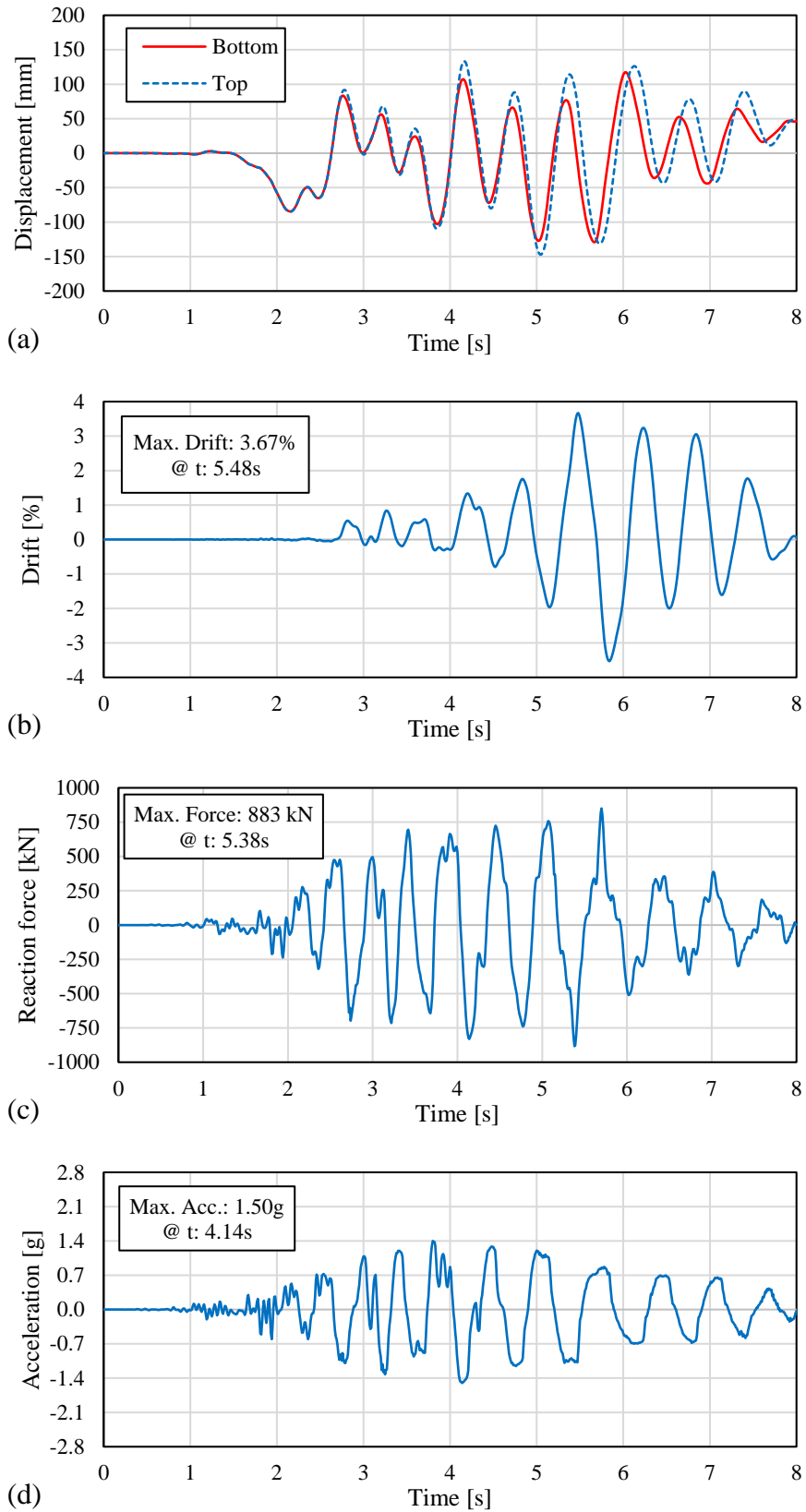


Figure 5.30. Dynamic analysis results of the TRM model; (a) displacement, (b) drift, (c) reaction force and (d) acceleration.

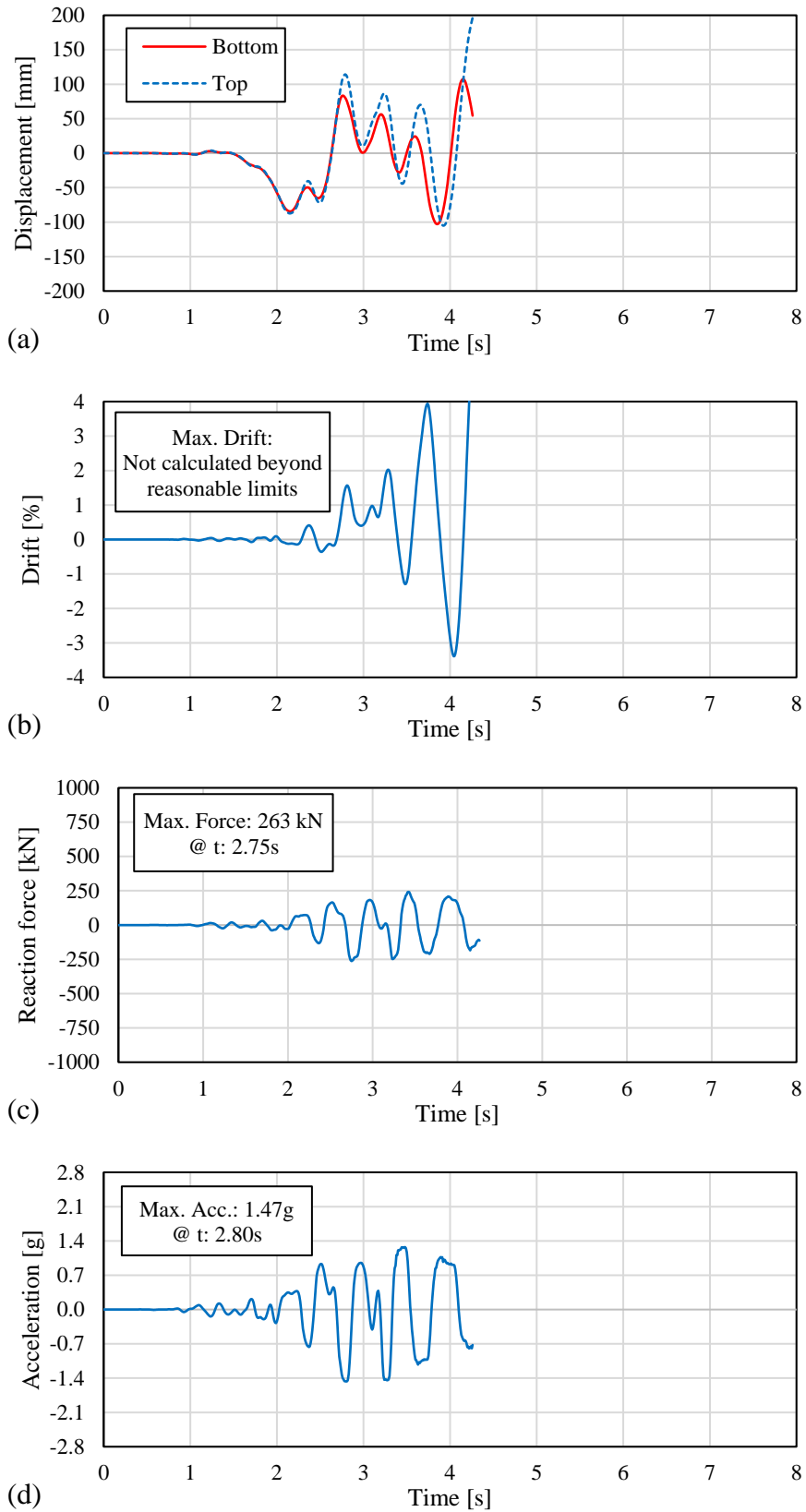


Figure 5.31. Dynamic analysis results of the BF model; (a) displacement, (b) drift, (c) reaction force and (d) acceleration.

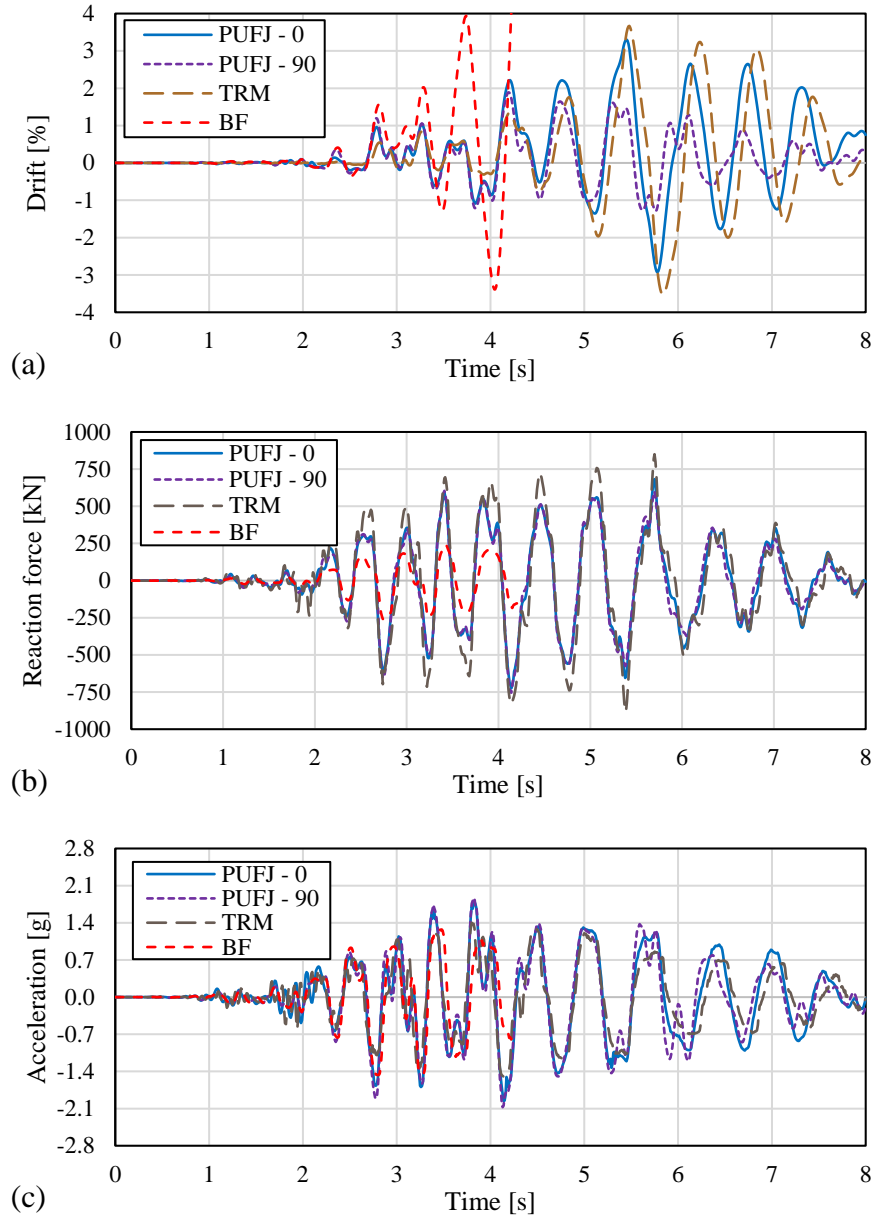


Figure 5.32. Comparison of the dynamic analysis results (a) drift, (b) reaction force and (c) acceleration.

Table 5.5. Dynamic analysis results of the all models.

	PUFJ - 0	PUFJ - 90	TRM	BF
Max. Drift [%]	3.31	1.89	3.67	-
Max. Reaction Force [kN]	726	755	883	263
Max. Acceleration [g]	1.96	2.07	1.50	1.47

The damage patterns of the numerical models are also investigated as shown in Figures 5.33-5.36. Although the numerical models differ from the original experiments to a certain extent, the damage evolution of the most experiment-like model of this study, namely

PUFJ – 0, exhibited similar masonry failure characteristics as of the shake-table tests mentioned in Section 4.2. The cracks were formed on the in-plane resisting masonries, emerged from the column edges and developed through the panel central zones. Despite the perfect symmetrical conditions against the loading direction, the damage patterns were different for the back and front views of the walls. This situation is also observed in the other models and attributed to the nature of dynamic forces which very often contribute to the inertia related additional torsional effects. Nevertheless, particularly the in-plane back view of the PUFJ – 0 model given in Figure 5.33 shows similarities regarding the failures observed at the end of Phase I of the experiments, where the “H” shape damages were the subject, see Section 4.2.

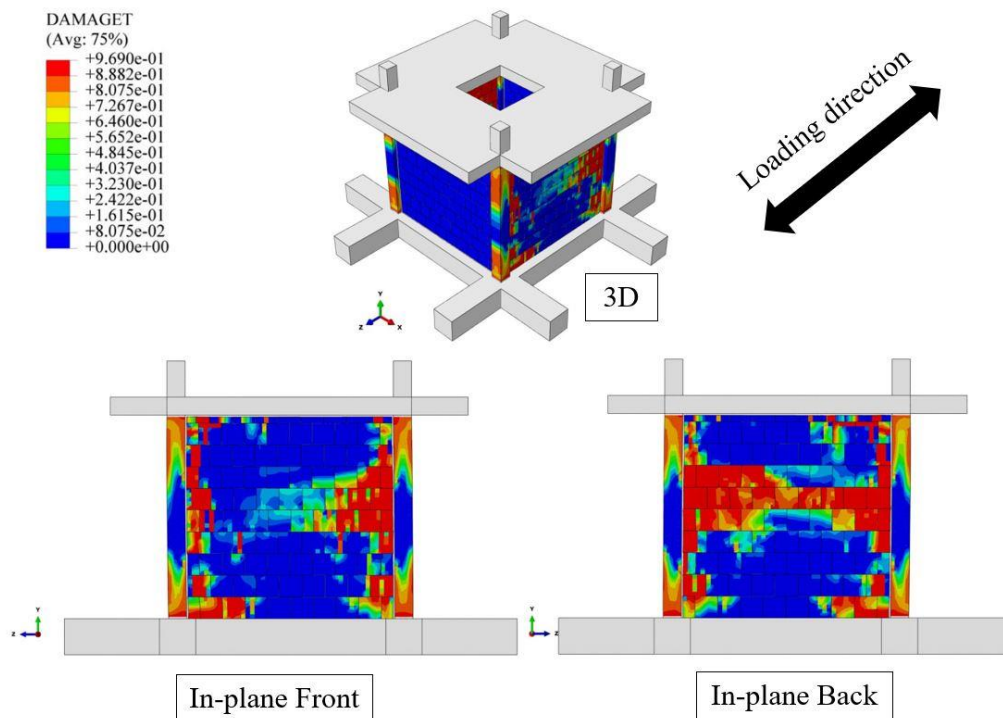


Figure 5.33. Damage visualization of the PUFJ – 0 model at the end of dynamic analysis.

In PUFJ – 90 model, where Type C walls were protected by the flexible joints in the entire perimeter, rather different damage pattern was observed. The cracks were concentrated at the lower portion of the walls, starting from a column edge and developing diagonally through to the opposite bottom corner, Figure 5.34. In terms of the out-of-plane performances, in both PUFJ models, the infill panels sustained their stability nearly without any damages. This outcome is also aligned with the experimental results, where the efficiency of the flexible joints was highly visible in this regard. However, this should be perceived as an additional unintentional outcome, since neither material testing (on small size specimens) nor numerical modeling exercises were conducted specifically regarding the OOP behavior.

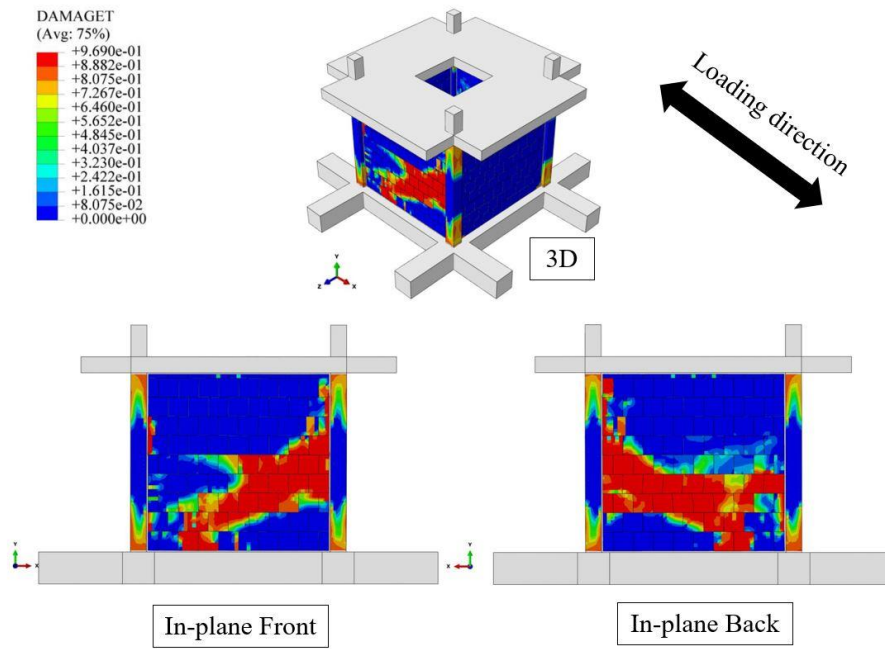


Figure 5.34. Damage visualization of the PUFJ – 90 model at the end of dynamic analysis.

On the other hand, due to the failure of the frame-masonry contact in the TRM model, the out-of-plane failure was inevitable, though the in-plane walls could withstand carrying loads despite having damages along the infill height at the column edges, as presented in Figure 5.35. This situation is considered to be one of the main reasons why the TRM model had a sharper strength loss in comparison to the PUFJ models, see Figure 5.32b.

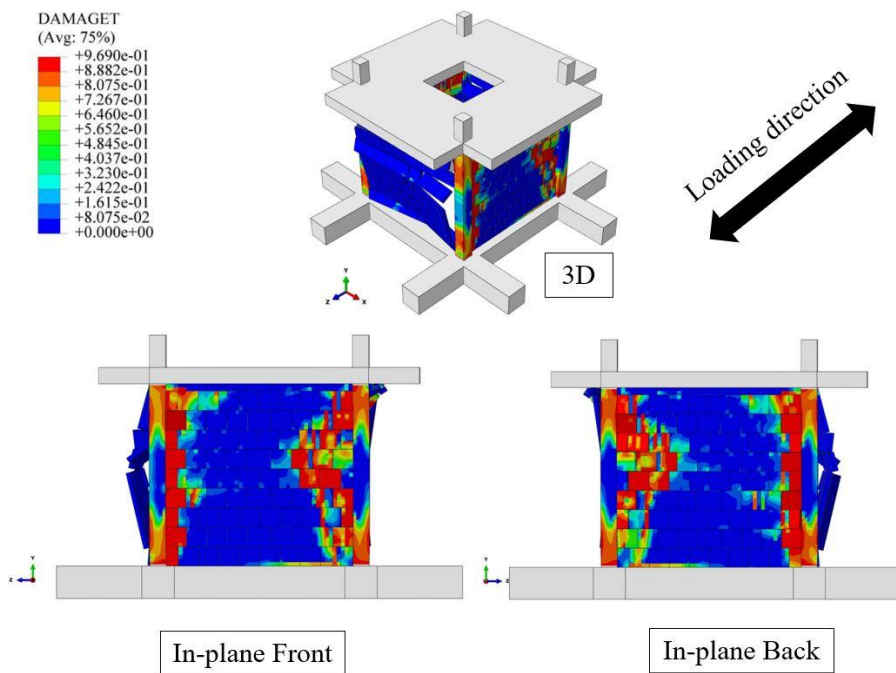


Figure 5.35. Damage visualization of the TRM model at the end of dynamic analysis.

Another reference model, BF, could not keep the stability until the end of analyses and exhibited the column-ends plastic hinge failure which is very typical for such systems, Figure 5.36. In this sense, all of the models had similar and expected damage patterns on the RC members, namely plastic hinge mechanisms at the both ends of the columns.

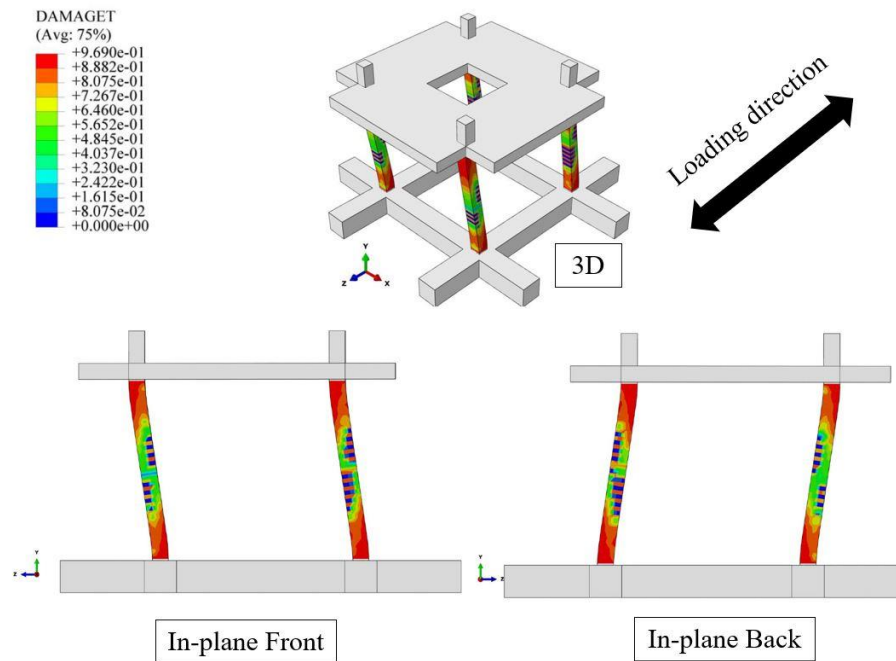


Figure 5.36. Damage visualization of the BF model at the end of dynamic analysis.

5.3.4 Chapter summary

This chapter focuses on the numerical simulations of the experimental investigations mentioned earlier in this study. For this purpose, firstly material constitutive models are introduced for each element which were used during the experiments. Following that, small size test specimens given in Section 4.1 are numerically modeled in order to calibrate the results before proceeding to the large size analyses. Later, the quasi-static in-plane shear tests are modeled and the outcomes are compared with the experimental ones, see Section 4.1. Despite having relatively higher deviations in some models, overall, satisfying match could be obtained. Moreover, shake-table tests are also numerically modeled using the dynamic analysis methods. However, as a result of the complexity of the challenge from the FEM perspective, several simplifications are made. Consequently, the dynamic analyses could be perceived as a modified look-alike replication of the seismic experiment. The findings in either large size models indicate that PUFJ in such buildings could be modeled successfully and analyzed for different loading and boundary conditions using the FEM solutions.

CHAPTER 6.

SIMPLE ANALYTICAL PROCEDURE

This chapter is dedicated to the endeavor of bringing a practical analytical solution for including the PUFJ impact in the regular equivalent strut models. In this way, only the in-plane behavior of the flexible joints is considered, since it is the most common approach for modeling infills as already mentioned in Chapter 3, where the literature review about the equivalent strut method is extensively provided. Accordingly, regardless of the strut numbers and other details, it was seen that the proposed models firstly elaborated the determination of the equivalent strut width of infills, w_{inf} , that is used for obtaining the diagonal stiffness. Among those, only very few considered the external loading conditions on the frames. In this regard, Amato et al. (2009) emphasized that vertical loads potentially affect the strut width values in a way that higher loads lead to some increment of the strut capacity due to the larger contact zones which cause stiffening effects. Therefore, this single strut approach is assimilated in this study because of its novelty and simplicity. The model is based on the original study of Papia et al. (2003), so that the strut width is expressed by Equation 6.1.

$$w_{inf} = d_{inf} k_v \frac{c_p}{z_{inf} (\lambda_{inf}^*)^{\beta_p}} \quad (6.1)$$

Where, d_{inf} is the diagonal infill length, c_p and β_p are coefficients related to the diagonal Poisson ratio, ν_d , and given in Equations 6.2-6.3, while z_{inf} describes the panel shape according to Equation 6.4. On the other hand, k_v takes into account the vertical load effects as given in Equation 6.5, which can be expressed by the vertical deformation parameter of the columns, ε_v , that is function of the compressive column load F_v , column cross sectional area A_{col} and elasticity modulus of the frame material E_f , as given in Equation 6.6

$$c_p = 0.249 - 0.0116 \nu_d + 0.567 \nu_d^2 \quad (6.2)$$

$$\beta_p = 0.146 + 0.0073 \nu_d + 0.126 \nu_d^2 \quad (6.3)$$

$$z_{inf} = 1 + 0.25(l_{inf}/h_{inf} - 1) \quad (6.4)$$

$$k_v = 1 + (18\lambda_{inf}^* + 200)\varepsilon_v \quad (6.5)$$

$$\varepsilon_v = \frac{F_v}{2A_{col}E_f} \quad (6.6)$$

Moreover, the stiffness characterization parameter, λ_{inf}^* , is defined in Equation 6.7, where E_d is the infill diagonal elasticity modulus and A_{bm} is the beam cross sectional area. The other variables t_{inf} , l_{inf} , h_{inf} , l'_{inf} and h'_{inf} represent the infilled frame dimensions, see Figure 6.1.

$$\lambda_{inf}^* = \frac{E_d t_{inf} h'_{inf}}{E_f A_{col}} \left(\frac{h'_{inf}{}^2}{l'_{inf}{}^2} + \frac{A_{col} l'_{inf}}{4A_{bm} h'_{inf}} \right) \quad (6.7)$$

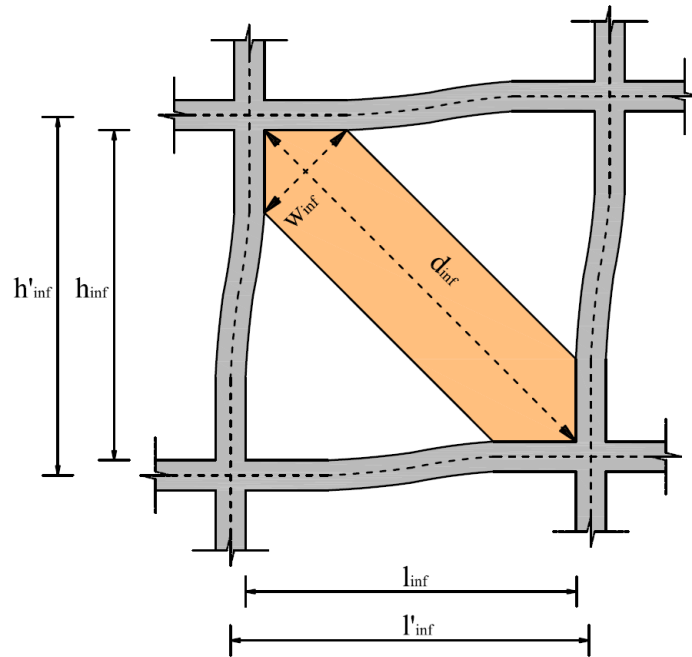


Figure 6.1. Geometrical features of the equivalent strut model.

For an accurate representation of the infill walls, evaluation of the initial elastic stiffness is not enough but post-cracking trend also needs to be defined. According to the experimental surveys, such behavior is often assumed with tri-linear branches, namely the initial phase until the first cracking, second phase where the stiffness degradation occurs up to the maximum load and in the third phase both strength and stiffness values are decreased, either assuming some residual strength or total strength loss ultimately. There are different approaches in terms of defining the aforementioned backbone curves, and these are often relied on experimental information limited to their original study. The research of De Risi et al. (2018) stands out in this regard, where a large set of database from the literature was investigated for the in-plane

behavior of the hollow clay brick infilled RC frames. In this way, the authors were able to compare the results of many experiments at once, thus a new tri-linear backbone curve proposal was made using the broadscale information. Their methodology was based on extracting the infill strengths alone from the available data, where both bare-frame and infilled frames were tested separately. When comparing the force responses of those at the same time steps or drift ratios and reducing the bare-frame ones from the infilled frames, it was possible to acquire the pure infill panel contribution, as schematically presented in Figure 6.2. Thanks to the collective data, a general representation could be made with relatively low CoV so that the strut axial load-displacement envelope curve was finally proposed, using the only infill contribution, Figure 6.2. It is important to emphasize that the strut analogy only considers the compressive axial forces but ignores the tensile ones, which are practically neglectable. The axial displacements in this manner, should be perceived as shortening effects, see Figure 6.3.

In the following paragraphs, a tri-linear strut model derived from the aforementioned original study is presented. The cyclic in-plane tests explained in Section 4.1 constitute the basis of model calibration. Therefore, there are some differences of this model when compared to the original study in terms of the determination of characteristic points.

The parameters required for the envelope curve depend on force and stiffness values. For this purpose, the traditional stiff mortar implemented structure (Frame A) is firstly calibrated, due to its relatively well-known behavior. In this regard, the cracking load (F_{cr}) is a fraction of the peak load (F_{peak}) and taken as $0.8F_{peak}$. On the other hand, F_{peak} is determined according to Panagiotakos and Fardis (1996), where it was assumed that ultimate shear stress on the bed joints at the failure of wallet specimens, τ_{ul} , is the dominant damage factor. Using this value and the area of strut (A_{str}) that is up to w_{inf} and infill thickness t_{inf} , F_{peak} could be obtained. Beyond this point, it is assumed a linear descending branch until reaching the zero-force value. In order to determine the displacement positions of each characteristic force point, stiffness values K_{cr} , K_{peak} , K_{soft} which are the products of initial cracking, secant peak and tangential softening slopes respectively are used. De Risi et al. (2018) employed the popular strut width equation of Mainstone (1971) for determining the stiffness values, whereas the strut width in here is calculated differently as explained above. Other than that, the slopes of cracking and softening branches are found better fit with the expression of Bertoldi et al. (1993), where K_{cr} and K_{soft} are taken as $4K_{peak}$ and $-0.02K_{peak}$ – reportedly from De Risi et al. (2018), respectively. In short, all stiffness properties are determined according to the experimental stiffness results which are obtained from the wallet tests, see

Section 4.1. However, slight modification was done regarding the K_{peak} , since the wallet experimental results exhibited high CoV (51.2%) among specimens, and as a result, the mean value of stiffness results (125.8 kN/mm) is reduced by 20% in order to match with large-size experimental results. On the other hand, it is still suggested to use this value directly from the experimental results for the other problems, in case CoV is considerably low unlike in this case. Moreover, K_{cr} and K_{soft} are directly calculated as fractions of the aforementioned mean stiffness value, as proposed by Bertoldi et al. (1993).

According to the experiments, it is seen that the flexible joints implemented frames have two main characteristics that differ from the one that is tied with the stiff mortar. These are; relatively softer initial stiffness and much higher bonding capacities at the masonry-to-frame joints. Such features lead to reach greater lateral displacement values or in other words enhanced ductility. In the light of these observations, only K_{cr} and K_{peak} are modified for matching with the results of PUFJ frames, namely Frame B and Frame C. Although F_{cr} and F_{peak} values are taken equal for all of the frame types, residual strengths are assigned on the flexible jointed frames unlike Frame A. Justification of this approach could be attributed to the strong bonding capacities of those that cause smaller strength drops. This assumption is also directly effective of reflecting the overall strength increment in the post-cracking phase, which is observed in the experiments. The envelope models are presented for different strut types (ST) in Figure 6.3. In addition, the process flow of the strut properties determination is given in Figure 6.4.

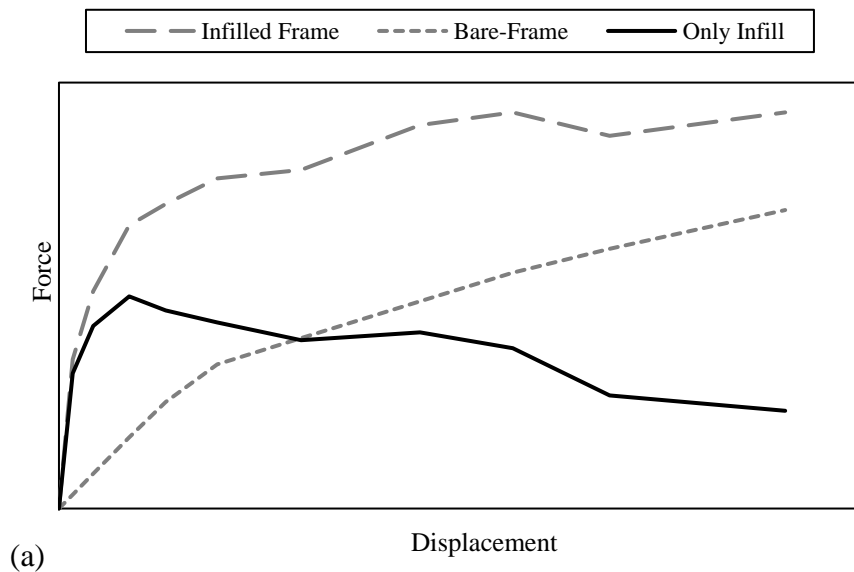


Figure 6.2. Force-displacement behavior of; (a) different frame configurations regarding the infill presence and (b) multi-linear idealization for the strut modeling.

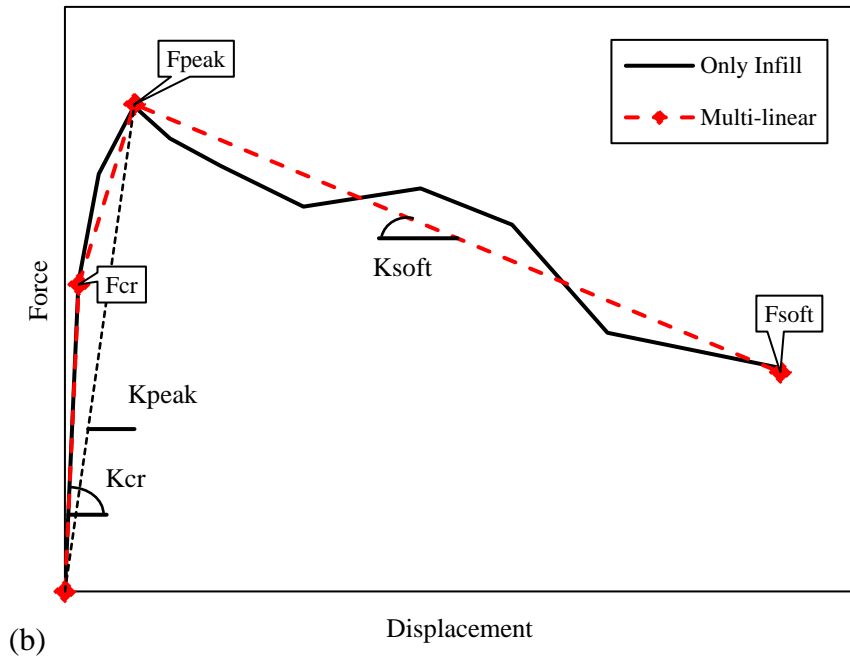


Figure 6.2. (continued).

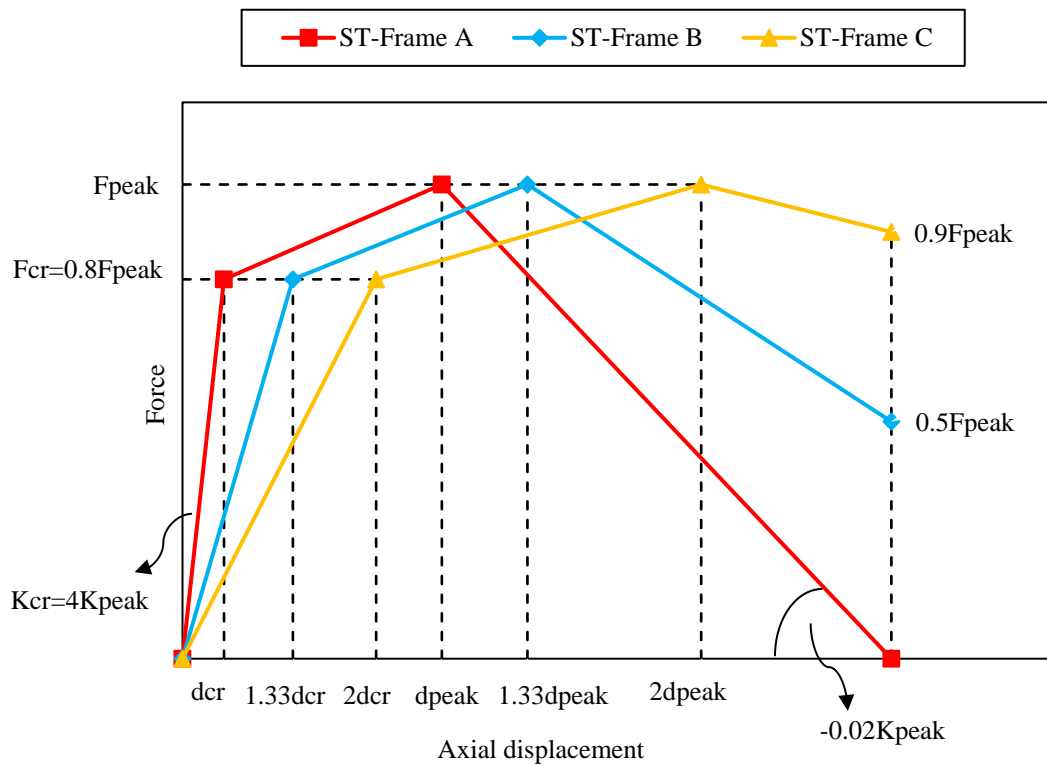


Figure 6.3. Force-displacement features of the proposed multi-linear strut model for different joint configurations.

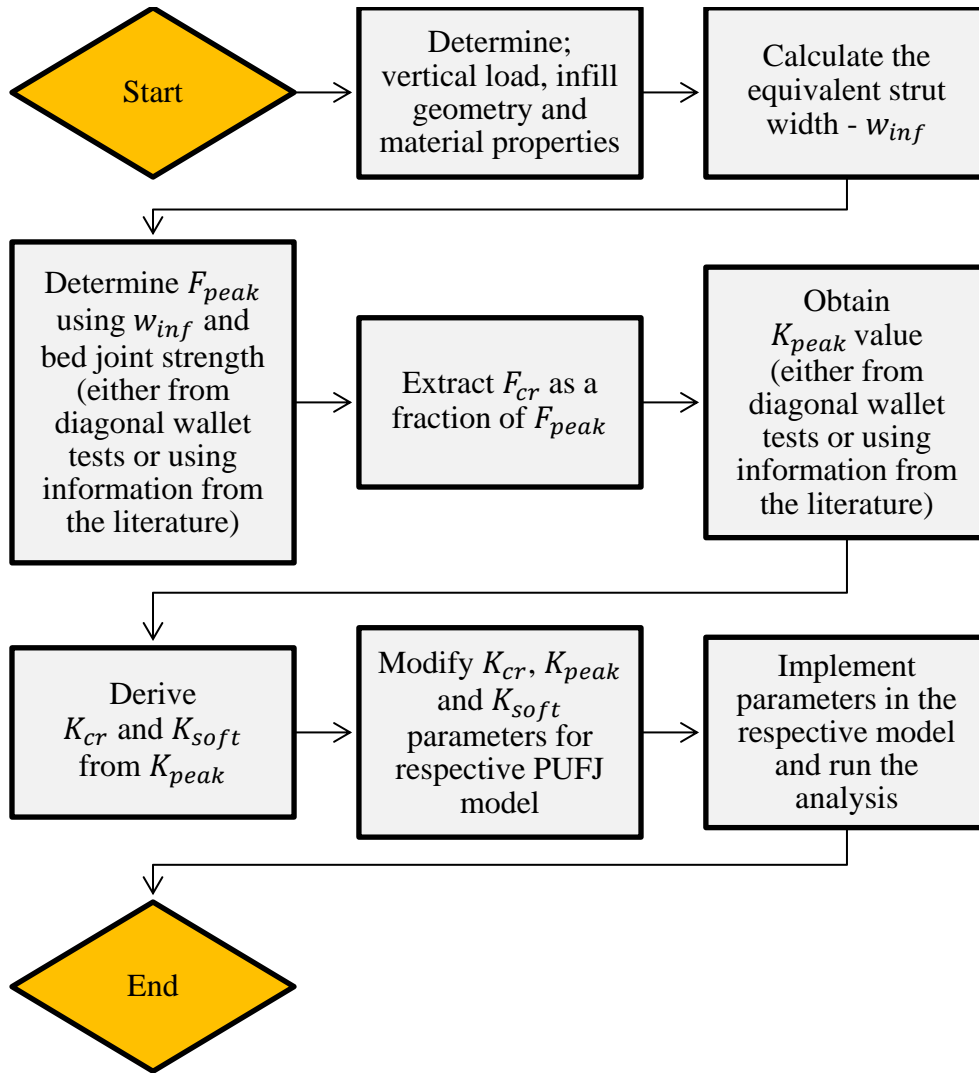


Figure 6.4. Process flow of the strut properties determination.

6.1 Analytical calibration results

The proposed model is analyzed by means of replacing the actual infill walls with the equivalent compressive struts. The analyses are run in the two-dimensional space of a professional structural engineering program, SAP2000 (Computers and Structures, 2015). Frame members are modeled with two-node bar elements which are connected by rigid tie links at the beam-column joints. Nonlinear behavior of those is actualized with the lumped plastic hinges at the frame ends having the length of half cross-sectional height. Furthermore, multi-linear plastic link elements (ML-Link) are utilized for defining the equivalent strut properties, which are connected diagonally at the frame corners in both directions. Figure 6.5 illustrates the model details.

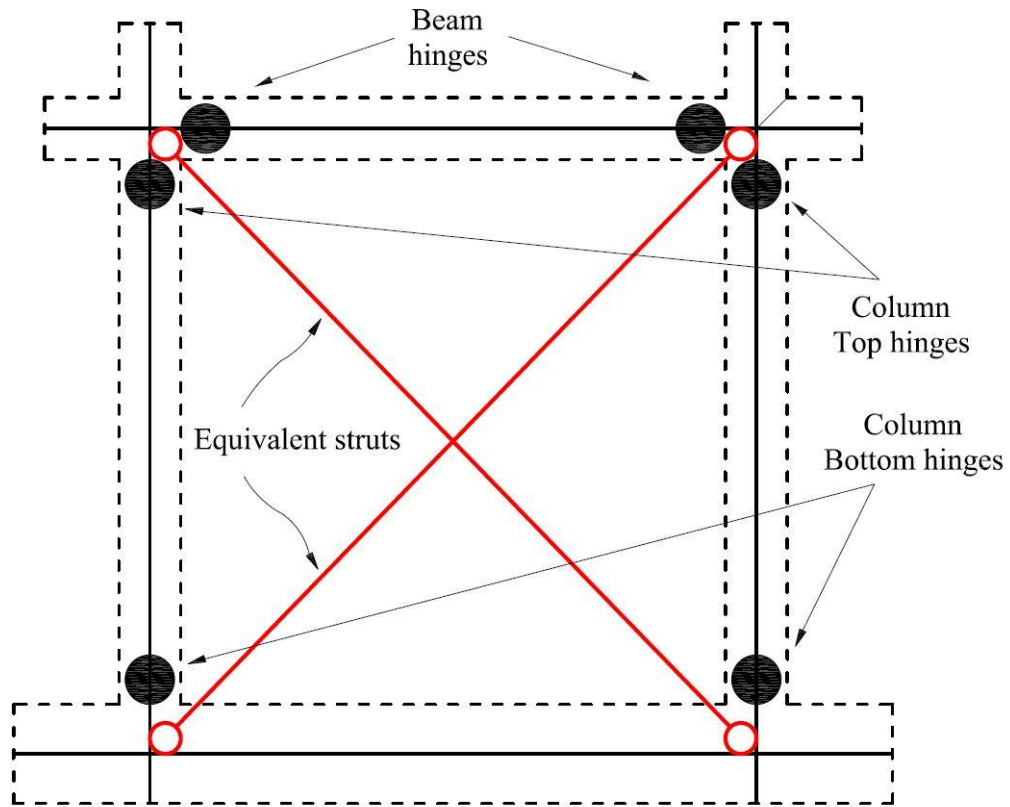


Figure 6.5. Modeling details for the calibration purposes.

First of all, the bare-frame is modeled in order to evaluate the reliability of material models other than the equivalent struts. Later, the infilled frames are exposed to gradually increasing unidirectional pushover displacements. The results are then compared with the backbone curves of the experimental cyclic loops for both directions. The load-displacement curves are presented in Figures 6.6. Overall, it can be said that the analytical results are sufficiently close to the experimental ones. Analytical models for the any frame type firstly exhibit stiffer behavior than the experimental results until yielding. Following that, softening trend could be achieved with well agreement, though Frame A and Frame B plot curves closer to the upper bound of the experiments whereas the bare-frame and Frame C provided values in between the results of two different directions. The input parameters for the equivalent strut envelope curves are also given in Table 6.1. In addition, these values are presented on a graph in Appendix B.

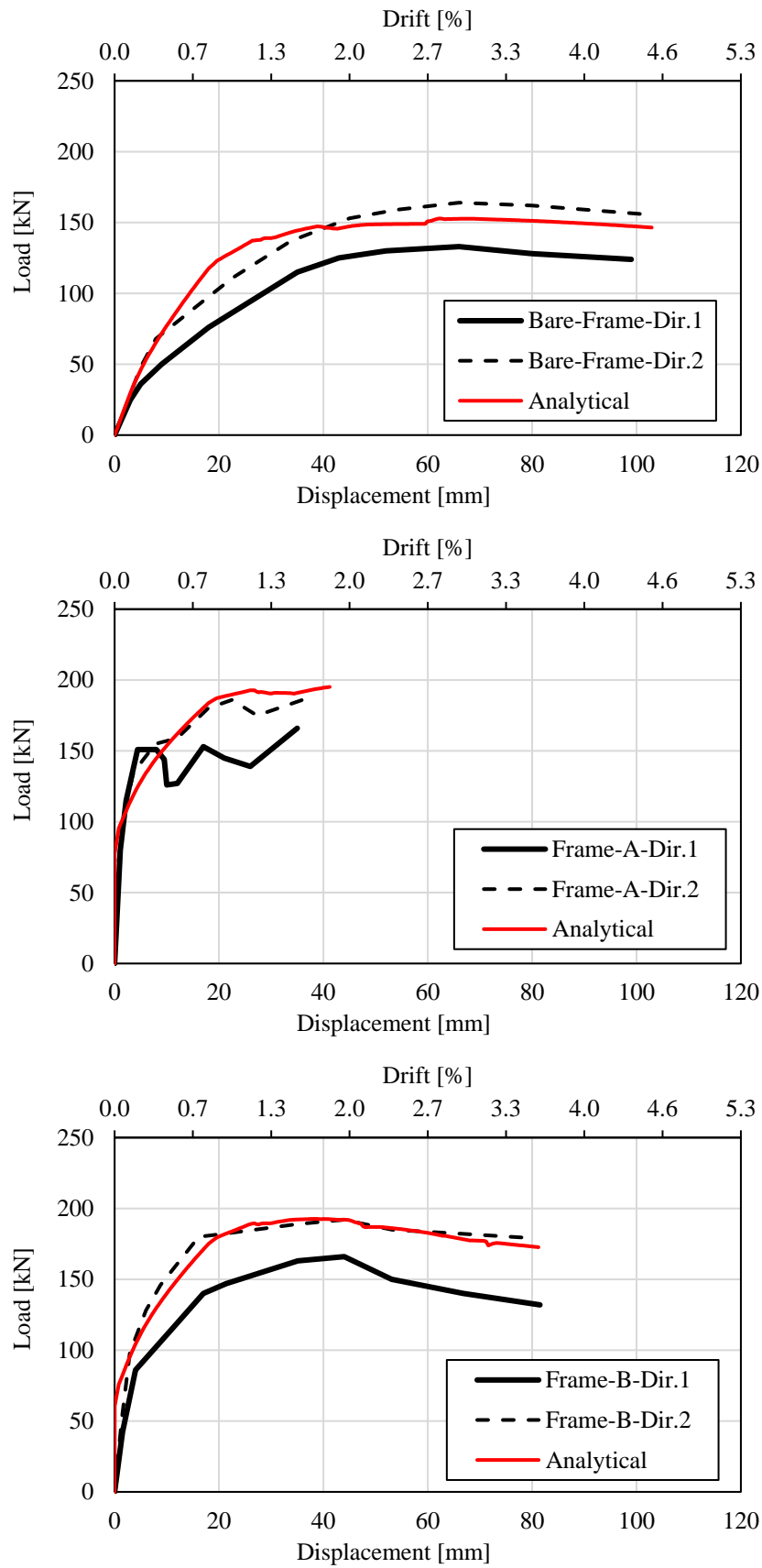


Figure 6.6. Comparison between the proposed analytical model and in-plane cyclic test results.

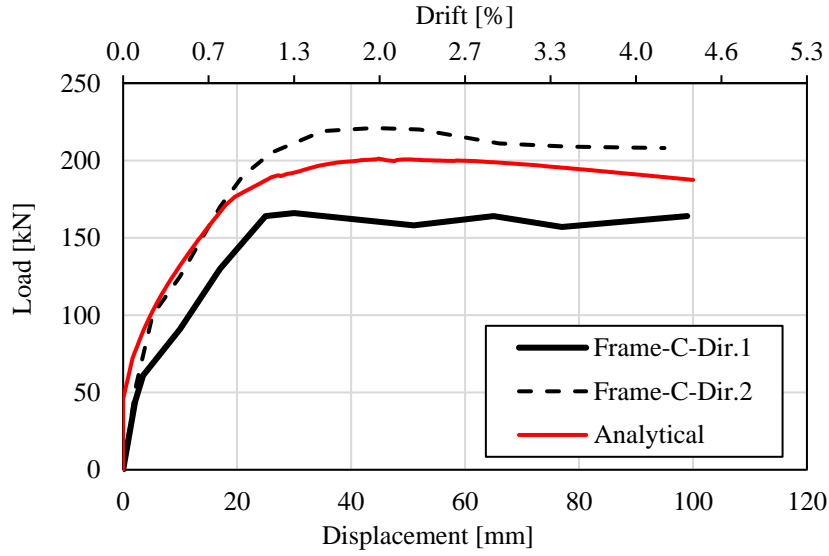


Figure 6.6. (continued).

Table 6.1. Characteristic points (equivalent strut values) of the proposed analytical model for the in-plane pushover tests.

Phase	Eq. strut - Frame A		Eq. strut - Frame B		Eq. strut - Frame C	
	Axial Disp. [mm]	Axial Force [kN]	Axial Disp. [mm]	Axial Force [kN]	Axial Disp. [mm]	Axial Force [kN]
Cracking	0.09	47.23	0.12	47.23	0.19	47.23
Peak	0.59	59.03	0.78	59.03	1.17	59.03
Softening	24.05	0.00	24.05	29.52	24.05	53.13

6.2 Dynamic response of the analytical models

Efficiency of the proposed strut model is also investigated under dynamic excitations. For this purpose, an RC residential building which was previously designed according to typical Turkish design practice is considered. The original building consisted of eight stories in elevation and multiple spans on the plan. It was specifically designed for representing a common structure type being constructed as a part of large-scale urban transformation endeavor in Istanbul province of Turkey. That being said, shallow beams placed within the ribbed flat-slab floors were connected to different sizes of columns. In the center of building where the stairway and elevator hole were enclosed, shear walls were utilized in order to provide the primary lateral force resisting mechanism against the earthquakes. However, only a portion of the original building is extracted for the analysis in this study, namely an outer two-bay and four-story part belongs to the upper stories as shown in Figure 6.7. Moreover, column size and frame reinforcement are also slightly modified for the simplification. Later, the bare-frame is filled with equivalent struts in both diagonal directions that represent the infill

walls, see Figure 6.8. The original building, where the details can be found in Akyildiz and Girgin (2017), was exposed to the time-history records. Since then, some major changes have been implemented in the Turkish norms, hence the current Turkish Seismic Code (AFAD, 2018) is considered in the analyses of this section. Among those updates, evaluation of the elastic response spectra is the particular interest of this study, due to the fact that it requires a new approach in terms of the determination of the spectral magnitudes. Background of the spectral approach is already discussed in Chapter 2. Therefore, the focus in below is only on the adaptation of this method for the current problem, without giving further explanation.

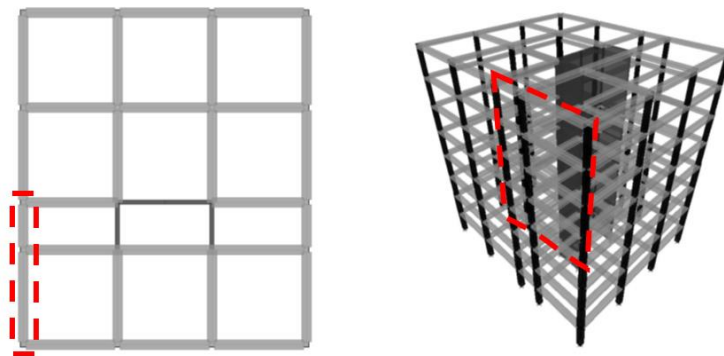


Figure 6.7. Extraction of the representative frame from the original model; plan (left) and three-dimensional (right) views.

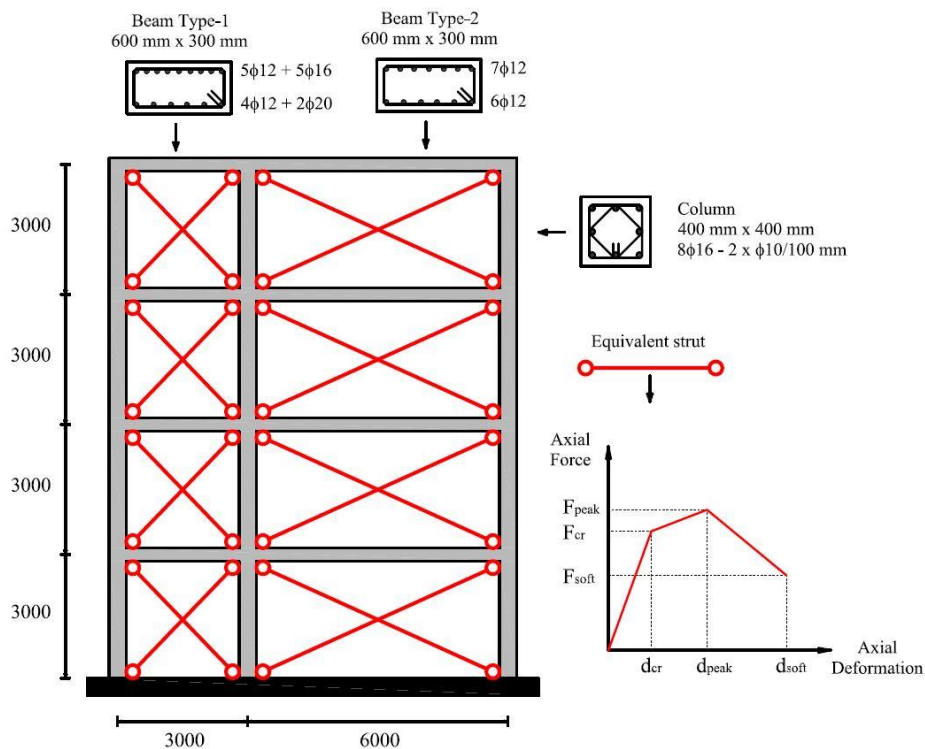


Figure 6.8. Details of the multi-story model created for the dynamic analyses.

The extracted structural frame is exposed to a real seismic event recorded in Kocaeli, Turkey, 1999 earthquake which was measured with moment magnitude (M_w) 7.4, and horizontal peak ground acceleration (PGA) 0.47g. In this study, it is assumed that the considered building is located in the highest seismic zone as per the hazard map created by Turkish authorities (AFAD, 2018), having spectral acceleration values for short (Sa, s) and one-second ($Sa, 1$) periods as 2.01g and 0.95g, respectively. These values are magnified with hypothetical local site conditions assuming very soft-rock or stiff-soil (ZD class in AFAD, 2018) and thus the design spectral acceleration (SDa) values are obtained. Finally, the elastic response spectra is plotted as shown in Figure 6.9. In order to satisfy the seismic code requirements, the original record is matched with the aforementioned target spectra using a special purpose software, SeismoMatch (Seismosoft, 2015). Furthermore, comparison between the original and matched records are also made in the time domain for acceleration, velocity and displacement results, Figure 6.10.

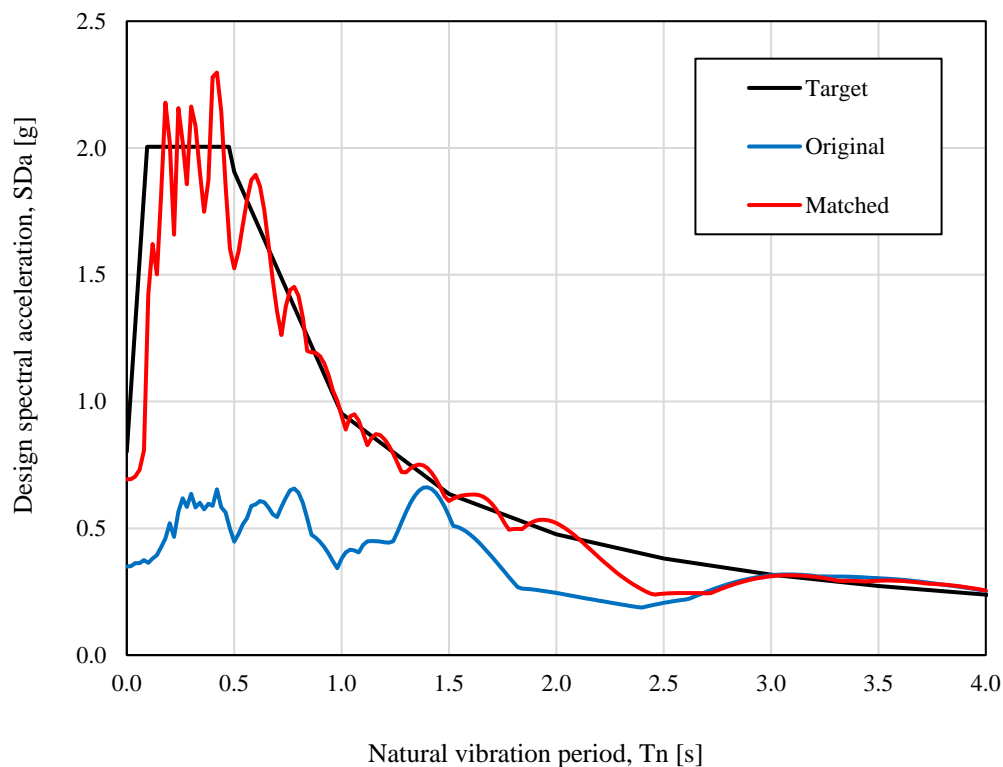


Figure 6.9. Elastic response spectra for the matched, original and target curves.

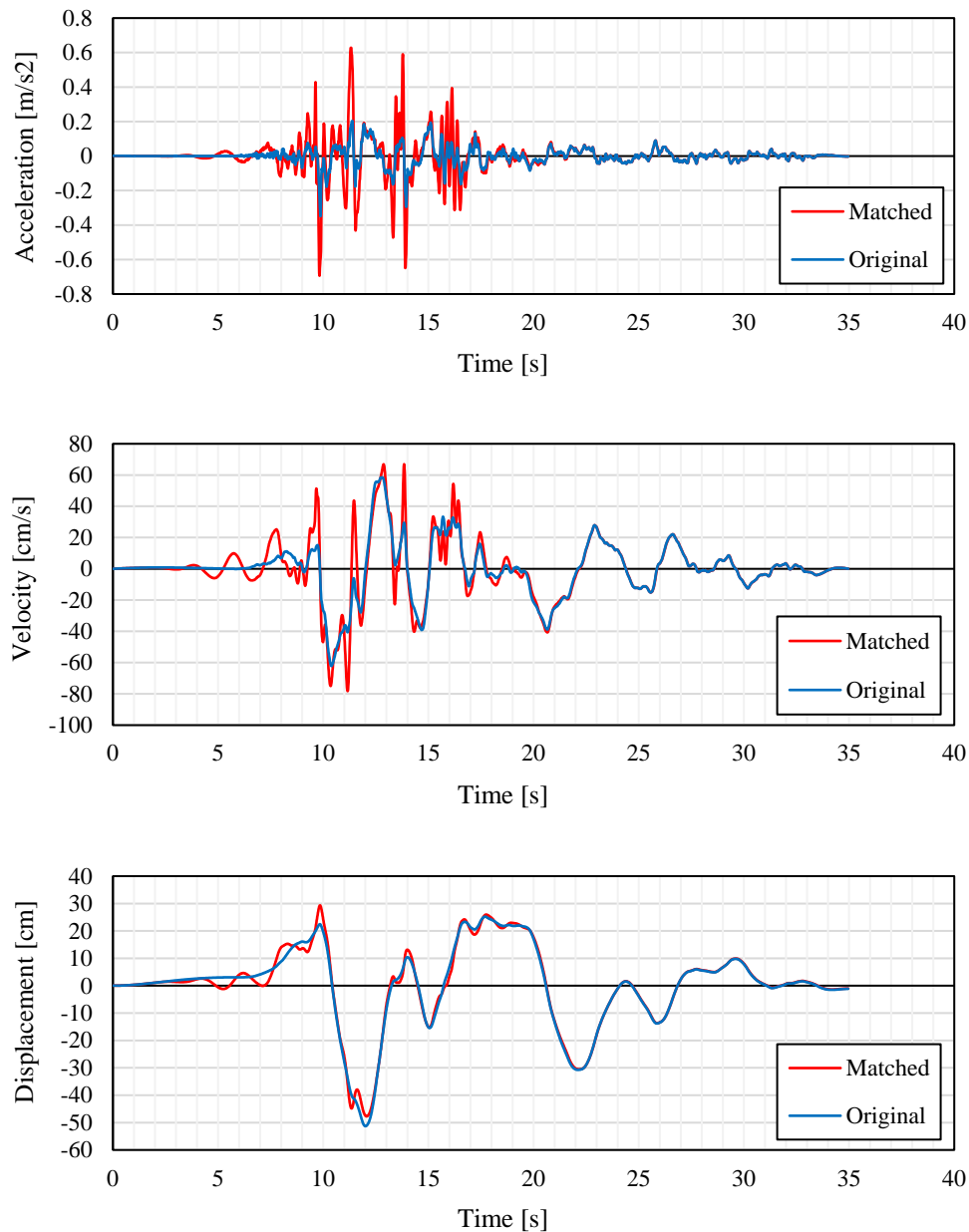


Figure 6.10. Comparison between the matched and original records in terms of the acceleration, velocity and displacement results.

In total, four different buildings are considered; Bare-frame (BF) for highlighting the infill absence situation, and the other three frames with the same labeling format mentioned previously for representing the different connection types. First of all, the equivalent struts are modeled. Since the equivalent strut properties depend on the geometrical shapes and effective vertical loads (here, only a constant load is considered for generalization), two different strut models are calibrated which are named after the infill dimensions. The details are given in Table 6.2.

Table 6.2. Characteristic points of the proposed analytical models for the dynamic analyses.

Phase	Infill dim. [m]	Eq. strut - Frame A		Eq. strut - Frame B		Eq. strut - Frame C	
		Axial Disp. [mm]	Axial Force [kN]	Axial Disp. [mm]	Axial Force [kN]	Axial Disp. [mm]	Axial Force [kN]
Cracking		0.11	54.45	0.14	54.45	0.22	54.45
Peak	6×3	0.68	68.06	0.90	68.06	1.35	68.06
Softening		27.73	0.00	27.73	34.03	27.73	61.25
Cracking		0.13	64.88	0.17	64.88	0.26	64.88
Peak	3×3	0.81	81.11	1.07	81.11	1.61	81.11
Softening		33.04	0.00	33.04	40.55	33.04	73.00

Upon determining the strut properties and creating the models, the buildings are subjected to the matched accelerograms at their base levels. The results are evaluated in terms of the displacement values of different stories given in Figures 6.11-6.12 and Tables 6.3-6.4, and their corresponding drift ratios, see Figure 6.13 and Table 6.5. Accordingly, it is clearly seen that presence of the infill walls substantially decrease the lateral deformations, which is especially visible on the top story level. At its highest value for each story level separately, strut type belongs to Frame A (ST-A) lead to displacement reduction in a range of 7%-13% that of the BF. Similarly, these values are found for the infilled building types of Frame B (ST-B) and Frame C (ST-C) as 8%-16% and 12%-24%, respectively. Regarding the drift outcomes, similar trend could be observed, as the infilled frames exhibit stiffer behavior with less drifts though the PUFJ implemented models, namely ST-B and ST-C, have slightly higher values than the ST-A frame. On the other hand, BF building has much greater drift results which reaches to 1.74% as its peak value. Such high drifts often cause serious damages especially on the column members, since many design codes restrict the design level drifts between approximately 1% - 2%, depends on the types of structural members. In this sense, importance of the infill presence is once again shown. Besides, it is worth to mention that ST-A building, where the stiff mortar is used as the bonding material, is assumed to have perfect bonding conditions due to the limitations of the equivalent strut modeling analogy. However, it is known that premature bonding failures most likely occur on such constructions, as shown in Chapter 4. Therefore, PUFJ implementation stands as an alternative solution in this regard, since the drift capacities are enhanced beyond the level of the stiff type joint, whereas reliable bonding conditions are provided as well.

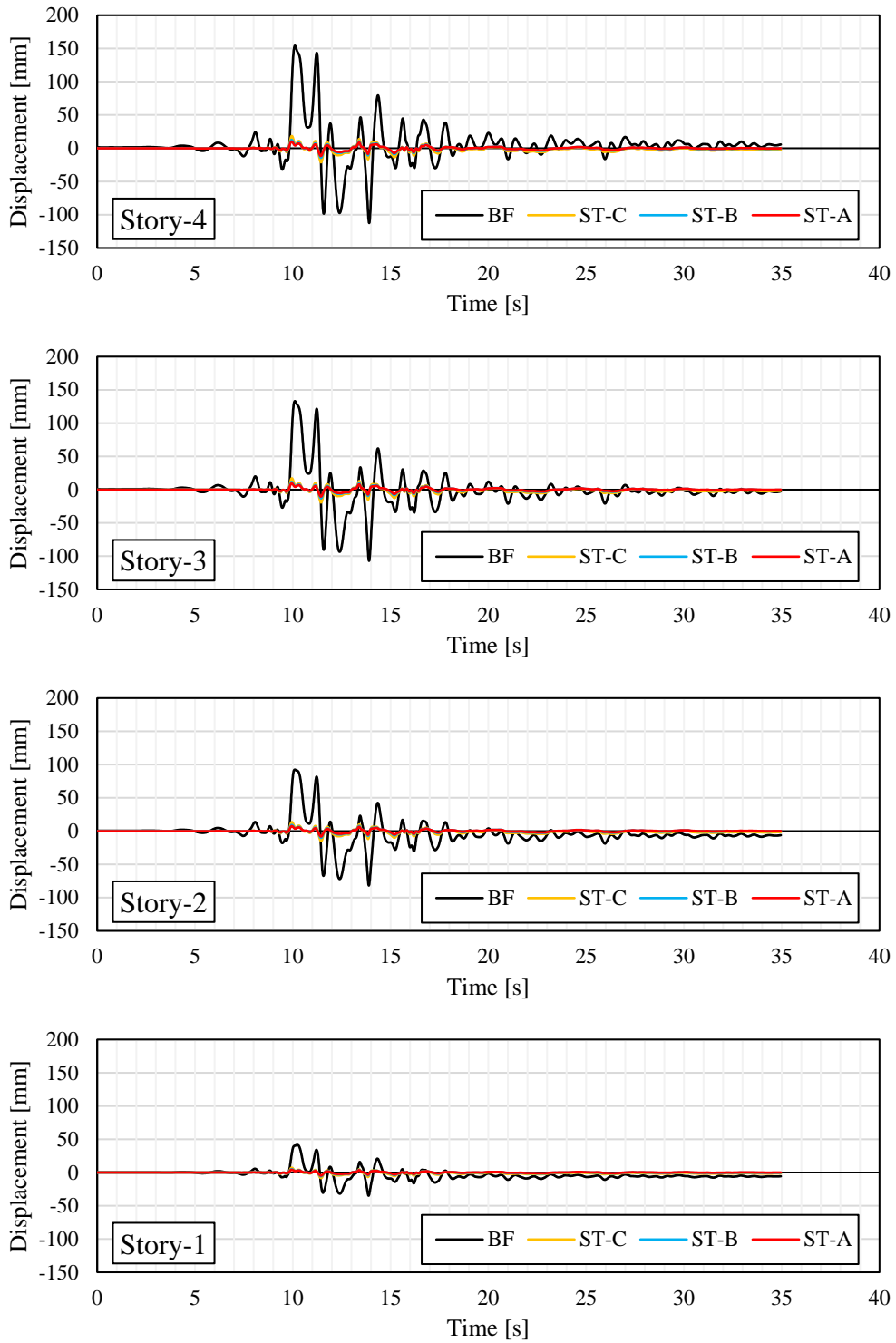
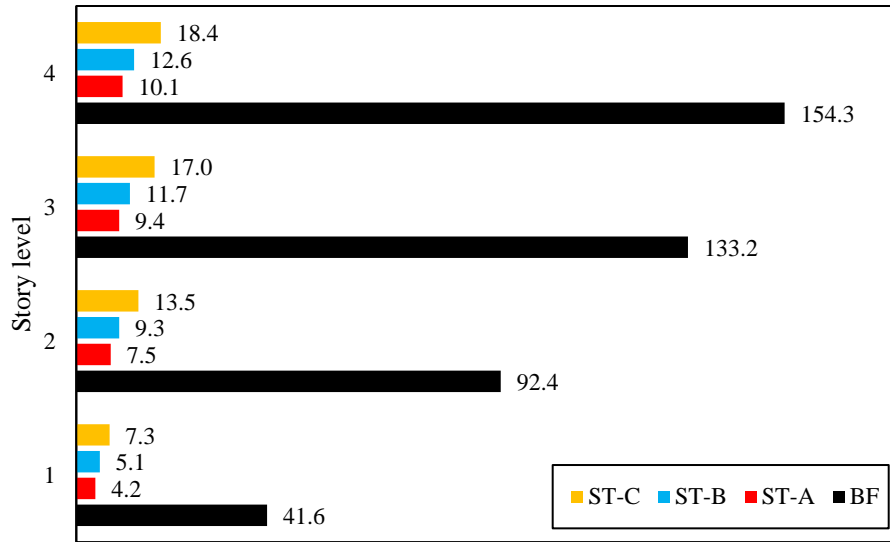
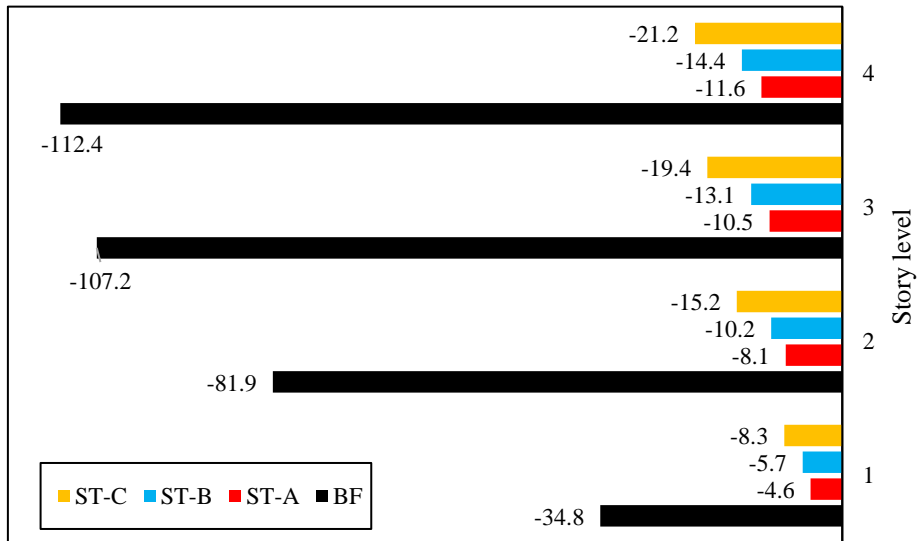


Figure 6.11. Displacement results of the different story levels under seismic loading.



(a) Displacement [mm]



(b) Displacement [mm]

Figure 6.12. Maximum displacement results under seismic loading; (a) positive and (b) negative directions.

Table 6.3. Maximum displacement results for different frame types.

Story	Positive displacement [mm]				Negative displacement [mm]			
	BF	ST-A	ST-B	ST-C	BF	ST-A	ST-B	ST-C
4	154.3	10.1	12.6	18.4	-112.4	-11.6	-14.4	-21.2
3	133.2	9.4	11.7	17.0	-107.2	-10.5	-13.1	-19.4
2	92.4	7.5	9.3	13.5	-81.9	-8.1	-10.2	-15.2
1	41.6	4.2	5.1	7.3	-34.8	-4.6	-5.7	-8.3

Table 6.4. Normalized maximum displacement results for different frame types.

Story	Normalized positive displacement [%]				Normalized negative displacement [%]			
	BF	ST-A	ST-B	ST-C	BF	ST-A	ST-B	ST-C
4	100	7	8	12	100	10	13	19
3	100	7	9	13	100	10	12	18
2	100	8	10	15	100	10	12	19
1	100	10	12	17	100	13	16	24

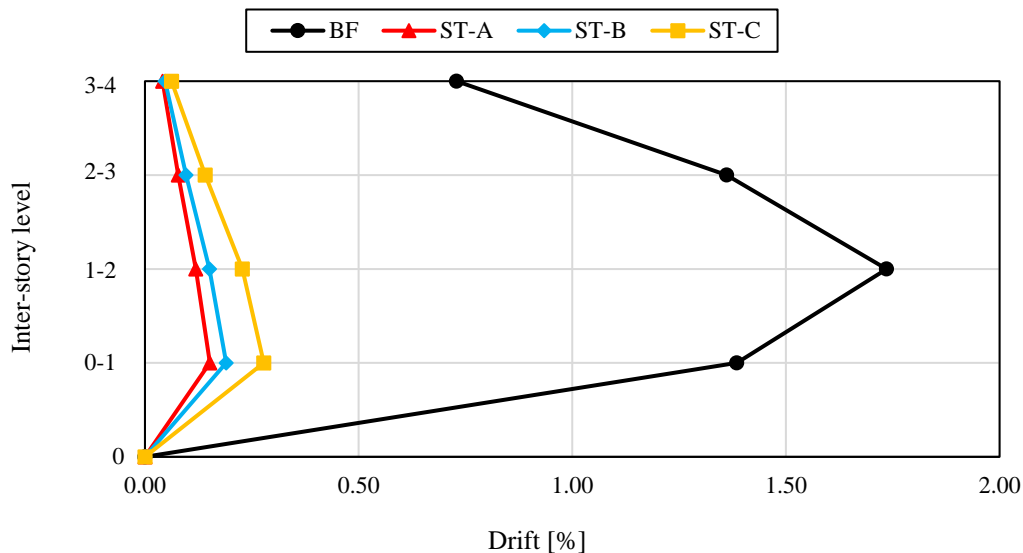


Figure 6.13. Visualization of the maximum drift results for different frame types.

Table 6.5. Maximum inter-story drift results for different frame types.

Story level (between)	Drift [%]			
	BF	ST-A	ST-B	ST-C
3 – 4	0.73	0.04	0.05	0.06
2 – 3	1.36	0.08	0.10	0.14
1 – 2	1.74	0.12	0.15	0.23
0 – 1	1.39	0.15	0.19	0.28

Moreover, strut individual performances are also evaluated under cyclic loads. The hysteresis model is not originally created for this study but an approach of Cavaleri and Di Trapani (2014) is adapted, where the authors proposed the pivot model parameters for the hollow clay infills that is previously mentioned in Chapter 3. As per their suggestion, the pivot hysteretic parameter (α_2) is taken equal to 0.25. It is crucial to state that the best option for obtaining this value is through some additional empirical results and multiple iterations, hence it is left out of the scope in this study. Because, the main aim is to compare between the influence of different connection types rather than establishing a general-purpose hysteretic

rule for all types of infills, which is itself a complex task and requires further investigation. Nevertheless, the rules for backbone curves are already estimated for each connection type as given above in this section, and it is seen in Figure 6.14 that the strut axial force-displacement trends match closely with the in-plane experiments given in Section 4.1. Because, visibly higher ductility as well as load carrying capacity could be achieved on PUFJ implemented struts that are represented by ML-links, namely ML-Link B and ML-Link C. Figure 6.14 shows the results of only a single strut positioned in the 6m×3m bay infill zone at the first story level.

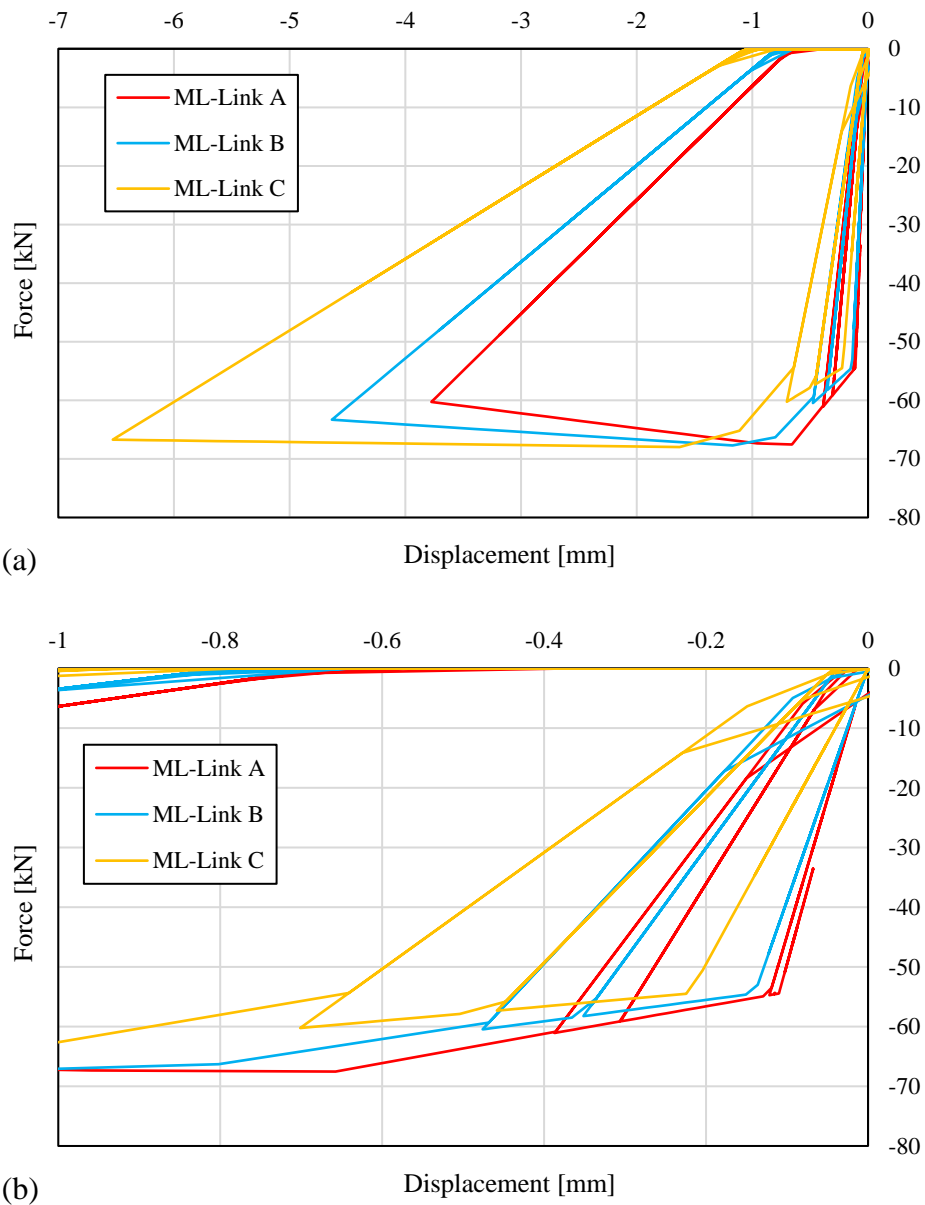


Figure 6.14. Hysteresis curves of the ML-Links; (a) full and (b) focused views.

6.3 Chapter summary

In this chapter, a practical solution for modeling PUFJ implemented infills is proposed. The method relies on the single equivalent strut analogy, which implies much simpler solution in this purpose. Rather than establishing a purely new strut model from scratch, previously developed different models are combined and modified for bringing an original solution to include the PUFJ effects. The in-plane experimental results given in Section 4.1 constitute the basis of model calibration. Therefore, it is always suggested to control the model parameters for the practitioners, as such models are very often depending on the specific material and geometry conditions. Other than that, it is seen that close match with the experimental results could be obtained, which is a sign that PUFJ implemented infill walls can be successfully modeled through simple approaches, hence it is suitable for the structural designers.

CHAPTER 7.

SUMMARY AND CONCLUSIONS

This dissertation aims at proposing an efficient method for protecting the masonry infilled multi-story RC frames against the detrimental effects of the earthquakes. The study is divided into several chapters that are given below with brief information. Furthermore, main findings are shared and suggestions for the future works are provided.

7.1 Scheme of the dissertation

In the first chapter, the problem statement is made gathering relevant information from the past ground shakes by means of providing the common failure mechanisms for highlighting the challenge. The proposed solution, namely polyurethane flexible joints (PUFJ), is introduced briefly with its possible usage areas. Later, the original idea of utilizing this method as a buffer material between the brittle structural elements – RC frame and masonry infills – is suggested, which claims to protect the building parts and thus provides an effective seismic energy absorbing solution. The objectives are determined in this regard and investigated through the next chapters of the study.

Second chapter describes the fundamentals of seismicity and principles of the earthquake engineering. Particularly infill walls are investigated in this manner. Consequently, a deeper comprehension of the problem could be made.

Third chapter is dedicated to a comprehensive literature review. At first, significant experimental works in this field are shared with their major outcomes. Hence, an overview of the challenge could be observed from the different perspectives. Since the scope of this study also covers the computational methods for bringing general solutions and establishing material constitutive models, some remarkable infill wall modeling techniques are also investigated. Last but not least, various masonry protection and retrofitting methods are presented, which enables to compare the PUFJ solution with the others and specify its position among those.

Detailed experimental investigation is given in the fourth chapter which is divided into two campaigns. In both, large-scale specimens are used and the materials are procured from the commonly available sources. Therefore, real-like building conditions could be obtained. The first campaign consists of the quasi-static in-plane shear tests on single-span specimens, where two alternative PUFJ implementation methods are compared with their traditional

counterpart, namely the stiff mortar. Among the alternative flexible joint solutions, three-edge PUFJ implementation represents the usage of method in already existing (old) buildings and labeled Type B wall, whereas the four-edge alternative – Type C wall – is suitable for the to-be-built (new) constructions. The hysteresis loading curves as well as the damage patterns are compared between different frame types. In the second experimental campaign, a three-dimensional single-story box shaped building is positioned on a shake-table, which later excited by various loading conditions including a real seismic record, different signal intensities as well as resonance frequency vibration tests. The same materials are used as of the quasi-static specimens, yet slight geometrical modifications exist. Both Type B and Type C walls are investigated simultaneously against the in-plane and out-of-plane loads following a series of multiple testing protocol. The outcomes are expressed by means of the relative drift results, frequency shifts and corresponding stiffness changes.

Fifth chapter elaborates on the aforementioned experimental campaigns from the numerical point of view. For this purpose, material constitutive models are firstly determined to be used in the finite elements method (FEM) environment. Following that, the most suitable analysis procedure is chosen and the small-size analyses are initially performed in order to calibrate the results with the actual tests. Later, the large-scale experiments are simulated, though some simplifications and modifications are made for adapting the natural physical conditions effectively into the computational world. The results are also evaluated partially different due to the same reason.

Finally, a simple analytical procedure is proposed that to be used by the structural engineers and designers working in the sector. The quasi-static experimental tests are primarily used for calibrating the analytical results. In this way, complexity of the masonry infilled systems is aimed to be reduced by means of replacing the multi-element walls with the single diagonal struts. Moreover, the established proposal is tested against the dynamic loads on multi-story frames using a commercially available structural engineering program.

7.2 General conclusions

Detailed findings are summarized at the end of each chapter. Therefore, the reader may refer to those parts, since rather a broadscale overview is done below. Because the first three chapters exclusively dedicated for providing a general overview about the background of the problem, the outcomes of other chapters are discussed here.

The quasi-static experimental campaign revealed that PUFJ implemented frames performed visibly better drift performances. Particularly Type C frame, where the masonry is surrounded completely by the flexible joints around its perimeter, exhibited the highest drift – around 4.4% – and strength capacity results. The three-edge PUFJ implemented Type B frame also performed visibly better than the traditionally stiff mortared specimen – Type A – especially in terms of the drift capacity, where 3.5% levels could be reached whereas the latter one failed at the 1.6% drift ratio due to the joint contact failure. The strength increment due to the flexible joints was especially visible for the Type C frame, though in any case PUFJ implemented solutions are capable of absorbing more seismic energy than their stiff mortared counterpart thanks to the greater drift capacities of those. It is worth to mention that majority of the seismic codes set their provisions as determining the target drift levels around 2%. The PUFJ solution provided outstanding results in this manner. On the other hand, the only frame without the infill walls – bare-frame (BF) – could carry significantly less lateral loads, which is already a largely known fact anymore and proven once again that the infill contribution is enormous and cannot be omitted.

The shake-table tests exhibited that polymer-based solutions, namely PUFJ and FRPU, can give the best results when used together, although the PUFJ itself was sufficient to sustain the building stability against the severe seismic intensities (1.64g ground acceleration at the peak). The drift level was also reached to 3.7% without any additional retrofitting interventions. The building with the combined protection of the PUFJ and FRPU was also exposed to the variety of other loads including long-duration forced vibration and resonance frequency tests, yet it was capable of sustaining the stability as well as the loading carrying capacity without any major failure.

The numerical endeavor proved the fact that it is possible to model the PUFJ solution on large size models as an earthquake protection method using the general-purpose FEM programs. This enables professionals to actualize the iterative solutions against their problems without the need of costly and time-consuming experiments. However, a large extent academic literacy is still the requirement, since the challenge involves multi-disciplinary knowledge and often requires preliminary small tests in order to calibrate the results for executing the reliable analyses. Specifically for the numerical models in this study; determining a proper masonry modeling technique is considered as the hardest one among the other issues, since the characteristics of the different materials and their simultaneous interactions need to be properly determined. Another challenge is related to selecting the most appropriate way of the job execution methods from the common ones, namely implicit or explicit solver. The latter one is

decided for this study due to its robust features of reaching the solutions when the contact problems or the large deflections are the concerns. On the other hand, this decision brings some difficulties regarding the analysis running time and convergence accuracy, which requires a special attention. Nevertheless, despite several simplifications that emerged due to the needs of aforementioned topics, the results of the numerical analyses are found adequately close to the experimental ones in general. The quasi-static cyclic loading simulations exhibited remarkable achievement especially in the earlier stages of the analyses. Although the damage patterns of the masonries did not represent the reality of the experiments, frame damages as well as the overall trends of the hysteresis curves reflected similar outcomes as of the experimental ones. When it comes to the dynamic analyses for simulating the shake-table experiments, more assumptions were essential to be made. Although the numerical analyses did not fully replicate the testing conditions, the trends of the damage patterns and the failure modes are perceived as fairly matching with the real conditions. As a one of the possible ways of making a quantitative comparison, a selected numerical model estimated the peak drift as 3.31%, which differs from the original experiments by only around 10%, where 3.7% highest drift ratio was measured.

The proposed analytical solution matches reasonably well with the experimental ones in terms of the load-deflection paths of the results. It is simple to determine the mechanical parameters of the strut analogy for different joint types, since the PUFJ solutions are adopted as the variations of the stiff mortar implemented frame. An important point to keep in mind that the model is exclusively simple and only developed for the monotonic loading conditions. The cyclic loading conditions are also checked during the multi-story analyses, however, the results are merely compared among the different frames rather than aiming at matching with the actual tests. Besides, the proposed model is only capable of simulating the in-plane actions. All in all, it is suitable to be used by the practitioners working in the field, yet it requires the awareness of the assumptions that are made.

Considering all information and outcomes gathered, the author claims that the study involves valuable novelties which might have positive impact not only scientifically, but on the societies as well, when it comes to the endeavor of the earthquake resistant building design. The proposed solutions are easy to implement, relatively affordable and cause similar financial burdens in the long-term when compared to the standard construction practices (Zima et al., 2022). In this sense, it is an attractive solution against the expensive systems like seismic base isolators, massive steel braces etc., hence particularly suitable for the developing countries, where it is practically impossible to rehabilitate the entire building stock with costly methods.

The numerical and analytical solutions introduced within this study are also thought to be practical in terms of analyzing the different variations of problems.

7.3 Suggestions for the future works

As a natural consequence of the any study, there are obviously some missing points that still remain to be unveiled. In this context, a couple of recommendations are listed below for the future studies that thought to be useful for moving this work forward.

- The extent of the experimental tests is advised to be broadened by means of sampling different material types and loading conditions. For example; various vertical loading levels for the quasi-static tests and utilizing other common masonry block elements different than the hollow clay bricks used in here. In addition, the experimental campaigns only consisted of the square shaped wall specimens. The wall height-width aspect ratios are strongly recommended to be diversified in this sense and tested on large scale specimens, since it is a known fact the infill masonry behavior might drastically change because of this reason.
- Several assumptions and simplifications were made for the numerical models in order to accelerate the analysis running time. Despite such efforts, and partially due to the complexity of the loading conditions, some analyses continued for weeks until reaching the reliable results. Future research for improving the accuracy of the numerical models and finding alternative ways for reducing the analysis time is needed.
- The proposed analytical model is essentially basic and intended to be used by the practitioners. On the other hand, it is suggested to be tested with the different experimental conditions mentioned above. The strut analogy topic is being developed for many decades already, however, no perfect all-in-one solution could be found yet, where in-plane and out-of-plane effects are successfully taken into consideration for any masonry type and loading conditions. Therefore, it should be noted that the proposed analytical model is very open to improvements.

APPENDIX A. PUFJ MESH SENSITIVITY ANALYSES

The assumptions and simplifications about the numerical modeling of PUFJ are previously given in Chapter 5. In any case, mesh sensitivity analyses are required especially for such highly deformable materials. In this sense, three different mesh sizes are checked; namely coarse (20 mm), fine (10 mm) and extra fine (5 mm). The geometrical dimensions of the mesh sensitivity models are determined in a way to represent the conditions of the large-scale experiments conducted in this study. For this purpose, a random frame-infill interface element with the dimensions of $2200 \times 50 \times 20$ (units in mm) is chosen and numerically analyzed through; tension, compression, and orthogonal two shear directions. The geometrical details are presented in Figure A.1. The results are given in Figures A.2-A.5. Except the tension analyses, the mesh types give close results regardless of the density. On the other hand, for the accurate and time-efficient analyses, 10 mm mesh size seems reasonably sufficient for the purposes of this study.

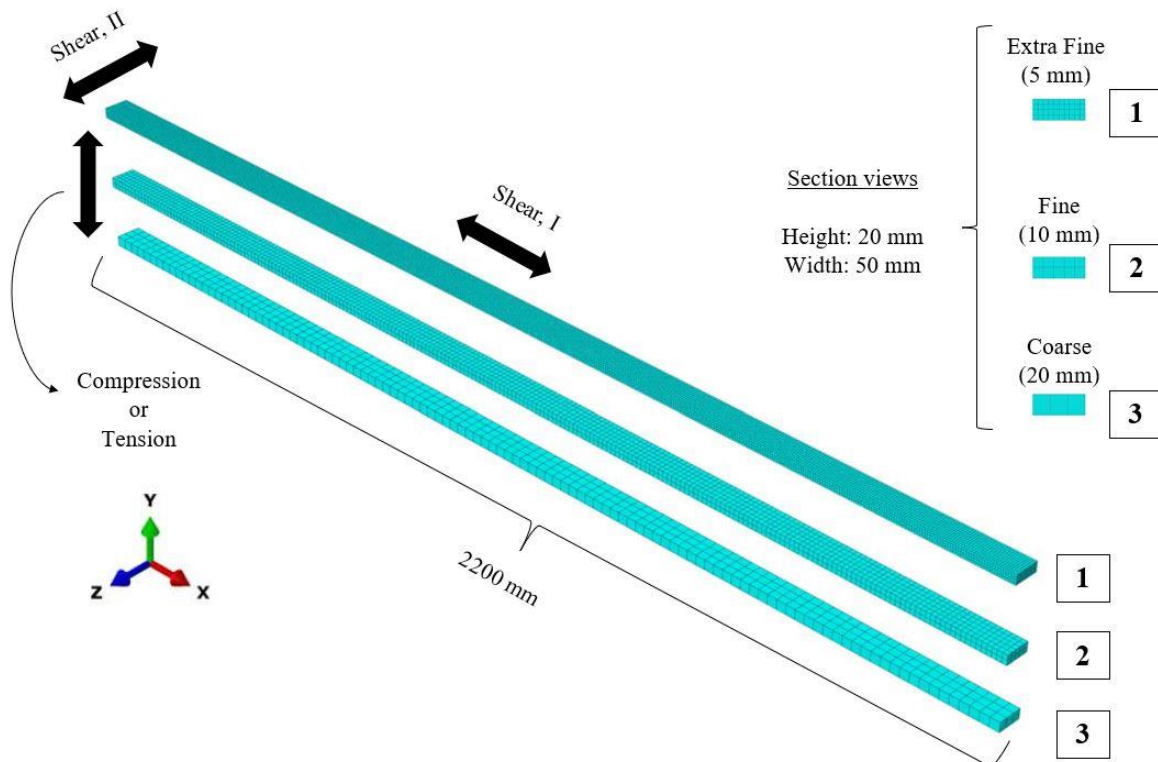


Figure A.1. Geometrical details and loading directions for the mesh sensitivity analyses.

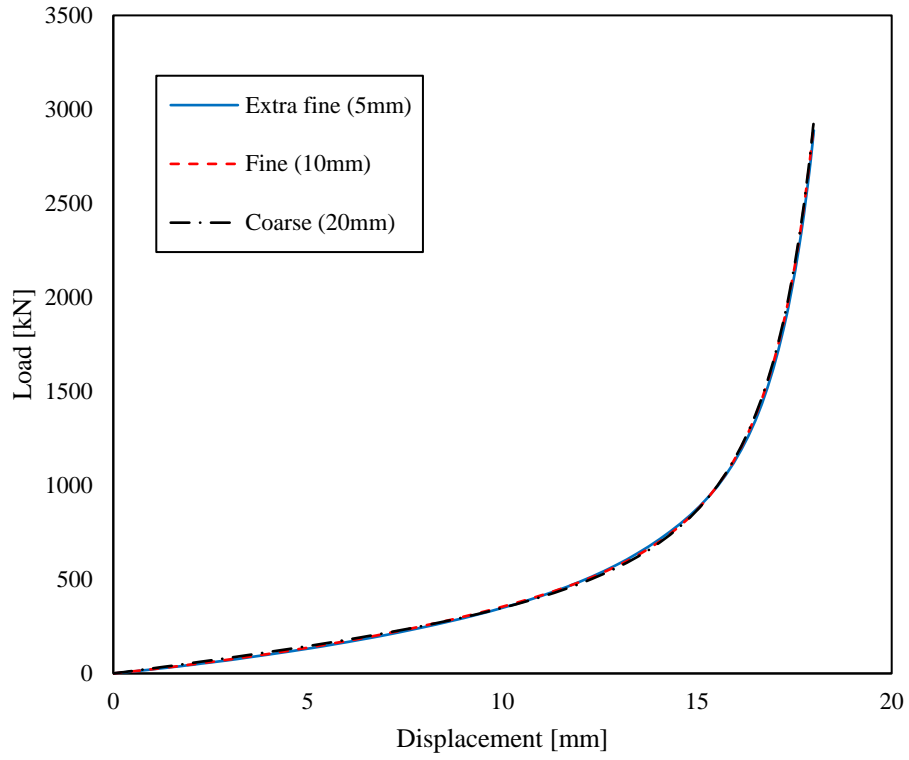


Figure A.2. Compression mesh sensitivity results.

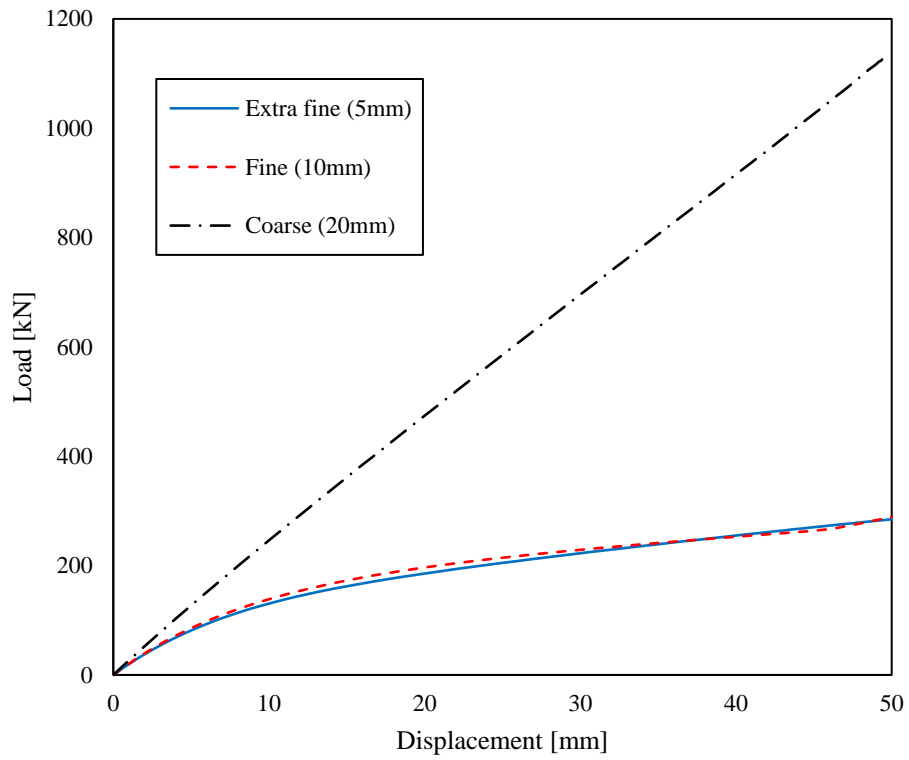


Figure A.3. Tension mesh sensitivity results.

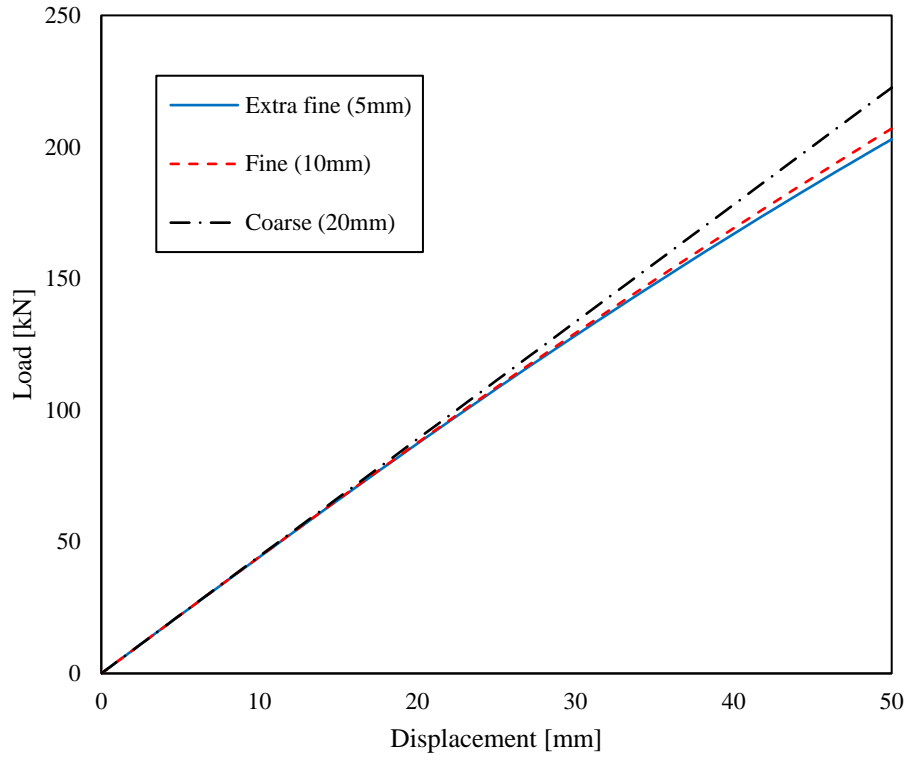


Figure A.4. Shear, I mesh sensitivity results.

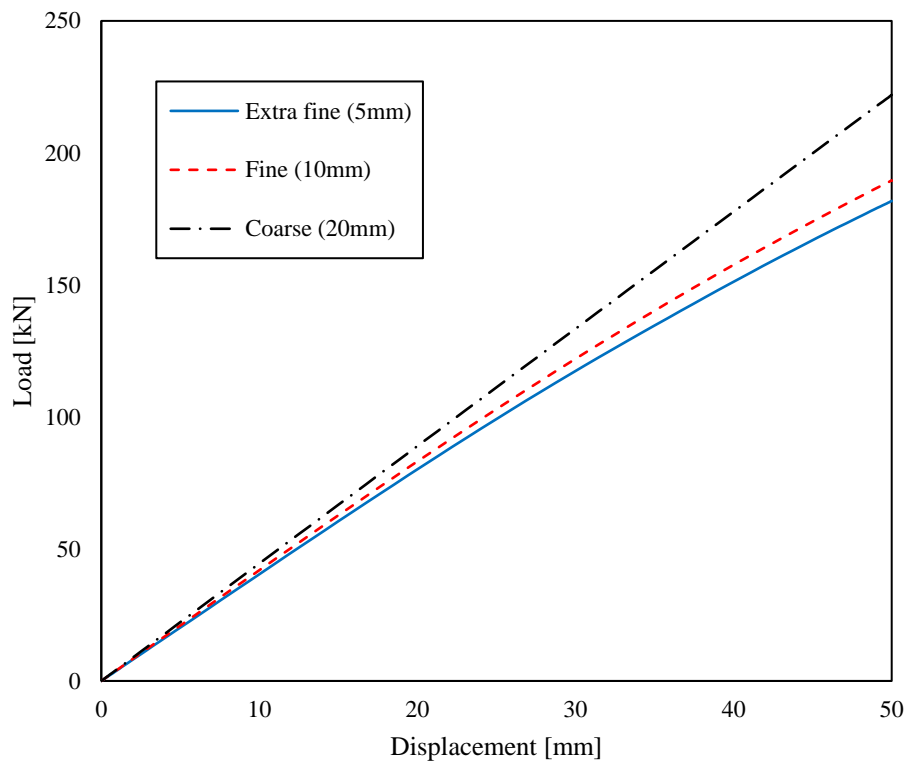


Figure A.5. Shear, II mesh sensitivity results.

APPENDIX B. MATERIAL MODELING DETAILS

Concrete

It is mentioned earlier that three phases exist for the compressive stress-strain relation of the concrete, see Section 5.1.1. Equations 5.9-5.15 are employed while plotting the curve in Figure 5.13a. All required parameters together with their descriptions are given in Table B.1. Moreover, the input values for the numerical analyses are also given in Table B.2.

Table B.1. Concrete parameters used for the numerical models.

Reference	Label	Unit	Value	Description
fib (2010)	f_{ck}	MPa	35	Characteristic compressive strength
	$f_{ck,cube}$	MPa	45	Characteristic compressive strength (cube)
	f_{cm}	MPa	43	Mean compressive strength
	ν	-	0.2	Poisson's ratio
	E_{ci}	MPa	35000	Initial elastic modulus
	E_{c1}	MPa	18200	Secant modulus at peak compressive strength
	ε_{c1}	-	2.30×10^{-3}	Strain at peak compressive strength
	$\varepsilon_{c,lim}$	-	3.50×10^{-3}	Limit strain (end of Phase II)
	k	-	1.923	Plasticity number (E_{ci}/E_{c1})
	G_{Fc}	N/mm	0.144	Fracture energy
	f_{ctm}	MPa	3.21	Tensile cracking strength
	ε_{c0}	-	4.91×10^{-4}	Ultimate elastic strain (end of Phase I)
Kratzig and Polling (2004)	l_{eq}	mm	50	Finite element mesh characteristic length
	G_{cl}	N/mm	71.83	Crushing energy ($\approx 500G_F$)
	b_c	-	0.70	Plastic-to-inelastic strain ratio for compression
	b_t	-	0.85	Plastic-to-inelastic strain ratio for tension
	γ_c	-	0.961	Parameter controlling the stress-strain curve swept area

The tensile behavior is rather simpler, since two phases exists; one for the initial linear elastic, and the second is parabolic softening, see Figure 5.6. The stress-strain curve is plotted using Equation 5.18 and presented in Figure 5.13b. All required parameters are already given above in Table B.1. The input values are provided in Table B.3.

Table B.2. Concrete compressive behavior input values.

Phase	Remark	Engineering strain [-]	Engineering stress [MPa]	Inelastic strain [-]	True stress [MPa]	Damage variable - dc [-]
I	$0.4f_{cm}$	4.91×10^{-4}	17.20	0.00	17.21	0.000
		9.44×10^{-4}	27.56	1.55×10^{-4}	27.58	0.056
II	f_{cm}, ε_{c1}	1.40×10^{-3}	36.03	3.64×10^{-4}	36.08	0.096
		1.85×10^{-3}	41.23	6.66×10^{-4}	41.30	0.145
		2.30×10^{-3}	43.00	1.07×10^{-3}	43.10	0.206
		2.60×10^{-3}	42.97	1.37×10^{-3}	43.08	0.250
		2.90×10^{-3}	42.86	1.67×10^{-3}	42.99	0.289
		3.20×10^{-3}	42.69	1.97×10^{-3}	42.83	0.326
		3.50×10^{-3}	42.45	2.28×10^{-3}	42.60	0.359
		7.29×10^{-3}	35.15	6.25×10^{-3}	35.41	0.649
		1.08×10^{-2}	26.12	9.97×10^{-3}	26.40	0.798
		1.40×10^{-2}	19.31	1.33×10^{-2}	19.58	0.877
III	$\varepsilon_{c,lim}$	1.69×10^{-2}	14.76	1.63×10^{-2}	15.01	0.919
		1.95×10^{-2}	11.74	1.90×10^{-2}	11.97	0.943
		2.18×10^{-2}	9.70	2.13×10^{-2}	9.91	0.958
		2.39×10^{-2}	8.29	2.34×10^{-2}	8.49	0.966
		2.56×10^{-2}	7.30	2.51×10^{-2}	7.49	0.972
		2.71×10^{-2}	6.59	2.65×10^{-2}	6.77	0.976
		2.83×10^{-2}	6.10	2.77×10^{-2}	6.27	0.979
		2.91×10^{-2}	5.76	2.85×10^{-2}	5.93	0.981
		2.97×10^{-2}	5.55	2.91×10^{-2}	5.71	0.982
		3.00×10^{-2}	5.45	2.94×10^{-2}	5.61	0.982

Table B.3. Concrete tensile behavior input values.

Stage	Inelastic strain [-]	True stress [MPa]	Damage variable - dt [-]
f_{ctm}	0.00	3.21	0.000
Parabolic softening with calibrated descending values	2.20×10^{-4}	2.75	0.295
	4.40×10^{-4}	2.09	0.525
	6.70×10^{-4}	1.76	0.666
	8.90×10^{-4}	1.57	0.748
	1.11×10^{-3}	1.44	0.802
	1.33×10^{-3}	1.34	0.839
	1.56×10^{-3}	1.26	0.867
	1.78×10^{-3}	1.19	0.887
	2.00×10^{-3}	1.14	0.902
	2.22×10^{-3}	1.09	0.914
	2.45×10^{-3}	1.05	0.925
	2.67×10^{-3}	1.01	0.932
	2.89×10^{-3}	0.98	0.939
	3.11×10^{-3}	0.95	0.945
	3.33×10^{-3}	0.93	0.950
	3.56×10^{-3}	0.90	0.954
	3.78×10^{-3}	0.88	0.957
	4.00×10^{-3}	0.86	0.961
	4.22×10^{-3}	0.84	0.963
	4.45×10^{-3}	0.83	0.966

Masonry

Similar to concrete, the masonry constitutive model consists of two distinctive stress-strain relations; compressive and tensile. The first one is created based on the homogenized approach (the isotropic model, namely single elasticity variable in any direction) for the bricks. Kaushik et al. (2007) proposed Equation 5.34 for obtaining the masonry peak compressive strength – $f'_{m,c}$, which depends on the compressive strength values of bricks (f_{br}) and mortar (f_{jm}). Similarly, Eurocode-6 (CEN, 2005) also propose an equation in case thin-layer mortar is used (as in this study). Accordingly, Equation B.1 is used for calculating the masonry compressive strength, where K_{EC} is a constant determined based on the specific masonry groups indicated as in Eurocode-6 (CEN, 2005). For the thin-layer mortar and Group 2 of masonry category, this value is taken as 0.70. Moreover, as previously mentioned in Section 4.1, the brick producer declared that f_{br} should be greater than or equal to 10 MPa. The mortar type M10 also corresponds to the 10 MPa strength level, see Section 4.1. Considering these values, a comparison is made between the proposals of Kaushik et al. (2007) and Eurocode-6 (CEN, 2005) approaches and given in Table B.4.

$$f'_{m,c} = K_{EC} f_{br}^{0.7} \quad (B.1)$$

Table B.4. Different approaches for the masonry compressive strength.

Proposal	Parameters			Result
	K_{EC}	f_{br} [MPa]	f_{jm} [MPa]	$f'_{m,c}$ [MPa]
Kaushik et al. (2007)	-	10	10	4.07
Eurocode-6 (CEN, 2005)	0.7	10	-	3.51

On the other hand, thanks to the data from the vertical compressive tests on the triplet specimens (see Section 4.1), it is possible obtain the actual strength of the walls directly from the experimental results (in the stronger bearing direction, parallel to the holes). For this direction, mean value of the $f'_{m,c}$ is determined as 7.53 MPa, by means of dividing the average force (≈ 96 kN, see Table 4.1) to the net area of the perforated brick surfaces (gross: 250 mm \times 100 mm) that has nearly 51% of the solid area. As a side note, this solid-to-gross surface area ratio is given as 0.50 throughout the dissertation which practically does not lead to any meaningful difference, yet provides convenient numerical simplifications (particularly for meshing) such as reducing the brick thickness to the exact half, Figure 5.16. Nevertheless, since the aforementioned proposals considerably underestimate the compressive strength, the actual test results are utilized for calculating the remaining parameters. Because the complete stress-strain relation is established in Kaushik et al. (2007), Equations 5.35-5.36 are employed for

obtaining the strain value at the peak stress, $\varepsilon'_{m,c}$, where the masonry Young's modulus, E_m , is firstly needs to be determined. For this purpose, diagonal shear tests on the wallet specimens are the convenient available sources. The wallet tests were performed according to the provisions of ASTM E519-07 (ASTM, 2010), see Section 4.1. The standard also proposes Equation B.2 for determining the S_{sw} – shear strength of the wallet specimens, corresponding the wallet surface net area – A_{wn} , where P_d is the diagonally applied load. Moreover, A_{wn} is a product of the wallet width – w_w , height – h_w , thickness – t_w , and the ratio of the solid area to gross – n_w , as given in Equation B.3. The geometrical details are shared in Figure 4.8.

$$S_{sw} = \frac{0.707P_d}{A_{wn}} \quad (B.2)$$

$$A_{wn} = \left(\frac{w_w + h_w}{2} \right) t_w n_w \quad (B.3)$$

Once the shear stress, S_{sw} , is obtained, the shear strain γ_{sw} can be extracted according to Equation B.4, where ΔV_w and ΔH_w are the vertical shortening under compressive and the horizontal elongation under tensile effects, respectively. Besides, the vertical gauge length is denoted with g_w .

$$\gamma_{sw} = \frac{\Delta V_w + \Delta H_w}{g_w} \quad (B.4)$$

Using this information, it is possible to calculate the shear modulus (modulus of rigidity) of the wallet specimens, G_w , Equation B.5. Following that, E_m can be obtained using Equation B.6 from Eurocode-6 (CEN, 2005), which states a relation between the elastic and shear modulus values of masonries.

$$G_w = \frac{S_{sw}}{\gamma_{sw}} \quad (B.5)$$

$$E_m = \frac{G_w}{0.4} \quad (B.6)$$

The calculated values and their respective descriptions are given in Table B.5. Other than that, the so-called elastic branches of the wallet tests for compressive and tensile regimes are presented in Figure B.1. Dark shaded curves indicate the experimental results, whereas the red lines are plotted using the peak load – $F_{d,max}$ and the assumed secant stiffness values which are used for obtaining the mean values of ΔV_w and ΔH_w . It is seen that satisfying match is achieved, which in return provides a reasonable E_m value that is used for the numerical analyses.

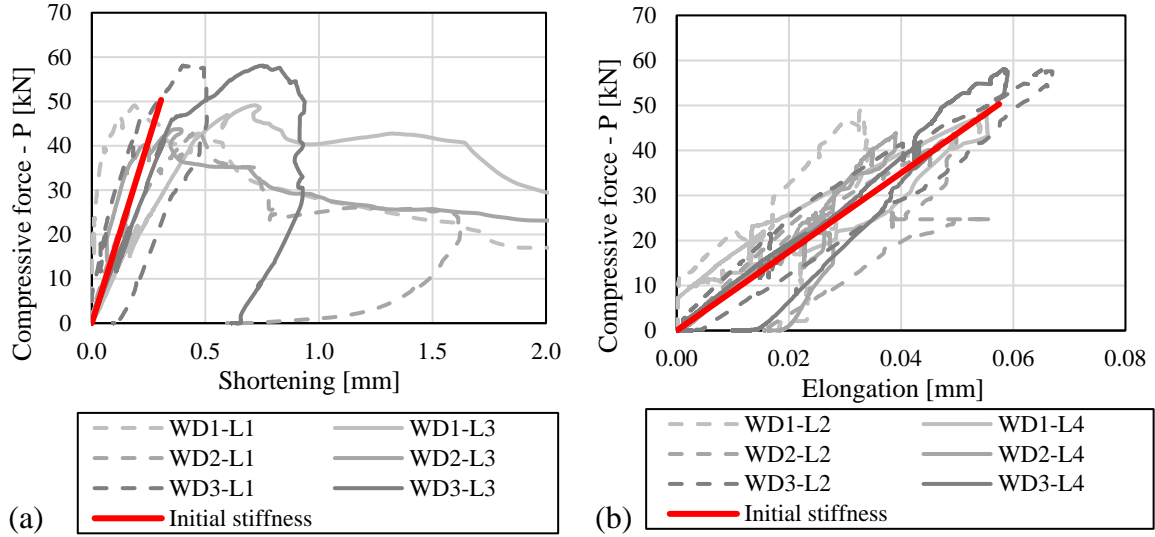


Figure B.1. Initial elastic regimes of the wallet specimens; (a) compressive and (b) tensile.

Table B.5. Masonry parameters used for the numerical models.

Label	Unit	Value	Description
P_d	N	50333	Mean peak load of the wallet tests ($F_{d,max}$ from Table 4.4)
w_w	mm	1000	Wallet width (Figure 4.8)
h_w	mm	950	Wallet height (Figure 4.8)
t_w	mm	100	Wallet thickness (equals to brick thickness in Figure 4.2)
n_w	-	0.50	Ratio of the solid area to gross - appx. 50% (Figure 5.16)
A_{wn}	mm ²	48750	Wallet surface net area (bed joint)
ΔV_w	mm	0.305	Vertical shortening (from gauges L1, L3 in Figure 4.8)
ΔH_w	mm	0.057	Horizontal elongation (from gauges L2, L4 in Figure 4.8)
g_w	mm	1000	Extensometer gauge length (L1, L2, L3, L4 in Figure 4.8)
γ_{sw}	-	3.63×10^{-4}	Shear strain
S_{sw}	MPa	0.730	Shear stress on the net area
G_w	MPa	2013	Shear modulus (modulus of rigidity)
E_m	MPa	5034*	Elastic modulus (Young's modulus)

* Rounded up to 5100 MPa for the numerical analyses

Upon determining E_m , the strain value corresponds to the peak stress, $\epsilon'_{m,c}$, is obtained using Equations 5.35-5.36, where C_j is found as 0.152 and $\epsilon'_{m,c}$ equals to 2.9×10^{-3} . Following that, the complete stress-strain relation for the compressive behavior is plotted using Equation 5.37. The values are given in Table B.6.

For the tensile behavior, $f'_{m,t}$ is taken $0.1f'_{m,c}$ as already discussed in Section 5.1. The softening branch, starting from the cracking point until the total strength loss, is represented by a parabolic curve with arbitrarily calibrated values that yield the fracture energy G_{Fm} equals to 0.078 N/mm. The details are shared in Table B.7.

Finally, the interface contact parameters are defined. That being said, Kj_{nn} , Kj_{ss} and Kj_{tt} are calculated using Equations 5.41-5.42. Elastic modulus of the bricks (E_{br}) and masonry

joint (E_{jm}) are taken as 5100 MPa and 2000 MPa, respectively. The first one equals to the masonry overall elastic modulus which is already explained above. This assumption is made, since the simplified-micro modeling technique is mostly correlated to the brick properties in a masonry overall modeling, especially when the thin-layer mortar is used such as in this case. Besides, there is a lack of information about the brick elastic properties in this regard, as no information is shared by the manufacturer and the laboratory tests did not include this specific topic. On the other hand, E_{jm} is determined by the proposal of Kaushik et al. (2007), which states that E_{jm} might be taken 200 times as of the mortar compressive strength that is around 10 MPa, see Section 4.1.1. Furthermore, though the actual construction practice in the laboratory tests aimed at providing 3 mm mortar joint thickness, h_{jm} , it is assumed to be 5 mm for the numerical analyses. The value is rounded up, since imperfections are very often encountered in terms of arranging a smooth thickness through the all surface, and having this value relatively higher cause more conservative results (lower stiffness values) that takes into account such defects indirectly. Lastly, the Poisson's ratio – ν , is assumed to be 0.15 and 0.20 for the brick and mortar elements respectively, without any specific testing but following some random approaches that can found in the literature. As a result, the shear modulus of bricks (G_{br}) and mortar joint (G_{jm}) can be extracted with respect to the elastic modulus using the well-known Equation B.7, and these are found as 2217 MPa and 833 MPa, respectively.

$$G = \frac{E}{2(1 + \nu)} \quad (\text{B.7})$$

It should be noted that, the contact stiffness formulation mentioned here is not primarily developed for the thin-layer mortar (Lourenco, 1996), yet it is noticed upon preliminary analyses that even significantly different values (roughly between 50% and 300% of the values used here) did not alter the global results much, specifically for this study. Therefore, no further investigation is made on it exclusively. In this sense, it is noticed that the damage criteria have higher influence on the results. The damage initiation stress for the normal direction (tj_n) is determined on the basis of several iterations, since there is a limited information that could be found in the literature about this topic. For example, Schneemayer et al. (2014) calculated the tensile strength of M10 mortar, which is the same type used in this study, as 1.75 MPa. However, this value yielded unrealistic results when compared to the experiments of this study. It gives a hint that, possibly, mortar-to-brick interface failure is the dominant mechanism that is difficult to distinguish when thin-layer mortar is used, which is also out of scope in this case since the joints are modeled implicitly as previously mentioned. Nasiri and Liu (2019)

determined tj_n equals to 0.40 MPa, by means of referring also some other researches. Eventually, this value is adapted in the numerical analyses, because it provided reasonable results. On the other hand, shear damage initiation stresses in the orthogonal directions, namely tj_s and tj_t , are taken equal and extracted from the triplet shear tests given in Section 4.1, by means of dividing the average ultimate shear force (22.5 kN) to the net area of the perforated brick surfaces and found 0.88 MPa. Lastly, the damage evolution is represented by an ultimate separation level assumed to be 0.50 mm, which is determined iteratively from the suggestions and test results of Lourenco (1996).

Table B.6. Masonry compressive behavior input values.

Stage	Engineering strain [-]	Engineering stress [MPa]	Inelastic strain [-]	True stress [MPa]	Damage variable – $d_{c,m}$ [-]
Parabolic ascending (hardening)	5.00×10^{-4}	2.37	0.00	2.37	0.000
	1.00×10^{-3}	4.30	1.57×10^{-4}	4.30	0.000
	1.60×10^{-3}	6.02	4.19×10^{-4}	6.03	0.000
	2.40×10^{-3}	7.31	9.63×10^{-4}	7.32	0.000
$\epsilon'_{m,c} @ f'_{m,c}$	2.90×10^{-3}	7.53	1.42×10^{-3}	7.55	0.000
$\epsilon'_{m,c} @ 0.9 f'_{m,c}$	3.80×10^{-3}	6.81	2.45×10^{-3}	6.83	0.095
$2.75 \epsilon'_{m,c} @ 0.2 f'_{m,c}$	7.98×10^{-3}	1.51	7.65×10^{-3}	1.52	0.799
Arbitrary softening for numerical stability	1.00×10^{-2}	1.22	9.71×10^{-3}	1.23	0.837
	1.20×10^{-2}	0.98	1.17×10^{-2}	0.99	0.869
	1.40×10^{-2}	0.79	1.37×10^{-2}	0.80	0.894
	1.60×10^{-2}	0.64	1.57×10^{-2}	0.65	0.913
	1.80×10^{-2}	0.55	1.77×10^{-2}	0.56	0.926
	2.00×10^{-2}	0.50	1.97×10^{-2}	0.51	0.932

Table B.7. Masonry tensile behavior input values.

Stage	Inelastic strain [-]	True stress [MPa]	Damage variable – $d_{t,m}$ [-]
$f'_{m,t} (\approx 0.1 f'_{m,c})$	0.00	0.75	0.000
Parabolic softening with calibrated descending values $G_{Fm} = 0.078$ N/mm	1.10×10^{-4}	0.53	0.293
	2.20×10^{-4}	0.38	0.490
	3.35×10^{-4}	0.29	0.618
	4.45×10^{-4}	0.22	0.701
	5.55×10^{-4}	0.18	0.755
	6.65×10^{-4}	0.16	0.791
	7.80×10^{-4}	0.14	0.818
	8.90×10^{-4}	0.12	0.842
	1.00×10^{-3}	0.11	0.860
	1.11×10^{-3}	0.09	0.878
	1.23×10^{-3}	0.08	0.893

Table B.7. (continued).

Stage	Inelastic strain [-]	True stress [MPa]	Damage variable – $d_{t,m}$ [-]
Parabolic	1.34×10^{-3}	0.07	0.910
softening	1.45×10^{-3}	0.06	0.925
with	1.56×10^{-3}	0.04	0.940
calibrated	1.67×10^{-3}	0.04	0.952
descending	1.78×10^{-3}	0.03	0.964
values	1.89×10^{-3}	0.02	0.976
$G_{Fm} = 0.078$ N/mm	2.00×10^{-3}	0.01	0.985

Reinforcement steel

Establishing the material constitutive model of the steel bars requires to take into consideration various parameters. Geometrical and mechanical features of both concrete and steel are utilized as the input values through Equations 5.21-5.33. In this way, the modified strength, strain and elastic modulus values are obtained. Details are provided in Table B.8.

Table B.8. Reinforcement steel parameters used for the numerical models.

Category	Label	Unit	Value	Description
Mechanical (input)	E_{st}	MPa	2.00×10^5	Steel elastic modulus (bare)
	$f_{y,st}$	MPa	550	Steel yield strength (bare)
	σ_{ti}	MPa	3.21	Concrete cracking strength
Geometry (input - rebar)	d_b	mm	16	Reinforcement bar diameter (generalized value)
	ρ_{st}	-	0.026	Longitudinal reinforcement ratio
	A_{st1}	mm ²	157	Area of stirrup (bar diameter: 10 mm)
	S_{st}	mm	100	Stirrup spacing
	A_s	mm ²	1608	Longitudinal reinforcement area
Geometry (input - concrete)	h_{cs}	mm	250	Column cross-section height
	d_{cs}	mm	210	Effective depth
	b_{cs}	mm	250	Column cross-section width
	C_c	mm	40	Concrete cover
	m_{cs}	-	5.39	Height and width dependant cross-sectional quantity
	$A_{c,eff}$	mm ²	53925	Effective concrete area
	ρ_{eff}	-	0.030	Effective reinforcement ratio
Geometry and Mechanical (product)	S_{rm}	mm	99.33	Minimum crack spacing length
	K_{st}^-	-	0.039	Coefficient for the stirrup effects
	K_{co}	-	2.50	Concrete cover and bar diameter dependant quantity
	K_{st}	-	3.80	Stirrup effect related coefficient
	δ_{st}^-	-	0.703	Maximum bar slip
	l_{st}	mm	33.28	Transmission length
	B_{st}	-	0.017	Strength and reinforcement ratio dependant quantity
	$f_{y,st}^*$	MPa	502	Embedded bar yield strength
Result	ε_{st}	-	2.51×10^{-3}	Strain corresponding to $f_{y,st}^*$
	E_{st}^*	MPa	106205	Modified elastic modulus
	E_{sp}^*	MPa	637	Modified hardening modulus

Equivalent strut parameters

Determination of the equivalent strut parameters starts with obtaining the strut width – w_{inf} . All required values are calculated for Frame A according to the Equations 6.1-6.7, and given Table B.9 with their explanations.

Table B.9. Details of the equivalent strut parameters for Frame A (stiff mortar frame).

Category	Label	Unit	Value	Description
External Loads	F_v	N	750000	Vertical load on the columns
	ε_v	-	1.71×10^{-4}	Vertical deformation parameter of the columns
Geometry	A_{col}	mm ²	62500	Single column cross sectional area
	A_{bm}	mm ²	62500	Single beam cross sectional area
	t_{inf}	mm	50	Wall thickness (only the net area is considered)
	h_{inf}	mm	2200	Wall clear height
	h'_{inf}	mm	2450	Frame height
	l_{inf}	mm	2200	Wall clear width
	l'_{inf}	mm	2450	Frame width
	d_{inf}	mm	3111	Wall diagonal length
Mechanical	ν_d	-	0.25	Diagonal Poisson ratio (approximate value)
	E_d	MPa	3600	Diagonal Young's modulus (Assumed as $\approx 0.707E_m$, considering aspect ratio)
	E_f	MPa	35000	RC frame concrete Young's modulus
Mechanical and Geometry	λ_{inf}^*	-	0.252	Stiffness characterization parameter
Product	k_v	-	1.035	Vertical load effects parameter
	z_{inf}	-	1.000	Panel shape parameter
	β_p	-	0.152	Poisson ratio related parameter
	c_p	-	0.282	Poisson ratio related parameter
Result	w_{inf}	mm	1118	Equivalent strut width

Following the process flow presented in Figure 6.4, the next step is determining the F_{peak} value using the w_{inf} . For this purpose, the ultimate shear stress on the bed joints at the failure of wallet specimens, τ_{ul} , is obtained from the triplet shear tests (see Chapter 4). The average of peak loading values of the all specimens was calculated as 22.5 kN, which corresponds to $\tau_{ul} = 0.88$ MPa considering only the net area of the perforated brick surfaces. Finally, F_{peak} is derived by means of multiplying τ_{ul} with the cross-sectional area of the diagonal strut, A_{srt} . It is important to mention that an adjustment multiplier with the value of 1.2 is added in this equation, since it provides higher accuracy with the experiments given in this study. As a result, the equation can be written as; $F_{peak} = 1.2 \tau_{ul} A_{srt}$. Later, the cracking load, F_{cr} , is calculated as a fraction of F_{peak} , where $F_{cr} = 0.8 F_{peak}$. The values are already provided for those in Table 6.1. Therefore, the remaining parameters, namely K_{peak} , K_{cr} and

K_{soft} are given here as 100.6, 503.2 and 2.52 (all in kN/mm), respectively. As previously mentioned in Chapter 6, while the force values remain the same for the PUFJ implemented frames (Frame B and Frame C) as of the stiff mortar frame (Frame A), cracking and peak displacement values – d_{cr} and d_{peak} – are multiplied by 1.33 and 2.00 for the Frame B and Frame C, respectively. Besides, the residual forces are determined as the variations of F_{peak} , where 50% (for Frame B) and 90% (Frame C) of the initial value were found adequately matching with the experiments, see Figure 6.3.

Here, only the values of analytical calibration results of the in-plane experimental tests (Section 6.1) are given with details. For the representation of the dynamic response in a hypothetical building (Section 6.2), the same steps are to be followed which can be easily done using the aforementioned information. Nevertheless, the w_{inf} values for the frame span types of 6×3 and 3×3 (see Figure 6.8 and Table 6.2) are calculated as 1289 mm and 1536 mm, respectively. A constant vertical load, F_v , is assumed as 700 kN for the both types as a simplicity. The remaining independent parameters, namely the mechanical ones only, are taken the same as given in Table B.9.

Moreover, the input values belong to different equivalent strut types are presented on force-axial displacement multi-linear curves in Figure B.2. The first values in the dialog boxes represent the horizontal axis (axial displacement), whereas the second ones show values on vertical axis (force).

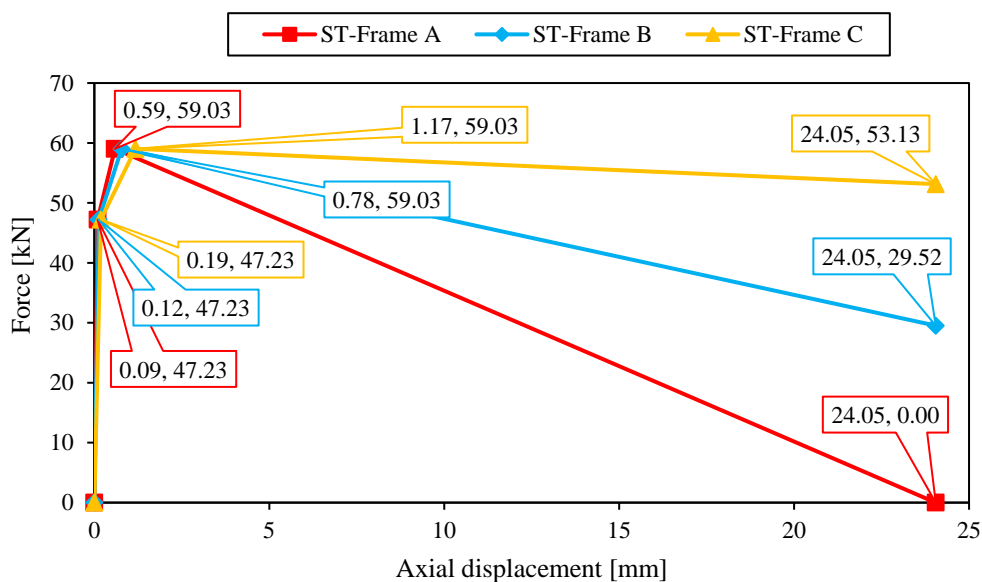


Figure B.2. Equivalent strut force-axial displacement input values for the pushover analyses.

APPENDIX C. ENERGY BALANCE OF THE NUMERICAL MODELS

Although the explicit analysis algorithm provides robust solutions, the results might be questionable sometimes especially for the quasi-static problems, unless sufficient time steps or required damping properties are introduced to the solver engine. An effective way of checking the accuracy of the analyses can be done using the energy balance equations. In short, total energy of the structural system (E_{TE}) should approach zero during the whole process (Tarque et al., 2014). This rule is expressed by Equation C.1, where E_{EW} , E_{IE} and E_{KE} represent the external work, internal energy, and kinetic energy, respectively. Some other energy types, such as viscoelastic one might also be included in this equation, but it is not extracted during the analyses. In this sense, the deviations in the equation could be attributed to the such type of different energy phenomenon, which are typically desired to be avoided as much as possible, unless specially designed as a part of the system feature.

Nevertheless, the large-scale quasi-static analyses given in Section 4.1 are evaluated in this manner. Since the models represent the quasi-static loading conditions, the kinetic energy of the model is also anticipated to be close to zero. Besides, the external and internal energies are desired to be on similar levels for a true representation of the nature. The results are given for the frame samples mentioned in Section 4.1, and presented in Figures C.1-C.4. Accordingly, it can be said that reasonable achievement could be obtained in this context for the all models, though, a sudden jump nearly at the end of analysis is observed for Frame B in Figure C.3, which indicates a deficiency probably about the solution description or it is a result of intensive material failures, yet in a limited portion, thus could be ignored.

$$E_{TE} = E_{KE} + E_{IE} + E_{VE} - E_{EW} \quad (C.1)$$

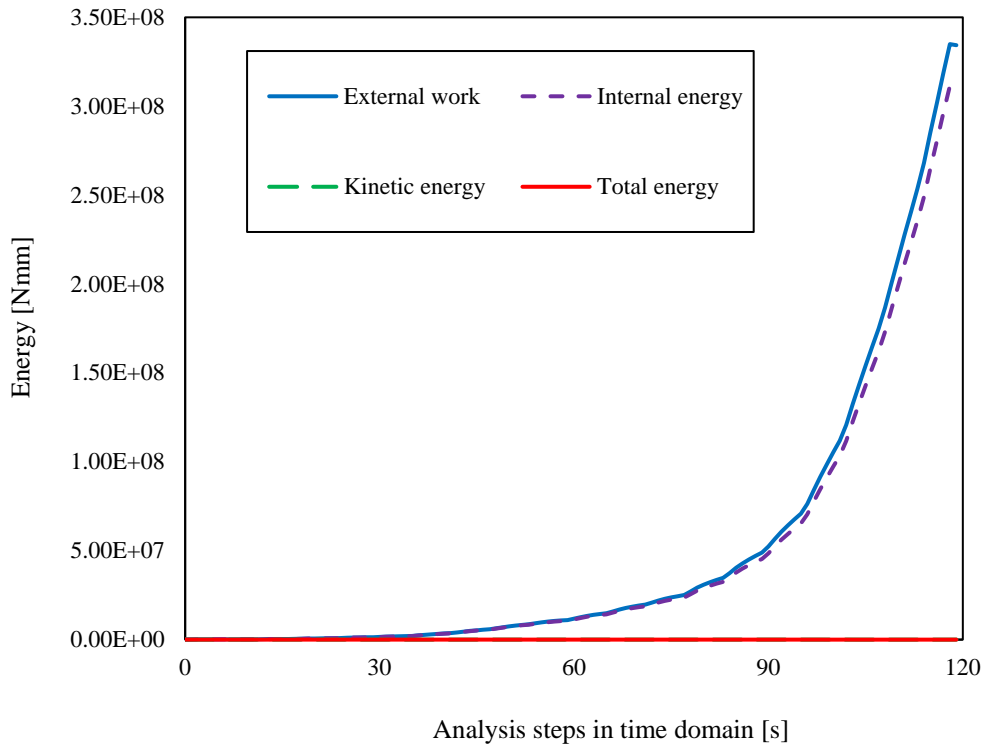


Figure C.1. Energy balance results of the Bare-Frame.

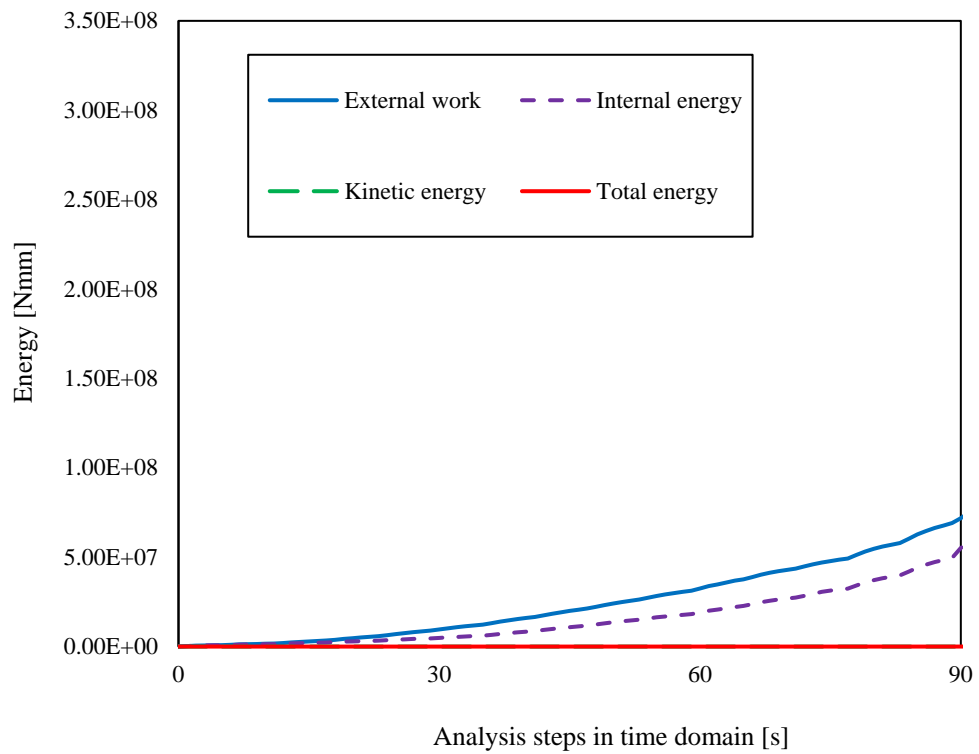


Figure C.2. Energy balance results of the Frame A.

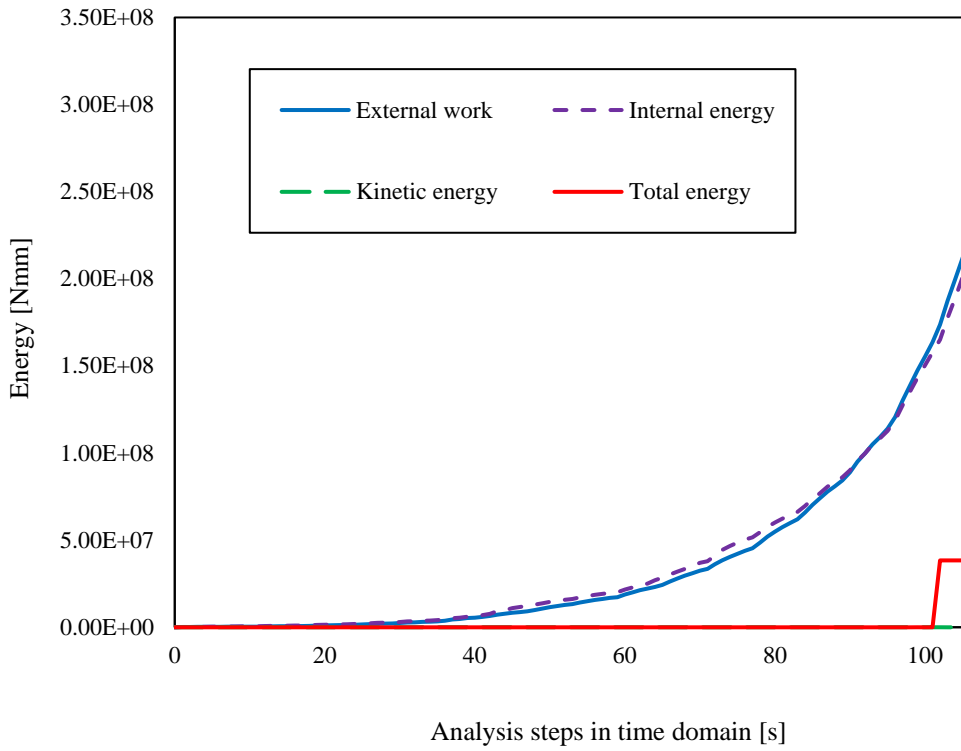


Figure C.3. Energy balance results of the Frame B.

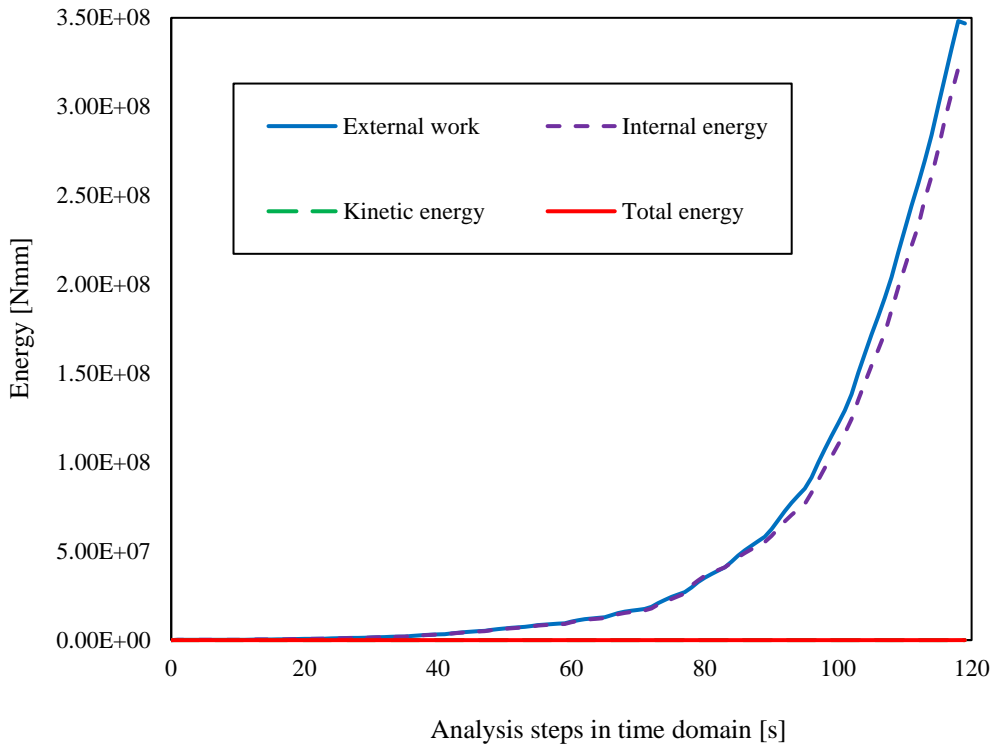


Figure C.4. Energy balance results of the Frame C.

APPENDIX D. MESHING DETAILS OF THE NUMERICAL MODELS

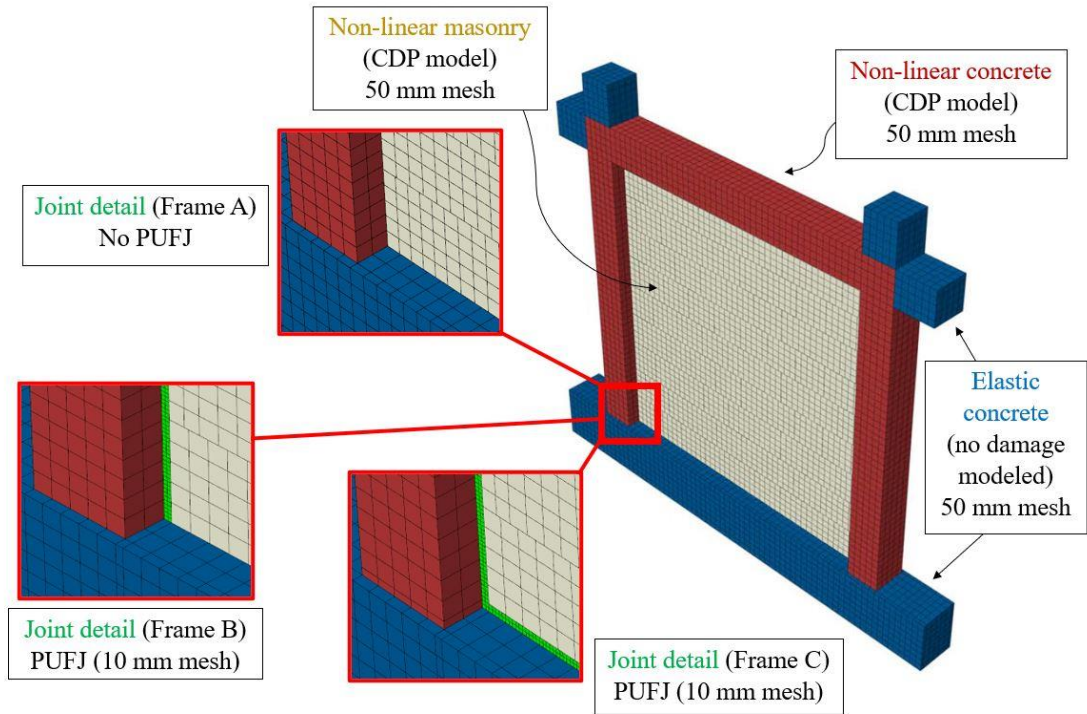


Figure D.1. Meshing details of the quasi-static in-plane numerical models.

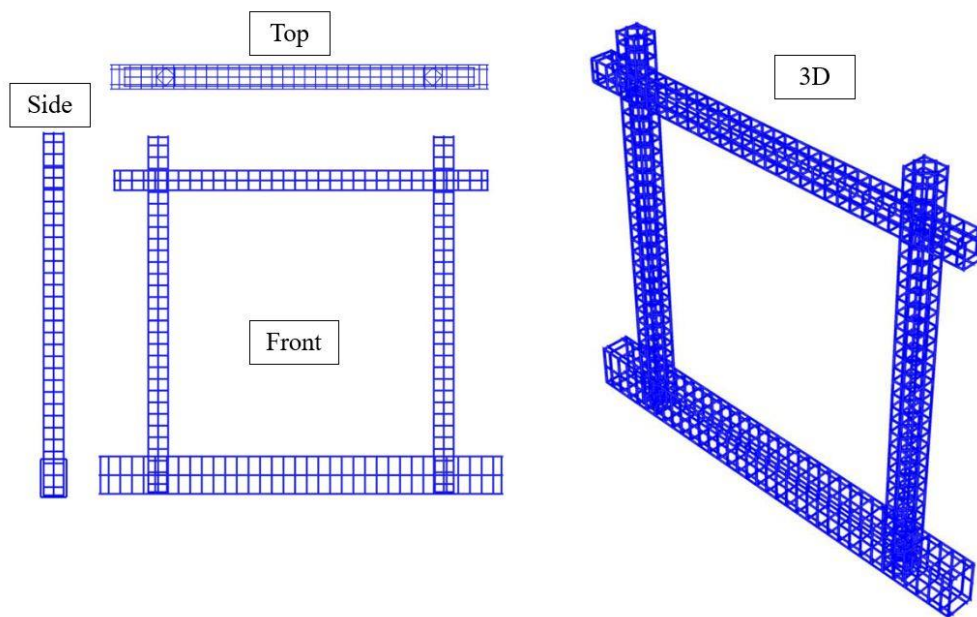


Figure D.2. Reinforcement details of the quasi-static in-plane numerical models from different view angles.

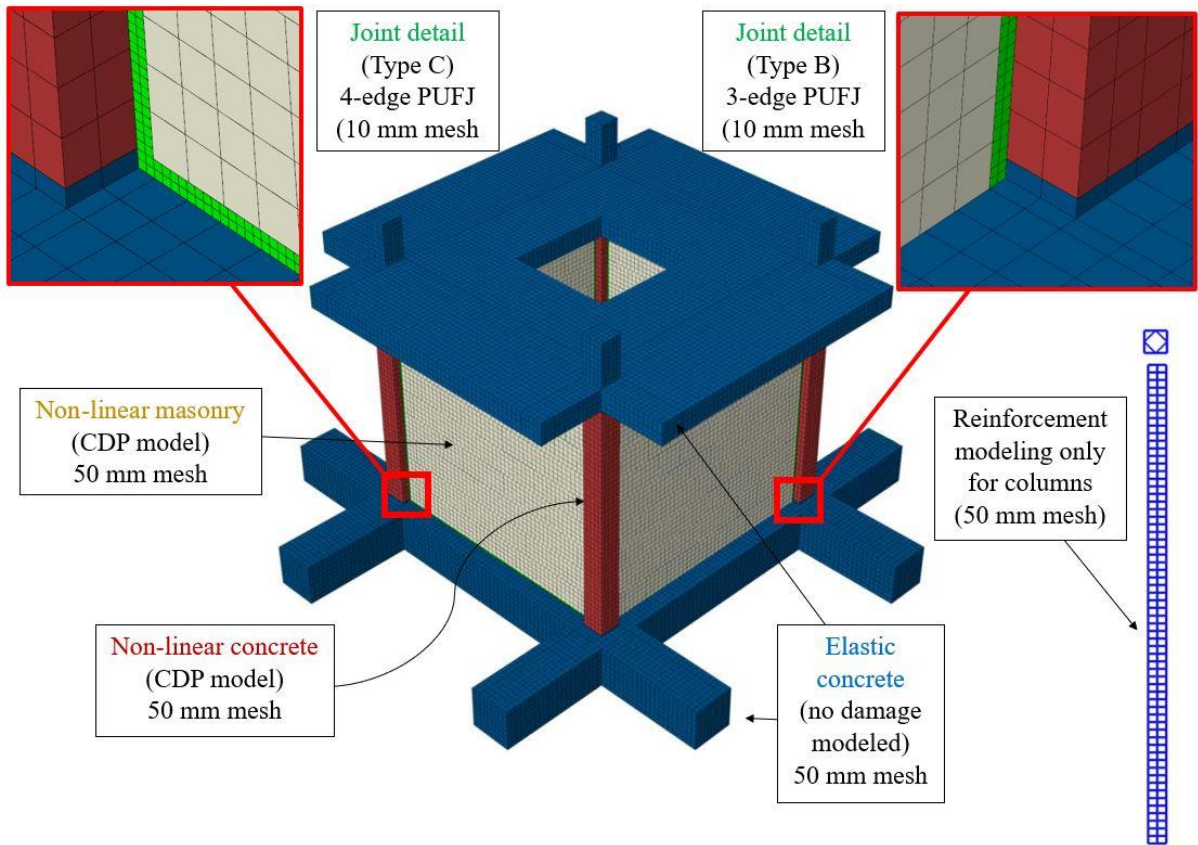


Figure D.3. Meshing and reinforcement details of the 3D dynamic analysis numerical models.

REFERENCES

- Abdul-Kadir, M. R. (1974). *The structural behaviour of masonry infill panels in framed structures* (PhD dissertation). University of Edinburgh, Edinburgh, Scotland.
- Abrams, D. P., Angel, R., & Uzarski, J. (1996). Out-of-plane strength of unreinforced masonry infill panels. *Earthquake Spectra*, 12(4), 825–844. <https://doi.org/10.1193/1.1585912>
- AFAD, Turkish Ministry of Interior, Disaster and Emergency Management Presidency, Turkish Seismic Code: Specifications for Structures to be Built in Disaster Areas (2018). Ankara, Turkiye.
- Akhoundi, F., Vasconcelos, G., Lourenço, P., Silva, L. M., Cunha, F., & Figueiro, R. (2018). In-plane behavior of cavity masonry infills and strengthening with textile reinforced mortar. *Engineering Structures*, 156, 145–160. <https://doi.org/10.1016/j.engstruct.2017.11.002>
- Al Louzi, R. A. K. (2015). *Seismic In-Plane Response of Reinforced Concrete Frames with Masonry Infill Walls* (PhD dissertation). Purdue University, West Lafayette, Indiana.
- Akyildiz, A. T., & Girgin, K. (2017). Investigation on Earthquake Safety of Buildings Constructed for the Urban Transformation of Istanbul (in Turkish). *DEU Journal of Science and Engineering*, 19(55), 100–121. <https://doi.org/10.21205/deufmd.2017195509>
- Akyildiz, A. T., Kwiecień, A., Zając, B., Triller, P., Bohinc, U., Rousakis, T., & Viskovic, A. (2020). Preliminary in-plane shear test of infills protected by PUFJ interfaces. In *Proceedings of the 17th International Brick/Block Masonry Conference (17thIB2MaC 2020), July 5-8, 2020, Kraków, Poland*. CRC Press. <https://doi.org/10.1201/9781003098508-137>
- Al-Chaar, G., Issa, M., & Sweeney, S. (2002). Behavior of masonry-infilled nonductile reinforced concrete frames. *Journal of Structural Engineering*, 128(8), 1055–1063. [https://doi.org/10.1061/\(asce\)0733-9445\(2002\)128:8\(1055\)](https://doi.org/10.1061/(asce)0733-9445(2002)128:8(1055))
- Aliaari, M., & Memari, A. M. (2005). Analysis of masonry infilled steel frames with seismic isolator subframes. *Engineering Structures*, 27(4), 487–500. <https://doi.org/10.1016/j.engstruct.2004.11.008>
- Aliaari, M., & Memari, A. M. (2007). Experimental evaluation of a sacrificial seismic fuse device for masonry infill walls. *Journal of Architectural Engineering*, 13(2), 111–125. [https://doi.org/10.1061/\(asce\)1076-0431\(2007\)13:2\(111\)](https://doi.org/10.1061/(asce)1076-0431(2007)13:2(111))
- Almusallam, T. H., & Al-Salloum, Y. A. (2007). Behavior of FRP strengthened infill walls under in-plane seismic loading. *Journal of Composites for Construction*, 11(3), 308–318. [https://doi.org/10.1061/\(asce\)1090-0268\(2007\)11:3\(308\)](https://doi.org/10.1061/(asce)1090-0268(2007)11:3(308))

- Altin, S., Anil, Ö., Kara, M. E., & Kaya, M. (2008). An experimental study on strengthening of masonry infilled RC frames using diagonal CFRP STRIPS. *Composites Part B: Engineering*, 39(4), 680–693. <https://doi.org/10.1016/j.compositesb.2007.06.001>
- Amato, G., Fossetti, M., Cavaleri, L., & Papia, M. (2009). An updated model of equivalent diagonal strut for infill panels. In *Eurocode 8 perspectives from the Italian Standpoint Workshop* (pp. 119–128). Napoli, Italy.
- Anadolu Agency. Retrieved August 29, 2022, from <https://twitter.com/anadoluimages/status/1281662993500180480>
- Anderson, D., & Brzev, S. (2009). *Seismic Design Guide for Masonry Buildings*. Canadian Concrete Masonry Producers Association.
- Aref, A. J., & Jung, W.-Y. (2003). Energy-dissipating polymer matrix composite-infill wall system for seismic retrofitting. *Journal of Structural Engineering*, 129(4), 440–448. [https://doi.org/10.1061/\(asce\)0733-9445\(2003\)129:4\(440\)](https://doi.org/10.1061/(asce)0733-9445(2003)129:4(440))
- ASCE (American Society of Civil Engineers), ASCE-7: Minimum Design Loads for Buildings and Other Structures. (2010). Reston, Virginia.
- Asteris, P. G. (2003). Lateral stiffness of brick masonry infilled plane frames. *Journal of Structural Engineering*, 129(8), 1071–1079. [https://doi.org/10.1061/\(asce\)0733-9445\(2003\)129:8\(1071\)](https://doi.org/10.1061/(asce)0733-9445(2003)129:8(1071))
- Asteris, P. G., Antoniou, S. T., Sophianopoulos, D. S., & Chrysostomou, C. Z. (2011). Mathematical Macromodeling of infilled frames: State of the art. *Journal of Structural Engineering*, 137(12), 1508–1517. [https://doi.org/10.1061/\(asce\)st.1943-541x.0000384](https://doi.org/10.1061/(asce)st.1943-541x.0000384)
- ASTM, E519/E519M – 10: Standard Test Method for Diagonal Tension (Shear) in Masonry Assemblages (2010). West Conshohocken, PA, USA.
- Asteris, P. G., Cotsovos, D. M., Chrysostomou, C. Z., Mohebkah, A., & Al-Chaar, G. K. (2013). Mathematical Micromodeling of infilled frames: State of the art. *Engineering Structures*, 56, 1905–1921. <https://doi.org/10.1016/j.engstruct.2013.08.010>
- Aykac, B., Aykac, S., Kalkan, I., & Bocek, M. (2016). The out-of-plane bending behavior of brick infill walls strengthened with perforated steel plates. *Ingeniería, Investigación y Tecnología*, 17(4), 429–435. <https://doi.org/10.1016/j.riit.2016.11.002>
- Aykaç, B., Özbek, E., Babayani, R., Baran, M., & Aykaç, S. (2017). Seismic strengthening of infill walls with perforated steel plates. *Engineering Structures*, 152, 168–179. <https://doi.org/10.1016/j.engstruct.2017.09.015>
- Baber, T. T., & Wen, Y.-K. (1981). Random vibration of hysteretic, degrading systems. *Journal of the Engineering Mechanics Division*, 107(6), 1069–1087. <https://doi.org/10.1061/jmcea3.0002768>

- Bachmann, H. (2003). *Seismic Conceptual Design of Buildings – Basic principles for engineers, architects, building owners, and authorities*. Swiss Federal Office for Water and Geology.
- Bazan, E., & Meli, R. (1980). Seismic analysis of structures with masonry walls. In *Proceedings of the Seventh World Conference on Earthquake Engineering: September 8-13, 1980, Istanbul, Turkey* (Vol. 5, pp. 633–640). International Association of Earthquake Engineering (IAEE).
- Bažant, Z. P., & Oh, B. H. (1983). Crack band theory for fracture of concrete. *Matériaux Et Constructions*, 16(3), 155–177. <https://doi.org/10.1007/bf02486267>
- Bernal, D., Döhler, M., Kojidi, S. M., Kwan, K., & Liu, Y. (2015). First mode damping ratios for buildings. *Earthquake Spectra*, 31(1), 367–381. <https://doi.org/10.1193/101812eqs311m>
- Bertoldi, S. H., Decanini L. D., & Gavarini, C. (1993). Telai tamponati soggetti ad azioni sismiche, un modello semplificato: confronto sperimentale e numerico. Atti del 6 Convegno Nazionale L'ingegneria sismica in Italia 1993:815–24.
- Billington, S. L., Kyriakides, M. A., Blackard, B., Willam, K., Stavridis, A., & Shing, P. B. (2009). Evaluation of a Sprayable, Ductile Cement-based Composite for the Seismic Retrofit of Unreinforced Masonry Infills. In *Proceedings of the 2009 ATC & SEI conference on improving the seismic performance of buildings and other structures: December 9-11, 2009, San Francisco, California* (pp. 823–834). Reston, VA; American Society of Civil Engineers.
- Bolhassani, M., Hamid, A. A., Lau, A. C. W., & Moon, F. (2015). Simplified Micro Modeling of partially grouted masonry assemblages. *Construction and Building Materials*, 83, 159–173. <https://doi.org/10.1016/j.conbuildmat.2015.03.021>
- Bolt, B. A. (2003). *Earthquakes*. W.H. Freeman.
- Bouc, R. (1967). Forced vibration of mechanical systems with hysteresis. In *4th Conference on Non-linear Oscillation, Prague, September 5th-9th*. Československá akademie věd. Ústav radiotechniky a elektroniky.
- Brezinski, C., & Wuytack, L. (2001). *Numerical analysis: Historical developments in the 20th century*. Elsevier Science.
- Buonopane, S. G., & White, R. N. (1999). Pseudodynamic testing of masonry infilled reinforced concrete frame. *Journal of Structural Engineering*, 125(6), 578–589. [https://doi.org/10.1061/\(asce\)0733-9445\(1999\)125:6\(578\)](https://doi.org/10.1061/(asce)0733-9445(1999)125:6(578))
- Butenweg, C., & Marinković, M. (2018). Damage reduction system for masonry infill walls under seismic loading. *Ce/Papers*, 2(4), 267–273. <https://doi.org/10.1002/cepa.863>
- Butenweg, C., Marinković, M., & Salatić, R. (2019). Experimental results of reinforced concrete frames with masonry infills under combined quasi-static in-plane and out-of-

- plane seismic loading. *Bulletin of Earthquake Engineering*, 17(6), 3397–3422. <https://doi.org/10.1007/s10518-019-00602-7>
- Calvi, G. M., & Bolognini, D. (2001). Seismic response of reinforced concrete frames infilled with weakly reinforced masonry panels. *Journal of Earthquake Engineering*, 5(2), 153–185. <https://doi.org/10.1080/13632460109350390>
- Cavaleri, L., & Di Trapani, F. (2014). Cyclic response of masonry infilled RC frames: Experimental results and simplified modeling. *Soil Dynamics and Earthquake Engineering*, 65, 224–242. <https://doi.org/10.1016/j.soildyn.2014.06.016>
- Cavaleri, L., Fossetti, M., & Papia, M. (2005). Infilled frames: Developments in the evaluation of cyclic behaviour under lateral loads. *Structural Engineering and Mechanics*, 21(4), 469–494. <https://doi.org/10.12989/sem.2005.21.4.469>
- Celep, Z. (2011). *Structural Dynamics* (in Turkish). Beta Dagitim.
- CEN (European Committee for Standardization), EN 1015-11: Methods of test for mortar for masonry - Part 11: Determination of flexural and compressive strength of hardened mortar (2019a). Brussels, Belgium.
- CEN (European Committee for Standardization), EN 12390-3: Testing hardened concrete - Part 3: Compressive strength of test specimens (2019b). Brussels, Belgium.
- CEN (European Committee for Standardization), Eurocode 2: Design of concrete structures - Part 1: General rules and rules for buildings (2004a). Brussels, Belgium.
- CEN (European Committee for Standardization), Eurocode 6: Design of masonry structures - Part 1-1: General rules for reinforced and unreinforced masonry structures (2005). Brussels, Belgium.
- CEN (European Committee for Standardization), Eurocode 8: Design of structures for earthquake resistance - Part 1: General rules, seismic actions and rules for buildings (2004b). Brussels, Belgium.
- Chen, W.-F., & Lui, E. M. (2006). *Handbook of Structural Engineering*. CRC Press.
- Chopra, A. K. (1995). *Dynamics of Structures: Theory and applications to earthquake engineering*. Prentice Hall.
- Chrysostomou, C. Z., Gergely, P., & Abel, J. F. (2002). A six-strut model for nonlinear dynamic analysis of steel infilled frames. *International Journal of Structural Stability and Dynamics*, 02(03), 335–353. <https://doi.org/10.1142/s0219455402000567>
- Clough, R. W., & Penzien, J. (1995). *Dynamics of Structures*. McGraw-Hill.
- Colangelo, F. (2005). Pseudo-dynamic seismic response of reinforced concrete frames infilled with non-structural brick masonry. *Earthquake Engineering & Structural Dynamics*, 34(10), 1219–1241. <https://doi.org/10.1002/eqe.477>

- Computers & Structures Inc. (2015). *CSI Analysis Reference Manual*. Berkeley, CA, USA.
- Costa, A.C., & Costa, A. G. (1987). (rep.). *Hysteretic model of force displacement relationships for seismic analysis of structures*. Lisbon, Portugal: National Laboratory for Civil Engineering (LNEC).
- Crisafulli, F. J. (1997). *Seismic behavior of reinforced concrete structures masonry infills* (PhD dissertation). University of Canterbury, Christchurch, New Zealand.
- Crisafulli, F. J., & Carr, A. J. (2007). Proposed macro-model for the analysis of infilled frame structures. *Bulletin of the New Zealand Society for Earthquake Engineering*, 40(2), 69–77. <https://doi.org/10.5459/bnzsee.40.2.69-77>
- Cumhur, A., Altundal, A., Kalkan, I., & Aykac, S. (2016). Behaviour of brick infill walls strengthened with expanded steel plates. *Bulletin of Earthquake Engineering*, 14(11), 3231–3258. <https://doi.org/10.1007/s10518-016-9927-2>
- da Porto, F., Guidi, G., Verlato, N., & Modena, C. (2015). Effectiveness of plasters and textile reinforced mortars for strengthening clay masonry infill walls subjected to combined in-plane/out-of-plane actions / Wirksamkeit von Putz und textildbewehrtem Mörtel bei der Verstärkung von Ausfachungswänden aus Ziegel. *Mauerwerk*, 19(5), 334–354. <https://doi.org/10.1002/dama.201500673>
- Dassault Systèmes. (2016). *Abaqus v2016 Analysis User's Manual*. Dassault Systèmes: Vélizy-Villacoublay, France.
- Dawe, J. L., Schriver, A. B., & Sofocleous, C. (1989). Masonry infilled steel frames subjected to dynamic load. *Canadian Journal of Civil Engineering*, 16(6), 877–885. <https://doi.org/10.1139/189-130>
- De Risi, M. T., Del Gaudio, C., Ricci, P., & Verderame, G. M. (2018). In-plane behaviour and damage assessment of masonry infills with hollow clay bricks in RC frames. *Engineering Structures*, 168, 257–275. <https://doi.org/10.1016/j.engstruct.2018.04.065>
- Decanini, L., Mollaioli, F., Andrea, M., & Saragoni, R. (2004). Seismic performance of masonry infilled r/c frames. In *13th World Conference on Earthquake Engineering: Conference Proceedings, Vancouver, British Columbia, Canada, August 1-6, 2004*. Vancouver, BC; International Association for Earthquake Engineering (IAEE).
- Dehestani, M., & Mousavi, S. S. (2015). Modified steel bar model incorporating bond-slip effects for embedded element method. *Construction and Building Materials*, 81, 284–290. <https://doi.org/10.1016/j.conbuildmat.2015.02.027>
- Dehghani, A., Fischer, G., & Nateghi Alahi, F. (2013). Strengthening masonry infill panels using engineered cementitious composites. *Materials and Structures*, 48(1-2), 185–204. <https://doi.org/10.1617/s11527-013-0176-4>
- Dhanasekhar, M., & Page, A. W. (1986). The influence of brick masonry infill properties on the behaviour of I nfilled frames. *Proceedings of the Institution of Civil Engineers*, 81(4), 593–605. <https://doi.org/10.1680/iicep.1986.463>

- Doğangün, A., Ural, A., Sezen, H., Güney, Y., & Fırat, F. (2013). The 2011 earthquake in Simav, Turkey and seismic damage to reinforced concrete buildings. *Buildings*, 3(1), 173–190. <https://doi.org/10.3390/buildings3010173>
- Doudoumis, I. N., & Mitsopoulou, E. N. (1986). Nonlinear analysis of multistorey infilled frames for unilateral contact conditions. In *Proceedings of the 8th Conference on Earthquake Engineering: Lisbon, 1986*. Lisboa; Laboratório Nacional de Engenharia Civil.
- Douglas, J. (2003). Earthquake ground motion estimation using strong-motion records: A review of equations for the estimation of peak ground acceleration and Response Spectral ordinates. *Earth-Science Reviews*, 61(1-2), 43–104. [https://doi.org/10.1016/s0012-8252\(02\)00112-5](https://doi.org/10.1016/s0012-8252(02)00112-5)
- Dowell, R. K., Seible, F., & Wilson, E. L. (1998). Pivot hysteresis model for reinforced concrete members. *ACI Structural Journal*, 95(5), 607–617.
- Durrani, A. J., & Luo, Y. H. (1994). Seismic retrofit of flat-slab buildings with masonry infills. In *NCEER Workshop on Seismic Response of Masonry Infills*. Buffalo, NY; National Center for Earthquake Engineering Research (NCEER).
- El-Dakhkhni, W. W., Elgaaly, M., & Hamid, A. A. (2003). Three-strut model for concrete masonry-infilled steel frames. *Journal of Structural Engineering*, 129(2), 177–185. [https://doi.org/10.1061/\(asce\)0733-9445\(2003\)129:2\(177\)](https://doi.org/10.1061/(asce)0733-9445(2003)129:2(177))
- El-Dakhkhni, W. W., Hamid, A. A., & Elgaaly, M. (2004a). Strength and stiffness prediction of masonry infill panels. In *13th World Conference on Earthquake Engineering: Conference Proceedings, Vancouver, British Columbia, Canada, August 1-6, 2004*. Vancouver, B.C.; International Association for Earthquake Engineering (IAEE).
- El-Dakhkhni, W. W., Hamid, A. A., & Elgaaly, M. (2004b). Seismic retrofit of concrete-masonry-infilled steel frames with glass fiber-reinforced polymer laminates. *Journal of Structural Engineering*, 130(9), 1343–1352. [https://doi.org/10.1061/\(asce\)0733-9445\(2004\)130:9\(1343\)](https://doi.org/10.1061/(asce)0733-9445(2004)130:9(1343))
- Erdem, I., Akyuz, U., Ersoy, U., & Ozcebe, G. (2006). An experimental study on two different strengthening techniques for RC frames. *Engineering Structures*, 28(13), 1843–1851. <https://doi.org/10.1016/j.engstruct.2006.03.010>
- Erol, G., & Karadogan, H. F. (2016). Seismic strengthening of infilled reinforced concrete frames by CFRP. *Composites Part B: Engineering*, 91, 473–491. <https://doi.org/10.1016/j.compositesb.2016.01.025>
- Faconi, L., Minelli, F., & Giuriani, E. (2018). Response of infilled RC frames retrofitted with a cementitious fiber-mesh reinforced coating in moderate seismicity areas. *Construction and Building Materials*, 160, 574–587. <https://doi.org/10.1016/j.conbuildmat.2017.11.033>

- Fardis, M. N., & Panagiotakos, T. B. (1997). Seismic design and response of bare and masonry-infilled reinforced concrete buildings. part II: Infilled structures. *Journal of Earthquake Engineering*, 1(3), 475–503. <https://doi.org/10.1080/13632469708962375>
- Fardis, M. N., Bousias, S. N., Franchioni, G., & Panagiotakos, T. B. (1999). Seismic response and design of RC structures with plan-eccentric masonry infills. *Earthquake Engineering and Structural Dynamics*, 28(2), 173–191.
- FEMA (Federal Emergency Management Agency), FEMA 273, NEHRP Guidelines for the seismic rehabilitation of buildings (1997). Washington, D.C.
- FEMA (Federal Emergency Management Agency), FEMA 306, Evaluation of earthquake damaged concrete and masonry wall buildings: Basic procedures manual (1999). Washington, D.C.
- FEMA (Federal Emergency Management Agency), FEMA 356, Prestandard and commentary for the seismic rehabilitation of buildings (2000). Washington, D.C.
- Fib (International Federation for Structural Concrete), Model Code for Concrete Structures (2010). Lausanne, Switzerland.
- Fiorato, A. E., Sozen, M. A., & Gamble, W. L. (1970). (rep.). *An investigation of the interaction of reinforced concrete frames with masonry filler walls*. Urbana, Illinois.
- Fiore, A., Netti, A., & Monaco, P. (2012). The influence of masonry infill on the seismic behaviour of RC frame buildings. *Engineering Structures*, 44, 133–145. <https://doi.org/10.1016/j.engstruct.2012.05.023>
- Flanagan, R. D., & Bennett, R. M. (1999). In-plane behavior of structural clay tile infilled frames. *Journal of Structural Engineering*, 125(6), 590–599. [https://doi.org/10.1061/\(asce\)0733-9445\(1999\)125:6\(590\)](https://doi.org/10.1061/(asce)0733-9445(1999)125:6(590))
- Flanagan, R. D., & Bennett, R. M. (2001). In-plane analysis of masonry infill materials. *Practice Periodical on Structural Design and Construction*, 6(4), 176–182. [https://doi.org/10.1061/\(asce\)1084-0680\(2001\)6:4\(176\)](https://doi.org/10.1061/(asce)1084-0680(2001)6:4(176))
- Flickr. Retrieved August 29, 2022, from <https://www.flickr.com/photos/blieusong/27217216147/>
- Furtado, A., Rodrigues, H., & Arêde, A. (2017). Calibration of a simplified macro-model for infilled frames with openings. *Advances in Structural Engineering*, 21(2), 157–170. <https://doi.org/10.1177/1369433217713923>
- Furtado, A., Rodrigues, H., Arêde, A., & Varum, H. (2015). Simplified macro-model for infill masonry walls considering the out-of-plane behaviour. *Earthquake Engineering & Structural Dynamics*, 45(4), 507–524. <https://doi.org/10.1002/eqe.2663>
- Furtado, A., Rodrigues, H., Arêde, A., & Varum, H. (2020). Experimental tests on strengthening strategies for masonry infill walls: A literature review. *Construction and Building Materials*, 263, 120520. <https://doi.org/10.1016/j.conbuildmat.2020.120520>

- Gams, M., Kwiecień, A., Korelc, J., Rousakis, T., & Viskovic, A. (2017). Modelling of deformable polymer to be used for joints between infill masonry walls and R.C. frames. *Procedia Engineering*, 193, 455–461. <https://doi.org/10.1016/j.proeng.2017.06.237>
- Gao, X., Stavridis, A., Bolis, V., & Preti, M. (2018). Experimental Study on the Seismic Performance of non-ductile RC Frames Infilled with Sliding Subpanels. In *Eleventh U.S. National Conference on Earthquake Engineering, June 25-29, 2018*. Los Angeles, CA; Integrating Science, Engineering & Policy.
- Ghosh, A. K., & Amde, A. M. (2002). Finite element analysis of infilled frames. *Journal of Structural Engineering*, 128(7), 881–889. [https://doi.org/10.1061/\(asce\)0733-9445\(2002\)128:7\(881\)](https://doi.org/10.1061/(asce)0733-9445(2002)128:7(881))
- Giardini, D., Wössner, J., & Danciu, L. (2014). Mapping Europe's seismic hazard. *Eos, Transactions American Geophysical Union*, 95(29), 261–262. <https://doi.org/10.1002/2014eo290001>
- Goodno, B. J., Pinelli, J. P., & Craig, J. I. (1996). An optimal design approach for passive damping of building structures using architectural cladding. In *Eleventh world conference on earthquake engineering: Acapulco, Mexico, June 23-28, 1996 ; 11 WCEE*. Oxford; Pergamon.
- Griffith, M. (2008). (rep.). *Seismic Retrofit of RC Frame Buildings with Masonry Infill Walls: Literature Review and Preliminary Case Study*. European Commission Joint Research Centre.
- Gur, T., Pay, A. C., Ramirez, J. A., Sozen, M. A., Johnson, A. M., Irfanoglu, A., & Bobet, A. (2009). Performance of school buildings in Turkey during the 1999 Düzce and the 2003 Bingöl earthquakes. *Earthquake Spectra*, 25(2), 239–256. <https://doi.org/10.1193/1.3089367>
- Haroun, M. A., & Ghoneam, E. H. (1997). Seismic performance testing of masonry-infilled frames retrofitted by fiber composite. In *Proceedings of the 15th International Modal Analysis Conference: February 3-6, 1997, Sheraton World Resort, Orlando, Florida* (pp. 1650–1656). essay, Society for Experimental Mechanics, Inc.
- Hashemi, A., & Mosalam, K. M. (2006). Shake-table experiment on reinforced concrete structure containing masonry infill wall. *Earthquake Engineering & Structural Dynamics*, 35(14), 1827–1852. <https://doi.org/10.1002/eqe.612>
- Hermanns, L., Fraile, A., Alarcón, E., & Álvarez, R. (2013). Performance of buildings with masonry infill walls during the 2011 Lorca earthquake. *Bulletin of Earthquake Engineering*, 12(5), 1977–1997. <https://doi.org/10.1007/s10518-013-9499-3>
- Hetényi Miklós Imre. (1946). *Beams on Elastic Foundation: Theory with applications in the fields of civil and mechanical engineering*. University of Michigan Press.
- Holmes, M. (1961). Steel frames with brickwork and concrete infilling. *Proceedings of the Institution of Civil Engineers*, 19(4), 473–478. <https://doi.org/10.1680/iicep.1961.11305>

- Hojdys, Ł., Krajewski, P., Kwiecień, A., Rousakis, T., Vanian, V., Tekieli, M., Viskovic, A., Ilki, A., Gams, M., Rakicevic, Z., Zajac, B., & Bogdanovic, A. (2023). Quick repair of damaged infill walls with externally bonded FRPU composites: Shake table tests. *Journal of Composites for Construction*, 27(1). [https://doi.org/10.1061/\(asce\)cc.1943-5614.0001268](https://doi.org/10.1061/(asce)cc.1943-5614.0001268)
- Huang, H., Burton, H. V., & Sattar, S. (2020). Development and utilization of a database of infilled frame experiments for numerical modeling. *Journal of Structural Engineering*, 146(6), 04020079. [https://doi.org/10.1061/\(asce\)st.1943-541x.0002608](https://doi.org/10.1061/(asce)st.1943-541x.0002608)
- Ilki, A., Goksu, C., Demir, C., & Kumbasar, N. (2007). Seismic analysis of a RC frame building with FRP-retrofitted infill walls. In *Proceedings of the 6th International Conference on Fracture Mechanics of Concrete and Concrete Structures, Catania, Italy, 17-22 June 2007*. London; Taylor & Francis.
- ITSAK (Institute of Engineering Seismology and Earthquake Engineering). (2014). (rep.). *Strong ground motion of the February 3, 2014 (M6.0) Cephalonia earthquake: Effects on soil and built environment in combination with the January 26, 2014 (M6.1) event*. Thessaloniki, Greece: Ministry of Infrastructures Transportation and Networks.
- Jiang, H., Liu, X., & Mao, J. (2015). Full-scale experimental study on masonry infilled RC moment-resisting frames under cyclic loads. *Engineering Structures*, 91, 70–84. <https://doi.org/10.1016/j.engstruct.2015.02.008>
- Johnston, H., Watson, C., Pampanin, S., & Palermo, A. (2014). Shake table testing of an integrated low damage building system. In *Second European conference on earthquake engineering and seismology, 24-29 August 2014*. Istanbul, Turkey.
- Ju, R.-S., Lee, H.-J., Chen, C.-C., & Tao, C.-C. (2012). Experimental study on separating reinforced concrete infill walls from steel moment frames. *Journal of Constructional Steel Research*, 71, 119–128. <https://doi.org/10.1016/j.jcsr.2011.10.004>
- Kadysiewski, S., & Mosalam, K. M. (2009). (rep.). *Modeling of Unreinforced Masonry Infill Walls Considering In-Plane and Out-of-Plane Interaction*. Berkeley, CA: Pacific Earthquake Engineering Research Center (PEER).
- Kakaletsis, D. (2011). Comparison of CFRP and alternative seismic retrofitting techniques for bare and infilled RC frames. *Journal of Composites for Construction*, 15(4), 565–577. [https://doi.org/10.1061/\(asce\)cc.1943-5614.0000196](https://doi.org/10.1061/(asce)cc.1943-5614.0000196)
- Kappos, A. J., Stylianidis, K. C., & Michailidis, C. N. (1998). Analytical models for brick masonry infilled R/C frames under lateral loading. *Journal of Earthquake Engineering*, 2(1), 59–87. <https://doi.org/10.1080/13632469809350314>
- Karamanski, T. (1967). Calculating infilled frames by the method of finite elements. In *"Tall buildings: Symposium tall buildings, department of civil engineering, University of Southampton, April 1966"*. essay.

- Kassem, N., Atta, A., & Etman, E. (2016). Structural behavior of strengthening masonry infilled frames subjected to lateral load using bonded and un-bonded CFRP. *KSCE Journal of Civil Engineering*, 21(3), 818–828. <https://doi.org/10.1007/s12205-016-1389-1>
- Kaushik, H. B., Rai, D. C., & Jain, S. K. (2007). Stress-strain characteristics of clay brick masonry under uniaxial compression. *Journal of Materials in Civil Engineering*, 19(9), 728–739. [https://doi.org/10.1061/\(asce\)0899-1561\(2007\)19:9\(728\)](https://doi.org/10.1061/(asce)0899-1561(2007)19:9(728))
- Kesner, K., & Billington, S. L. (2005). Investigation of infill panels made from engineered cementitious composites for seismic strengthening and retrofit. *Journal of Structural Engineering*, 131(11), 1712–1720. [https://doi.org/10.1061/\(asce\)0733-9445\(2005\)131:11\(1712\)](https://doi.org/10.1061/(asce)0733-9445(2005)131:11(1712))
- King, G. J. W., & Pandey, P. C. (1978). The analysis of infilled frames using finite elements. *Proceedings of the Institution of Civil Engineers*, 65(4), 749–760. <https://doi.org/10.1680/iicep.1978.2707>
- Kisiel, P. (2015). The stiffness and bearing capacity of polymer flexible joint under shear load. *Procedia Engineering*, 108, 496–503. <https://doi.org/10.1016/j.proeng.2015.06.111>
- Kisiel, P. (2018). *Model Approach for Polymer Flexible Joints in Precast Elements Joints of Concrete Pavements* (PhD dissertation). Cracow University of Technology, Cracow, Poland.
- Klinger, R. E., & Bertero, V. V. (1976). (rep.). *Infilled Frames in Earthquake-Resistant Construction*. Washington, DC: National Science Foundation.
- Koçak, A., Kalyoncuoğlu, A., & Zengin, B. (2013). Effect of infill wall and wall openings on the fundamental period of RC Buildings. *WIT Transactions on The Built Environment*. <https://doi.org/10.2495/eres130101>
- Koutas, L., Bousias, S. N., & Triantafillou, T. C. (2015a). Seismic strengthening of masonry-infilled RC frames with TRM: Experimental study. *Journal of Composites for Construction*, 19(2), 04014048. [https://doi.org/10.1061/\(asce\)cc.1943-5614.0000507](https://doi.org/10.1061/(asce)cc.1943-5614.0000507)
- Koutas, L., Triantafillou, T. C., & Bousias, S. N. (2015b). Analytical modeling of masonry-infilled RC frames retrofitted with textile-reinforced mortar. *Journal of Composites for Construction*, 19(5), 04014082. [https://doi.org/10.1061/\(asce\)cc.1943-5614.0000553](https://doi.org/10.1061/(asce)cc.1943-5614.0000553)
- Koutromanos, I., Kyriakides, M., Stavridis, A., Billington, S., & Shing, P. B. (2013). Shake-table tests of a 3-story masonry-infilled RC frame retrofitted with Composite Materials. *Journal of Structural Engineering*, 139(8), 1340–1351. [https://doi.org/10.1061/\(asce\)st.1943-541x.0000689](https://doi.org/10.1061/(asce)st.1943-541x.0000689)
- Koutromanos, I., Stavridis, A., Shing, P. B., & Willam, K. (2011). Numerical modeling of masonry-infilled RC frames subjected to seismic loads. *Computers & Structures*, 89(11-12), 1026–1037. <https://doi.org/10.1016/j.compstruc.2011.01.006>

- Krätzig, W. B., & Pölling, R. (2004). An elasto-plastic damage model for reinforced concrete with minimum number of material parameters. *Computers and Structures*, 82(15-16), 1201–1215. <https://doi.org/10.1016/j.compstruc.2004.03.002>
- Kubalski, T., Butenweg, C., Marinković, M., & Klinkel, S. (2017). Investigation of the seismic behaviour of infill masonry using numerical modelling approaches. In *16th World Conference on Earthquake Engineering: Conference Proceedings, Santiago, Chile, January 9-13, 2017*. Chilean Association on Seismology and Earthquake Engineering (ACHISINA).
- Kwiecień, A. (2012). Polymer Flexible Joints in Masonry and Concrete Structures (in Polish). In *Monography, A Series of Civil Engineering* (No. 414). Kraków, Poland.
- Kwiecień, A. (2013). Highly deformable polymers for repair and strengthening of cracked masonry structures. *GSTF Journal of Engineering Technology*, 2(1). https://doi.org/10.5176/2251-3701_2.1.53
- Kwiecień, A., & Kuboń, P. (2012). Dynamic analysis of damaged masonry building repaired with the flexible joint method. *Archives of Civil Engineering*, 58(1), 39–55. <https://doi.org/10.2478/v.10169-012-0003-2>
- Kwiecień, A., Gams, M., Rousakis, T., Viskovic, A., & Korelc, J. (2017b). Validation of a New Hyperviscoelastic Model for Deformable Polymers Used for Joints between RC Frames and Masonry Infills. *Engineering Transactions*, 65(1), 113–121.
- Kwiecień, A., Gams, M., Viskovic, A., Kisiel, P., Korelc, J., & Rousakis, T. (2017a). Use of polymer flexible joint between RC frames and masonry infills for improved seismic performance. In *Proceedings of the SMAR Conference, Zurich, Switzerland, 27–29 August, 2017*.
- Kwiecień, A., Rakicevic, Z., Bogdanovic, A., Manojlovski, F., Poposka, A., Shoklarovski, A., Rousakis, T., Ilki, A., Gams, M., & Viskovic, A. (2021). PUFJ and FRPU earthquake protection of infills tested in resonance. In *Proceedings of the 1st Croatian Conference on Earthquake Engineering (1CroCEE), 22–24 March, 2021*.
- Kwiecień, A., Zająć, B., & Jankowski, R. (2008). Static and dynamic properties of a flexible joint working in cracked historical masonries. In *Proceedings of the VI International Conference on Structural Analysis of Historic Construction, Bath, United Kingdom, July 2-4, 2008*. CRC Press.
- Kwiecień, K., Kwiecień, A., Stryzewska, T., Szumera, M., & Dudek, M. (2020). Durability of PS-polyurethane dedicated for composite strengthening applications in masonry and concrete structures. *Polymers*, 12(12), 2830. <https://doi.org/10.3390/polym12122830>
- Kyriakides, M. A., & Billington, S. L. (2014). Cyclic response of nonductile reinforced concrete frames with unreinforced masonry infills retrofitted with engineered cementitious composites. *Journal of Structural Engineering*, 140(2), 04013046. [https://doi.org/10.1061/\(asce\)st.1943-541x.0000833](https://doi.org/10.1061/(asce)st.1943-541x.0000833)

- Kytinou, V. K., Chalioris, C. E., & Karayannis, C. G. (2020). Analysis of residual flexural stiffness of steel fiber-reinforced concrete beams with steel reinforcement. *Materials*, *13*(12), 2698. <https://doi.org/10.3390/ma13122698>
- Lasowicz, N., Kwiecień, A., & Jankowski, R. (2020). Experimental study on the effectiveness of polyurethane flexible adhesive in reduction of structural vibrations. *Polymers*, *12*(10), 2364. <https://doi.org/10.3390/polym12102364>
- Lee, H.-S., & Woo, S.-W. (2001). Effect of masonry infills on seismic performance of a 3-storey R/C frame with non-seismic detailing. *Earthquake Engineering and Structural Dynamics*, *31*(2), 353–378. <https://doi.org/10.1002/eqe.112>
- Lee, J., & Fenves, G. L. (1998). Plastic-damage model for cyclic loading of concrete structures. *Journal of Engineering Mechanics*, *124*(8), 892–900. [https://doi.org/10.1061/\(asce\)0733-9399\(1998\)124:8\(892\)](https://doi.org/10.1061/(asce)0733-9399(1998)124:8(892))
- Leeanansaksiri, A., Panyakapo, P., & Ruangrassamee, A. (2018). Seismic capacity of masonry infilled RC frame strengthening with expanded metal ferrocement. *Engineering Structures*, *159*, 110–127. <https://doi.org/10.1016/j.engstruct.2017.12.034>
- Liau, T. C., & Lee, S. W. (1977). On the behaviour and the analysis of multi-storey infilled frames subject to lateral loading. *Proceedings of the Institution of Civil Engineers*, *63*(3), 641–656. <https://doi.org/10.1680/iicep.1977.32593>
- Liau, T.-C., & Kwan, K.-H. (1984). Nonlinear behaviour of non-integral infilled frames. *Computers & Structures*, *18*(3), 551–560. [https://doi.org/10.1016/0045-7949\(84\)90070-1](https://doi.org/10.1016/0045-7949(84)90070-1)
- Longo, F., Wiebe, L., da Porto, F., & Modena, C. (1994). Seismic response history analysis including out-of-plane collapse of unreinforced masonry infill walls in RC frame structures. In *Proceedings of the 16th International Brick and Block Masonry Conference (IBMaC), 26-30 June, 2016, Padova, Italy*. CRC Press.
- Lotfi, H. R., & Shing, P. B. (1991). An appraisal of smeared crack models for masonry shear wall analysis. *Computers & Structures*, *41*(3), 413–425. [https://doi.org/10.1016/0045-7949\(91\)90134-8](https://doi.org/10.1016/0045-7949(91)90134-8)
- Lotfi, H. R., & Shing, P. B. (1994). Interface model applied to fracture of masonry structures. *Journal of Structural Engineering*, *120*(1), 63–80. [https://doi.org/10.1061/\(asce\)0733-9445\(1994\)120:1\(63\)](https://doi.org/10.1061/(asce)0733-9445(1994)120:1(63))
- Lourenco, P. B. (1996). *Computational strategies for masonry structures* (PhD dissertation). Delft University Press, Delft, The Netherlands.
- Lourenco, P. B. (1997). (rep.). *An Anisotropic Macro-Model for Masonry Plates and Shells: Implementation and Validation*. Delft University of Technology.
- Lublinter, J., Oliver, J., Oller, S., & Oñate, E. (1989). A plastic-damage model for concrete. *International Journal of Solids and Structures*, *25*(3), 299–326. [https://doi.org/10.1016/0020-7683\(89\)90050-4](https://doi.org/10.1016/0020-7683(89)90050-4)

- Lunn, D. S., & Rizkalla, S. H. (2011). Strengthening of infill masonry walls with FRP Materials. *Journal of Composites for Construction*, 15(2), 206–214. [https://doi.org/10.1061/\(asce\)cc.1943-5614.0000088](https://doi.org/10.1061/(asce)cc.1943-5614.0000088)
- Madan, A., Reinhorn, A. M., Mander, J. B., & Valles, R. E. (1997). Modeling of masonry infill panels for structural analysis. *Journal of Structural Engineering*, 123(10), 1295–1302. [https://doi.org/10.1061/\(asce\)0733-9445\(1997\)123:10\(1295\)](https://doi.org/10.1061/(asce)0733-9445(1997)123:10(1295))
- Maekawa, K., Okamura, H., & Pimanmas, A. (2003). Non-linear mechanics of reinforced concrete. <https://doi.org/10.1201/9781482288087>
- Mainstone, R. J. (1971). On the stiffness and strengths of infilled frames. *Proceedings of the Institution of Civil Engineers*, 4, 57–90.
- Mainstone, R. J. (1974). Supplementary note on the stiffness and strengths of infilled frames. *Building Research Station, Garston, UK*.
- Mainstone, R. J., & Weeks, G. A. (1970). The influence of bounding frame on the racking stiffness and strength of brick walls. In *Second International Brick Masonry Conference (SIBMAC)* (pp. 165–171). Watford; Building Research Establishment.
- Mallick, D. V., & Severn, R. T. (1967). The behaviour of infilled frames under static loading. *Proceedings of the Institution of Civil Engineers*, 38(4), 639–656. <https://doi.org/10.1680/iicep.1967.8192>
- Mallick, D. V., & Severn, R. T. (1968). Dynamic characteristics of infilled frames. *Proceedings of the Institution of Civil Engineers*, 39(2), 261–287. <https://doi.org/10.1680/iicep.1968.8091>
- Mander, J. B., Priestley, M. J., & Park, R. (1988). Theoretical stress-strain model for confined concrete. *Journal of Structural Engineering*, 114(8), 1804–1826. [https://doi.org/10.1061/\(asce\)0733-9445\(1988\)114:8\(1804\)](https://doi.org/10.1061/(asce)0733-9445(1988)114:8(1804))
- Marinković, M., & Butenweg, C. (2019). Innovative Decoupling System for the seismic protection of masonry infill walls in reinforced concrete frames. *Engineering Structures*, 197, 109435. <https://doi.org/10.1016/j.engstruct.2019.109435>
- McKenna, F. (2011). OpenSees: A framework for earthquake engineering simulation. *Computing in Science & Engineering*, 13(4), 58–66. <https://doi.org/10.1109/mcse.2011.66>
- Mehrabi, A. B., & Shing, P. B. (1997). Finite element modeling of masonry-infilled RC frames. *Journal of Structural Engineering*, 123(5), 604–613. [https://doi.org/10.1061/\(asce\)0733-9445\(1997\)123:5\(604\)](https://doi.org/10.1061/(asce)0733-9445(1997)123:5(604))
- Mehrabi, A. B., Benson Shing, P., Schuller, M. P., & Noland, J. L. (1996). Experimental evaluation of masonry-infilled RC frames. *Journal of Structural Engineering*, 122(3), 228–237. [https://doi.org/10.1061/\(asce\)0733-9445\(1996\)122:3\(228\)](https://doi.org/10.1061/(asce)0733-9445(1996)122:3(228))

- Mehrabi, A. B., Shing, P. B., Schuller, M. P., & Noland, J. L. (1994). (rep.). *Performance of Masonry-Infilled R/C Frames Under In-Plane Lateral Loads*. University of Colorado at Boulder.
- Milanesi, R. R., Totoev, Y., Morandi, P., Rossi, A., & Magenes, G. (2019). Estimation of basic dynamic characteristics of pliable masonry infills with horizontal sliding joints from in-plane test results. *Proceedings of the 7th International Conference on Computational Methods in Structural Dynamics and Earthquake Engineering (COMPDYN 2019)*. <https://doi.org/10.7712/120119.7093.19097>
- Misir, I. S., Ozcelik, O., Girgin, S. C., & Kahraman, S. (2012). Experimental work on seismic behavior of various types of masonry infilled RC frames. *Structural Engineering and Mechanics*, 44(6), 763–774. <https://doi.org/10.12989/sem.2012.44.6.763>
- Mochizuki, S. (1989). Inelastic behavior of framed shear wall governed by slip failure wall panel . In *Proceedings: Ninth World Conference on Earthquake Engineering, August 2-9, 1988, Tokyo-Kyoto, Japan* (Vol. 4). Tokyo, Japan; Japan Association for Earthquake Disaster Prevention.
- Mohammadi, M., Akrami, V., & Mohammadi-Ghazi, R. (2011). Methods to improve infilled frame ductility. *Journal of Structural Engineering*, 137(6), 646–653. [https://doi.org/10.1061/\(asce\)st.1943-541x.0000322](https://doi.org/10.1061/(asce)st.1943-541x.0000322)
- Mohyeddin, A., Goldsworthy, H. M., & Gad, E. F. (2013). FE modelling of RC frames with masonry infill panels under in-plane and out-of-plane loading. *Engineering Structures*, 51, 73–87. <https://doi.org/10.1016/j.engstruct.2013.01.012>
- Morandi, P., Milanesi, R. R., & Magenes, G. (2018). Innovative solution for seismic-resistant masonry infills with sliding joints: In-plane experimental performance. *Engineering Structures*, 176, 719–733. <https://doi.org/10.1016/j.engstruct.2018.09.018>
- Mosalam, K. M., White, R. N., & Gergely, P. (1997). Static response of infilled frames using quasi-static experimentation. *Journal of Structural Engineering*, 123(11), 1462–1469. [https://doi.org/10.1061/\(asce\)0733-9445\(1997\)123:11\(1462\)](https://doi.org/10.1061/(asce)0733-9445(1997)123:11(1462))
- Munjal, P., & Singh, S. B. (2020). Out-of-plane response of ECC-strengthened masonry walls. *Journal of Structural Integrity and Maintenance*, 5(1), 18–30. <https://doi.org/10.1080/24705314.2019.1692165>
- Nasiri, E., & Liu, Y. (2017). Development of a detailed 3D FE model for analysis of the in-plane behaviour of masonry infilled concrete frames. *Engineering Structures*, 143, 603–616. <https://doi.org/10.1016/j.engstruct.2017.04.049>
- Nasiri, E., & Liu, Y. (2019). The out-of-plane behaviour of concrete masonry infills bounded by reinforced concrete frames. *Engineering Structures*, 184, 406–420. <https://doi.org/10.1016/j.engstruct.2019.01.098>
- Negro, P., & Verzeletti, V. (1996). Effect of infills on the global behaviour of r/c frames: energy considerations from pseudodynamic tests. *Earthquake Engineering and Structural Dynamics*, 25(8), 753–773.

- Nicola, T., Leandro, C., Guido, C., & Enrico, S. (2015). Masonry infilled frame structures: State-of-the-art review of Numerical Modelling. *Earthquakes and Structures*, 8(1), 225–251. <https://doi.org/10.12989/eas.2015.8.1.225>
- Noh, N. M., Liberatore, L., Mollaioli, F., & Tesfamariam, S. (2017). Modelling of masonry infilled RC frames subjected to cyclic loads: State of the art review and modelling with openses. *Engineering Structures*, 150, 599–621. <https://doi.org/10.1016/j.engstruct.2017.07.002>
- Okazaki, T., Nakashima, M., Suita, K., & Matusmiya, T. (2007). Interaction between cladding and structural frame observed in a full-scale steel building test. *Earthquake Engineering & Structural Dynamics*, 36(1), 35–53. <https://doi.org/10.1002/eqe.618>
- Ozden, S., Akguzel, U., & Ozturan, T. (2011). Seismic Strengthening of Infilled Reinforced Concrete Frames with Composite Materials. *ACI Structural Journal*, 108(4), 414–422.
- Ozkaynak, H., Yuksel, E., Yalcin, C., Dindar, A. A., & Buyukozturk, O. (2013). Masonry infill walls in reinforced concrete frames as a source of structural damping. *Earthquake Engineering & Structural Dynamics*, 43(7), 949–968. <https://doi.org/10.1002/eqe.2380>
- Panagiotakos, T. N., & Fardis, M. N. (1996). Seismic response of infilled RC frames structures. In *Eleventh world conference on earthquake engineering: Acapulco, Mexico, June 23-28, 1996; 11 WCEE*. Oxford; Pergamon.
- Papanicolaou, C. G., Triantafyllou, T. C., Karlos, K., & Papathanasiou, M. (2007). Textile-reinforced mortar (TRM) versus FRP as strengthening material of urm walls: In-plane cyclic loading. *Materials and Structures*, 40(10), 1081–1097. <https://doi.org/10.1617/s11527-006-9207-8>
- Papia, M., Cavaleri, L., & Fossetti, M. (2003). Infilled frames: Developments in the evaluation of the stiffening effect of infills. *Structural Engineering and Mechanics*, 16(6), 675–693. <https://doi.org/10.12989/sem.2003.16.6.675>
- Parducci, A., & Mezzi, M. (1980). Repeated horizontal displacements of infilled frames having different stiffness and connection systems – experimental analysis. In *Proceedings of the Seventh World Conference on Earthquake Engineering, September 8-13, 1980, Istanbul, Turkey* (pp. 193–196). Ankara; Turkish National Committee on Earthquake Engineering.
- Paulay, T., & Priestley, M. J. N. (1992). *Seismic design of reinforced concrete and masonry buildings*. Wiley.
- Polyakov, S. V. (1956). Masonry in framed buildings (Translation into English by G.L.Cairns). essay, Gosudarstvennoe Izdatelstvo po Stroitelstvu I Arkhitekture Moscow .
- Preti, M., Bettini, N., & Plizzari, G. (2012). Infill walls with sliding joints to limit infill-frame seismic interaction: Large-scale experimental test. *Journal of Earthquake Engineering*, 16(1), 125–141. <https://doi.org/10.1080/13632469.2011.579815>
- Preti, M., Bolis, V., & Stavridis, A. (2017). Seismic infill–frame interaction of masonry walls partitioned with horizontal sliding joints: Analysis and simplified modeling. *Journal of*

- Preti, M., Migliorati, L., & Giuriani, E. (2015). Experimental testing of engineered masonry infill walls for post-earthquake structural damage control. *Bulletin of Earthquake Engineering*, 13(7), 2029–2049. <https://doi.org/10.1007/s10518-014-9701-2>
- Pujol, S., & Fick, D. (2010). The test of a full-scale three-story RC structure with masonry infill walls. *Engineering Structures*, 32(10), 3112–3121. <https://doi.org/10.1016/j.engstruct.2010.05.030>
- Razzaghi, M. S., & Javidnia, M. (2015). Evaluation of the effect of infill walls on seismic performance of RC dual frames. *International Journal of Advanced Structural Engineering*, 7(1), 49–54. <https://doi.org/10.1007/s40091-015-0081-x>
- Rodrigues, H., Varum, H., & Costa, A. (2008). A non-linear masonry infill macro-model to represent the global behaviour of buildings under cyclic loading. *International Journal of Mechanics and Materials in Design*, 4(2), 123–135. <https://doi.org/10.1007/s10999-008-9070-6>
- Rodrigues, H., Varum, H., & Costa, A. (2010). Simplified macro-model for infill masonry panels. *Journal of Earthquake Engineering*, 14(3), 390–416. <https://doi.org/10.1080/13632460903086044>
- Rousakis, T., Ilki, A., Kwiecien, A., Viskovic, A., Gams, M., Triller, P., Ghiassi, B., Benedetti, A., Rakicevic, Z., Colla, C., Halici, O. F., Zając, B., Hojdys, Ł., Krajewski, P., Rizzo, F., Vanian, V., Sapalidis, A., Papadouli, E., & Bogdanovic, A. (2020). Deformable polyurethane joints and fibre grids for resilient seismic performance of reinforced concrete frames with Orthoblock brick infills. *Polymers*, 12(12), 2869. <https://doi.org/10.3390/polym12122869>
- Rousakis, T., Kwiecien, A., Viskovic, A., Ilki, A., Tiller, P., Ghiassi, B., Benedetti, A., Gams, M., Rakicevic, Z., Halici, O. F., Zając, B., Hojdys, Ł., Krajewski, P., Rizzo, F., Colla, C., Gabrielli, E., Sapalidis, A., Papadouli, E., Vanian, V., & Bogdanovic, A. (2022). Quick reparation of infills in RC frames after seismic damages – experimental tests on shaking table. In: *Ilki, A., Ispir, M., Inci, P. (eds) 10th International Conference on FRP Composites in Civil Engineering. CICE 2021. Lecture Notes in Civil Engineering, vol 198. Springer, Cham.* https://doi.org/10.1007/978-3-030-88166-5_132
- Rousakis, T., Vanian, V., Fanaradelli, T., & Anagnostou, E. (2021). 3D FEA of infilled RC framed structures protected by seismic joints and FRP jackets. *Applied Sciences*, 11(14), 6403. <https://doi.org/10.3390/app11146403>
- Saatcioglu, M., Mitchell, D., Tinawi, R., Gardner, N. J., Gillies, A. G., Ghobarah, A., Anderson, D. L., & Lau, D. (2001). The August 17, 1999, Kocaeli (Turkey) earthquake — damage to structures. *Canadian Journal of Civil Engineering*, 28(4), 715–737. <https://doi.org/10.1139/cjce-28-4-715>
- Sachanski, S. (1960). Analysis of the earthquake resistance of frame buildings taking into consideration the carrying capacity of the filling masonry. In *Proceedings of the Second*

- World Conference on Earthquake Engineering* (pp. 2127–2141). Tokyo; Science Council of Japan.
- Sahota, M. K., & Riddington, J. R. (2001). Experimental investigation into using lead to reduce vertical load transfer in infilled frames. *Engineering Structures*, 23(1), 94–101. [https://doi.org/10.1016/s0141-0296\(00\)00025-0](https://doi.org/10.1016/s0141-0296(00)00025-0)
- Saneinejad, A., & Hobbs, B. (1995). Inelastic design of infilled frames. *Journal of Structural Engineering*, 121(4), 634–650. [https://doi.org/10.1061/\(asce\)0733-9445\(1995\)121:4\(634\)](https://doi.org/10.1061/(asce)0733-9445(1995)121:4(634))
- Schneemayer, A., Schranz, C., Kolbitsch, A., & Tschegg, E. K. (2014). Fracture-mechanical properties of mortar-to-brick interfaces. *Journal of Materials in Civil Engineering*, 26(9). [https://doi.org/10.1061/\(asce\)mt.1943-5533.0000955](https://doi.org/10.1061/(asce)mt.1943-5533.0000955)
- Schubert, P. (1994). Tensile and flexural strength of masonry: influences, test methods, test results. In *Proceedings of the 10th international brick and block masonry conference (IBMaC), 5-7 July, 1994, University of Calgary, Calgary, Alberta, Canada* (pp. 895–907). eds. N.G. Shrive and A. Huizer; Masonry Council of Canada.
- Seismosoft. (2015). SeismoMatch: Earthquake Software for Response Spectrum Matching (version 2.1.0). *Seismosoft Ltd. Pavia, Italy*.
- Sevil, T., Baran, M., Bilir, T., & Canbay, E. (2011). Use of steel fiber reinforced mortar for seismic strengthening. *Construction and Building Materials*, 25(2), 892–899. <https://doi.org/10.1016/j.conbuildmat.2010.06.096>
- Sezen, H., Elwood, K. J., Whittaker, A. S., Mosalam, K. M., Wallace, J. W., & Stanton, J. F. (2000). (rep.). *Structural Engineering Reconnaissance of the August 17, 1999, Kocaeli (Izmit), Turkey, Earthquake* (PEER 2000/09). Berkeley, CA: Pacific Earthquake Engineering Research Center.
- Sharbatdar, M. K., & Tajari, A. (2021). Experimental in-plane seismic strengthening of masonry infilled reinforced concrete frames by engineered cementitious composites (ECC). *Construction and Building Materials*, 293, 123529. <https://doi.org/10.1016/j.conbuildmat.2021.123529>
- Singh, H., Paul, D. K., & Sastry, V. V. (1998). Inelastic dynamic response of reinforced concrete infilled frames. *Computers & Structures*, 69(6), 685–693. [https://doi.org/10.1016/s0045-7949\(98\)00124-2](https://doi.org/10.1016/s0045-7949(98)00124-2)
- SIST (Slovenski Standard), SIST EN 1052-3:2004: Methods of test for masonry - Part 3: Determination of initial shear strength (2004).
- Smolira, M. (1973). Analysis of infilled shear walls. *Proceedings of the Institution of Civil Engineers*, 55(4), 895–912. <https://doi.org/10.1680/iicep.1973.4146>
- Soroushian, P. (1983). *Inelastic modeling and seismic analysis of reinforced masonry shear walls: Design recommendations and Energy Methods* (PhD dissertation). Cornell University, Ithaca, New York.

- Soroushian, P., Obaseki, K., & Choi, K. B. (1988). Nonlinear modeling and seismic analysis of masonry shear walls. *Journal of Structural Engineering*, 114(5), 1106–1119. [https://doi.org/10.1061/\(asce\)0733-9445\(1988\)114:5\(1106\)](https://doi.org/10.1061/(asce)0733-9445(1988)114:5(1106))
- Spence, R., Bommer, J., del Re, D., Bird, J., Aydinoglu, N., & Tabuchi, S. (2003). Comparing Loss Estimation with Observed Damage: A Study of the 1999 Kocaeli Earthquake in Turkey. *Bulletin of Earthquake Engineering*, 1(1), 83–113. <https://doi.org/10.1023/a:1024857427292>
- Stafford Smith, B. (1962). Lateral stiffness of infilled frames. *Journal of the Structural Division*, 88(6), 183–199. <https://doi.org/10.1061/jsdeag.0000849>
- Stafford Smith, B. (1966). Behavior of square infilled frames. *Journal of the Structural Division*, 92(1), 381–404. <https://doi.org/10.1061/jsdeag.0001387>
- Stafford Smith, B. (1967). Methods for predicting the lateral stiffness and strength of multi-storey infilled frames. *Building Science*, 2(3), 247–257. [https://doi.org/10.1016/0007-3628\(67\)90027-8](https://doi.org/10.1016/0007-3628(67)90027-8)
- Stafford Smith, B., & Carter, C. (1969). A method of analysis for infilled frames. *Proceedings of the Institution of Civil Engineers*, 44(1), 31–48. <https://doi.org/10.1680/iicep.1969.7290>
- Stavridis, A., & Shing, P. B. (2010). Finite-element modeling of nonlinear behavior of masonry-infilled RC frames. *Journal of Structural Engineering*, 136(3), 285–296. [https://doi.org/10.1061/\(asce\)st.1943-541x.116](https://doi.org/10.1061/(asce)st.1943-541x.116)
- Stavridis, A., Koutromanos, I., & Shing, P. B. (2011). Shake-table tests of a three-story reinforced concrete frame with masonry infill walls. *Earthquake Engineering & Structural Dynamics*, 41(6), 1089–1108. <https://doi.org/10.1002/eqe.1174>
- Stylianidis, K. C. (1988). Cyclic Behaviour of infilled R/C frames. In *Proceedings of the Eighth international brick and block masonry conference (IBMaC), 19-21 September, 1988, Trinity College, Dublin, Republic of Ireland* (pp. 792–799). London, UK; Elsevier Applied Science.
- Szczecina, M., & Winnicki, A. (2015). Calibration of the CDP model parameters in Abaqus. In *The 2015 World Congress on Advances in Structural Engineering and Mechanics (ASEM15), August 25-29, 2015*. Incheon, Korea.
- Tarque, N., Camata, G., Spacone, E., Varum, H., & Blondet, M. (2014). Nonlinear dynamic analysis of a full-scale unreinforced Adobe Model. *Earthquake Spectra*, 30(4), 1643–1661. <https://doi.org/10.1193/022512eqs053m>
- Tassios, T. P. (1984). Masonry infill and rc walls under cyclic actions. In *Third international symposium on wall structures: Warsaw, June 1984*. Warsaw, Poland; Centre for Building Systems, Research and Development.

- Thiruvengadam, V. (1985). On the natural frequencies of infilled frames. *Earthquake Engineering & Structural Dynamics*, 13(3), 401–419. <https://doi.org/10.1002/eqe.4290130310>
- Thomé, V. (2001). From finite differences to finite elements. *Journal of Computational and Applied Mathematics*, 128(1-2), 1–54. [https://doi.org/10.1016/s0377-0427\(00\)00507-0](https://doi.org/10.1016/s0377-0427(00)00507-0)
- Tiedemann, H. (1980). A statistical evaluation of the importance of non-structural damage to buildings. In *Proceedings of the Seventh World Conference on Earthquake Engineering: September 8-13, 1980, Istanbul, Turkey* (Vol. 5, pp. 617–624). International Association of Earthquake Engineering (IAEE).
- Totoev, Y., & Al Harthy, A. (2016). Semi interlocking masonry as infill wall system for earthquake resistant buildings: A Review. *The Journal of Engineering Research [TJER]*, 15(2), 33. <https://doi.org/10.24200/tjer.vol13iss1pp33-41>
- Triller, P., Kwiecień, A., Bohinc, U., Zając, B., Rousakis, T., & Viskovic, A. (2022). Preliminary in-plane shear test of damaged infill strengthened by FRPU. In: *Ilki, A., Ispir, M., Inci, P. (eds) 10th International Conference on FRP Composites in Civil Engineering. CICE 2021. Lecture Notes in Civil Engineering, vol 198. Springer, Cham.* https://doi.org/10.1007/978-3-030-88166-5_162
- Tsantilis, A. V., & Triantafillou, T. C. (2018). Innovative seismic isolation of masonry infills using cellular materials at the interface with the surrounding RC frames. *Engineering Structures*, 155, 279–297. <https://doi.org/10.1016/j.engstruct.2017.11.025>
- UNESCO. Retrieved March 24, 2023, from <https://whc.unesco.org/en/story-mostar-bridge/>
- USGS. *Earthquakes*. U.S. Geological Survey. Retrieved August 10, 2022, from <https://www.usgs.gov/programs/earthquake-hazards/earthquakes>
- Vailati, M., & Monti, G. (2016). Earthquake-resistant and thermo-insulating infill panel with recycled-plastic joints. *Earthquakes and Their Impact on Society*, 417–432. https://doi.org/10.1007/978-3-319-21753-6_15
- Vailati, M., Monti, G., & Di Gangi, G. (2017). Earthquake-safe and energy-efficient infill panels for modern buildings. *Earthquake Engineering and Structural Dynamics in Memory of Ragnar Sigbjörnsson*, 233–261. https://doi.org/10.1007/978-3-319-62099-2_12
- Valiasis, T. N., & Stylianidis, K. C. (1989). Masonry infilled R/C frames under horizontal loading - Experimental results. *Euro Earthq Eng*, 3(3), 10–20.
- Valluzzi, M. R., da Porto, F., Garbin, E., & Panizza, M. (2014). Out-of-plane behaviour of infill masonry panels strengthened with composite materials. *Materials and Structures*, 47(12), 2131–2145. <https://doi.org/10.1617/s11527-014-0384-6>
- Viskovic, A., Zuccarino, L., Kwiecień, A., Zając, B., & Gams, M. (2017). Quick seismic protection of weak masonry infilling in filled framed structures using flexible joints.

Key Engineering Materials, 747, 628–637.
<https://doi.org/10.4028/www.scientific.net/kem.747.628>

Wikipedia. Retrieved August 29, 2022, from <https://en.wikipedia.org/wiki/Colosseum>

Yuksel, E., Ozkaynak, H., Buyukozturk, O., Yalcin, C., Dindar, A. A., Surmeli, M., & Tastan, D. (2010). Performance of alternative CFRP retrofitting schemes used in infilled RC frames. *Construction and Building Materials*, 24(4), 596–609. <https://doi.org/10.1016/j.conbuildmat.2009.09.005>

Zarnic, R., & Tomazevic, M. (1986). Study of the behavior of masonry infilled reinforced concrete frames subjected to seismic loading. In *Proceedings of the Eighth World Conference on Earthquake Engineering, July 21-28, 1984, San Francisco, California, U.S.A* (pp. 1315–1325). Englewood Cliffs, NJ; Prentice-Hall.

Zarnic, R., Gostic, S., Crewe, A. J., & Taylor, C. A. (2001). Shaking table tests of 1:4 reduced-scale models of masonry infilled reinforced concrete frame buildings. *Earthquake Engineering and Structural Dynamics*, 30(6), 819–834. <https://doi.org/10.1002/eqe.39>

Zdanowicz, Ł., Kisiel, P., & Kwiecień, A. (2015). Stress redistribution in concrete floor on ground due to application of polymer flexible joint to fill expansion joint. *Procedia Engineering*, 108, 467–474. <https://doi.org/10.1016/j.proeng.2015.06.172>

Zdanowicz, Ł., Seręga, S., Tekieli, M., & Kwiecień, A. (2020). Polymer flexible joint as a repair method of concrete elements: Flexural testing and numerical analysis. *Materials*, 13(24), 5732. <https://doi.org/10.3390/ma13245732>

Zima, K., Wiczorek, D., & Kwiecień, A. (2022). Analysis of selected aspects of the life cycle for flexible joints between reinforced concrete frames and masonry infills. In *Proceedings of the International Conference on Istanbul and Earthquakes, March 4, 2022, Istanbul, Turkey*. Istanbul Aydin University Publications.